Source modelling at the dawn of gravitational-wave astronomy

Davide Gerosa

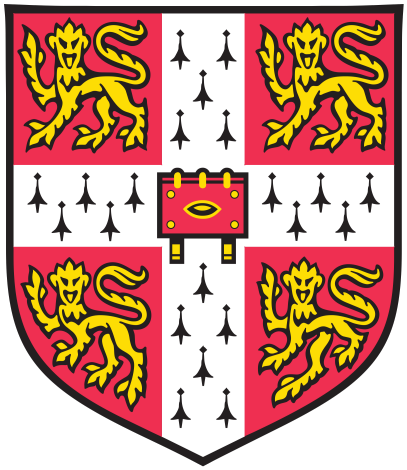

University of Cambridge

Department of Applied Mathematics and Theoretical Physics

Darwin College

September 2016

This dissertation is submitted for the degree of Doctor of Philosophy

I got something running around my head
That just won't keep
In the silence I hear my heart beating,
time slippin' away
I got a time bomb ticking deep inside of me
I gotta tell you what I wanna say
I keep searching for you, darling
Searching everywhere I go
And when I find you there's gonna be
Just one thing that you gotta know...

Bruce Springsteen

Preface

Summary

The age of gravitational-wave astronomy has begun. Gravitational waves are propagating spacetime perturbations ("*ripples in the fabric of space-time*") predicted by Einstein's theory of General Relativity. These signals propagate at the speed of light and are generated by powerful astrophysical events, such as the merger of two black holes and supernova explosions. The first detection of gravitational waves was performed in 2015 with the LIGO interferometers. This constitutes a tremendous breakthrough in fundamental physics and astronomy: it is not only the first direct detection of such elusive signals, but also the first irrefutable observation of a black-hole binary system. The future of gravitational-wave astronomy is bright and loud: the LIGO experiments will soon be joined by a network of ground-based interferometers; the space mission eLISA has now been fully approved by the European Space Agency with a proof-of-concept mission called LISA Pathfinder launched in 2015. Gravitational-wave observations will provide unprecedented tests of gravity as well as a qualitatively new window on the Universe. Careful theoretical modelling of the astrophysical sources of gravitational-waves is crucial to maximize the scientific outcome of the detectors. In this Thesis, we present several advances on gravitational-wave source modelling, studying in particular: (i) the precessional dynamics of spinning black-hole binaries; (ii) the astrophysical consequences of black-hole recoils; and (iii) the formation of compact objects in the framework of scalar-tensor theories of gravity. All these phenomena are deeply characterized by a continuous interplay between General Relativity and astrophysics: despite being a truly relativistic messenger, gravitational waves encode details of the astrophysical formation and evolution processes of their sources. We work out signatures and predictions to extract such information from current and future observations. At the dawn of a revolutionary era, our work contributes to turning the promise of gravitational-wave astronomy into reality.

Declaration

This dissertation is the result of my own work and includes nothing which is the outcome of work done in collaboration except as declared in the Preface and specified in the text. It is not substantially the same as any that I have submitted, or, is being concurrently submitted for a degree or diploma or other qualification at the University of Cambridge or any other University or similar institution except as declared in the Preface and specified in the text. I further state that no substantial part of my dissertation has already been submitted, or, is being concurrently submitted for any such degree, diploma or other qualification at the University of Cambridge or any other University of similar institution except as declared in the Preface and specified in the text. It does not exceed the prescribed word limit for the relevant Degree Committee.

Research overview

Most of the material presented in this dissertation has been published in international peer-reviewed journals and completed in scientific collaborations. In theoretical astrophysics, the order of authors in a publication reflects the importance of the contribution given to the project. I personally lead all my first-author publications, including those presented here. The main contributions presented in this Thesis can be summarised as follows.

- Chapter 1 consists in a review on gravitational-wave astronomy, and is unpublished.
- The main body of Chapter 2 is based on [206] with some inclusions from [269]; Appendix 2.A is based on [203]. This material has been completed in collaboration with Michael Kesden, Ulrich Sperhake, Emanuele Berti and Richard O'Shaughnessy. Michael Kesden started developing the analytics of effective-potential formalism and the precession-average approach which were then better understood and finalised by myself. The numerical implementation has been developed entirely by myself. Ulrich Sperhake, Emanuele Berti and Richard O'Shaughnessy provided invaluable guidance and suggestions throughout the project.
- The main body of Chapter 3 is based on [205], while Appendix 3.A consists of unpublished material. This piece of research has been completed in collaboration with Michael Kesden, Ulrich Sperhake, Emanuele Berti, Richard O'Shaughnessy, Antoine Klein and Daniele Trifiró. I derived the instability thresholds analytically and verified it numerically. Michael Kesden and Richard O'Shaughnessy understood that the

precessional period must be infinite for unstable binaries. Antoine Klein provided the numerical code to realise Fig. 3.4.

- Chapter 4 is based on [209] and has been completed in collaboration with Alberto Sesana. I developed the galaxy potential modelling and the numerical infrastructure to compute galaxy merger trees, while Alberto Sesana developed the analytical framework to estimate galaxy merger rates.

- Chapter 5 is based on [211] and has been completed in collaboration with Benedetta Veronesi, Giuseppe Lodato and Giovanni Rosotti. I developed the analytical estimates of the relevant timescales, the accretion prescriptions, the cosmological study and the kick analysis. Giuseppe Lodato pointed out the importance of non-linear warps and the stabilising effect of the companion. I was helped in finalising this project by Benedetta Veronesi (undergraduate student supervised by Giuseppe Lodato) and Giovanni Rosotti, who provided insights on planetary migration.

- Chapter 6 is based on [207] and has been completed in collaboration with Christopher Moore. I first realised that kicks can be detected directly using mass estimates, while Christopher Moore developed the numerical implementation of Doppler-shifted waveforms and the Fisher matrix analysis.

- Chapter 7 is based on [210] and has been completed in collaboration with Christian Ott and Ulrich Sperhake. Christian Ott provided the General-Relativity version of the code, as well as guidance on supernova physics. Ulrich Sperhake first started the derivation of the equations of motion in scalar-tensor theory and their numerical implementation. This was later checked and finalised by myself. I took care of all production runs and the analysis of the results.

Among the results presented here, Refs. [205, 269, 207] are published in Physical Review Letters; Refs. [269, 207] have been covered by press offices (see [423, 424]); and Refs. [205, 207] have been selected as "PRL Editors' suggestion" for their broad impact on gravitational-wave astronomy. The scientific papers [514, 247, 208], the community review [71] and the conference proceedings [201] were also completed during the course of my Ph.D and are not discussed in this Thesis. In total, I completed 12 publications during my Ph.D. My publication lists further features Refs. [317, 204] which were published before my Cambridge appointment started. Overall, I currently list 14 scientific publications in international peer-reviewed journals, with an h-index of 10. Beside scientific publications, an important outcome of my Ph.D research is the open-source numerical code PRECESSION

(Sec. 2.A and [203]). My research also provided educational activities, with two summer undergraduate students who worked under my supervision on black-hole binary spin precession [534] and black-hole superkicks.

Cambridge, September 2016

Davide Gerosa

Contents

Preface **5**

Summary . . . 5

Declaration . . . 6

Research overview . . . 6

Contents **9**

List of Figures . . . 13

List of Tables . . . 14

List of Acronyms . . . 15

1 A tale of astronomy and relativity **17**

Executive summary . . . 17

1.1 Light and gravity . . . 17

1.2 Sources and detectors . . . 19

1.2.1 Compact binaries are natural emitters . . . 19

1.2.2 Interferometers are natural receivers . . . 20

1.3 The interplay between astrophysics and relativity . . . 21

1.4 Main findings . . . 23

2 Multi-timescale analysis of black-hole binary spin precession **27**

Outlook . . . 27

Executive summary . . . 28

2.1 A tale of three timescales . . . 28

2.2 Analytic solutions on the precessional time scale . . . 30

2.2.1 Parametrization of precessional dynamics . . . 31

2.2.2 Effective potentials and resonances . . . 35

2.2.3 Morphological classification . . . 38

2.2.4 Time dependence . . . 45

2.3 Precession-averaged evolution on the inspiral timescale . . . 48
2.3.1 Averaging the average . . . 48
2.3.2 The large-separation limit . . . 51
2.3.3 Efficient binary transfer . . . 53
2.4 Morphological phase transitions . . . 58
2.4.1 Phenomenology of phase transitions . . . 58
2.4.2 Dependence on mass and spin asymmetry . . . 61
2.4.3 Predicting spin morphology at small separations . . . 65
2.5 Towards GW astronomy . . . 67
Appendix . . . 69
2.A PRECESSION: an open-source python module . . . 69
2.A.1 Installation . . . 69
2.A.2 A first working example . . . 70
2.A.3 Documentation and source distribution . . . 70

3 Up-down instability of spinning black-hole binaries **73**
Outlook . . . 73
Executive summary . . . 74
3.1 Spin-aligned configurations . . . 74
3.1.1 The role of BH spin (anti)alignment . . . 74
3.1.2 Generic spin precession . . . 75
3.2 Stability of aligned configurations . . . 76
3.2.1 Precessional (in)stability . . . 77
3.2.2 Inspiral dynamics . . . 78
3.3 Binaries may start precessing while being observed . . . 80
Appendix . . . 81
3.A Details on the stability analysis . . . 81
3.A.1 Derivatives of the effective potentials . . . 81
3.A.1.1 Up-up and down-down . . . 81
3.A.1.2 Up-down . . . 82
3.A.1.3 Down-up . . . 83
3.A.2 Precessional period . . . 84

4 Missing black holes in brightest cluster galaxies **87**
Outlook . . . 87
Executive summary . . . 88
4.1 Looking for superkicks . . . 88

4.2 BCG merger modeling . . . 90
4.2.1 BH final mass, spin and kick velocity . . . 91
4.2.2 BCG mass-density and potential profile . . . 94
4.2.3 Recoiled SMBH return timescales . . . 99
4.2.3.1 Dynamical-friction model . . . 100
4.2.3.2 Bounce model . . . 103
4.2.4 BCG merger rates . . . 105
4.2.5 Putting the pieces together . . . 108
4.2.6 Possible caveats . . . 109
4.3 Results and discussion . . . 111
4.3.1 Host properties: cluster shape and BCG merger rate . . . 112
4.3.1.1 Bounce and DF models . . . 112
4.3.1.2 Fiducial, Optimistic and Pessimistic models . . . 115
4.3.2 SMBH properties: spin magnitude and initial occupation fraction . . . 115
4.3.2.1 Spin magnitude . . . 116
4.3.2.2 Initial BCG occupation fraction . . . 117
4.3.3 Triaxiality and wandering SMBHs . . . 119
4.4 Strong gravity in BCGs . . . 122

5 Differential disc accretion and black-hole spin alignment 125
Outlook . . . 125
Executive summary . . . 126
5.1 Gas interactions: inspiral and alignment . . . 126
5.2 Binary and disc modelling . . . 128
5.2.1 Gas-driven inspiral . . . 129
5.2.2 Self-gravity condition . . . 132
5.2.3 BH spin alignment . . . 134
5.2.4 Effect of the companion on disc-spin alignment . . . 136
5.2.5 Cavity pile-up and differential accretion . . . 138
5.3 Results: differential misalignment . . . 142
5.3.1 Misaligned primary BHs . . . 142
5.3.1.1 Fiducial values of the parameters . . . 142
5.3.1.2 Predicted timescales . . . 144
5.3.2 Cosmologically-motivated distributions . . . 146
5.3.3 Differential misalignment and kick velocity . . . 148
5.4 Light secondaries prevent primaries from aligning . . . 151

6 Direct measurements of black-hole kicks **155**
Outlook . . . 155
Executive summary . . . 156
6.1 Direct vs. indirect observations of recoiling BHs . . . 156
6.2 Doppler mass shift . . . 157
6.3 Kicked waveforms . . . 160
6.4 Evidence for the linear momentum carried by GWs . . . 164

7 Stellar collapse in scalar-tensor theories of gravity **165**
Outlook . . . 165
Executive summary . . . 166
7.1 Compact-object formation to test GR . . . 166
7.2 Evolution equations . . . 169
7.2.1 A tale of two formulations . . . 169
7.2.2 Equation of motions . . . 171
7.2.2.1 Metric equations. . . . 173
7.2.2.2 Scalar-field equations. . . . 174
7.2.2.3 Matter equations in flux-conservative form. . . . 175
7.3 Physical setup . . . 176
7.3.1 Equation of state . . . 176
7.3.2 Coupling function . . . 178
7.3.3 Initial profiles . . . 181
7.3.4 GW extraction and detector sensitivity curves . . . 184
7.4 Numerical implementation . . . 186
7.4.1 Second-order finite differences and high-resolution shock capturing . . . 186
7.4.2 Self-convergence test . . . 189
7.5 Results and discussion . . . 191
7.5.1 Core-collapse dynamics . . . 191
7.5.2 Monopole GW emission . . . 195
7.5.2.1 Effect of the EOS . . . 196
7.5.2.2 Effect of the ST parameters. . . . 198
7.6 Future prospects and improvements . . . 203

Bibliography **207**

Acknowledgments **255**

List of Figures

2.1 Reference frames used to study binary BH spin precession 31
2.2 Effective potentials and contours of constant effective spin 35
2.3 Solutions for the evolution of the spin angles during a precession cycle . . . 40
2.4 The three morphologies of BH binary spin precession 41
2.5 Effective potentials in three different sets of spin morphologies 42
2.6 The (J, ξ) parameter space for binary BHs 44
2.7 Time-dependent solutions on the precessional timescale 46
2.8 Evolution of the total angular momentum during the inspiral 51
2.9 Comparison between orbit-averaged and precession-averaged evolutions . . 55
2.10 Numerical performance of binary transfer 57
2.11 Precessional solutions and morphological phase transitions 58
2.12 Evolution of the spin morphology 60
2.13 Fraction of binaries in the three precessional morphologies 62
2.14 Parameter-space exploration of morphological transitions 63
2.15 Morphologies and the asymptotic values of the spin angles 65
2.A.1 Minimal working example of the PRECESSION code 71

3.1 Effective-potential loops for up-down binaries 76
3.2 Spin-orbit resonances across the instability thresholds 78
3.3 Evolution of BH binaries in the $J\xi$ plane 79
3.4 GW waveform from up-down BH binaries 80

4.1 BCG kinematical properties 95
4.2 Observationally based BCG-halo relation 98
4.3 Relation between BCG and DM halo mass 99
4.4 SMBH return timescales 101
4.5 Return timescale fitting curve 104
4.6 BCG mass growth and number of major mergers 107
4.7 Return time and recoil velocity distributions 113
4.8 BCG occupation fractions 114
4.9 Deviations from the SMBH/host relation in replenished galaxies 116
4.10 Initial and final BCG occupation fraction 118
4.11 Wandering off center SMBHs 119

5.1 Effect of the companion on the location of the warp radius 136
5.2 Accretion rates of the two members of a BH binary 139
5.3 Pile-up at the edge of the disc cavity and differential accretion 141
5.4 Alignment and inspiral timescales 144
5.5 Mass ratio distributions in the synthetic SMBH binary populations 146
5.6 Fraction of aligned BH spins 148
5.7 Maximum kicks velocity as a function of the misalignment angles 150

6.1 GW shift due to BH kicks 158
6.2 Mismatches introduced by BH recoils 161
6.3 Detectability of BH kicks with LIGO and eLISA 163

7.1 Experimental constraints on the ST-theory parameters 180
7.2 Mass-density and scalar-field profiles for the initial data 183
7.3 Convergence test of stellar collapse in ST theory 190
7.4 Evolution of various initial profiles during collapse 192
7.5 Evolution of the central values of the mass density and lapse function . . . 193
7.6 Effect of the hybrid EOS on the emitted waveform 197
7.7 Effect of α_0 on frequency domain waveforms for monopole GWs 199
7.8 Effect of β_0 on frequency domain waveforms for monopole GWs 200

List of Tables

2.1 Parameter-space exploration of morphological transitions 64

5.1 Choice of binary and disc parameters 142
5.2 Transition between aligned and misaligned spins 145

List of Acronyms

ΛCDM: Λ Cold Dark Matter
AGN: Active Galactic Nucleus
BCG: Brightest Cluster Galaxy
BH: Black Hole
DECIGO: DECi-hertz Interferometer Gravitational-wave Observatory
DF: Dynamical Friction
DM: Dark Matter
E-ELT: European Extremely Large Telescope
eLISA: evolving Laser Interferometer Space Antenna
EOS: Equation Of State
ESA: European Space Agency
ET: Einstein Telescope
GR: General Relativity
GW: Gravitational Wave
ISCO: Innermost Stable Circular Orbit
LIGO: Laser Interferometer Gravitational-Wave Observatory
LISA: Laser Interferometer Space Antenna
NASA: National Aeronautics and Space Administration
NFW: Navarro-Frenk-White
NS: Neutron Star
ODE: Ordinary Differential Equation
PN: Post-Newtonian
PSD: Power Spectral Density
PTA: Pulsar Timing Array
SMBH: SuperMassive Black Hole
SN: SuperNova
SNR: Signal-to-Noise Ratio
SPH: Smoothed-Particle Hydrodynamics
ST: Scalar Tensor
SXS: Simulating eXtreme Spacetimes
TMT: Thirty Meter Telescope
WH: Woosley and Heger
ZAMS: Zero-Age Main Sequence

Chapter 1

A tale of astronomy and relativity

Executive summary

This Chapter provides a brief introduction, mostly based on order-of-magnitude estimates, to the field of Gravitational-Wave (GW) astronomy. Out aim is not to rival with excellent reviews [214, 506, 104, 417, 456, 444] and textbooks [372, 418, 230, 343] on the topic, but rather to highlight (in a perhaps unorthodox way) some of the peculiarities that make this growing field of science so innovative and exciting. This includes a comparison between electromagnetic waves and GWs (Sec. 1.1) and the interplay between astrophysics and relativity in determining the inspiral rate of Black Hole (BH) binaries (Sec. 1.3). We conclude with a summary of the main findings presented in this Thesis (Sec. 1.4).

1.1 Light and gravity

We are on the verge of a revolution in astronomy and relativity: we are entering the age of observational GW astronomy. Most (if not all) of the information we have collected about the Universe came to us through photons: since Galileo Galilei pointed his first telescope to the sky, we started exploring the Universe we live in, from the small scales where stars and planets form, to large scales comparable to the size of the entire Universe. In the past 70 years, our understanding of the Universe has been greatly revolutionized as we went beyond optical light and started exploring new bands of the electromagnetic spectrum. From radio waves to gamma rays, the opening of a new electromagnetic band always came not only with a deeper understanding of known sources (such as stars and galaxies), but also with serendipitous discoveries that shaped modern astrophysics. Some examples includes the discovery of the Cosmic Microwave Background [412], the identification of quasars [460],

pulsars [239], X-ray binaries [538, 95], gamma-ray bursts [281] and (more recently) fast radio bursts [326].

Since 2015, we can observe the Universe in an entirely new way, complementary to the electromagnetic spectrum. Predicted (although with controversies [175]) by Einstein himself in 1916 [172, 173, 174], GWs are ripples in the fabric of space-time: perturbations of the space-time itself travelling at the speed of light. GWs carry towards us a new set of information on the Universe, of a completely distinct kind than electromagnetic waves.

(i) While photons are emitted by charged particles, GWs are emitted by distributions of mass and momentum. On very fundamental grounds, through GWs we are sensible to a very different sector of the Universe.

(ii) Photons strongly couple to ordinary matter: although this property makes them easy to detect with our telescopes (and even naked eyes), it also implies that electromagnetic waves are likely to be scattered and/or absorbed by the intervening material, which therefore deteriorates the information we infer about their sources. Conversely, GWs couples very weakly to ordinary matter. Direct detection of GWs does require extraordinarily challenging experiments, but, at the same time, lets us probe the highly energetic dynamics of their sources directly. This point is particularly striking when considering particle decoupling in the early Universe. While the Universe became transparent to photons (neutrinos) about $\sim 4 \times 10^6$ yr (1 s) after the Big Bang, primordial gravitational radiation is emitted as early as $\sim 10^{-30}$ s after the Big Bang [456]. This signal is expected to be very weak (and certainly beyond the reach of any current experiment), but will tell us about the laws of physics at the very beginning of time.

(iii) Much like conservation of charge prevents monopole radiation in electromagnetism, monopole GWs are not allowed in General Relativity (GR) because of mass conservation. Momentum conservation further prevents propagating dipole gravitational radiation. Unlike electromagnetism, the lowest allowed propagating multipole of GWs is the quadrupole. This feature of GR is indeed crucial for astrophysics, as it makes binary systems (which are very abundant in any astrophysical context) a very natural source of GWs. We stress here however, that the absence of monopole and dipole gravitational radiation is a specific property of GR, which is absent in many of the viable alternative theories of gravity [134, 71].

1.2 Sources and detectors

1.2.1 Compact binaries are natural emitters

Since GWs are generated by quadrupole distribution of matter, the most natural (and indeed the first discovered [250, 13]) emitters of GWs are binary systems. Binary systems emit GWs at a frequency which is roughly twice the orbital frequency, because mass distribution repeats twice during each orbital cycle.

Let us define the quadrupole mass tensor

$$Q_{jk} = \int \rho x_j x_k d^3x \,, \tag{1.1}$$

where ρ is the mass density and x_i $(i = 1, 2, 3)$ are the spatial coordinates. The amplitude of the emitted GWs at leading order is (e.g. [372, 456])

$$h_{ij} = \frac{G}{c^4}\frac{2}{d}\frac{d^2 Q_{jk}}{dt^2} \,, \tag{1.2}$$

where d is the luminosity distance between the source and the observer. A simple order-of-magnitude estimate for the GW strain h emitted by a binary system is

$$h \sim \frac{G}{c^4}\frac{Mr^2}{T^2 d} \sim \frac{G}{c^4}\frac{Mv^2}{d} \,. \tag{1.3}$$

where r is the orbital separation, T is the orbital period, v is the orbital velocity and M is the total mass of the binary. A GW of strain h causes a deformation $\Delta L \sim hL$ over a spacetime region of length scale L. In other words, a detector of length L is sensible to a GW of strain h only if L can be measured with an accuracy $\Delta L = Lh$.

From these very simple estimates, one can immediately rule out detection of man-made GW sources. Imagine two small cars of $\sim 10^3$ kg, moving at the (very large) speed of 10^3 km/h on a track of 1 km radius. The GW strain observed at the closest possible distance of a single GW wavelength $\lambda \sim 5000$ km (similar to the Earth's radius) is $h \sim 10^{-40}$. Measuring lengths with such accuracy is beyond any current and foreseeable future technological capability. In order to obtain sensible GW strain values, one needs very compact binaries, with high orbital velocity. Astrophysics is kind enough to provide such objects: BHs [Neutron Starts (NSs)] have compactnesses of the order of $GM/Rc^2 \sim 1$ (~ 0.1) and, when part of a binary system, their orbital velocities reach a sizable fraction of the speed of light. Two stellar-mass BHs of $M \sim 10 M_\odot \sim 10^{31}$ kg at a separation of ~ 10 Schwarzschild radii orbit as fast as $v \sim 0.1c \sim 10^7$ m/s. Even at $d \sim 100$ Mpc

(further than the Virgo Cluster), the GW emission from such binary system results in a strain on Earth which is roughly $h \sim 10^{-21}$: 20 orders of magnitude more powerful than artificial sources. In order to measure such a signal with a km-scale detector, the length of the detector has to be measured with an accuracy of $\Delta L \sim 10^{-18}$ m, which smaller than the size of a single proton! This extreme scientific and technological challenge can now be faced.

1.2.2 Interferometers are natural receivers

Following decades of experiments involving resonant bars [537, 42, 528, 43, 357], the main current experimental technique to detect GWs relies on Michelson-Morley based laser interferometers [212, 375, 168]. In a nutshell, GWs stretch and shorten the two laser arms, thus producing an interference pattern. If distinguishable from instrumental and environment noise, the detection of such interference pattern can be used to reconstruct the properties of the GW source. In order to increase the effective length of the interferometer arms, modern ground-based interferometers use optical cavities of Fabry-Perot type, such that laser beams bounce many times along each arm before reaching the detection sensor. Given a displacement ΔL produced by a GW on the interferometer arms, the phase difference between the two light beams is roughly $\Delta\Phi = 2b\Delta L/\lambda_{\rm r}$ where $\lambda_{\rm r} \sim 10^{-8}$ cm is the reduced wavelength of the laser light and b is the number of bounces of the light in each arm. In order to successfully detect GWs, various noise sources need to be overcome to reach the incredible precision of $\Delta L \sim 10^{-18}$ m. The most important noise sources for ground-based interferometers are seismic noise, suspension thermal noise and quantum fluctuations in the number of photons reaching the photo detector (photon shot noise) (see e.g. [444]).

The ground-based LIGO (Laser Interferometer Gravitational-Wave Observatory) interferometers were constructed in the late 1990s in the USA and operated in science mode in 2005-2007 (Initial LIGO) and later in 2009-2010 (Enhanced LIGO) [22]. Although no GW was detected, this initial phase provided several astrophysical results (e.g. [21, 1, 4]) and key technological developments [22, 5, 2]. Following major experimental upgrades [228, 3], the Advanced LIGO detectors came finally online in 2015. At the very beginning of its science operations, LIGO detected its first GW signal, now dubbed GW150914 [13, 18, 6, 12, 9, 10, 20, 19, 350]. The source of GW150914 has been identified with the inspiral and merger of two BHs of $36^{+5}_{-A} M_\odot$ and $29^{+4}_{-4} M_\odot$ at $z = 0.09^{+0.03}_{-0.04}$. During its first operation run (September 2015 - January 2016), LIGO detected two BH binary mergers with high confidence, together with another lower-confidence event [11, 7]. Later in 2016, the European instrument VIRGO [23] will enter the LIGO network for the first

joint observation run. The Japanese detector KAGRA [41] and the proposed LIGO India [16] are expected to become operational in the next few years, while programs for third-generation detectors [such as the Einstein Telescope (ET) [429]] are currently under study. Ground-based detectors are sensible to GW frequencies of the order of $10-1000$ Hz. Their main targets are stellar-scale sources, such as stellar-mass BH binaries, NS binaries and Supernova (SN) explosions.

Longer detector arms are needed to observe lower frequency GW sources ($10^{-4}-10^{-1}$ Hz), which necessarily requires space-based detectors. The eLISA (evolving Laser Interferometer Space Antenna) space mission [27, 28, 469] (an evolved concept of the proposed LISA spacecrafts [150]) is now under development following the selection of its science theme for the third large-scale mission of ESA's (European Space Agency) "Cosmic Vision Program" [176]. A joint partnership with NASA (National Aeronautics and Space Administration) is currently being finalized. eLISA will consist of a constellation of three spacecrafts connected by laser links, equivalent to either two or three Michelson Interferometers with arms of $\sim 10^6$ km. eLISA will measure hundreds, if not thousands, of merging Supermassive Black Hole (SMBH) binaries up to cosmological redshift [48, 282, 501] as well as extreme-mass-ratio inspirals [195, 29, 44] and possibly even cosmological phase transitions [82, 116]. As a proof of technology, NASA and ESA launched the LISA Pathfinder mission in 2015 [33, 358] which successfully exceeded all requirements [32].

At even lower frequencies ($\sim 10^{-9}$ Hz), BHs with masses $\sim 10^9 M_\odot$ are currently being targeted by Pulsar Timing Arrays (PTAs) [345, 346, 261, 295]. This experimental technique relies on accurate timing of several pulsars using radio telescopes, effectively using the distance between us and the pulsars as arms of giant interferometers.

1.3 The interplay between astrophysics and relativity

The field of GW astronomy lies in between astrophysics and relativity. Although GWs themselves are a relativistic messenger, the dynamics of their sources is deeply affected by the astrophysical environment they live in: astrophysics is vital to predict and understand the properties of sources emitting GWs in the sensitivity windows of our detectors. To illustrate the importance of such interplay, here we discuss a simple example where astrophysics and relativity fruitfully play together, namely the inspiral rate of BH binaries.

Astrophysical BHs are present in the Universe in two well separated mass regimes. Stellar-mass BHs ($M \sim 10 M_\odot$) [120] constitute the endpoints of the life of some massive stars; while SMBHs ($M \sim 10^5 - 10^{10} M_\odot$) are hosted at the center of most galaxies [293] and constitute a fundamental ingredient to understand the evolution of large-scale structures

in the Universe. In both regimes, BHs are expected (and observed!) to form binary systems. Stellar-mass BH binaries are expected to form from isolated binaries stars [421] and dynamical interactions in dense stellar clusters [67]; while the formation of supermassive BH binaries is a natural outcome of galaxy mergers [541, 60].

Let us ask the following question: how long does a BH binary take to merge? Can astrophysical BH binaries merge within a Hubble time? Are astrophysical BH mergers relevant in nature?

Consider a BH binary with total mass M and mass ratio q on a circular orbit with separation r. GW emission dissipates energy and angular momentum, causing the binary orbit to shrink at the rate given by the Peters and Mathews approximation [415, 414]

$$\frac{dr}{dt} = -\frac{64}{5}\frac{G^3 M^3}{c^5 r^3}\frac{q}{(1+q)^2}\,. \tag{1.4}$$

The timescale on which the separation decreases because of GW emission

$$t_{\rm RR} \sim \frac{r}{|dr/dt|} \propto r^4\,, \tag{1.5}$$

is a steep power law of the separation r. GW emission is an efficient mechanism to dissipate angular momentum and shrink the binary's orbit only at small separation, while the emission rate gets weaker and weaker as the separation increases. In order to merge within a Hubble time $\sim 1.4\times 10^{10}$yr, the binary separation as to be smaller than the critical separation

$$r_{\rm GW} = 1.2\times 10^{11}\left(\frac{t_{\rm RR}}{1.4\times 10^{10}{\rm yr}}\right)^{1/4}\left(\frac{M}{M_\odot}\right)^{3/4}{\rm cm}. \tag{1.6}$$

which is roughly $\sim 10R_\odot$ (~ 0.01 pc) for stellar-mass (supermassive) BH binaries. In both the stellar-mass and the supermassive case, the separation $r_{\rm GW}$ is at the same time

i) much smaller than the separations at which binaries form;

ii) much greater than the separations at which binaries become detectable in GWs.

Because of (i), BH binaries take longer than the age of the Universe to enter the sensitivity windows of GW detectors *if* the inspiral is purely driven by GW emission. BH mergers are relevant phenomena in nature only if their astrophysical environments provide viable mechanisms to dissipate energy and angular momentum at separations $r \gtrsim r_{\rm GW}$. Stellar-mass BH binary formation channels often involve a so-called *common-envelope* phase [256, 403], where an already formed BH and a stellar core orbit in a shared hydrogen

envelope. The binding energy of the envelope is transferred to the binary, whose separation decreases by a factor ~ 1000. The issue is perhaps more severe in the SMBH context [135], where the search for viable astrophysical mechanisms to dissipate angular momentum is commonly referred to as *the final parsec problem* [370]. Proposed mechanisms include stellar scattering [123] (which however needs to be enhanced by some degree of triaxiality of the galactic potential to be a viable process [363]), and viscous dissipation through gas in the form of accretion discs [353] (although fragmentation may constitute a serious issue [319]).

Point (ii) above implies that if BH binaries become detectable in GWs, their dynamics is ruled by GR. GW signals can be often modelled in the elegant framework of vacuum GR, neglecting environmental effects that may deteriorate our measurements (e.g. [49, 50]). Depending on binary separation and mass-ratio, GW waveforms are modelled using techniques such as the Post-Newtonian (PN) expansion [86, 194], BH perturbation theory [455, 74] and numerical relativity [122, 496, 117]. Decoupling of the source dynamics and the astrophysical environment ultimately allows for the construction of accurate waveform templates, which constitutes a vital ingredient to perform GW detections [505, 8].

The fields of astronomy and relativity share a dominant role in our understanding of GW sources. **The interplay between astrophysics and GR is the leitmotif connecting the various topics presented in this Thesis.** We would like to introduce the reader to the main body of this work using the words of Thomas Gold, at his after-dinner speech at the 1st Symposium of Relativistic Astrophysics (Dallas TX, 1963). Shortly after the discovery of the first quasar [460], this seminal conference –where the term "Relativistic Astrophysics" was actually invented [468]– saw for the first time relativists and astrophysicists conveying together [254]:

> *Here we have a case that allowed one to suggest that the relativists with their sophisticated works were not only magnificent cultural ornaments but might actually be useful in science! Everyone is pleased: the relativists who feel they are being appreciated, who are suddenly experts in a field they hardly knew existed; the astrophysicists for having enlarged their domain by the annexation of another subject: general relativity. It is all very pleasing, so let us hope it is right!*

1.4 Main findings

The remaining content of this Thesis is organized in six Chapters, which address three main topics in relativistic astrophysics.

Chapters 2 and 3 tackle **spin precession in BH binaries**. In Chapter 2 we develop a thorough analysis of the dynamics of spinning BH binaries using innovative multi-timescale techniques. Spinning BH binaries present a remarkably interesting phenomenology because relativistic spin-spin and spin-orbit couplings cause the BH spins and the orbital plane to precess about the direction of the total angular momentum. Precessing binaries are deeply characterized by a timescale hierarchy: the orbital timescale is very short compared to the spin-precession timescale which, in turn, is much shorter than the radiation reaction timescale on which the orbit is shrinking due to GW emission. The binary dynamics has typically been studied in an orbit-averaged fashion, where one only tracks the evolution of the orbit itself, not the instantaneous position of each BH. Here we develop an innovative approach where we also average over the precessional time, thus considering the spin precessional cones as a whole, without tracking the spin's secular motion. This approach lets us define a new PN framework to study the evolution of precessing binary BHs. Our new solutions improve our understanding of spin precession in much the same way that the conical sections for Keplerian orbits provide additional insights beyond Newton's $1/r^2$ law. On the computational side, the new precession-averaged approach leads to an enormous speed-up, allowing us to evolve binaries from arbitrarily large separations, previously inaccessible. Our numerical tools are made available to the scientific community through the open-source code PRECESSION. In Chapter 3 we revisit the dynamics of BH binaries with aligned spins in light of our new multi-timescale methods developed for precessing systems. We unveiled a new dynamical instability in BH binaries where the spin of the more (less) massive BH is aligned (antialigned) to the angular momentum of the binary. When entering the instability region, any perturbation to such aligned (hence non-precessing) binaries will trigger large precession cycles. The onset of the instability lies in the sensitivity windows of current and future GW detectors, thus predicting binaries that start precessing while being observed!

In Chapters 4, 5 and 6 we study the **astrophysical consequences of BH recoils**. In the late inspiral and final coalescence of BH binaries, GWs are emitted anisotropically. The system loses net linear momentum and the remnant BH is consequently kicked in the opposite direction. Surprisingly, numerical-relativity simulations predict that the final kick can reach magnitudes up to ~ 5000 km/s ("superkicks"). This exceeds the escape speed of even the most massive galactic bulges, opening up the possibility of BH ejections. A direct consequence of high velocity kicks is that the SMBH occupation fraction in galaxies may be altered, providing an indirect way to test the strong-gravity physics behind BH mergers. In Chapter 4, we investigate the consequences of superkicks on the population of SMBHs in

the Universe residing in massive elliptical galaxies, showing that any future measurement of missing or undermassive BHs will point towards the occurrence of a superkick at recent times ($z \lesssim 1$). Such measurements are within the reach of future 30m-scale telescopes. The frequent occurrence of large kicks is difficult to reconcile with observations, as almost all large galaxies are found to host SMBHs. One solution to this problem is to align the BH spins before merger, because numerical relativity simulations only predict large recoils for merging BHs with substantially misaligned spins. Alignment can be achieved (and superkicks avoided) via gaseous interactions with surrounding accretion discs. In Chapter 5, we present an analytical timescale argument to tackle the disc-spin alignment problem in gas-rich galaxies. Using insights from the theory of planetary migration (which shares many physical mechanisms with SMBH accretion physics), we show that the binary mass ratio plays a major role in determining the degree of spin alignment. In particular, we find that light BHs may prevent their more massive companions from aligning. Chapter 6 presents a preliminary analysis to point out that BH kicks actually constitute a direct observable in GW astronomy. As the kick is imparted, the binary's center of mass accelerates and the emitted GW waveform gets Doppler-shifted. We devise a strategy to incorporate such effect into existing waveform models, and show that the identification of such *kicked* waveforms can be easily performed with the space-based detector eLISA. Direct observations of BH kicks will be of fundamental nature, since they will provide direct evidence for linear momentum carried by GWs.

Finally, Chapter 7 presents a study of **NS and BH formation in Scalar Tensor (ST) theories of gravity**. Although Solar System and binary-pulsar experiments have tested and confirmed GR with remarkable accuracy, the strong-field regime of the theory is still largely untested. Testing GR requires developing GW signatures in alternative theories of gravity, to be contrasted against future observations. Modifications of GR often lead to the introduction of additional degrees of freedom, inherited from some underlying high-energy theory. The simplest and most famous of these models are ST theories, where the spacetime metric is coupled non-minimally to one scalar field. The phenomenology of relativistic stars is remarkably interesting in such theories. The presence of a non-perturbative effect called "spontaneous scalarization" (somewhat similar to spontaneous magnetization in ferromagnets) makes the core-collapse dynamics and the formation of NSs and BHs qualitatively different from GR, thus providing an ideal way to constrain the parameters of the theory. Here we present the first simulations of collapse of realistic stars till the formation of the compact remnant using modern prescriptions for the microphysics and advanced shock-capturing numerical schemes. The most promising sources of scalar

radiation are protoneutron stars collapsing to BHs. In case of such an event, LIGO will be able to place the first constraints on ST theories in the strong-field, highly dynamical regime of gravity.

To summarize, the main scientific findings presented in this Thesis are:

- a first analysis of spinning BH binaries using multi-timescales techniques; development of a new PN approach to study such systems;
- discovery of a precessional instability in BH binaries with (anti)aligned spins;
- identification of missing SMBHs in large elliptical galaxies as a signature of the occurrence of superkicks at low redshifts;
- reinvestigation of the disc-spin alignment problem in merging SMBH binaries, using insight from planetary migration;
- identification of BH kicks as direct GW observables, through modelling of their Doppler-shifted waveforms;
- state-of-the-art numerical-relativity simulations of stellar collapse in ST theories of gravity.

Chapter 2

Multi-timescale analysis of black-hole binary spin precession

Outlook

The dynamics of precessing binary BHs in the PN regime has a strong timescale hierarchy: the orbital timescale is very short compared to the spin-precession timescale which, in turn, is much shorter than the radiation-reaction timescale on which the orbit is shrinking due to gravitational-wave emission. We exploit this timescale hierarchy to develop a multi-scale analysis of binary BH dynamics. The definition of an effective potential allows us to solve the orbit-averaged spin-precession equations analytically for arbitrary mass ratios and spins. These solutions are quasiperiodic functions of time: after a fixed period the BH spins return to their initial relative orientations and jointly precess about the total angular momentum by a fixed angle. We then implement a quasi-adiabatic approach to evolve these solutions on the longer radiation-reaction time. Our procedure leads to an innovative "precession-averaged" PN approach to studying precessing binary BHs. We use our new solutions to classify binary BH spin precession into three distinct morphologies, then investigate phase transitions between these morphologies as BH binaries inspiral. These precession-averaged PN inspirals can be efficiently calculated from arbitrarily large separations, thus making progress towards bridging the gap between astrophysics and numerical relativity.

Executive summary

This Chapter is organized as follows. In Sec. 2.1 we introduce the timescale hierarchy that characterizes the dynamics of BH binaries. In Sec. 2.2 we derive explicit solutions for generic BH binary spin precession at 2PN order on timescales short compared to the radiation-reaction time. In Sec. 2.3, we use our new solutions to precession average the radiation reaction on the binary at 1PN order and demonstrate how this precession averaging improves the computational efficiency with which GW-induced inspirals can be calculated compared to previous approaches relying solely on orbit averaging. Sec. 2.4 explores phase transitions between the three precessional morphologies, which are readily identified using our new formalism and have potentially interesting observational consequences. Finally, we conclude in Sec. 2.5, highlighting the relevance of our new PN approach to both the theoretical understanding of binary BHs and observational GW astronomy. Our numerical implementation is described in Appendix 2.A.

The material presented in this Chapter is based on [269, 206, 203].

2.1 A tale of three timescales

The two-body problem was a major engine of historical progress in physics and astronomy. It can be solved analytically in Newtonian gravity; its solutions are the well known Keplerian orbits. The analogs to Newtonian point masses in GR are binary BHs. Astrophysical BH binaries have spins [267, 439, 354, 368] in addition to their masses. Full solutions to the two-body problem in GR must therefore include spin evolution in addition to orbital motion. Einstein's equations must be solved numerically [426, 113, 45] when the binary separation r is comparable to the gravitational radius GM/c^2, but PN approximations may be used when $r \gg GM/c^2$ [418] (here M is the total mass of the binary).

Spinning BH binary dynamics is remarkably complex and interesting. BH binary systems have three angular momenta, the two spins and the orbital angular momentum, all coupled to each other. Spin-orbit and spin-spin couplings cause these angular momenta to precess, changing their orientation in space on the precession timescale [31, 276]. On the longer radiation-reaction timescale, GWs take energy and momentum out of the system, thus shrinking the orbit [415, 414]. These emitted GWs encode all the richness of the precessional dynamics but are also more challenging to detect and characterize than GWs emitted by non-precessing systems [100, 229, 140, 526, 182, 399, 125, 126].

In this Chapter we introduce a multi-timescale analysis of the dynamics of spinning, precessing binary BHs. Multi-timescale analyses are commonly used in binary dynamics.

For example, in eccentric binaries the orbital period, periastron precession, and radiation-reaction timescales usually differ by orders of magnitude; the dynamics of these systems can be studied using techniques that explicitly exploit this timescale hierarchy, such as osculating orbital elements [313] or the variation of constants [147]. Exploiting timescale hierarchies leads to deeper understanding of the dynamics because different physical processes are decoupled and individually analyzed.

Precessing binary BHs evolve on three distinct timescales:

1. BH binaries orbit each other (changing the binary separation $\mathbf{r}$) on the orbital time $t_{\rm orb} \sim r^{3/2}/(GM)^{1/2}$,

2. the spins and the orbital angular momentum change direction on the precession time $t_{\rm pre} \sim c^2 r^{5/2}/(GM)^{3/2}$ [31],

3. the magnitudes of the orbital energy and angular momentum decrease on the radiation-reaction time $t_{\rm RR} \sim c^5 r^4/(GM)^3$ [415].

In the post-Newtonian (PN) regime, $r \gg GM/c^2$ and these timescales are widely separated:

$$t_{\rm orb} \ll t_{\rm pre} \ll t_{\rm RR}\,. \tag{2.1}$$

BH binaries complete many orbits before their angular momenta appreciably precess, and the angular momenta complete many precession cycles before the separation decreases significantly.

The first inequality ($t_{\rm orb} \ll t_{\rm pre}$) has been widely exploited to understand spin dynamics and approximate the GW signal. This approximation forms the foundation of the orbit-averaged spin-precession equations for adiabatic quasicircular orbits examined extensively in the pioneering study of Apostolatos et al. [31] and later extended by Arun et al. [38, 39]. Using these equations, several authors have systematically explored the physics of spin precession and their implications for GW detection [301, 302] and astrophysics [76, 270]. Following the early work by Schnittman on spin-orbit resonances [463], PN spin dynamics has been used to predict the final spins [270] and recoils [271, 76] following BH binary mergers, select initial conditions for numerical-relativity simulations [329], characterize formation scenarios for stellar-mass BH binaries [204], and address the distinguishability of these scenarios by future GW observations [208, 529, 221].

The second inequality ($t_{\rm pre} \ll t_{\rm RR}$) has received less attention because until now there were no explicit solutions for generic spin precession (unlike the Keplerian orbits that readily allowed orbit averaging in previous work). Here we present new solutions for spin

precession that allow us to fully exploit the timescale hierarchy of Eq. (2.1). We show that spin precession is quasi-periodic implying that the relative orientations of the three angular momenta are fully specified by a single parameter, the magnitude of the total spin, that oscillates on the precession time. These solutions improve our understanding of spin precession in much the same way that the solutions $r(f) = a(1-e^2)/(1+e\cos f)$ for Keplerian orbits provide additional insight beyond Newton's law $\ddot{\mathbf{r}} = -GM\hat{\mathbf{r}}/r^2$. As is common in multi-timescale analyses, once the dynamics on the shorter time has been solved, the behavior of the system on the longer time scale can be studied as a quasi-adiabatic process. We evolve our precessional solutions during the inspiral by double-averaging the PN equations over both the orbital and the precessional timescales. Semi-analytical precession-averaged inspirals turn out to be extremely efficient and can be carried out from infinitely large separation with negligible computational cost.

While our focus in this work is on spin precession, our study benefits from several recent investigations which also used separation of timescales to efficiently and accurately approximate both the dynamics and the associated GW signal. A series of papers by Klein et al. [283, 125, 284] used a multi-scale analysis to construct semianalytic approximations to the frequency-domain waveforms for generic two-spin precessing binaries. Lundgren and O'Shaughnessy [338] used this timescale hierarchy to construct semianalytic approximations to the inspiral of precessing binaries with a single significant spin. The GWs emitted during the full inspiral-merger-ringdown of spinning, precessing binaries were also investigated using phenomenological models based on a single "effective spin" approximation [461, 224, 462] and the effective-one-body framework [406]. We mainly focus on the relative orientation of the momenta; the evolution of the global orientation of the system will be addressed elsewhere [554].

From now on in this Chapter, we use geometrical units ($G = c = 1$) and write vectors in boldface, denoting the corresponding unit vectors by hats and their magnitude as (e.g.) $L = |\mathbf{L}|$. Latin subscripts ($i = 1, 2$) label the BHs in the binary. Binaries are studied at separations $r \geq 10M$, taken as a simple but *ad hoc* threshold for the breakdown of the PN approximation [105, 114, 106]. Animated versions of some figures are available online at the URLs listed in [200].

2.2 Analytic solutions on the precessional time scale

In this Section we focus on the binary dynamics on the precessional time. Angular momentum conservation (Sec. 2.2.1) and the existence of a further constant of motion (Sec. 2.2.2) provide a simple parametrization of the binary dynamics through the identification of ef-

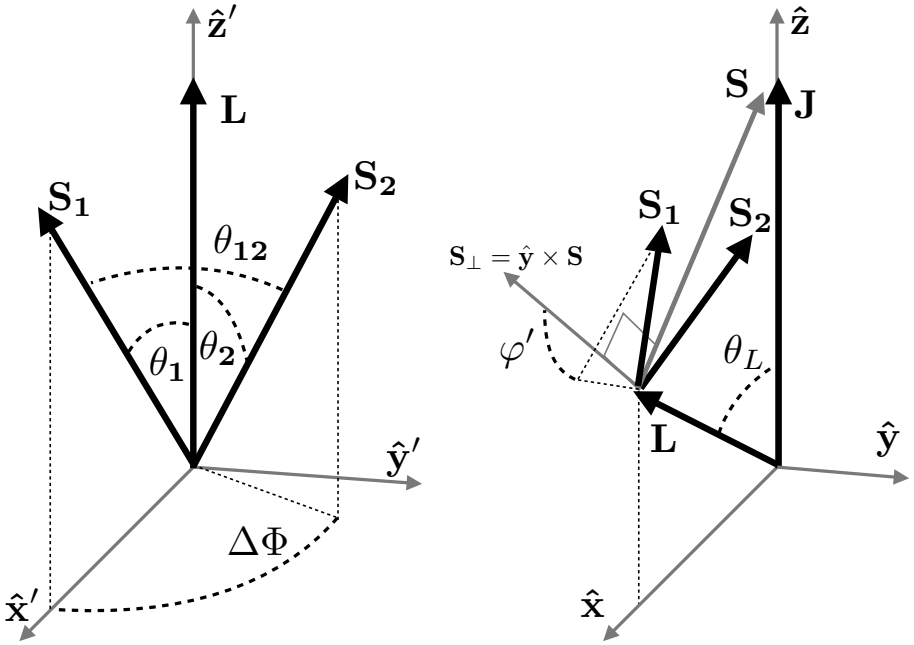

Figure 2.1: Reference frames used in this Chapter to study binary BH spin precession. The angles θ_1, θ_2, $\Delta\Phi$, and θ_{12} are defined in a frame aligned with the orbital angular momentum $\mathbf{L}$ (left panel). The binary dynamics can also be studied in a frame aligned with the total angular momentum $\mathbf{J}$ (right panel). Once $\mathbf{L}$ is taken to lie in the xz-plane, its direction is specified by S through the angle θ_L. The angle φ' corresponds to rotations of $\mathbf{S_1}$ and $\mathbf{S_2}$ about the total spin $\mathbf{S}$. The two frames pictured here are not inertial because the direction of $\mathbf{L}$ changes together with the spins to conserve $\mathbf{J}$. These angles are defined in Eqs. (2.2-2.5), (2.9) and (2.16).

fective potentials. Solutions are classified according to the precession geometry (Sec. 2.2.3) and eventually expressed in an inertial frame (Sec. 2.2.4).

2.2.1 Parametrization of precessional dynamics

Let us consider binary BHs on a circular orbit.[1] Let m_1 and m_2 denote the BH masses, in terms of which we can define the mass ratio $q = m_2/m_1 \leq 1$, the total mass $M = m_1 + m_2$, and the symmetric mass ratio $\eta = m_1 m_2/M^2$. The spin magnitudes $S_i = m_i^2 \chi_i$ $(i = 1, 2)$ are most conveniently parametrized in terms of the dimensionless Kerr parameter $0 \leq \chi_i \leq 1$, while the magnitude of the orbital angular momentum is related to the binary separation r through the Newtonian expression $L = \eta (r M^3)^{1/2}$.

The three angular momenta $\mathbf{L}$, $\mathbf{S_1}$ and $\mathbf{S_2}$ in principle constitute a nine-dimensional parameter space. However, there exist numerous constraints on the evolution of these parameters, greatly reducing the number of degrees of freedom. At the PN order considered

[1] Our approach can be readily generalized to nonzero eccentricity without complicating the geometry since the orbital pericenter precesses on a shorter timescale than the BH spins do. We restrict our attention to circular orbits since radiation reaction is expected to suppress the eccentricity at large separations for most astrophysical systems [415, 414].

here, the magnitudes of both spins are conserved throughout the inspiral (see e.g. [105]), reducing the number of degrees of freedom from nine to seven. The magnitude of the orbital angular momentum is conserved on the precession time (although it shrinks on the radiation-reaction time), further reducing the number of degrees of freedom from seven to six. The total angular momentum $\mathbf{J} = \mathbf{L} + \mathbf{S_1} + \mathbf{S_2}$ is also conserved on the precession time, reducing the number of degrees of freedom from six to three. As described in greater detail in the next subsection, the projected effective spin ξ [141, 431] is also conserved by both the orbit-averaged spin-precession equations at 2PN and radiation reaction at 2.5 PN order, providing a final constraint that reduces the system to just two degrees of freedom. In an appropriately chosen non-inertial reference frame precessing about $\mathbf{J}$, precessional motion associated with one of these degrees of freedom can be suppressed, implying that the relative orientations of the three angular momenta $\mathbf{L}$, $\mathbf{S_1}$ and $\mathbf{S_2}$ can be specified by just a single coordinate! We will provide an explicit analytic construction of this procedure in this and the following subsections.

We begin by introducing two alternative reference frames in which the relative orientations of the three angular momenta can be specified explicitly. As shown in the left panel of Fig. 2.1, one may choose the z'-axis to lie along $\mathbf{L}$, the x'-axis such that $\mathbf{S_1}$ lies in the $x'z'$-plane, and the y'-axis to complete the orthonormal triad. In this frame only three independent coordinates are needed to describe the relative orientations of the angular momenta; we choose them to be the angles

$$\cos\theta_1 = \hat{\mathbf{S}}_\mathbf{1} \cdot \hat{\mathbf{L}}\,, \tag{2.2}$$

$$\cos\theta_2 = \hat{\mathbf{S}}_\mathbf{2} \cdot \hat{\mathbf{L}}\,, \tag{2.3}$$

$$\cos\Delta\Phi = \frac{\hat{\mathbf{S}}_\mathbf{1} \times \hat{\mathbf{L}}}{|\hat{\mathbf{S}}_\mathbf{1} \times \hat{\mathbf{L}}|} \cdot \frac{\hat{\mathbf{S}}_\mathbf{2} \times \hat{\mathbf{L}}}{|\hat{\mathbf{S}}_\mathbf{2} \times \hat{\mathbf{L}}|}, \tag{2.4}$$

where the sign of $\Delta\Phi$ is given by (cf. Fig. 2.1)

$$\operatorname{sgn}\Delta\Phi = \operatorname{sgn}\{\mathbf{L} \cdot [(\mathbf{S_1} \times \mathbf{L}) \times (\mathbf{S_2} \times \mathbf{L})]\}. \tag{2.5}$$

The relative orientations of the three angular momenta can alternatively be specified in a frame aligned with the total angular momentum $\mathbf{J}$. For fixed values of L, S_1, and S_2, the allowed range for $J = |\mathbf{J}|$ is

$$J_{\rm min} \leq J \leq J_{\rm max} \tag{2.6}$$

where

$$J_{\rm min} = \max(0, L - S_1 - S_2, |S_1 - S_2| - L) \ , \tag{2.7}$$

$$J_{\rm max} = L + S_1 + S_2 \ . \tag{2.8}$$

As shown in the right panel of Fig. 2.1, one can choose the z-axis parallel to $\mathbf{J}$ and the x-axis such that $\mathbf{L}$ lies in the xz-plane:

$$\mathbf{J} = J\hat{\mathbf{z}} \quad \text{and} \quad \mathbf{L} = L\sin\theta_L\hat{\mathbf{x}} + L\cos\theta_L\hat{\mathbf{z}} \ . \tag{2.9}$$

The third unit vector $\hat{\mathbf{y}} = \hat{\mathbf{z}} \times \hat{\mathbf{x}}$ completes the orthonormal triad. The total spin $\mathbf{S} = \mathbf{S}_1 + \mathbf{S}_2 = \mathbf{J} - \mathbf{L}$ will also lie in the xz-plane:

$$\mathbf{S} = -L\sin\theta_L\hat{\mathbf{x}} + (J - L\cos\theta_L)\hat{\mathbf{z}} \ , \tag{2.10}$$

implying

$$\cos\theta_L = \frac{J^2 + L^2 - S^2}{2JL} \ . \tag{2.11}$$

We can also define a unit vector

$$\hat{\mathbf{S}}_\perp = \frac{(J - L\cos\theta_L)\hat{\mathbf{x}} + L\sin\theta_L\hat{\mathbf{z}}}{S} \tag{2.12}$$

which also lies in the xz-plane but is orthogonal to $\hat{\mathbf{S}}$.

While the magnitudes L and J of the orbital and total angular momenta are conserved on the precession timescale, the same is not true for the total-spin magnitude S, which oscillates within the range

$$S_{\rm min} \le S \le S_{\rm max} \ , \tag{2.13}$$

where

$$S_{\rm min} = \max(|J - L|, |S_1 - S_2|) \ , \tag{2.14}$$

$$S_{\rm max} = \min(J + L, S_1 + S_2) \ . \tag{2.15}$$

S can be used as a generalized coordinate to specify the directions of the angular momenta $\mathbf{J}$, $\mathbf{L}$, and $\mathbf{S}$; we can see from Eqs. (2.9-2.11) that it is the only coordinate needed to specify these directions in the xyz-frame.

Specifying the directions of the individual spins $\mathbf{S_1}$ and $\mathbf{S_2}$ in the xyz-frame requires an additional generalized coordinate, which can be chosen to be the angle φ' between $\hat{\mathbf{S}}_\perp$ in Eq. (2.12) and the projection of $\mathbf{S_1}$ into the plane spanned by $\hat{\mathbf{S}}_\perp$ and $\hat{\mathbf{y}}$, as shown in the right panel of Fig. 2.1. This angle corresponds to rotations of $\mathbf{S_1}$ and $\mathbf{S_2}$ about $\mathbf{S}$ and is given analytically by

$$\cos\varphi' = \frac{\hat{\mathbf{S}}_\mathbf{1}\cdot\hat{\mathbf{S}}_\perp}{|\hat{\mathbf{S}}_\mathbf{1}\times\hat{\mathbf{S}}|}\,. \tag{2.16}$$

In terms of the two coordinates S and φ' varying on the precession timescale, the three angular momenta in the xyz-frame are

$$\mathbf{L} = \frac{A_1A_2}{2J}\hat{\mathbf{x}} + \frac{J^2+L^2-S^2}{2J}\hat{\mathbf{z}}\,, \tag{2.17}$$

$$\begin{aligned}\mathbf{S_1} &= \frac{S^2+S_1^2-S_2^2}{2S}\hat{\mathbf{S}} + \frac{A_3A_4}{2S}(\cos\varphi'\hat{\mathbf{S}}_\perp + \sin\varphi'\hat{\mathbf{y}})\\ &= \frac{1}{4JS^2}[-(S^2+S_1^2-S_2^2)A_1A_2 + (J^2-L^2+S^2)A_3A_4\cos\varphi']\hat{\mathbf{x}}\\ &\quad + \frac{1}{2S}A_3A_4\sin\varphi'\hat{\mathbf{y}}\\ &\quad + \frac{1}{4JS^2}[(S^2+S_1^2-S_2^2)(J^2-L^2+S^2) + A_1A_2A_3A_4\cos\varphi']\hat{\mathbf{z}}\,,\end{aligned} \tag{2.18}$$

$$\begin{aligned}\mathbf{S_2} &= \frac{S^2+S_2^2-S_1^2}{2S}\hat{\mathbf{S}} - \frac{A_3A_4}{2S}(\cos\varphi'\hat{\mathbf{S}}_\perp + \sin\varphi'\hat{\mathbf{y}})\\ &= -\frac{1}{4JS^2}[(S^2+S_2^2-S_1^2)A_1A_2 + (J^2-L^2+S^2)A_3A_4\cos\varphi']\hat{\mathbf{x}}\\ &\quad - \frac{1}{2S}A_3A_4\sin\varphi'\hat{\mathbf{y}}\\ &\quad + \frac{1}{4JS^2}[(S^2+S_2^2-S_1^2)(J^2-L^2+S^2) - A_1A_2A_3A_4\cos\varphi']\hat{\mathbf{z}}\,,\end{aligned} \tag{2.19}$$

where we defined:

$$A_1 \equiv [J^2-(L-S)^2]^{1/2}\,, \qquad A_2 \equiv [(L+S)^2-J^2]^{1/2}\,, \tag{2.20}$$

$$A_3 \equiv [S^2-(S_1-S_2)^2]^{1/2}\,, \qquad A_4 \equiv [(S_1+S_2)^2-S^2]^{1/2}\,. \tag{2.21}$$

All the A_i's are real and positive in the ranges specified by Eqs. (2.6) and (2.13).

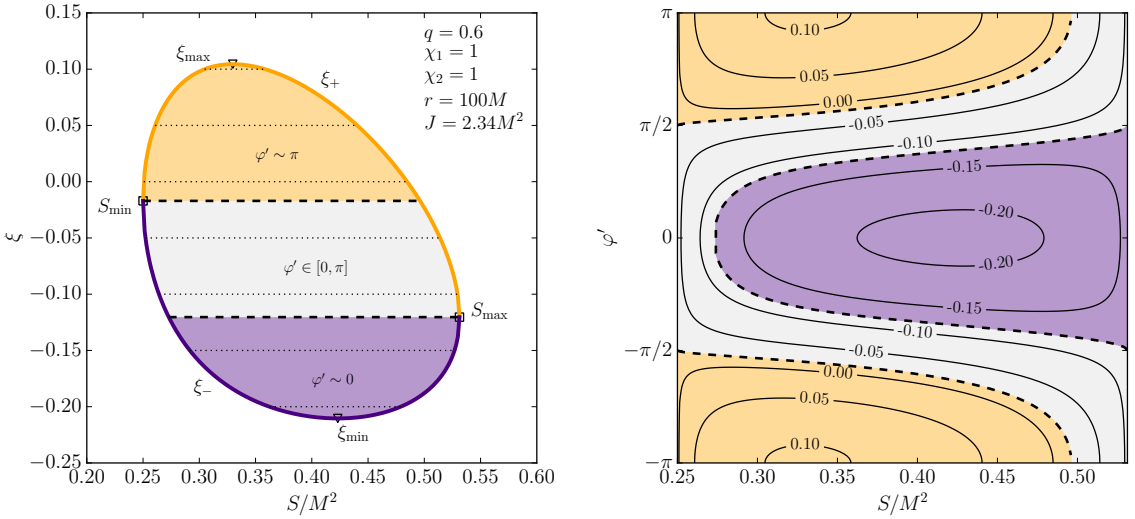

Figure 2.2: *Left:* Effective potentials $\xi_\pm(S)$ for binary BHs with $q = 0.6$, $\chi_1 = \chi_2 = 1$, $r = 100M$, and $J = 2.34M^2$. Conservation of the projected effective spin ξ constrains the BH spins to precess along horizontal lines bounded by the effective-potential curves. The horizontal dashed lines intersecting the effective potentials at $S_{\min}$ and $S_{\max}$ (marked by empty squares) divide BH spin precession into three different morphological phases distinguished by whether the angle φ' defined by Eq. (2.16) oscillates about π (top orange region), circulates from $-\pi$ to π (middle grey region), or oscillates about 0 (bottom purple region). The effective potentials admit two extrema $\xi_{\min}$ and $\xi_{\max}$ (marked by empty triangles) corresponding to the spin-orbit resonances discovered in [463]. *Right:* Contours of constant $\xi(S, \varphi')$ given by Eq. (2.23) for the same binary parameters. As BH binary spins precess along the horizontal dashed lines in the left panel, they move along the curves in the $S\varphi'$-plane in the right panel illustrating the three morphological phases.

2.2.2 Effective potentials and resonances

As anticipated in the previous subsection, there is an additional conserved quantity that can be used to eliminate φ' and thereby specify $\mathbf{L}$, $\mathbf{S_1}$, and $\mathbf{S_2}$ with the single generalized coordinate S. This quantity is the projected effective spin [141, 431]

$$\xi \equiv M^{-2}\left[(1+q)\,\mathbf{S}_1 + \left(1+\frac{1}{q}\right)\mathbf{S}_2\right]\cdot\hat{\mathbf{L}} \tag{2.22}$$

which is a constant of motion of the orbit-averaged spin-precession equations at 2PN order and is also conserved by radiation reaction at 2.5 PN order. Using Eqs. (2.17-2.19), we can express ξ as a function of S and φ'

$$\xi(S,\varphi') = \frac{(J^2-L^2-S^2)[S^2(1+q)^2-(S_1^2-S_2^2)(1-q^2)]-(1-q^2)A_1A_2A_3A_4\cos\varphi'}{4qM^2S^2L}\,. \tag{2.23}$$

Conservation of ξ restricts binary evolution to one-dimensional curves $\xi(S, \varphi') = \xi$ in the $S\varphi'$-plane as shown in the right panel of Fig. 2.2. The simple dependence of $\xi(S, \varphi')$ on

φ' motivates us to define two "effective potentials" corresponding to the extreme cases $\cos\varphi' = \mp 1$ for which $\mathbf{L}$, $\mathbf{S_1}$ and $\mathbf{S_2}$ are all coplanar:

$$\xi_\pm(S) = \frac{(J^2 - L^2 - S^2)[S^2(1+q)^2 - (S_1^2 - S_2^2)(1-q^2)] \pm (1-q^2)A_1A_2A_3A_4}{4qM^2S^2L}\,. \tag{2.24}$$

At $S_{\rm min}$ and $S_{\rm max}$

$$\xi_-(S_{\rm min}) = \xi_+(S_{\rm min})\,, \qquad \xi_-(S_{\rm max}) = \xi_+(S_{\rm max})\,, \tag{2.25}$$

because one of the A_i's defined in Eqs. (2.20-2.21) vanishes if $S = S_{\rm min}$ or $S = S_{\rm max}$. The functions $\xi_\pm(S)$ thus form a loop that encloses all allowed values of S and ξ, as shown in the left panel of Fig. 2.2. BH binaries are constrained to evolve back and forth along horizontal line segments of constant ξ bounded by the two effective potentials $\xi_\pm(S)$. The turning points in the evolution of S are given by the solutions of $\xi_\pm(S) = \xi$, where the binary meets an effective potential. Once squared, the equation $\xi_\pm(S) = \xi$ reduces to the following cubic equation in S^2:

$$\sigma_6 S^6 + \sigma_4 S^4 + \sigma_2 S^2 + \sigma_0 = 0\,, \tag{2.26}$$

where

$$\sigma_6 = q(1+q)^2\,, \tag{2.27}$$

$$\sigma_4 = (1+q)^2[-2J^2q + L^2\left(1+q^2\right) + 2LM^2\xi q + (1-q)\left(S_2^2 - qS_1^2\right)]\,, \tag{2.28}$$

$$\begin{aligned}\sigma_2 = {}& 2(1+q)^2(1-q)[J^2(qS_1^2 - S_2^2) - L^2(S_1^2 - qS_2^2)] + q(1+q)^2(J^2-L^2)^2 \\ & - 2LM^2\xi q(1+q)[(1+q)(J^2-L^2) + (1-q)(S_1^2 - S_2^2)] + 4L^2M^4\xi^2q^2\,,\end{aligned} \tag{2.29}$$

$$\begin{aligned}\sigma_0 = {}& (1-q^2)[L^2(1-q^2)(S_1^2 - S_2^2)^2 - (1+q)(qS_1^2 - S_2^2)(J^2-L^2)^2 \\ & + 2LM^2q\xi(S_1^2 - S_2^2)(J^2 - L^2)]\,,\end{aligned} \tag{2.30}$$

which admits at most three real solutions for $S > 0$. The number of solutions in the range allowed by Eq. (2.13) must be even because the two effective potentials form a closed loop and the Jordan curve theorem requires the number of intersections between a continuous closed loop and a line to be even [231] (although these intersections can coincide at extrema). Since two is the largest even number less than three, the equation $\xi_\pm(S) = \xi$ will generally have two solutions which we denote by $S_\pm$ ($S_- \leq S_+$).

The total-spin magnitude S will oscillate between S_- and S_+ implying that spin precession is quasi-periodic (this will be shown explicitly in Sec. 2.2.4 below). The motion of the spins is not fully periodic because in an inertial frame the basis vectors $\hat{\mathbf{x}}$ and $\hat{\mathbf{y}}$ will generally not precess about $\mathbf{J}$ by a rational multiple of π radians in the time it takes S to complete a full cycle from S_- and S_+ and back again. The turning points $S = S_\pm$ lie on the effective potentials, implying from the definition $\cos\varphi' = \mp 1$ that all three vectors $\mathbf{L}$, $\mathbf{S_1}$, and $\mathbf{S_2}$ are coplanar. The qualitative evolution of φ' is related to the nature of the turning points $S_\pm$. This is illustrated in Fig. 2.2, where horizontal lines in the effective-potential diagram (left panel) correspond to contours of constant $\xi(S, \varphi')$, computed using Eq. (2.23) (right panel). Three different cases are possible.

1. Both turning points lie on ξ_+:

$$\xi_+(S_+) = \xi_+(S_-) = \xi\,. \tag{2.31}$$

   φ' oscillates about π never reaching 0 (orange region in Fig. 2.2).

2. One turning point is on ξ_- and the other is on ξ_+:

$$\xi_\pm(S_-) = \xi_\mp(S_+) = \xi\,. \tag{2.32}$$

   φ' monotonically circulates from $-\pi$ to π during each precession cycle (grey region in Fig. 2.2).

3. Both turning points lie on ξ_-:

$$\xi_-(S_+) = \xi_-(S_-) = \xi\,. \tag{2.33}$$

   φ' oscillates about 0 never reaching π (purple region in Fig. 2.2).

The boundaries between the three regions are given by those values of ξ at which one of the turning points $S_\pm$ coincides with either $S_{\rm min}$ or $S_{\rm max}$ (dashed lines in Fig. 2.2). Note that $\xi(S_{\rm min})$ may be less or greater than $\xi(S_{\rm max})$ depending on the values of q, χ_i, r and J.

The two turning points are degenerate ($S_+ = S_-$) at the extrema $\xi_{\rm min}$ and $\xi_{\rm max}$ of the

effective potentials. At these extrema the derivatives

$$\frac{d\xi_\pm}{dS} = \frac{1+q}{2qM^2S^3L}\Bigg\{(1-q)(J^2-L^2)(S_1^2-S_2^2) - (1+q)S^4 \\ \pm \frac{1-q}{A_1A_2A_3A_4}\Big[S^8 - (J^2+L^2+S_1^2+S_2^2)S^6 + (J^2+L^2)(S_1^2-S_2^2)^2S^2 \\ + (S_1^2+S_2^2)(J^2-L^2)^2S^2 - (S_1^2-S_2^2)^2(J^2-L^2)^2\Big]\Bigg\} \tag{2.34}$$

vanish and $S = S_- = S_+$ is constant. Since

$$\lim_{S\to S_{\rm min}} \frac{d\xi_+}{dS} \geq \lim_{S\to S_{\rm min}} \frac{d\xi_-}{dS}\,, \tag{2.35}$$

$$\lim_{S\to S_{\rm max}} \frac{d\xi_+}{dS} \leq \lim_{S\to S_{\rm max}} \frac{d\xi_-}{dS}\,, \tag{2.36}$$

and at most two turning points can exist, it follows that ξ_+ admits a single maximum in $[S_{\rm min}, S_{\rm max}]$ and ξ_- admits a single minimum in $[S_{\rm min}, S_{\rm max}]$. The effective potentials therefore have exactly two distinct extrema for each value of the constants J, r, q, χ_1 and χ_2. As clarified below, these special configurations correspond to the spin-orbit resonances discovered by other means in [463].

The equal-mass limit $q \to 1$ corresponds to $\xi_+(S) = \xi_-(S)$ [cf. Eq. (2.24)] implying that S is constant for all values of ξ [note that $\xi_\pm(S_{\rm min}) \neq \xi_\pm(S_{\rm max})$]. This fact was noted at least as early as 2008 by Racine [431] and it was recently exploited in numerical-relativity simulations [334, 329], but the constancy of S is a peculiarity of the equal-mass case and does not hold for generic binaries. The dynamics of equal-mass binaries will be specifically targeted in [534].

2.2.3 Morphological classification

Although the evolution of φ' already provides a way to characterize the precessional dynamics (Fig. 2.2), a more intuitive understanding can be gained by switching back to the **L**-aligned frame illustrated in the left panel of Fig. 2.1. Substituting Eqs. (2.17-2.19) and (2.23) into Eq. (2.2-2.4), we can express the angles θ_1, θ_2 and $\Delta\Phi$ as functions of S, J and

ξ. This yields the remarkably simple expressions

$$\cos\theta_1 = \frac{1}{2(1-q)S_1}\left[\frac{J^2-L^2-S^2}{L} - \frac{2qM^2\xi}{1+q}\right], \tag{2.37}$$

$$\cos\theta_2 = \frac{q}{2(1-q)S_2}\left[-\frac{J^2-L^2-S^2}{L} + \frac{2M^2\xi}{1+q}\right], \tag{2.38}$$

$$\cos\Delta\Phi = \frac{\cos\theta_{12} - \cos\theta_1\cos\theta_2}{\sin\theta_1\sin\theta_2}, \tag{2.39}$$

where the angle $\theta_{12} = \arccos\hat{\mathbf{S}}_\mathbf{1}\cdot\hat{\mathbf{S}}_\mathbf{2}$ between the two spins can also be written in terms of S:

$$\cos\theta_{12} = \frac{S^2 - S_1^2 - S_2^2}{2S_1S_2}. \tag{2.40}$$

Equations (2.37-2.39) parametrize double-spin binary precession using a single parameter S. Some examples of the evolution of these angles over a precessional cycle are given in Fig. 2.3. The evolution of θ_1 and θ_2 is monotonic as S evolves between its two turning points $S_\pm$; over a full precessional cycle these angles oscillate between two extrema lying on the effective potentials (dotted curves in Fig. 2.3). The evolution of $\Delta\Phi$ can be classified into three morphological phases similar to that of φ':

1. $\Delta\Phi$ oscillates about 0 (never reaching π) if

$$\Delta\Phi(S_-) = \Delta\Phi(S_+) = 0\,; \tag{2.41}$$

2. $\Delta\Phi$ circulates through the full range $[-\pi,\pi]$ if

$$\Delta\Phi(S_\pm) = 0 \quad \text{and} \quad \Delta\Phi(S_\mp) = \pi\,; \tag{2.42}$$

3. $\Delta\Phi$ oscillates about π (never reaching 0) if

$$\Delta\Phi(S_-) = \Delta\Phi(S_+) = \pi\,. \tag{2.43}$$

The evolution of $\Delta\Phi$ allows us to unambiguously categorize the precessional dynamics into the three different classes listed above. We refer to these classes as *morphologies* because of the different shapes traced out by the BH spins over a precession cycle. These three possibilities (libration about $\Delta\Phi = 0°$, circulation, and libration about $\Delta\Phi = 180°$) are shown in the left, center, and right panels of Fig. 2.4. We show some examples of how the allowed region inside the effective-potential loop is divided between these three morphologies in Fig. 2.5. BH binaries in the two oscillating morphologies are adjacent to

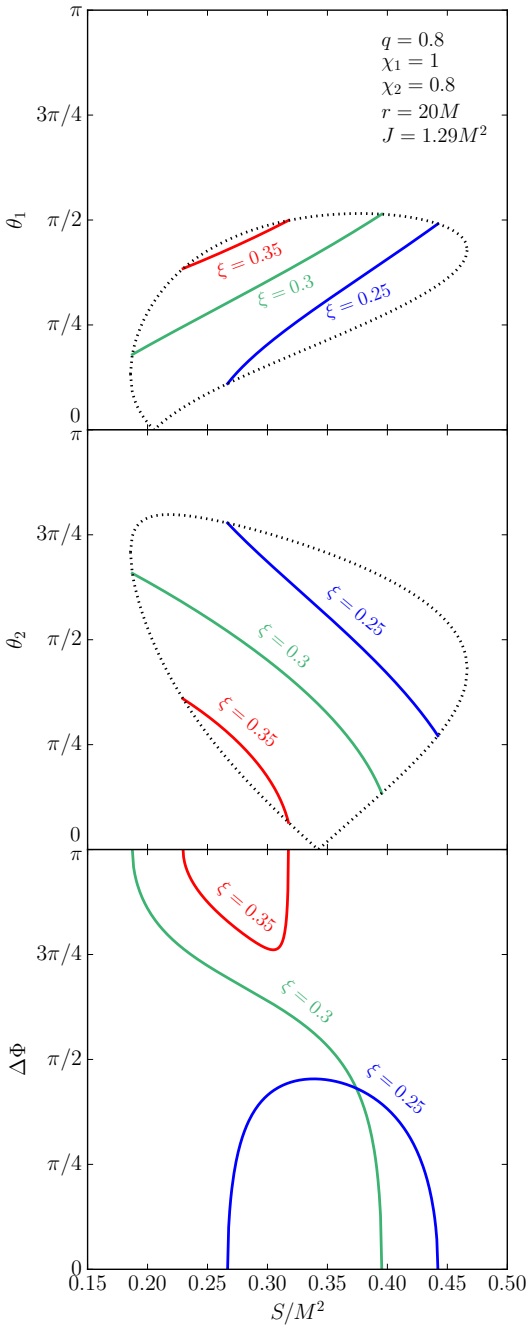

Figure 2.3: Analytical solutions given by Eqs. (2.37-2.39) for the evolution of the angles θ_1 (top panel), θ_2 (middle panel), and $\Delta\Phi$ (bottom panel) during a precession cycle. The evolution of three binaries with $\xi = 0.25$ (blue), 0.3 (green) and 0.35 (red) is shown for $q = 0.8$, $\chi_1 = 1$, $\chi_2 = 0.8$, $r = 20M$ and $J = 1.29M^2$. The evolution of θ_1 and θ_2 is monotonic during each half of a precession cycle and is bounded by the dotted lines for which $\cos\varphi = \mp 1$ [these curves can be found by substituting $\xi_\pm(S)$ for ξ in Eqs. (2.37-2.39)]. Three classes of solutions are possible and define the binary morphology: $\Delta\Phi$ can oscillate about 0 ($\xi = 0.25$), circulate ($\xi = 0.3$) or oscillate about π ($\xi = 0.35$). An animated version of this figure is available online at [200], where precession solutions are evolved on $t_{\rm RR}$.

the extrema of the effective potentials ($\xi_{\rm min}$ and $\xi_{\rm max}$), while circulating binaries (if present) fill the gap in between. Schnittman's spin-orbit resonances [463] can be reinterpreted as the limits of the two oscillating morphologies when the "precessional amplitude" $S_+ - S_-$ goes to zero at $\xi_{\rm min}$ and $\xi_{\rm max}$, much like how circular orbits are the limits of eccentric orbits as the amplitude of the radial oscillations goes to zero.

According to the criteria listed in Eqs. (2.41-2.43), boundaries between the three morphologies (shown by horizontal dashed lines in Fig. 2.5) occur at values of ξ where $\cos\Delta\Phi$ given by Eq. (2.39) changes discontinuously at one of the turning points $S_\pm$ along the

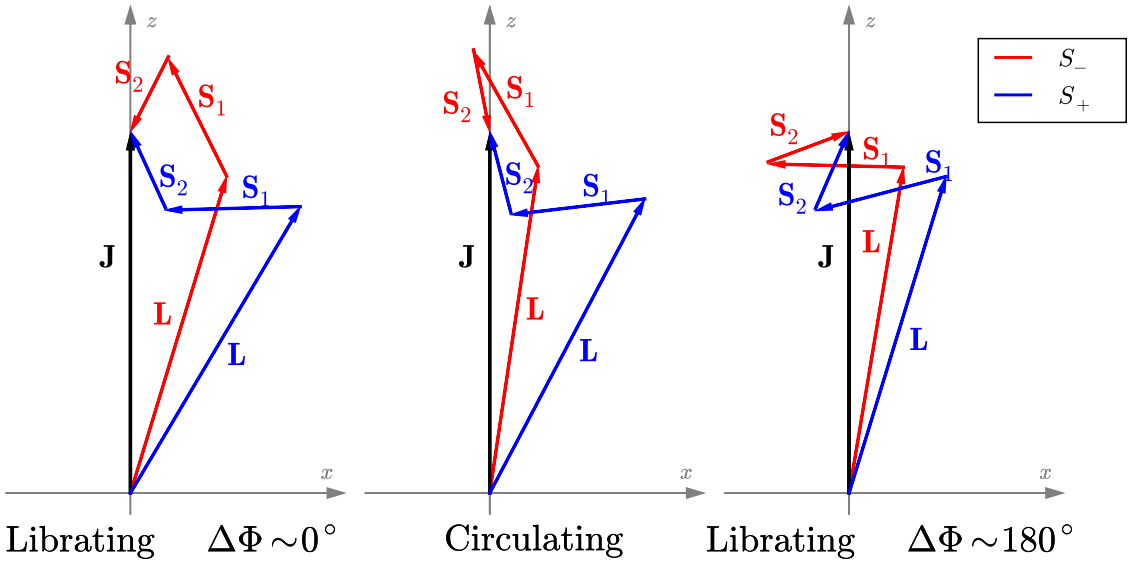

Figure 2.4: The three morphologies of BH binary spin precession. The angular momenta $\mathbf{J}$, $\mathbf{L}$, and $\mathbf{S}_i$ are all in the xz–plane at $S = S_\pm$. In all three panels the binaries have maximal spins, $q = 0.8$, $L = 0.781M^2$ ($r = 10M$), and $J = 0.85M^2$. The left, middle, and right panels correspond to $\xi = -0.025$, 0.025 and 0.15, respectively. If the components of $\mathbf{S}_i$ perpendicular to $\mathbf{L}$ are aligned with each other at both roots $S_\pm$, $\Delta\Phi$ librates about 0°. If they are aligned at one root and anti-aligned at the other, $\Delta\Phi$ circulates. If they are anti-aligned at both roots, $\Delta\Phi$ librates about π. An animated version of this figure evolving on the radiation-reaction time $t_{\rm RR}$ is available online [200].

effective-potential loop $\xi_\pm(S)$. We know that $\Delta\Phi$ is either 0 or π along $\xi_\pm(S)$ because $\mathbf{L}$, $\mathbf{S}_1$, and $\mathbf{S}_2$ are coplanar when $\cos\varphi' = \pm 1$ (see Fig. 2.1). A discontinuity can only occur when the denominator of Eq. (2.39) vanishes, i.e. where one of the spins is either aligned or anti-aligned with the orbital angular momentum ($\sin\theta_i = 0$). These discontinuities can only happen at the turning points $S_\pm$ because of the monotonic evolution of θ_i during each half of the precession cycle, as shown in the top and middle panels of Fig. 2.3. The four contours $\cos\theta_i = \pm 1$ ($\sin\theta_i = 0$) are shown by dotted curves in Fig. 2.5; we see that a boundary between morphologies occurs whenever these curves are tangent to the effective-potential loop $\xi_\pm(S)$. These boundaries had previously been described as unstable resonances [463].

The geometrical constraints imposed by Eqs. (2.6) and (2.13) imply that some morphologies may not be allowed for given values of L, J, q, χ_1, and χ_2. Three qualitatively different scenarios can occur, exemplified by the three panels of Fig. 2.5:

1. *Left panel:* BH spins precess in all three of the morphologies listed in Eqs. (2.41-2.43). Libration about the coplanar configuration $\Delta\Phi = 0$ occurs for values of ξ close to $\xi_{\rm min}$, libration about the $\Delta\Phi = \pi$ configuration is found near $\xi_{\rm max}$, and $\Delta\Phi$ circulates for intermediate values of ξ. Our analysis in [269] was restricted to this case and later

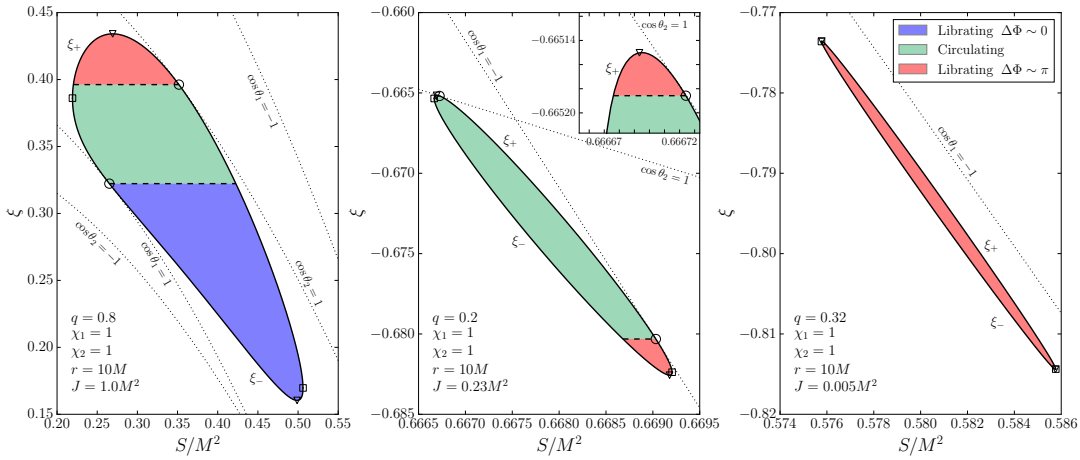

Figure 2.5: Effective potentials $\xi_\pm(S)$ of Eq. (2.24) for values of L, J, S_1, and S_2 leading to three different sets of spin morphologies. The loop formed by the two curves encloses all allowed configurations for the constants listed in the legends. As in the left panel of Fig. 2.2, empty squares mark the extrema of S ($S_{\rm min}$ and $S_{\rm max}$), empty triangles mark the extrema of ξ ($\xi_{\rm min}$ and $\xi_{\rm max}$), and conservation of ξ restricts the BH spins to precess along horizontal lines between the turning points $S_\pm$. BH binary spin precession can be classified into three different morphologies by the behavior of $\Delta\Phi$ during a precession cycle: oscillation about 0 (blue region), circulation from $-\pi$ to π (green region), or oscillation about π (red region). The dashed boundaries between these morphologies occur at values of ξ where the dotted curves $\cos\theta_i = \pm 1$ intersect the effective-potential loop, as shown by the empty circles. All three morphologies are present if one intersection occurs on $\xi_+(S)$ and a second occurs on $\xi_-(S)$ (left panel), oscillation of $\Delta\Phi$ about 0 is forbidden if two intersections occur on either $\xi_+(S)$ or $\xi_-(S)$ (middle panel), and only oscillations about π are allowed if there are no such intersections (right panel).

expanded in [206] to the general case.

2. *Middle panel:* $\Delta\Phi$ oscillates about π for ξ close to both $\xi_{\rm min}$ and $\xi_{\rm max}$, with circulation still allowed for intermediate values of ξ.

3. *Right panel:* $\Delta\Phi$ oscillates about π for all values $\xi_{\rm min} < \xi < \xi_{\rm max}$ (circulation and oscillation about 0 are both forbidden).

To distinguish these scenarios, it is useful to examine the values of $\Delta\Phi$ on the effective-potential loop at the extrema $\xi_{\rm min}$ and $\xi_{\rm max}$. Although it is straightforward to evaluate $\Delta\Phi$ numerically at $\xi_{\rm max}$, one can gain more intuition by instead evaluating it at $S_{\rm min}$. The value of $\Delta\Phi$ is the same at these two points since the slope of the effective-potential loop $\xi_+(S)$ connecting them is positive while that of the $\cos\theta_i = \pm 1$ contours is negative (as can be seen in Fig. 2.5). The curves therefore cannot be tangent to each other implying that $\Delta\Phi$ must remain constant on this portion of the loop. Equation (2.14) requires that $S_{\rm min}$ equals the greater of $|J - L|$ and $|S_1 - S_2|$; in the former case $\mathbf{L}$ and $\mathbf{J}$ are aligned, while in the latter case $\mathbf{S}_1$ and $\mathbf{S}_2$ are anti-aligned. In either case, the components of $\mathbf{S}_1$ and $\mathbf{S}_2$ perpendicular to $\mathbf{L}$ are anti-aligned ($\Delta\Phi = \pi$). This implies that $\Delta\Phi$ will oscillate

about π near $\xi_{\rm max}$ for all values of J, L, S_1, and S_2 (as can be seen in all three panels of Fig. 2.5).

The values of $\Delta\Phi$ on the effective-potential loop at $\xi_{\rm min}$ and $S_{\rm max}$ are also the same because the segment of the curve connecting them has a positive slope. Equation (2.15) indicates that $S_{\rm max}$ equals the lesser of $|J + L|$ and $|S_1 + S_2|$; in the former case $\mathbf{L}$ and $\mathbf{J}$ are anti-aligned, while in the latter case $\mathbf{S}_1$ and $\mathbf{S}_2$ are aligned. The former case again requires the components of $\mathbf{S}_1$ and $\mathbf{S}_2$ perpendicular to $\mathbf{L}$ to be anti-aligned ($\Delta\Phi = \pi$) but now the latter case requires these components to be aligned ($\Delta\Phi = 0$). For values of J, L, S_1, and S_2 for which this latter case applies, $\Delta\Phi$ will oscillate about 0 near $\xi_{\rm min}$ and we have determined that all three morphologies are possible, as shown in the left panel of Fig. 2.5.

To distinguish the remaining two scenarios (whether or not $\Delta\Phi$ circulates for intermediate values of ξ), we must examine the intersections of the $\cos\theta_i = \pm 1$ contours with the effective-potential loop $\xi_\pm(S)$. There can be either zero or two of such intersections. If no intersections occur, $\Delta\Phi$ remains equal to π around the entire loop just as it is at $\xi_{\rm max}$ and only oscillations about this value are possible, as shown in the right panel of Fig. 2.5. If there are two intersections, they must happen on the two portions of the loop with negative slopes (the segment connecting $S_{\rm min}$ and $\xi_{\rm min}$ and the segment connecting $S_{\rm max}$ and $\xi_{\rm max}$). If both intersections happen on the *same* segment, $\Delta\Phi$ switches from π to 0 and back again as one traverses the loop from $\xi_{\rm max}$ to $\xi_{\rm min}$ resulting in the introduction of a circulating phase before restoring oscillations about π near $\xi_{\rm min}$, as seen in the middle panel of Fig. 2.5. If the two intersections happen on *different* segments, $\Delta\Phi$ switches to 0 at the first turning point and then to π at the other leading to oscillations about 0 near $\xi_{\rm min}$, as seen previously in the left panel of Fig. 2.5.

To summarize, the number of allowed morphologies in the effective-potential diagrams of Fig. 2.5 depends on the magnitude of the total angular momentum J:

1. All three phases are allowed if

$$J > S_1 + S_2 - L\,. \tag{2.44}$$

   This condition implies $S_{\rm max} = S_1 + S_2$ and hence $\Delta\Phi(\xi_{\rm min}) = 0$ (Fig. 2.5, left panel).

2. For lower values of J such that

$$L - |S_1 - S_2| < J < S_1 + S_2 - L\,, \tag{2.45}$$

   $\Delta\Phi$ will oscillate about π near $\xi_{\rm min}$ and $\xi_{\rm max}$ and circulate from $-\pi$ to π for in-

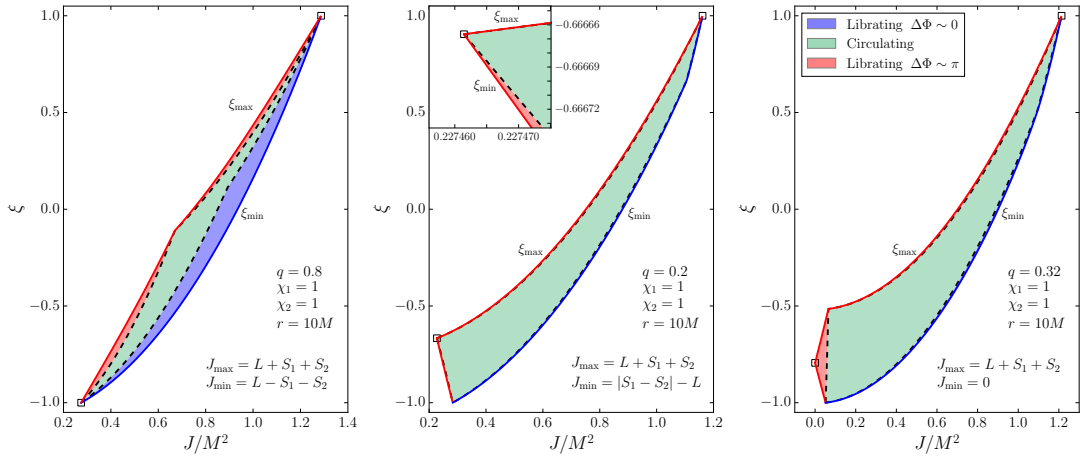

Figure 2.6: The (J, ξ) parameter space for binary BHs with different minimum allowed total angular momentum $J_{\min}$. BH binary spin morphology is shown with different colors, as indicated in the legend. The extrema $\xi_{\min}(J)$ and $\xi_{\max}(J)$ of the effective potentials constitute the edges of the allowed regions and are marked by solid blue (red) curves for $\Delta\Phi = 0$ (π). Dashed lines mark the boundaries between the different morphologies. The parameters q, χ_1, χ_2 and r are chosen as in Fig. 2.5, whose panels can be thought of as vertical (constant J) "sections" of this figure (where we suppress the S dependence). The lowest allowed value of ξ occurs at $J = |L - S_1 - S_2|$ in all three panels. Three phases are present for each vertical section with $J > |L - S_1 - S_2|$. This condition may either cover the entire parameter space (left panel) or leave room for additional regions where vertical sections include two different phases in which $\Delta\Phi$ oscillates about π and a circulating phase in between (center panel) or only a single phase where the spins librate about $\Delta\Phi = \pi$ (right panel). An animated version of this figure evolving on the radiation-reaction time $t_{\rm RR}$ is available online [200].

termediate values of ξ (Fig. 2.5, middle panel). The first inequality ensures that two (anti)aligned configurations ($\sin\theta_i = 0$) can be found, while the second prevents $\Delta\Phi = 0$.

3. Finally, for

$$J < \min(S_1 + S_2 - L, L - |S_1 - S_2|)\,, \tag{2.46}$$

the condition $\sin\theta_i = 0$ cannot be satisfied and $\Delta\Phi$ must oscillate about π (Fig. 2.5, right panel).

Whether these conditions can be satisfied is determined by the limits on J given by Eq. (2.6). In particular, $J_{\min} = L - S_1 - S_2$ is a sufficient but not necessary condition for all three morphologies to coexist, while $J_{\min} = 0$ is a necessary but not sufficient condition for the single-phase case. The three-phase case was considered in our first *Letter* [269] and is the only allowed case at sufficiently large binary separations ($L > S_1 + S_2$).

The $J\xi$-plane shown in Fig. 2.6 shows all binary BH spin configurations for fixed values of q, χ_1, χ_2 and r at once. Since J and ξ are constant on the precession time $t_{\rm pre}$, the

position of binary BHs in this figure is fixed on this timescale. The effective-potential diagrams of Fig. 2.5 can be thought of as vertical sections of Fig. 2.6 at fixed J where the S direction has been expanded. Each panel of Fig. 2.6 refers to a different choice of $J_{\rm min}$ from Eqs. (2.7). $\Delta\Phi$ can only oscillate about 0 if $J > |L - S_1 - S_2|$. From Eq. (2.22), the limit $J = |L - S_1 - S_2|$ corresponds to the lowest allowed value of ξ. For separations large enough that $L > S_1 + S_2$, this configuration also corresponds to $J_{\rm min}$ in which case $\Delta\Phi$ can oscillate about 0 for all allowed values of J (Fig. 2.6, left panel). If L is sufficiently small to admit values of J such that $J < |L - S_1 - S_2|$, a new region of the parameter space where $\Delta\Phi = 0$ is forbidden appears at small J (middle and right panels of Fig. 2.6). If even lower values $J < |S_1 - S_2| - L$ can be reached (i.e., if $J_{\rm min} = 0$), the leftmost region of the $J\xi$-plane does not even allow a circulating phase (right panel of Fig. 2.6).

The center and right panels of Fig. 2.6 reveal that the regions for which $\Delta\Phi$ oscillates (shown in blue and red) are very small for $L < S_1 + S_2$. This follows from the fact that these small values of the orbital angular momentum can only be achieved in the PN regime ($r \gtrsim 10M$) for low mass ratios. Oscillation of $\Delta\Phi$ relies upon coupling between the two BH spins, and the spin $\mathbf{S}_2$ becomes increasingly ineffective at maintaining this coupling as $q \to 0$ (cf. Sec. 2.4.2 below for more details). Nonetheless, a small region of the parameter space is always occupied by librating binaries as ξ approaches the resonant values $\xi_{\rm min}$ and $\xi_{\rm max}$. For each value of ξ (horizontal sections of Fig. 2.6), one $\Delta\Phi = 0$ resonance and one $\Delta\Phi = \pi$ resonance occur at the largest ($\Delta\Phi = 0$) and the lowest ($\Delta\Phi = \pi$) allowed values of J. The effective spin ξ is therefore a good parameter to identify the resonant solutions, as we pointed out in [208].

2.2.4 Time dependence

Although S fully parametrizes the precessional dynamics, time-dependent expressions may be useful as well. The BH spins obey the 2PN precession equations [276, 431, 185, 87]

$$\frac{d\mathbf{S_1}}{dt} = \frac{1}{2r^3}\left[(4+3q)\mathbf{L} - \frac{3qM^2\xi}{1+q}\hat{\mathbf{L}} + \mathbf{S_2}\right] \times \mathbf{S_1}\,, \tag{2.47}$$

$$\frac{d\mathbf{S_2}}{dt} = \frac{1}{2r^3}\left[\left(4+\frac{3}{q}\right)\mathbf{L} - \frac{3M^2\xi}{1+q}\hat{\mathbf{L}} + \mathbf{S_1}\right] \times \mathbf{S_2}\,, \tag{2.48}$$

which include the quadrupole-monopole interaction computed in [431]. These equations are averaged over the binary's orbital period $t_{\rm orb}$ and describe the evolution of the spins on the precession timescale $t_{\rm pre}$. Equations (2.47-2.48) imply that the orbit-averaged evolution

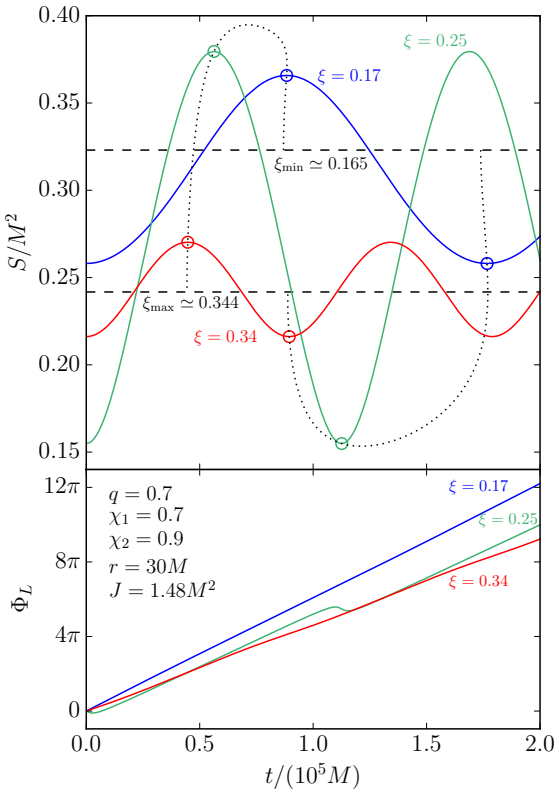

Figure 2.7: Time-dependent solutions for the total-spin magnitude S (top panel) and the orbital-angular-momentum phase Φ_L (bottom panel). We set $q = 0.7$, $\chi_1 = 0.7$, $\chi_2 = 0.9$, $r = 30M$ and $J = 1.48M^2$ and integrate Eq. (2.49) for three values of ξ corresponding to the three different spin morphologies: $\Delta\Phi$ oscillates about 0 ($\xi = 0.17$, blue), circulates ($\xi = 0.25$, green), and oscillates about π ($\xi = 0.34$, red). Initial conditions have been chosen such that $S = S_-$ and $\Phi_L = 0$ at $t = 0$. The oscillations in S induce small wiggles in Φ_L on top of a mostly linear drift. Spin-orbit resonances (horizontal dashed lines, top panel) correspond to configurations for which S is constant and can be interpreted as zero-amplitude limits of generic oscillatory solutions. The projections of the effective potentials, i.e. parametric curves $[\tau(\xi)/2, S_+(\xi)]$ and $[\tau(\xi), S_-(\xi)]$, are shown with dotted lines. An animated version of this figure is available online [200].

of $S = |\mathbf{S_1} + \mathbf{S_2}|$ is given by:

$$\frac{dS}{dt} = -\frac{3(1-q^2)}{2q}\frac{S_1 S_2}{S}\frac{(\eta^2 M^3)^3}{L^5}\left(1 - \frac{\eta M^2 \xi}{L}\right)\sin\theta_1 \sin\theta_2 \sin\Delta\Phi$$
$$= \pm\frac{3}{2}\eta M\left[1 - \xi\left(\frac{r}{M}\right)^{-1/2}\right]\left(\frac{r}{M}\right)^{-5/2}\sqrt{(\xi_+ - \xi)(\xi - \xi_-)}\,. \tag{2.49}$$

Integrating Eq. (2.49) yields solutions $S(t)$, and that specifies $\mathbf{L}$, $\mathbf{S}_1$, and $\mathbf{S}_2$ as functions of time through substitution into Eqs. (2.17-2.19). Some examples of $S(t)$ for different values of ξ are shown in the top panel of Fig. 2.7.

These time-dependent solutions confirm the scenario outlined in Sec. 2.2.2, with S oscillating between two turning points S_- and S_+ at which $dS/dt = 0$. At these turning points, the three angular momenta are coplanar [from Eq. (2.49), $dS/dt = 0$ implies either $\sin\Delta\Phi = 0$ or $\sin\theta_i = 0$] and the binary BHs lie on the effective potentials ($\xi_\pm(S_\pm) = \xi$). The spin-orbit resonances $\xi_{\rm min}$ and $\xi_{\rm max}$ are shown with dashed lines in Fig. 2.7 and correspond to the zero-amplitude limits of the generic oscillatory solutions. From Eq. (2.49), we can define the precessional period τ as the time needed to complete a full cycle in S,

$$\tau(L, J, \xi) = 2\int_{S_-}^{S_+}\frac{dS}{|dS/dt|}\,. \tag{2.50}$$

The precession timescale $t_{\rm pre} \sim (2\pi M/\eta)(r/M)^{5/2}$ provides an order-of-magnitude estimate for this exact precessional period. The period τ remains finite at the spin-orbit resonances $\xi_{\rm min}$ and $\xi_{\rm max}$ in much the same way that the period of a simple harmonic oscillator remains finite in the limit of small oscillations.

The time evolution of the three angular momenta $\mathbf{L}$, $\mathbf{S_1}$ and $\mathbf{S_2}$ is fully given by Eqs. (2.17-2.19) and (2.49) when described in the non-inertial frames of Fig. 2.1. However, $\mathbf{J}$ and $\mathbf{L}$ will generally not be confined to a plane in an inertial frame. The direction of $\mathbf{J}$ is fixed on the precession time scale $t_{\rm pre}$, and hence so is $\hat{\mathbf{z}}$. The two remaining basis vectors will precess about the z-axis

$$\frac{d\hat{\mathbf{x}}}{dt} = \Omega_z \hat{\mathbf{z}} \times \hat{\mathbf{x}} = \Omega_z \hat{\mathbf{y}} \tag{2.51}$$

$$\frac{d\hat{\mathbf{y}}}{dt} = \Omega_z \hat{\mathbf{z}} \times \hat{\mathbf{y}} = -\Omega_z \hat{\mathbf{x}}\,. \tag{2.52}$$

The solution to these two equations gives $\hat{\mathbf{x}}(t)$ and $\hat{\mathbf{y}}(t)$ and hence $\mathbf{L}(t)$, $\mathbf{S}_1(t)$, and $\mathbf{S}_2(t)$ in an inertial frame from Eqs. (2.17-2.19) and (2.23). The orbital angular momentum $\mathbf{L}$ precesses about $\mathbf{J}$ with frequency Ω_z given by

$$\Omega_z = \frac{J}{2}\left(\frac{\eta^2 M^3}{L^2}\right)^3 \left\{1 + \frac{3}{2\eta}\left(1 - \frac{\eta M^2 \xi}{L}\right) - \frac{3(1+q)}{2qA_1^2 A_2^2}\left(1 - \frac{\eta M^2 \xi}{L}\right)\right. \tag{2.53}$$
$$\left. \times \left[4(1-q)L^2(S_1^2 - S_2^2) - (1+q)(J^2 - L^2 - S^2)(J^2 - L^2 - S^2 - 4\eta M^2 L\xi)\right]\right\}.$$

This equation can be derived by substituting Eqs. (2.47-2.48) and (2.51-2.52) into the time derivative of Eq. (2.10). For concreteness, let us specify an inertial frame such that $\mathbf{L}$ lies in the xz-plane at $S = S_-$. At the point on a precession cycle specified by the total-spin magnitude S, the direction of $\mathbf{L}$ is specified by the polar angles θ_L from Eq. (2.11) and the azimuthal angle

$$\Phi_L = \begin{cases} \displaystyle\int_{S_-}^{S} \Omega_z \frac{dS}{|dS/dt|} & \text{for} \quad S : S_- \to S_+ \\ \displaystyle\frac{\alpha}{2} + \int_{S}^{S_+} \Omega_z \frac{dS}{|dS/dt|} & \text{for} \quad S : S_+ \to S_- \end{cases} \tag{2.54}$$

where the two cases refer to the first and the second half of the precession cycle, and

$$\alpha(L, J, \xi) = 2\int_{S_-}^{S_+} \Omega_z \frac{dS}{|dS/dt|} \tag{2.55}$$

is the total change in the azimuthal angle Φ_L over a full precession cycle. Solutions $\Phi_L(t)$

are shown in the bottom panel of Fig. 2.7. The angle Φ_L mainly exhibits a linear drift due to the leading PN order term in Eqs. (2.47-2.48). Spin-spin couplings are of higher PN order and cause small wiggles on top of this linear drift. Binaries in spin-orbit resonances ($\xi_{\rm min}$ and $\xi_{\rm max}$) precess at a constant rate Ω_z with all three vectors $\mathbf{L}$, $\mathbf{S_1}$, and $\mathbf{S_2}$ jointly precessing about $\mathbf{J}$. Just as $\Delta\Phi$ is ill defined if either of the $\mathbf{S_i}$ is aligned with $\mathbf{L}$ ($\cos\theta_i = \pm 1$), Φ_L and thus α are ill defined if $\mathbf{L}$ is aligned with $\mathbf{J}$ ($\cos\theta_L = \pm 1$). This occurs for values of J and ξ for which $S_- = S_{\rm min} = |J - L|$ or $S_+ = S_{\rm max} = J + L$, corresponding to some of the transitions between the different classes of the evolution of φ' (dashed lines in Fig. 2.2).

We stress here that the time-dependent expressions reported in this Section are only valid on times $t \sim \tau \ll t_{\rm RR}$, i.e. when the precessional dynamics approximately decouples from the inspiral. This approximation breaks down at small separations, where the difference between the three timescales is smaller (cf. Sec. 2.3.3).

2.3 Precession-averaged evolution on the inspiral timescale

The previous Section focused on spin dynamics on the precessional timescale. We now consider how spin precession evolves as the BHs inspiral due to radiation reaction. Our main tool is a precession-averaged equation to model the binary inspiral (derived in Sec. 2.3.1 below) that will allow us to overcome numerical limitations of previous analyses [270, 271, 76, 204, 208] and evolve binary BHs inwards from arbitrarily large separations (Sec. 2.3.2). This improved computational scheme relying on our new multi-scale analysis allows us to more efficiently "transfer" binary BHs from the large separations where they form astrophysically down to the small separations relevant for GW detection. In Sec. 2.3.3 we compare the results of our precession-averaged evolution against the standard integration of the merely orbit-averaged spin-precession equations.

2.3.1 Averaging the average

In the usual PN formulation (see e.g. [276]), the timescale hierarchy $t_{\rm orb} \ll t_{\rm pre} \ll t_{\rm RR}$ is exploited to average the evolution equations for $\mathbf{L}$, $\mathbf{S}_1$, and $\mathbf{S}_2$ over the orbital period T. We already saw above how this orbit averaging can be used to increase the computational efficiency with which spin precession can be calculated [Eqs. (2.47-2.48) can be integrated with time steps $t_{\rm orb} \ll \Delta t \ll t_{\rm pre}$ much longer than the orbital timescale]. Radiation

reaction can be similarly orbit averaged:

$$\left\langle \frac{d\mathbf{L}_{\rm RR}}{dt} \right\rangle_{\rm orb} = \frac{1}{T}\int_0^{2\pi} \frac{d\mathbf{L}_{\rm RR}}{dt}\,\frac{d\psi}{d\psi/dt}\,, \tag{2.56}$$

where $d\mathbf{L}_{\rm RR}/dt$ is the instantaneous change in the orbital angular momentum due to GW radiation reaction and ψ is the true anomaly parametrizing the orbital motion. The flux $d\mathbf{L}_{\rm RR}/dt$ depends implicitly on both ψ and the angular momenta $\mathbf{L}$, $\mathbf{S}_1$, and $\mathbf{S}_2$; the former dependence can be averaged over since we have analytic solutions to the orbital motion as function of ψ, while the angular momenta may be held fixed, since they barely evolve over an orbital period. Spin precession may be calculated on the radiation-reaction timescale by numerically integrating the coupled system of Ordinary Differential Equations (ODEs) given by Eqs. (2.47-2.48) and (2.56) with the time step Δt given above.

We derived analytic solutions to the orbit-averaged spin-precession equations (2.47-2.48) in Sec. 2.2 that depend on the magnitudes L and J that evolve on the radiation-reaction timescale $t_{\rm RR}$. In a similar spirit to the orbit averaging discussed above, we can use these solutions to *precession average* the evolution equations for L and J. We define the precession average of some scalar quantity X to be

$$\langle X\rangle_{\rm pre} \equiv \frac{2}{\tau}\int_{S_-}^{S_+} \langle X\rangle_{\rm orb}\frac{dS}{|dS/dt|} \tag{2.57}$$

where dS/dt is given as a function of S in Eq. (2.49). We can hold L, J, and ξ fixed on the right-hand side of this equation because they barely evolve during a precession cycle, much as we held the vectorial angular momenta fixed in the orbit averaging since they evolve on the longer timescale $t_{\rm pre} \gg t_{\rm orb}$.

Since ξ is conserved by radiation reaction at 2.5PN order [141, 431], we need only to find precession-averaged evolution equations for L and J to evolve our spin-precession solutions on the radiation-reaction timescale $t_{\rm RR}$. Since $L^2 = \mathbf{L}\cdot\mathbf{L}$, $dL/dt = \hat{\mathbf{L}}\cdot d\mathbf{L}_{\rm RR}/dt$ and the precession-averaged evolution of L is given by

$$\left\langle \frac{dL}{dt} \right\rangle_{\rm pre} = \frac{2}{\tau}\int_{S_-}^{S_+} \hat{\mathbf{L}}\cdot\left\langle \frac{d\mathbf{L}_{\rm RR}}{dt} \right\rangle_{\rm orb}\frac{dS}{|dS/dt|}\,. \tag{2.58}$$

We similarly have $dJ/dt = \hat{\mathbf{J}}\cdot d\mathbf{J}_{\rm RR}/dt$, but since $\mathbf{J} = \mathbf{L}+\mathbf{S}_1+\mathbf{S}_2$ and GW emission does not directly affect the individual spins ($d\mathbf{S}_{i,\rm RR}/dt = 0$), $d\mathbf{J}_{\rm RR}/dt = d\mathbf{L}_{\rm RR}/dt$ and we have

$$\left\langle \frac{dJ}{dt} \right\rangle_{\rm pre} = \frac{2}{\tau}\int_{S_-}^{S_+} \hat{\mathbf{J}}\cdot\left\langle \frac{d\mathbf{L}_{\rm RR}}{dt} \right\rangle_{\rm orb}\frac{dS}{|dS/dt|}\,. \tag{2.59}$$

The orbit-averaged angular momentum flux $\langle d\mathbf{L}_{\rm RR}/dt\rangle_{\rm orb}$ up to 1PN is given by [276]

$$\left\langle \frac{d\mathbf{L}_{\rm RR}}{dt} \right\rangle_{\rm orb} = -\frac{32}{5}\frac{\eta L}{M}\left(\frac{M}{r}\right)^4 \left[\left(1-\frac{2423+588\eta}{336}\frac{M}{r}\right)\hat{\mathbf{L}} + \mathcal{O}\left(\frac{M}{r}\right)^{3/2}\right] . \tag{2.60}$$

Note that this expression is parallel to $\hat{\mathbf{L}}$ and independent of S. Substituting this result into Eq. (2.59) yields

$$\left\langle \frac{dJ}{dt} \right\rangle_{\rm pre} = \frac{2}{\tau}\int_{S_-}^{S_+} \hat{\mathbf{L}}\cdot\left\langle \frac{d\mathbf{L}_{\rm RR}}{dt} \right\rangle_{\rm orb} \cos\theta_L \frac{dS}{|dS/dt|} , \tag{2.61}$$

where we used Eq. (2.9), and $\cos\theta_L$ is given in Eq. (2.11) as a function of S. Finally, Eqs. (2.58) and (2.61) together lead to

$$\left\langle \frac{dJ}{dL} \right\rangle_{\rm pre} = \frac{1}{2LJ}(J^2+L^2-\langle S^2\rangle_{\rm pre}) , \tag{2.62}$$

which reduces the computation of binary BH spin precession on the radiation-reaction timescale to solving a single ODE! Equation (2.62) is independent of the details of spin precession (which are encoded in $\langle S^2\rangle_{\rm pre}$) and is also independent of the PN expansion for $\langle d\mathbf{L}_{\rm RR}/dt\rangle_{\rm orb}$ provided this is parallel to $\hat{\mathbf{L}}$ and independent of S. As shown in Eq. (2.60), both of these conditions are satisfied at 1PN level but break down at higher PN order. We address the range of validity of our approach in Sec. 2.3.3, where we also perform extensive comparisons with full integrations of the conventional orbit-averaged equations.

Examples of solutions to Eq. (2.62) are shown in Fig. 2.8, where J is evolved from $r = 10^9 M$ to $r = 10M$. Solutions $J(r)$ are bounded at all separations by the spin-orbit resonances $\xi_{\rm min}$ and $\xi_{\rm max}$ which extremize the magnitude J for each fixed ξ (cf. Sec. 2.2.3 and Fig. 2.6). We perform ODE integrations using the LSODA algorithm [241] as wrapped by the PYTHON module SCIPY [262]; integrations of Eq. (2.62) are numerically feasible for arbitrary values of $q < 1$, $\chi_1 \leq 1$, $\chi_2 \leq 1$, and *arbitrarily* large initial separation. Our numerical code is publicly available, as described in Appendix 2.A.

Our solutions to the spin-precession equations also depend on the direction $\hat{\mathbf{J}}$, since this defines the z-axis in the orthonormal frame of Fig. 2.1. The precession-averaged evolution of this direction is

$$\left\langle \frac{d\hat{\mathbf{J}}}{dt} \right\rangle_{\rm pre} = \frac{1}{J}\left\langle \left\langle \frac{d\mathbf{L}_{\rm RR}}{dt} \right\rangle_{\rm orb} - \frac{dJ}{dt}\hat{\mathbf{J}} \right\rangle_{\rm pre} \tag{2.63}$$

which is proportional to the precession average of the total angular momentum radiated perpendicular to $\hat{\mathbf{J}}$. Although the vector given by the right-hand side of Eq. (2.63) will

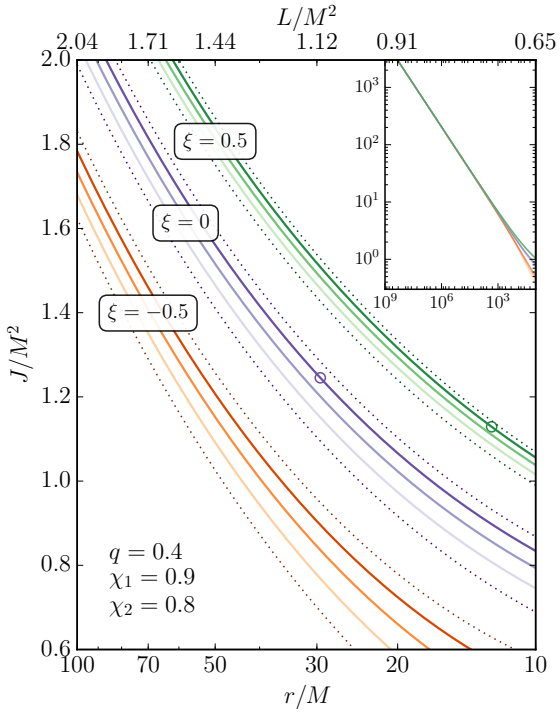

Figure 2.8: Evolution of the total angular momentum magnitude J during the inspiral. Three binary configurations are considered here: $\xi = -0.5$ (orange), 0 (purple) and 0.5 (green) for $q = 0.4$, $\chi_1 = 0.9$, $\chi_2 = 0.8$. Equation (2.62) is solved for several different initial conditions (solid lines, sequential colors) as the separation r and the angular momentum $L = \eta(rM^3)^{1/2}$ decrease. Solutions are bounded at all separations by the spin-orbit resonances (dotted lines) which extremize the allowed value of J for fixed ξ. Two of the binaries pictured here cross one of the resonant conditions $\alpha = 2\pi n$ (empty circles) where changes in the direction $\hat{\mathbf{J}}$ are expected. The inset shows the same evolutions for a wider separation range.

generally not vanish over a single precession cycle, if the angle α given by Eq. (2.55) above is not an integer multiple of 2π this vector will precess about $\hat{\mathbf{J}}$ in an inertial frame. This implies that $\hat{\mathbf{J}}$ will precess in a narrow cone in an inertial frame on the radiation-reaction timescale remaining approximately constant [31, 53]. As shown for some of the binaries of Fig. 2.8, the condition $\alpha = 2\pi n$ for integer n is indeed satisfied in generic inspirals at meaningful separations. Preliminary results indicate that interesting spin dynamics arises at these newly identified resonances [554]. Here we restrict our attention to the relative orientations of the three angular momenta as specified by the three angles in Eqs. (2.37-2.39).

2.3.2 The large-separation limit

We can gain additional physical insight by examining Eq. (2.62) in the large-separation limit $L/M^2 \to \infty$. Let us define

$$\kappa \equiv \frac{J^2 - L^2}{2L}\,, \tag{2.64}$$

such that Eq. (2.62) becomes

$$\frac{d\kappa}{dL} = -\frac{\langle S^2\rangle_{\rm pre}}{2L^2}\,. \tag{2.65}$$

The right-hand side vanishes fast enough at large separations where $S \ll L$, implying that

$$\kappa_\infty \equiv \lim_{r/M\to\infty} \kappa \tag{2.66}$$

is constant. This implies that κ provides a more convenient label for precessing binary BHs at large separations because it asymptotes to a constant while J diverges. At large separations J evolves as

$$J = \sqrt{L(2\kappa + L)} \simeq \sqrt{L\,(2\kappa_\infty + L)}\,, \tag{2.67}$$

as illustrated in the inset of Fig. 2.8. From Eq. (2.64) and $\mathbf{J} = \mathbf{L} + \mathbf{S}$ one also obtains

$$\kappa_\infty = \lim_{r/M\to\infty} \mathbf{S}\cdot\hat{\mathbf{L}} \tag{2.68}$$

implying that κ asymptotes to the projection of the total spin onto the orbital angular momentum. The constant κ_∞ can be calculated for a binary at finite separation by integrating $d\kappa/dL$ all the way to $r/M \to \infty$. This integration can be performed by defining $u = 1/2L$ such that $d\kappa/du = \langle S^2\rangle_{\rm pre}$ can be integrated over a compact domain.

The two constants κ_∞ and ξ are linear combinations of the asymptotic values of the inner products $\hat{\mathbf{S}}_\mathbf{i}\cdot\hat{\mathbf{L}}$ defined in Eqs. (2.37-2.39) in the large-separation limit. The constancy of these inner products at large separations is also apparent from Eqs. (2.47-2.48), where the $\mathbf{S_i}$ will precess about $\mathbf{L}$ when spin-orbit coupling dominates over spin-spin coupling. From Eqs. (2.22) and (2.68) one finds

$$\cos\theta_{1\infty} \equiv \lim_{r/M\to\infty} \hat{\mathbf{S}}_\mathbf{1}\cdot\hat{\mathbf{L}} = \frac{-M^2\xi + \kappa_\infty(1+q^{-1})}{S_1(q^{-1}-q)}\,, \tag{2.69}$$

$$\cos\theta_{2\infty} \equiv \lim_{r/M\to\infty} \hat{\mathbf{S}}_\mathbf{2}\cdot\hat{\mathbf{L}} = \frac{M^2\xi - \kappa_\infty(1+q)}{S_2(q^{-1}-q)}\,. \tag{2.70}$$

The terms in Eqs. (2.37-2.39) proportional to S^2 become increasingly significant at smaller separations and induce oscillations in θ_i on the precession timescale, while the breakdown of the asymptotic approximation to $J(L)$ given in Eq. (2.67) causes J (and hence θ_i) to deviate on the radiation-reaction timescale for binary BHs with different values of ξ, as seen in Fig. 2.8. The constraints $|\cos\theta_{1\infty}| \leq 1$ and $|\cos\theta_{2\infty}| \leq 1$ define the physically allowed values of ξ and κ_∞. These parameters, or equivalently $\theta_{1\infty}$ and $\theta_{2\infty}$, can be used to identify an entire BH binary inspiral (as far as the relative orientation of the angular momenta is concerned) without reference to a particular separation or frequency, as typically done in GW applications [208, 398, 526, 129, 182, 398, 399].

2.3.3 Efficient binary transfer

Our new precession-averaged equation for dJ/dL (2.62) can be used to efficiently "transfer" binary BHs from the large separations at which they form astrophysically to the smaller separations at which the GWs they emit become detectable. This equation can be integrated with a time step $t_{\rm pre} \ll \Delta t' \ll t_{\rm RR}$ much longer than the time step $t_{\rm orb} \ll \Delta t \ll t_{\rm pre}$ on which merely orbit-averaged equations must be integrated. This greater efficiency comes at the cost of no longer being able to keep track of the precessional phase, in much the same way that orbit-averaged equations do not explicitly evolve the orbital phase. This is not a major problem for population-synthesis studies however, because evolution over a timescale $\Delta t'$ will randomize the precessional phase, as described below. If one needs to track the precessional phase below a certain separation (such as that corresponding to the lowest detectable GW frequencies) one can randomly initialize the phase at this separation and then employ orbit-averaged equations [203]. The following procedure explicitly outlines how to evolve the spin orientations of a population of binary BHs from large to small separations.

1. Given a sample of binary BHs specified by values of q, χ_1 and χ_2, choose a distribution $p_i(\theta_1, \theta_2, \Delta\Phi)$ for the angles that describes the spin orientations at an initial separation r_i. This initial distribution is determined by the interactions between BHs and their astrophysical environment that lead to binary formation (cf. [204, 63, 190, 264] on stellar-mass BHs and [167, 211, 474, 92, 367] on supermassive BH binaries; see also Chapters 4 and 5 of this Thesis).

2. Rewrite this initial distribution as a distribution $p_i(J, \xi)$ using the relations

$$S = [S_1^2 + S_2^2 + 2S_1S_2(\sin\theta_1 \sin\theta_2 \cos\Delta\Phi + \cos\theta_1 \cos\theta_2)]^{1/2} \,, \tag{2.71}$$

$$J = [L^2 + S^2 + 2L(S_1 \cos\theta_1 + S_2 \cos\theta_2)]^{1/2} \,, \tag{2.72}$$

$$\xi = \frac{qS_1 \cos\theta_1 + S_2 \cos\theta_2}{\eta M^2 (1+q)} \,. \tag{2.73}$$

3. Evolve each member of the distribution $p_i(J, \xi)$ to a smaller separation r_f using Eq. (2.62) for dJ/dL (ξ remains constant). This yields a final distribution $p_f(J, \xi)$.

4. For each member of the distribution $p_f(J, \xi)$, create a distribution of values of S in the range $S_-(J, \xi) \leq S \leq S_+(J, \xi)$ weighted by $(dS/dt)^{-1}$ given by Eq. (2.49). BH binaries spend less time at values of S where the "velocity" dS/dt is large. This yields a distribution $p_f(S, J, \xi)$.

5. Convert $p_f(S, J, \xi)$ into a distribution of final angles $p_f(\theta_1, \theta_2, \Delta\Phi)$ using Eqs. (2.37-2.39) and a randomly chosen sign for $\Delta\Phi$.

Examples of this binary transfer are given in Fig. 2.9 for three different initial spin distributions.

1. *Isotropic sample* (top panels): Both spin vectors are isotropically distributed (flat uncorrelated distributions in $\cos\theta_1$, $\cos\theta_2$ and $\Delta\Phi$).

2. *One aligned BH* (middle panels): One BH spin (either the spin of the primary or the spin of the secondary) is aligned within 10° of the orbital angular momentum, while the other spin angle θ_i has a flat distribution in $[0^\circ, 180^\circ]$; $\Delta\Phi$ is also flat in $[-180^\circ, 180^\circ]$.

3. *Gaussian spikes* (bottom panels): θ_1 and θ_2 have Gaussian distributions peaked at 45° and 135° with deviations of 10°; $\Delta\Phi$ is kept flat in $[-180^\circ, 180^\circ]$.

We evolve these distributions from $r_i = 1000M$ to $r_f = 10M$ and show marginalized distributions of the three angles θ_1, θ_2, and $\Delta\Phi$ at several intermediate separations. An animated version of this figure can be found online [200]. The isotropic sample remains isotropic, as found previously using the orbit-averaged equations [92]. A greater fraction of the binaries in the distribution with one aligned BH undergoes a phase transition from a circulating to a librating morphology, as described in Sec. 2.4 below and also found in previous studies with the orbit-averaged equations [204]. If the angles θ_i initially have Gaussian distributions, these Gaussians will spread out as the inspiral proceeds.

We use the BH binary inspirals from $r_i = 1000M$ to $r_f = 10M$ shown in Fig. 2.9 to compare the efficiency of our new precession-averaged approach to the integration of the standard – i.e., orbit-averaged – PN equations. In the standard approach, one must numerically integrate ten coupled ODEs specifying the directions of the three angular momenta and the magnitude of the orbital velocity; we use the PN equations quoted by [270, 76]. We implement the same 2PN spin-precession equations[2] given by Eqs. (2.47-2.48) but include radiation reaction up to 3.5PN order, as in Eq. (2.6) of [270]. Integrations are performed using the same algorithm specified above [262, 241, 203]. The agreement between the two approaches is seen to be excellent up to $r \sim 50M$, and minor discrepancies emerge at smaller separations.

Two approximations made in the precession-averaged approach may explain these discrepancies. While ξ is held constant throughout the inspiral in the precession-averaged

[2] Higher-order PN corrections to the spin-precession equations have been computed in [347, 94, 93]; their implementation is left to future work.

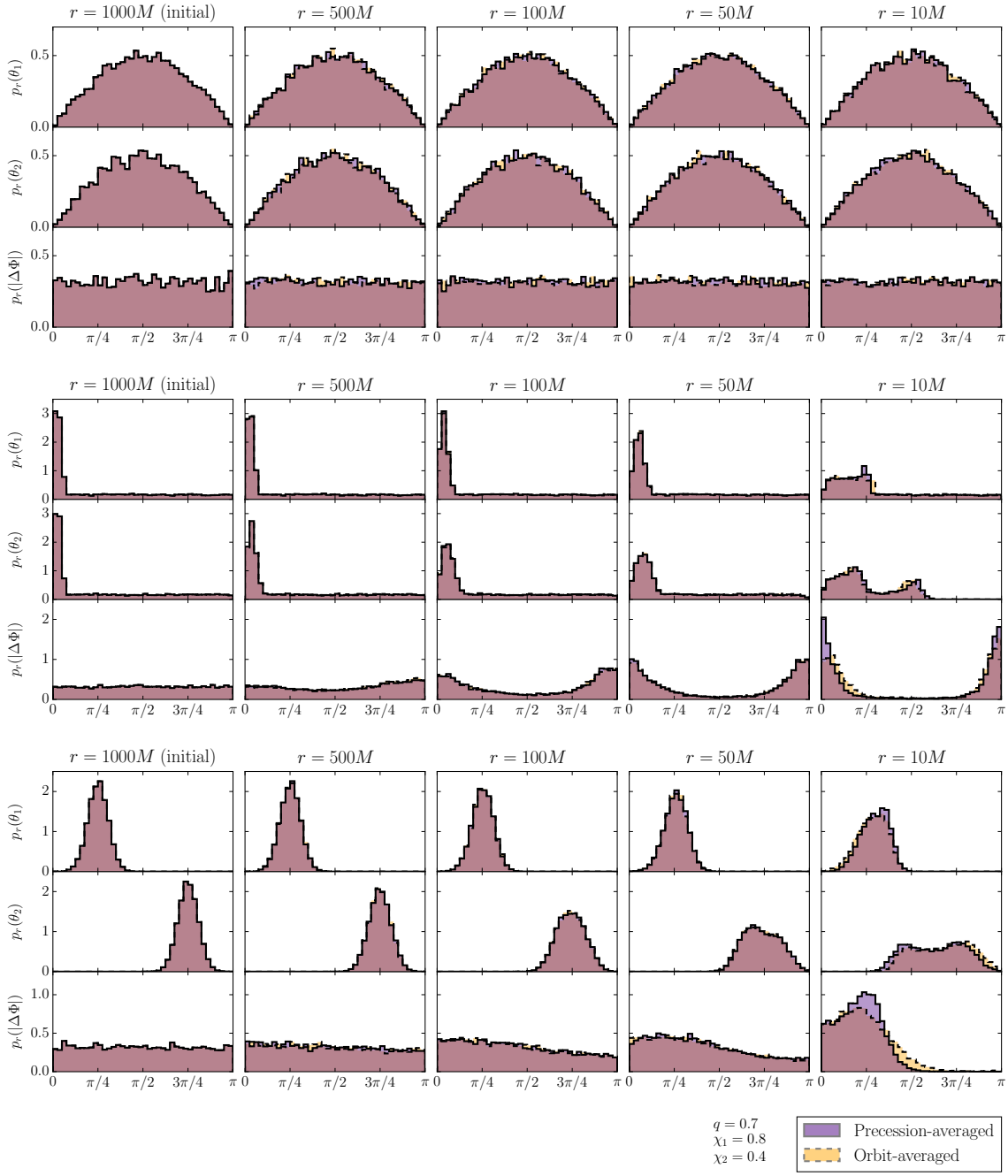

Figure 2.9: Precession-averaged BH binary inspirals as described in Sec. 2.3.3 (purple/darker) compared to numerical integration of the orbit-averaged PN equations [270, 76] (orange/lighter). Marginalized distributions of the spin angles θ_1, θ_2, and $|\Delta\Phi|$ (rows) are shown at several separations along the inspirals [columns: $r_i = 1000M$, $500M, 100M, 50M$, and $10M$]. The three initial spin distributions are isotropic (top panels), one aligned BH (middle panels), and Gaussian spikes (bottom panels) as described in Sec. 2.3.3. The two approaches are in good agreement except for minor deviations in the distribution of $\Delta\Phi$ at $r \sim 10M$. We take $q = 0.7$, $\chi_1 = 0.8$ and $\chi_2 = 0.4$ for all binary BHs. An animated version of this figure is available online [200].

approach (consistent with 2.5PN radiation reaction), conservation of ξ is not enforced in the orbit-averaged approach, which employs 3.5 PN radiation reaction. The largest deviations $\Delta\xi$ in the latter approach are of the order 10^{-10}; ξ is effectively constant in the PN regime ($r \gtrsim 10M$). Numerical-relativity simulations may be used to test conservation of ξ at smaller separations. We have verified that additional PN corrections in Eq. (2.60), implemented in our orbit-average code up to 3.5PN, introduce very mild corrections to the evolution of J: the largest variations observed in our evolutions are of order $\Delta J \sim 10^{-2}$.

The second and less reliable approximation involves the timescale hierarchy itself. The precession time $t_{\rm pre} \sim (r/M)^{5/2}$ and radiation-reaction time $t_{\rm RR} \sim (r/M)^4$ become more comparable at lower separations, reducing the effectiveness of our quasi-adiabatic approach. The precession-averaging procedure defined in Eq. (2.57) assumes that quantities like L and J varying on $t_{\rm RR}$ remain constant over a full precession cycle τ, but this assumption will break down as the timescale hierarchy becomes invalid.

Figure 2.9 shows that differences between the two approaches are most pronounced in $p_r(\Delta\Phi)$. This variable is the most sensitive to the precessional dynamics; predictions for the angles θ_1 and θ_2 remain reasonably accurate even at $r \sim 10M$. The differences seem to average out for wider distributions (top panels) but become more evident for more compact initial distributions (bottom panels). Averaging over the precessional dynamics prevents us from tracking the precession phase, implying that the two approaches will make different predictions for quantities (like S and $\Delta\Phi$) varying on the precession timescale when the initial separation is sufficiently small that memory of the initial phases has not been fully forgotten. Predictions of physical quantities varying on the radiation-reaction timescale (like J and the precession morphology) will remain robust down to small separations, as explored in Secs. 2.4.2 and 2.4.3 below.

We compare the computational efficiency of the precession- and orbit-averaged approaches in Fig. 2.10. Isotropic samples of 100 binary BHs are transferred from large initial separations r_i to a final separation $r_f = 10M$. The CPU time required by the two approaches scales differently with the initial separation. The orbit-averaged (OA) equations must be integrated with a time step shorter than the precession time, implying that the total number of time steps scales as

$$N_{\rm OA} \propto \int_{r_f}^{r_i} \frac{dr}{\dot{r}_{GW}\, t_{\rm pre}} \sim r_i^{3/2}\,, \tag{2.74}$$

where $\dot{r}_{GW} \propto r^{-3}$ as given by the quadrupole formula [415, 414]. The ratio $t_{\rm RR}/t_{\rm pre} \propto r^{3/2}$ increases dramatically at large separations leading to a corresponding increase in the computational cost. In the precession-averaged (PA) approach, the integration of dJ/dL

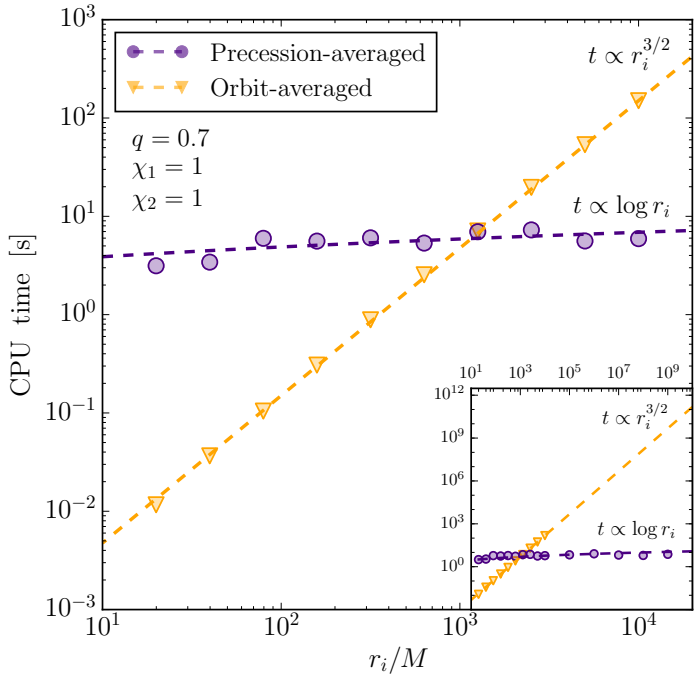

Figure 2.10: CPU time needed to evolve BH binaries from an initial separation r_i to a final separation $r_f = 10M$ using our new precession-averaged approach (purple circles) and the standard orbit-averaged approach (orange triangles). Each CPU time is averaged over $N = 100$ executions with isotropic initial spin orientation (flat distributions in $\cos\theta_1$, $\cos\theta_2$ and $\Delta\Phi$). Dashed lines show the expected scalings: $t \propto r_i^{3/2}$ for the orbit-averaged approach and $t \propto \log r_i$ for our new precession-averaged approach. These computations have been performed on a single core of a 2013 Intel i5-3470 3.20GHz CPU.

in Eq. (2.62) only requires time steps proportional to L, hence

$$N_{\rm PA} \propto \int_{L_f}^{L_i} \frac{dL}{L} \sim \log(L_i) \propto \log(r_i)\,. \tag{2.75}$$

The precession-averaged approach is very efficient at large separations because the solutions to Eq. (2.62) become very smooth in this limit as seen from Eq. (2.67) and Fig. 2.8. Precession-averaged inspirals may even be computed from infinite separations through a change of variables to $u \equiv (2L)^{-1}$. The integrator spends most of the computational time at small separations, where spin effects – notably the numerical evaluation of $S_\pm$ – need to be tracked with high accuracy to avoid violations of the constraints (2.6). As shown in Fig. 2.10, these expected scalings are well reproduced by both of our integrators (cf. Sec. 2.A).

In addition to the time needed to integrate Eq. (2.62), the precession-averaged approach must generate a final distribution for S (step 4 above), implying that the computational cost does not go to zero as $r_i \to r_f$. While this step makes the calculation of a single BH binary inspiral non-deterministic and more expensive, precession averaging effectively reduces the dimensionality of the BH binary population during the inspiral. If the n members of this final distribution for S are regarded as distinct binaries, the total number of integrations required to produce a fixed number of binary BHs at r_f is reduced by a factor of n in the precession-averaged approach compared to the orbit-averaged approach.

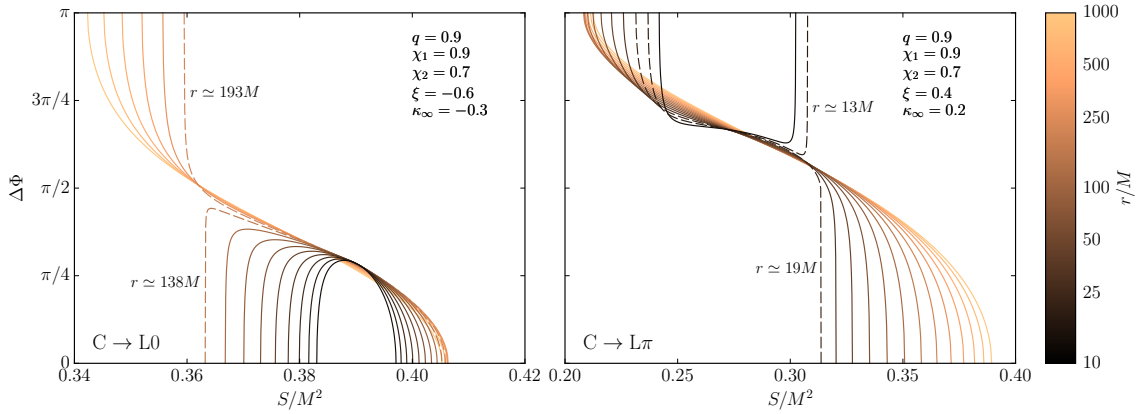

Figure 2.11: Precessional solutions $\Delta\Phi(S)$ of Eqs. (2.37-2.39) as J and L evolve during inspirals according to Eq. (2.62). These solutions are colored according to the separation r/M as shown in the color bar on the right (orange/lighter for large separations and black/darker for small separations). Binaries in the left (right) panel transition from the circulating morphology to the morphology in which $\Delta\Phi$ librates about 0 (π) at the transition radius $r_{\rm tr} \simeq 152M$ ($18.9M$); separations bracketing the transition radius are marked with dashed lines. Parameters are set to the values indicated in the legends. An animated version of this figure is available online [200].

2.4 Morphological phase transitions

As BH binaries inspiral on the radiation-reaction timescale, they can transition between the spin-precession morphologies described in Sec. 2.2.3. Binary BH spins predominantly circulate at large separations but increasingly transition into one of the two librating morphologies as spin-spin coupling becomes important (Sec. 2.4.1). The probability of encountering one of these morphological phase transitions during the inspiral depends on the asymmetry between the masses and the spin magnitudes of the two BHs (Sec. 2.4.2). Asymmetric binaries are more likely to circulate, while binary BHs with comparable mass and spin ratios populate the librating morphologies. BH binary spin morphologies at finite separations can be determined from their asymptotic spin orientations $\cos\theta_{i\infty}$ (or equivalently ξ and κ_∞) as discussed in Sec. 2.4.3.

2.4.1 Phenomenology of phase transitions

As extensively discussed in Sec. 2.2.3, BH binary spin precession can be unambiguously classified into one of the three morphologies depending on the values of q, χ_1, χ_2, ξ, r (or L), and J. While the first four of these parameters remain constant throughout the inspiral, r and J evolve on the radiation-reaction timescale according to Eq. (2.62) and $L = \eta(rM^3)^{1/2}$. Binaries may therefore change their precessional morphology while evolving towards merger. The boundaries between different morphologies (cf. Sec. 2.2.3) are set by the (anti)alignment condition $\sin\theta_i = 0$; the binary morphology changes whenever

radiation reaction brings J and L to values that satisfy this condition (which can only occur on the effective-potential loop $\xi_\pm(S)$, as seen in Fig. 2.5). Figure 2.11 shows two examples of these phase transitions. At the radii $r_{\rm tr}$ where phase transitions occur, $\Delta\Phi$ changes discontinuously either at S_- (left panel) or S_+ (right panel), causing the solutions $\Delta\Phi(S)$ of Eqs. (2.37-2.39) to transition between the qualitatively different shapes seen in the bottom panel of Fig. 2.3. The binary BHs in the left (right) panel evolve from the circulating morphology to the morphology in which $\Delta\Phi$ oscillates about 0 (π).

A more complete phenomenology of phase transitions is illustrated in Fig. 2.12. The evolution of $\cos\theta_1$ and $\cos\theta_2$ along the inspiral is shown for a variety of initial conditions $\cos\theta_{i\infty}$. At each separation r, the angles θ_i vary on the precession time within a finite range specified by the conditions $\xi = \xi_\pm(S)$ (cf. Fig. 2.3). These envelopes vary on the radiation-reaction time as J evolves according to Eq. (2.62); their width shrinks to a zero as $r/M \to \infty$ according to Eqs. (2.69-2.70), and tends to thicken at smaller separations because of the increasing importance of terms proportional to S^2 in Eqs. (2.37-2.39). Horizontal bars above each panel track the binary morphologies, which we label as **C**, **L0**, and **L$\boldsymbol{\pi}$** for circulation, libration about $\Delta\Phi = 0$, and libration about $\Delta\Phi = \pi$. These morphologies change whenever one of the allowed ranges reach the boundaries $\cos\theta_i = \pm 1$.

All binaries circulate at large separation because the angles $\cos\theta_1$ and $\cos\theta_2$ are approximately constant (Sec. 2.3.2) and $\Delta\Phi$ from Eq. (2.39) is monotonic in S, thus satisfying Eq. (2.42). Some binaries (leftmost panels of Fig. 2.12) remain in the circulating morphology until the PN approximation breaks down ($r = 10M$). Other binaries undergo a single transition into a librating phase (middle columns of Fig. 2.12); $\Delta\Phi$ will oscillate about 0 (π) following this transition if the alignment condition $\sin\theta_i = 0$ is satisfied at S_- (S_+). Since $\cos\theta_1$ ($\cos\theta_2$) decreases (increases) monotonically with S [cf. Eqs. (2.37-2.39)], the above conditions can be summarized as

$$\cos\theta_1 = 1 \quad \text{or} \quad \cos\theta_2 = -1 : \quad \mathbf{C} \longrightarrow \mathbf{L0}\,, \tag{2.76}$$

$$\cos\theta_1 = -1 \quad \text{or} \quad \cos\theta_2 = 1 : \quad \mathbf{C} \longrightarrow \mathbf{L\boldsymbol{\pi}}\,. \tag{2.77}$$

These phase transitions were seen in previous (orbit-averaged) simulations [463] and referred to as *spin locking*, because the BH spins locked into libration about the spin-orbit resonances at $\xi_{\rm min}$ and $\xi_{\rm max}$. As the the librating binaries continue to inspiral, some may transition back into the circulating phase, as pictured in the rightmost column of Fig. 2.12.

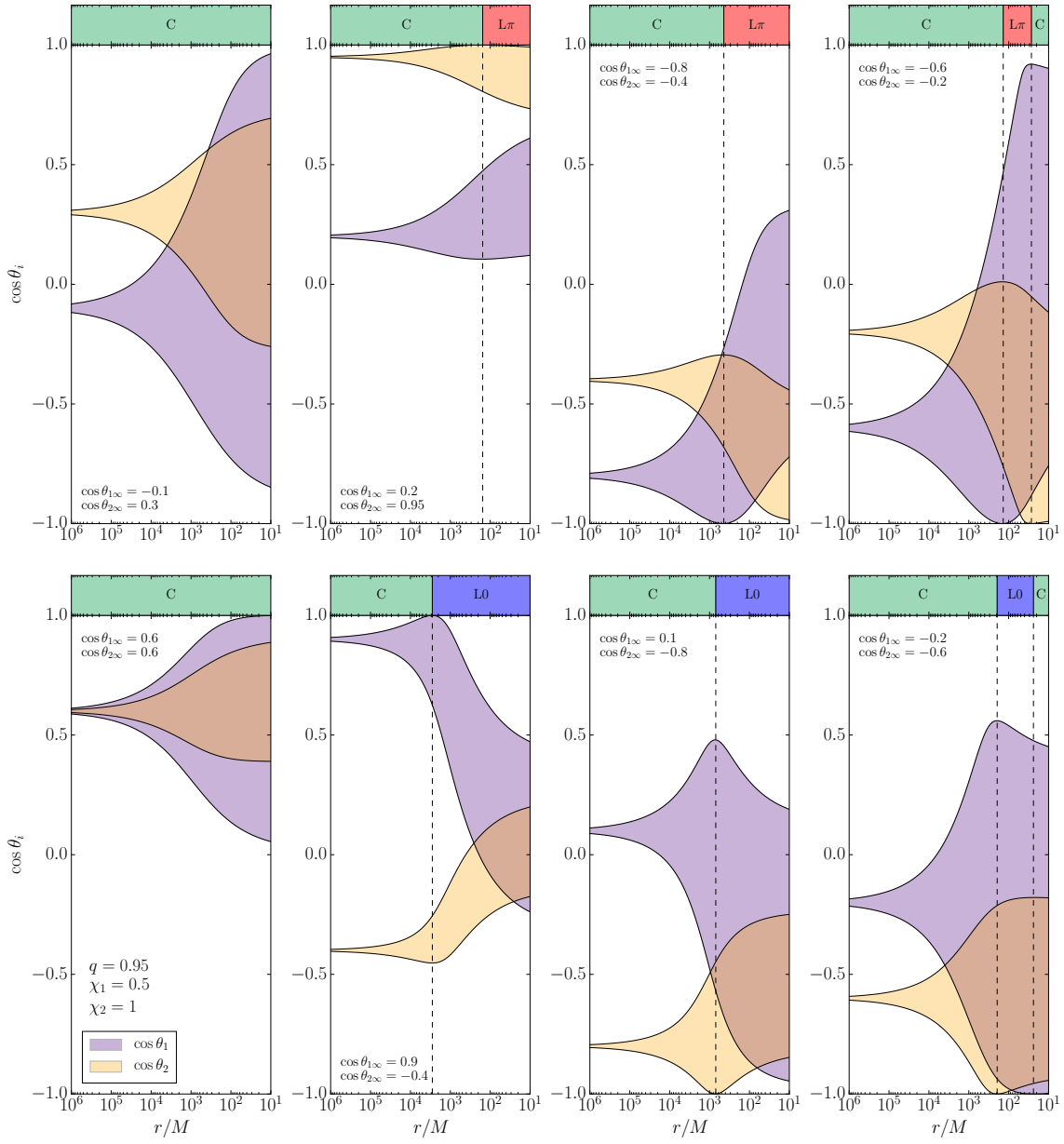

Figure 2.12: Evolution of the spin morphology and the allowed ranges of the spin angles θ_i over a precession cycle as functions of the binary separation r. Each panel shows the range of $\cos\theta_1$ (purple/darker) and $\cos\theta_2$ (orange/lighter) for different initial conditions $\cos\theta_{i\infty}$. The current morphology is tracked by the horizontal bar above each panel. Morphologies are indicated as **C** (green) for circulating, **L0** (blue) for $\Delta\Phi$ librating about 0, and **Lπ** (red) for $\Delta\Phi$ librating about π. The morphology changes whenever $\cos\theta_i = \pm 1$ (vertical dashed lines). BH binaries in the leftmost column do not undergo any transitions in the PN regime; one transition into a librating morphology occurs for binary BHs in the center columns; two transitions (circulating to librating, librating to circulating) occur for binary BHs in the rightmost column. The mass ratio and spin magnitudes are $q = 0.95$, $\chi_1 = 0.5$, and $\chi_2 = 1$ in all panels.

The conditions for this second transition are

$$\cos\theta_1 = -1 \quad \text{or} \quad \cos\theta_2 = 1 : \quad \mathbf{L0} \longrightarrow \mathbf{C}\,, \tag{2.78}$$

$$\cos\theta_1 = 1 \quad \text{or} \quad \cos\theta_2 = -1 : \quad \mathbf{L}\boldsymbol{\pi} \longrightarrow \mathbf{C}\,. \tag{2.79}$$

As discussed further in Sec. 2.4.2 below, this second phase transition occurs in the PN regime ($r \gtrsim 10M$) only in some corners of the parameter space ($q \lesssim 1$ and $\chi_1 \neq \chi_2$). We have not found any additional transitions in the PN regime, but multiple transitions may occur at the smaller separations accessible to numerical-relativity simulations.

2.4.2 Dependence on mass and spin asymmetry

The asymmetry in the masses m_i and spin magnitudes χ_i determines which of the eight scenarios depicted in Fig. 2.12 a binary will experience during its inspiral. The alignment conditions $\sin\theta_1 = 0$ and $\sin\theta_2 = 0$ tend to be satisfied at similar values of ξ for symmetric binaries ($q \to 1$ and $\chi_1 \simeq \chi_2$), shrinking the circulating (green) region in the left panel of Fig. 2.5 and enhancing the fraction of librating binaries. This point is illustrated in Fig. 2.13 below, which shows the fraction of isotropic binaries in each of the three morphologies as functions of the binary separation. Each panel is computed by averaging over a sample of binaries isotropically distributed at large separations (flat distributions in $\cos\theta_{1\infty}$ and $\cos\theta_{2\infty}$); all binaries in each sample share the same mass ratio and spin magnitudes. As the separation decreases, binaries transition from the circulating to librating morphologies. The fraction of binaries experiencing these transitions strongly depends on the mass ratio q. If the mass ratio is low ($q \lesssim 0.6$), most binaries remain circulating down to very small separations $r \sim 10M$. Comparable-mass binaries ($q \gtrsim 0.6$) are more likely to undergo a phase transition in the PN regime. The typical transition radius $r_{\rm tr}$ at which these phase transitions occur is also very sensitive to the mass ratio [463, 270]; transitions occur in the very late inspiral for low mass ratios while $r_{\rm tr}$ can be as large as $10^5 M$ for $q \simeq 0.99$. Very long evolutions are needed to capture all of the morphological transitions for nearly equal-mass binaries; such long inspirals are prohibitively expensive in the standard orbit-averaged approach (as seen in Fig. 2.10) but can easily be calculated within our new precession-averaged formalism.

A more extensive exploration of how BH binary spin morphology depends on the binary parameters is shown in Fig. 2.14 and Table 2.1. Isotropic distributions at $r/M = \infty$ are evolved down to $r = 10M$, where their morphologies are determined; as shown in the upper panel of Fig. 2.9, these initially isotropic distributions remain isotropic at smaller

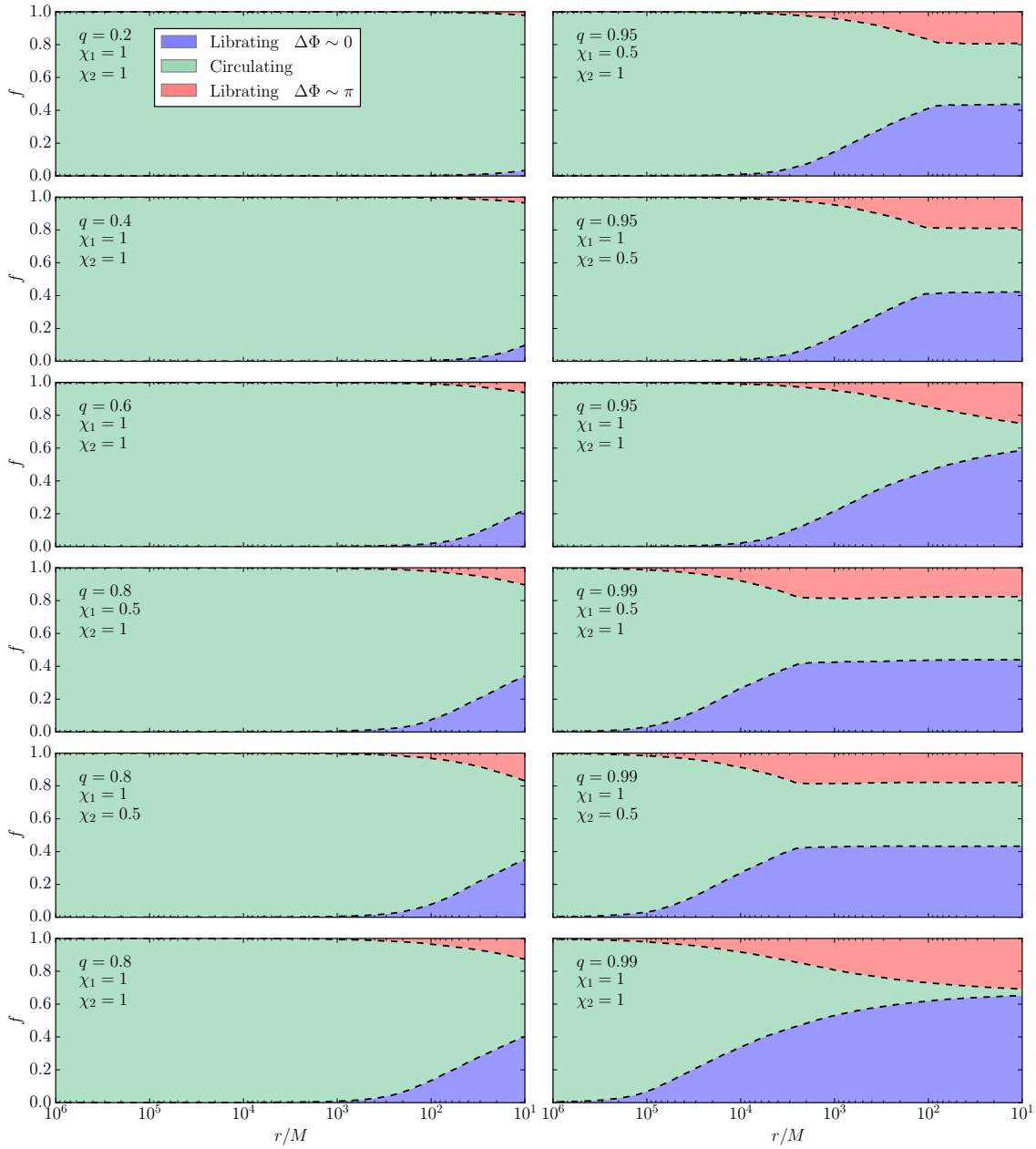

Figure 2.13: The fraction f of isotropic binaries in each of the three precessional morphologies as functions of the binary separation. Each panel refers to different values of q, χ_1 and χ_2 as indicated in the legends. The fraction of binaries in which $\Delta\Phi$ circulates (green, middle region of each panel), oscillates about 0 (blue, bottom region of each panel), or oscillates about π (red, top region of each panel) is shown as the binary orbit shrinks, with dashed lines separating the different morphologies. The fraction of binaries in librating morphologies generally grows during the inspiral; this growth is stronger as $q \to 1$ but may stall for nearly equal masses and $\chi_1 \neq \chi_2$, as seen in panels in the right column.

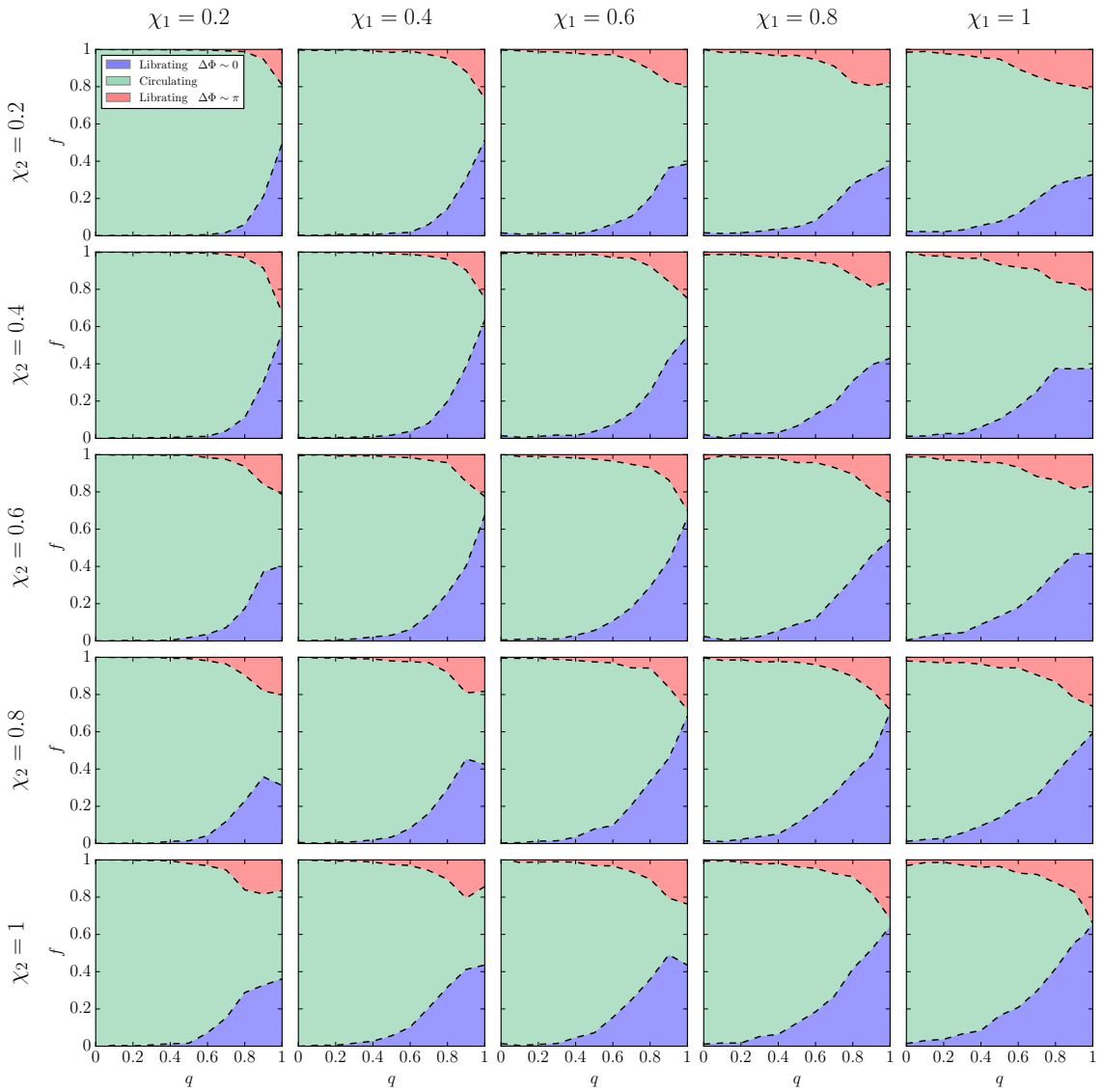

Figure 2.14: The fraction f of isotropic binary BHs for which $\Delta\Phi$ circulates (green, middle region), oscillates about 0 (blue, bottom region), or oscillates about π (red, top region) at a binary separation $r = 10M$ as functions of the mass ratio q. Dashed lines separate the different morphologies. Each panel corresponds to a different value of χ_1 (columns) and χ_2 (rows). The fraction of binary BHs in librating morphologies increases as the mass asymmetry decreases ($q \to 1$). For nearly equal masses ($q \gtrsim 0.9$), asymmetry in the spin magnitudes increases the fraction of binaries in the circulating morphology as can be seen by comparing panels on and off of the diagonal. Some data used in this plot are listed in Table 2.1. The website [200] contains an animated version of this figure, where the panels are shown at decreasing binary separations.

separations. The fraction of binaries in each morphology at $r = 10M$ is shown as functions of q for a grid of values of the spin magnitudes χ_1 and χ_2. As was already seen in Fig. 2.13, the likelihood of phase transitions depends on the mass ratio q; more librating binaries are found for comparable-mass binary BHs at any fixed separation.

Spin magnitudes also affect the fraction of binary BHs in each morphology. As one

$\chi_2 = 0.2$

$\chi_1 = 0.2$				$\chi_1 = 0.4$				$\chi_1 = 0.6$				$\chi_1 = 0.8$				$\chi_1 = 1$			
q	L0	C	Lπ	q	L0	C	Lπ	q	L0	C	Lπ	q	L0	C	Lπ	q	L0	C	Lπ
0.05	0.00	1.00	0.00	0.05	0.00	0.99	0.00	0.05	0.01	0.98	0.01	0.05	0.01	0.98	0.01	0.05	0.02	0.96	0.01
0.2	0.00	1.00	0.00	0.2	0.01	0.99	0.00	0.2	0.01	0.98	0.01	0.2	0.02	0.97	0.01	0.2	0.02	0.95	0.02
0.4	0.00	1.00	0.00	0.4	0.01	0.98	0.01	0.4	0.01	0.97	0.02	0.4	0.04	0.93	0.04	0.4	0.06	0.90	0.04
0.6	0.01	0.99	0.00	0.6	0.02	0.97	0.01	0.6	0.06	0.91	0.03	0.6	0.08	0.86	0.06	0.6	0.12	0.77	0.10
0.8	0.06	0.93	0.01	0.8	0.14	0.81	0.05	0.8	0.20	0.69	0.11	0.8	0.28	0.54	0.18	0.8	0.27	0.55	0.18
0.95	0.35	0.53	0.12	0.95	0.41	0.40	0.19	0.95	0.38	0.44	0.18	0.95	0.35	0.46	0.19	0.95	0.32	0.48	0.21

$\chi_2 = 0.4$

q	L0	C	Lπ	q	L0	C	Lπ	q	L0	C	Lπ	q	L0	C	Lπ	q	L0	C	Lπ
0.05	0.00	1.00	0.00	0.05	0.00	0.99	0.00	0.05	0.01	0.98	0.01	0.05	0.01	0.97	0.01	0.05	0.01	0.98	0.01
0.2	0.00	1.00	0.00	0.2	0.00	0.99	0.00	0.2	0.01	0.98	0.01	0.2	0.03	0.96	0.01	0.2	0.03	0.95	0.02
0.4	0.00	0.99	0.00	0.4	0.01	0.99	0.00	0.4	0.01	0.97	0.01	0.4	0.03	0.94	0.03	0.4	0.06	0.91	0.03
0.6	0.01	0.99	0.00	0.6	0.04	0.95	0.01	0.6	0.07	0.90	0.03	0.6	0.13	0.82	0.05	0.6	0.17	0.75	0.08
0.8	0.11	0.86	0.03	0.8	0.20	0.76	0.04	0.8	0.25	0.67	0.08	0.8	0.31	0.57	0.13	0.8	0.38	0.46	0.16
0.95	0.43	0.36	0.21	0.95	0.51	0.32	0.17	0.95	0.49	0.31	0.20	0.95	0.41	0.41	0.17	0.95	0.37	0.43	0.20

$\chi_2 = 0.6$

q	L0	C	Lπ	q	L0	C	Lπ	q	L0	C	Lπ	q	L0	C	Lπ	q	L0	C	Lπ
0.05	0.00	1.00	0.00	0.05	0.00	0.99	0.00	0.05	0.01	0.99	0.00	0.05	0.02	0.97	0.02	0.05	0.01	0.97	0.01
0.2	0.00	1.00	0.00	0.2	0.01	0.99	0.01	0.2	0.01	0.98	0.01	0.2	0.01	0.97	0.01	0.2	0.04	0.93	0.03
0.4	0.00	0.99	0.00	0.4	0.02	0.97	0.01	0.4	0.03	0.95	0.02	0.4	0.06	0.92	0.02	0.4	0.09	0.87	0.04
0.6	0.04	0.95	0.02	0.6	0.06	0.92	0.02	0.6	0.11	0.86	0.03	0.6	0.12	0.84	0.04	0.6	0.18	0.75	0.07
0.8	0.17	0.76	0.06	0.8	0.26	0.70	0.04	0.8	0.29	0.64	0.07	0.8	0.33	0.56	0.10	0.8	0.37	0.49	0.14
0.95	0.39	0.43	0.19	0.95	0.54	0.28	0.18	0.95	0.55	0.23	0.22	0.95	0.50	0.28	0.22	0.95	0.47	0.36	0.17

$\chi_2 = 0.8$

q	L0	C	Lπ	q	L0	C	Lπ	q	L0	C	Lπ	q	L0	C	Lπ	q	L0	C	Lπ
0.05	0.00	1.00	0.00	0.05	0.00	0.99	0.00	0.05	0.00	0.99	0.01	0.05	0.01	0.98	0.01	0.05	0.02	0.96	0.02
0.2	0.00	1.00	0.00	0.2	0.01	0.99	0.00	0.2	0.01	0.98	0.01	0.2	0.02	0.96	0.01	0.2	0.03	0.94	0.03
0.4	0.01	0.98	0.01	0.4	0.02	0.97	0.01	0.4	0.04	0.95	0.02	0.4	0.05	0.93	0.02	0.4	0.10	0.87	0.04
0.6	0.04	0.94	0.02	0.6	0.08	0.89	0.02	0.6	0.10	0.87	0.03	0.6	0.18	0.78	0.04	0.6	0.21	0.73	0.06
0.8	0.23	0.68	0.10	0.8	0.29	0.63	0.08	0.8	0.34	0.61	0.06	0.8	0.38	0.52	0.10	0.8	0.38	0.49	0.13
0.95	0.34	0.47	0.19	0.95	0.44	0.37	0.19	0.95	0.57	0.21	0.22	0.95	0.59	0.18	0.23	0.95	0.54	0.22	0.24

$\chi_2 = 1$

q	L0	C	Lπ	q	L0	C	Lπ	q	L0	C	Lπ	q	L0	C	Lπ	q	L0	C	Lπ
0.05	0.00	1.00	0.00	0.05	0.00	1.00	0.00	0.05	0.01	0.99	0.00	0.05	0.01	0.98	0.01	0.05	0.02	0.95	0.02
0.2	0.00	1.00	0.00	0.2	0.01	0.99	0.01	0.2	0.01	0.98	0.01	0.2	0.02	0.97	0.01	0.2	0.04	0.95	0.01
0.4	0.01	0.98	0.01	0.4	0.03	0.96	0.01	0.4	0.05	0.94	0.01	0.4	0.06	0.92	0.02	0.4	0.08	0.88	0.04
0.6	0.07	0.90	0.03	0.6	0.10	0.87	0.03	0.6	0.15	0.81	0.03	0.6	0.18	0.77	0.04	0.6	0.21	0.72	0.07
0.8	0.29	0.55	0.16	0.8	0.32	0.58	0.10	0.8	0.36	0.54	0.10	0.8	0.41	0.49	0.09	0.8	0.42	0.46	0.12
0.95	0.34	0.48	0.17	0.95	0.42	0.40	0.17	0.95	0.46	0.32	0.22	0.95	0.58	0.17	0.25	0.95	0.59	0.16	0.24

Table 2.1: Fractions of isotropic binary BHs in each of the three precessional morphologies (**L0**: $\Delta\Phi$ oscillates about 0, **C**: $\Delta\Phi$ circulates, **Lπ**: $\Delta\Phi$ oscillates about π) at $r = 10M$ as shown in Fig. 2.14. For a grid of values in χ_1 (columns), χ_2 (rows) and, q (first column in each mini-table), we report the fraction of binaries in each morphology. The sum of the three fractions may differ from unity because of rounding errors.

moves along the diagonal of Fig. 2.14 in the direction of increasing $\chi_1 = \chi_2$, a slightly higher fraction of binaries are found in librating morphologies because of increased spin-spin coupling [463]. The corner of the parameter space characterized by mass symmetry and spin asymmetry ($q \to 1$ and $\chi_1 \neq \chi_2$) presents a peculiar phenomenology, as seen in the right panels of Fig. 2.13, where the fraction of binaries in each morphology approaches constant values for $r \lesssim 1000M$. This behavior can be explained by recognizing that in this region of parameter space binaries may undergo two morphological transitions in the PN regime, as seen in the rightmost panels of Fig. 2.12. The number of binaries experiencing their first phase transition from circulation to libration is nearly canceled by the number of

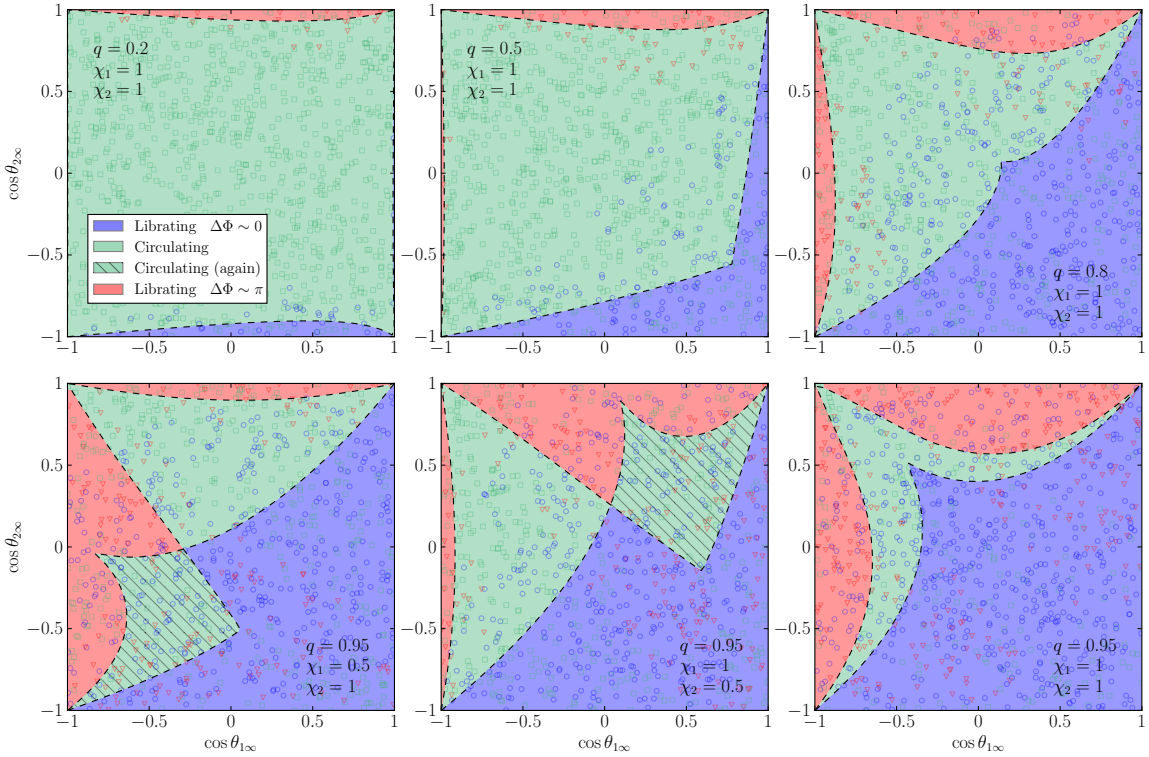

Figure 2.15: Spin morphologies at $r_f = 10M$ as functions of the asymptotic values of the spin angles $\theta_{i\infty}$. The mass ratio q and spin magnitudes χ_i for each panel are indicated in the legends. Evolving BH binaries along the four lines $\cos\theta_i = \pm 1$ at r_f out to $r/M \to \infty$ using our new precession-averaged approach yields the dashed curves separating the different final morphologies: $\Delta\Phi$ oscillates about 0 (blue), oscillates about π (red), circulates without ever having experienced a phase transition (plain green), or circulates after having experienced a phase transition to libration and then a second phase transition back to circulation (hatched green). The morphology within each region defined by the dashed boundaries is determined by which of the conditions $\cos\theta_i = \pm 1$ these boundaries satisfy, as described in Sec. 2.4.3. The points show the locations of binaries in the $\cos\theta_1 - \cos\theta_2$ plane at r_f and are colored by their morphology at that separation [$\Delta\Phi$ oscillates about 0 (blue circles), oscillates about π (green squares), or circulates (red triangles)]. Because morphology depends on $\Delta\Phi$ in addition to θ_1 and θ_2 at finite separation, the projection onto the $\cos\theta_1 - \cos\theta_2$ plane can lead points of different morphologies to occur at the same positions, particularly for comparable-mass binaries $q \simeq 1$ where the θ_i's oscillate with greater amplitude. The website [200] contains an animated version of this figure in which r_f evolves.

binaries undergoing a second phase transition back to the circulating morphology, leading to almost constant fractions of binaries in each morphology. This effect also accounts for the kinks in the morphology fractions at $q \simeq 0.9$ in the off-diagonal ($\chi_1 \neq \chi_2$) panels of Fig. 2.14.

2.4.3 Predicting spin morphology at small separations

We described in great detail in Sec. 2.2.3 how to determine the BH binary spin morphology from the binary parameters at a given separation, but astrophysical binary BHs are often formed at much larger separations than where we are interested in observing them.

Although BH binaries can be efficiently evolved to smaller separations using the precession-averaged approach described in Sec. 2.3.3, we can in fact predict the spin morphology at a final separation r_f based solely upon the asymptotic values of $\theta_{1\infty}$ and $\theta_{2\infty}$ [or equivalently ξ and κ_∞ according to Eqs. (2.69-2.70)] without the need to integrate dJ/dL down to r_f. This can be achieved by recognizing that the curves in the $\cos\theta_{1\infty} - \cos\theta_{2\infty}$ plane separating the final morphologies at r_f correspond to binary BHs experiencing phase transitions at r_f, i.e. binaries for which $\cos\theta_i(r_f) = \pm 1$. These binaries constitute the four borders of the $\cos\theta_1 - \cos\theta_2$ plane at r_f; using our expression for dJ/dL in Eq. (2.62) to integrate binary BHs along these borders out to $r/M \to \infty$, we obtain four curves in the $\cos\theta_{1\infty} - \cos\theta_{2\infty}$ plane, as seen in Fig. 2.15. These curves define regions **I** and **II** in the $\cos\theta_{1\infty} - \cos\theta_{2\infty}$ plane with the following boundaries:

$$\begin{aligned}
&\textbf{I}. \quad && \cos\theta_{1\infty} = +1, && \cos\theta_{2\infty} = -1, \\
&\qquad && \cos\theta_1(r_f) = +1, && \cos\theta_2(r_f) = -1; \\
&\textbf{II}. \quad && \cos\theta_{1\infty} = -1, && \cos\theta_{2\infty} = +1, \\
&\qquad && \cos\theta_1(r_f) = -1, && \cos\theta_2(r_f) = +1.
\end{aligned}$$

The final morphology at r_f for each point in the $\cos\theta_{1\infty} - \cos\theta_{2\infty}$ plane is determined by whether or not that point is contained in the two regions:

- Outside both region **I** and region **II**: $\Delta\Phi$ circulates (no phase transitions, plain green in Fig. 2.15).
- Inside region **I** but not region **II**: $\Delta\Phi$ oscillates about 0 (one phase transition, blue in Fig. 2.15).
- Inside region **II** but not region **I**: $\Delta\Phi$ oscillates about π (one phase transition, red in Fig. 2.15).
- Inside both region **I** and region **II**: $\Delta\Phi$ circulates (two phase transitions, hatched green in Fig. 2.15).

These conditions on the final morphology are consistent with the criteria for phase transitions given in Eqs. (2.76-2.77) and (2.78-2.79). Once the boundaries of regions **I** and **II** have been established we can determine the final morphology of *any* BH binary from its initial conditions at astrophysically large separations without further need to integrate dJ/dL down to r_f. A binary with spin orientations lying in the green, red or blue region of Fig. 2.15 at large separations will be found with $\Delta\Phi$ circulating, oscillating about 0 or oscillating about π at the end of the inspiral.

Measuring BH binary spin morphology directly offers several advantages over explicitly measuring the spin angles θ_1, θ_2 and $\Delta\Phi$. Spin morphology encodes information about BH binary spin precession but is more robust than the spin angles in that it only varies on the radiation-reaction time (being a function of L, J, and ξ). Measurement of only the two angles θ_1 and θ_2 at small separations constrains neither the morphology at small separations nor the initial conditions at large separations, as can be seen from the scatter points in Fig. 2.15, which show an isotropic sample of binaries at r_f. Points corresponding to the circulating and both librating morphologies lie right on top of each other in this plot, evidence of both the importance of the third angle $\Delta\Phi$ and the large oscillations in θ_i at small separations seen in Fig. 2.12. By contrast, spin morphology is a direct memory of a BH binary's initial position in the $\cos\theta_{1\infty} - \cos\theta_{2\infty}$ plane, as seen in Fig. 2.15. Astrophysical scenarios of BH binary formation can favor some regions in this plane over others [204], implying that GW observations of spin morphology can constrain BH binary formation [208].

2.5 Towards GW astronomy

BH binaries evolve on three distinct timescales: the orbital time $t_{\rm orb}$, the precession time $t_{\rm pre}$, and the radiation-reaction time $t_{\rm RR}$. In the PN regime ($r \gg r_g$), these timescales obey a strict hierarchy: $t_{\rm orb} \ll t_{\rm pre} \ll t_{\rm RR}$. All of the parameters needed to describe binary BHs evolve on a distinct timescale: the vectorial binary separation $\mathbf{r}$ on $t_{\rm orb}$, the angular-momentum directions $\hat{\mathbf{L}}$ and $\hat{\mathbf{S}}_i$ on $t_{\rm pre}$, and the orbital-angular-momentum magnitude L and total angular momentum $\mathbf{J}$ on $t_{\rm RR}$. The mass ratio q and spin magnitudes S_i remain constant throughout the inspiral. We exploited this timescale hierarchy and conservation of the projected effective spin ξ [141, 431] throughout the inspiral to solve the orbit-averaged 2PN equations of BH spin precession given by Eq. (2.47-2.48). The solutions given by Eq. (2.37-2.39) for the three angles θ_1, θ_2, and $\Delta\Phi$ that specify the relative orientations of $\mathbf{L}$, $\mathbf{S}_1$, and $\mathbf{S}_2$ are remarkably simple and are given parametrically in terms of a single variable, the total-spin magnitude S, that evolves on $t_{\rm pre}$.

These solutions fully determine how the relative orientations of the three angular momenta evolve over a precession cycle as S oscillates back and forth between extrema $S_\pm$. We find that spin precession can be classified into three distinct morphologies depending on whether $\Delta\Phi$ oscillates about 0, oscillates about π, or circulates through the full range $[-\pi, +\pi]$ over a precession cycle. For binary BHs with a given mass ratio q and spin magnitudes S_i, the precessional morphology at a binary separation r is determined by J and ξ, implying that the morphology only evolves on the radiation-reaction time $t_{\rm RR}$. Spin-

orbit coupling dominates over the higher-PN-order spin-spin coupling at large separations implying that all binary BHs formed at such large separations begin in the circulating morphology. Since ξ is constant to high accuracy throughout the inspiral, evolving our solutions (2.37-2.39) and their associated morphology to smaller separations (lower values of L) only requires an expression for dJ/dL due to radiation reaction. All previous studies of radiation reaction have relied on orbit-averaged expressions for $d\mathbf{L}_{\rm RR}/dt$ that must be integrated numerically with time steps $\Delta t \lesssim t_{\rm pre}$. Our new solutions (2.37-2.39) allow us to *precession average* these expressions to derive Eq. (2.62) for dJ/dL that can be integrated with a time step $t_{\rm pre} \ll \Delta t' \lesssim t_{\rm RR}$. The computational cost of calculating inspirals from an initial separation r_i in our new precession-averaged approach scales as $\log r_i$, leading to vast savings over the traditionally orbit-averaged approach (which scales as $r_i^{3/2}$) for the large initial separations relevant to astrophysical BH binary formation.

Using our new expression for dJ/dL, we can evolve our initially circulating binary BHs to smaller separations, where they may experience a phase transition to one of the two librating morphologies. Some of these librating binary BHs may subsequently undergo a second phase transition back to circulation before reaching a binary separation $r = 10M$ below which the PN approximation itself begins to break down. Our precession-averaged calculation of the inspiral agrees well with the orbit-averaged approach down to nearly this separation where small discrepancies appear because of dynamically generated inhomogeneity in the precessional phase as the timescale hierarchy fails. Unlike the angles θ_1, θ_2 and $\Delta\Phi$, that vary rapidly on the precession time at small separations, the precession morphology at small separations is directly determined by the asymptotic values $\theta_{i\infty}$ of these angles at large separations, providing a memory of BH binary formation potentially accessible to GW detectors.

Although this work focuses on BH binary spin precession, our analysis also facilitates the calculation and interpretation of GW signals. Fast templates suitable for GW detection and parameter estimation are being developed using our new precessional solutions and precession-averaged equation for radiation reaction [127]. The insights underpinning our approach (most notably the use of a hierarchical coordinate system that better respects the separation of timescales intrinsic in the binary dynamics) are also helping us to assess whether the precessional morphology of binary BHs in spin-orbit resonances can be reliably identified in the context of full GW parameter estimation [208, 514]. We find that BH binary spin orientations can be significantly constrained at realistic signal-to-noise ratios, suggesting that observations of BH binary spin precession as described in this work may soon provide a new window into the astrophysical origins of BH binaries and GR itself.

Appendix

2.A PRECESSION: an open-source python module

The numerical code developed to obtain the results presented in this Chapter has been publicly released [203]. The code, called PRECESSION, is distributed as an open-source PYTHON module. In a nutshell, PRECESSION performs BH binary inspirals tracking their precessional dynamics using both standard orbit-averaged and our new precession-averaged approaches. It also conveniently implements fitting formulae obtained from numerical-relativity simulations to predict mass, spin and recoil of BH remnants following binary mergers (cf. Sec. 4.2.1). PRECESSION combines the flexibility of the high-level programming language PYTHON with existing scientific libraries written in C and FORTRAN to bypass speed bottlenecks.

In this Appendix we give a general overview of the code. Sec. 2.A.1 describes code installation; Sec. 2.A.2 presents a minimal working example; Sec. 2.A.3 provides details on documentation and source distribution.

2.A.1 Installation

PRECESSION is a PYTHON [522] module and is part of the PYTHON Package Index:

`pypi.python.org/pypi/precession`.

The code can be installed in a single line through the package management system `pip`:

```
pip install precession
```

Useful options to the command above include `--user` for users without root privileges and `--upgrade` to update a pre-existing installation. The scientific libraries NUMPY [521], SCIPY [262], MATPLOTLIB [251] and PARMAP [395] are specified as prerequisites and, if not present, will be installed/updated together with PRECESSION. PRECESSION has been tested on PYTHON 2.7 distributions; porting to PYTHON 3 is under development.

Once PRECESSION has been installed, it has to be imported typing

```
import precession
```

from within a PYTHON console or script. The main module `precession` contains ~ 80 functions for a total of ~ 1700 code lines. The submodule `precession.test` consists

of $\sim$ 300 code lines divided in 7 examples routines. If needed, this has to be imported separately typing

```
import precession.test
```

2.A.2 A first working example

A minimal working example of some features of PRECESSION is shown in Fig. 2.A.1. We encourage the reader to execute this code snippet typing

```
precession.test.minimal()
```

We initialize a BH binary at the extremely large separation of 10 billion gravitational radii ($r = 10^{10}M$) and evolve it down to small separations ($r = 10M$) where the PN approximation breaks down. The integration is performed using precession-averaged PN equations of motion, as described in Sec. 2.3. The evolution of the BH spins along such an enormous separation range is computed in less than 6 seconds using a single core of a standard off-the-shelf desktop machine.

2.A.3 Documentation and source distribution

PRECESSION is currently in its v1.0 release. The code is under active development and additional features will be added regularly. Various parts of the code were used in the following published results [205, 206, 211, 269, 209, 514**?**], as well as in Chapters 2, 3, 4, 5 and 6 of this Thesis.

The source code is distributed under GIT version-control system at

`github.com/dgerosa/precession` (code),

and it is released under the CC BY 4.0 license. Extensive code documentation can be generated automatically in html format from the PYTHON's docstrings using the text processor PDOC [197]. Documentation is regularly uploaded to a dedicated branch of the GIT repository and it is available at

`dgerosa.github.io/precession` (documentation).

The same information can also be accessed using PYTHON's built-in help system, e.g. `help(precession.function)`. Additional resources and results are available at

`davidegerosa.com/precession`.

Ref. [203] provides a complete user guide of the code, where each function is carefully described and extensive example routines are provided.

Source code:

```
t0=time.time()
q=0.75    # Mass ratio
chi1=0.5  # Primary's spin magnitude
chi2=0.95 # Secondary's spin magnitude
print "Take a BH binary with q=%.2f, chi1=%.2f and
 ↪   chi2=%.2f" %(q,chi1,chi2)
sep=numpy.logspace(10,1,10) # Output separations
t1= numpy.pi/3.  # Spin orientations at r_vals[0]
t2= 2.*numpy.pi/3.
dp= numpy.pi/4.
M,m1,m2,S1,S2=precession.get_fixed(q,chi1,chi2)
t1v,t2v,dpv=precession.evolve_angles(t1,t2,dp,sep,q,S1,S2)
print "Perform BH binary inspiral"
print "log10(r/M) \t theta1 \t theta2 \t deltaphi"
for r,t1,t2,dp in zip(numpy.log10(sep),t1v,t2v,dpv):
    print "%.0f \t\t %.3f \t\t %.3f \t\t %.3f" %(r,t1,t2,dp)
t=time.time()-t0
print "Executed in %.3fs" %t
```

Screen output:

```
Take a BH binary with q=0.75, chi1=0.50 and chi2=0.95
Perform BH binary inspiral
log10(r/M)  theta1  theta2  deltaphi
10          1.047    2.094  -2.330
9           1.047    2.094  1.811
8           1.047    2.095  2.341
7           1.046    2.095  2.827
6           1.050    2.093  0.351
5           1.055    2.089  -0.211
4           1.046    2.095  -1.588
3           0.991    2.133  -2.271
2           0.909    2.190  -1.903
1           0.505    2.439  -1.188
Executed in 5.526s
```

Figure 2.A.1: Source code (top) and screen output (bottom) of the example `test.minimal` described in Sec. 2.A.2. We select a BH binary at $r = 10^{10}M$ and track the directions of the two spins and the orbital angular momentum during its PN inspiral till $r = 10M$. We use precession-averaged PN equations, which require random samplings of the precessional phase, see Sec. 2.3.3 (different code executions will therefore return different values of the spin angles). The execution time reported is obtained using a single core of a 2013 Intel i5-3470 3.20GHz CPU. These lines can be executed typing `precession.test.minimal()`.

Chapter 3

Up-down instability of spinning black-hole binaries

Outlook

Binary BHs on quasicircular orbits with spins aligned with their orbital angular momentum have been test beds for analytic and numerical relativity for decades, not least because symmetry ensures that such configurations are equilibrium solutions to the spin-precession equations. In this Chapter we show that these solutions can be unstable when the spin of the higher-mass BH is aligned with the orbital angular momentum and the spin of the lower-mass BH is antialigned. Spins in these configurations are unstable to precession to large misalignment when the binary separation r is between the values $r_{\rm ud\pm} = (\sqrt{\chi_1} \pm \sqrt{q\chi_2})^4 (1-q)^{-2} M$, where M is the total mass, $q \equiv m_2/m_1$ is the mass ratio, and χ_1 (χ_2) is the dimensionless spin of the more (less) massive BH. This instability exists for a wide range of spin magnitudes and mass ratios and can occur in the strong-field regime near the merger. This study consists in a direct application of the formalism presented in Chapter 2 to characterize fully generic spin precession. This instability provides a channel to circumvent astrophysical spin alignment at large binary separations, allowing significant spin precession prior to merger affecting both GW and electromagnetic signatures of stellar-mass and supermassive binary BHs.

Executive summary

This Chapter is organized as follows. In Sec. 3.1 we briefly introduce the problem of BH spin alignment and briefly summarize some of our previous findings. In Sec. 3.2 we detail our stability analysis. Finally, Sec. 3.3 outlines the observational consequences of this newly discovered instability. To facilitate the presentation of our main results, most of the technical calculations are postponed to Appendix 3.A.

The material presented in this Chapter is based on [205].

3.1 Spin-aligned configurations

In this Section we first introduce the astrophysical implications of spin-alignment in BH binaries (Sec. 3.1.1), and later summarize our findings presented in Chapter 2 on generic BH spin precession (Sec. 3.1.2).

3.1.1 The role of BH spin (anti)alignment

BHs have been observed through electromagnetic observations in two distinct regimes: stellar-mass BHs ($5M_\odot \lesssim m \lesssim 100M_\odot$) accrete from companions in X-ray binaries [97, 95, 538], while supermassive BHs shine as quasars or Active Galactic Nuclei (AGN) [249, 340]. Stellar-mass BH mergers are now also directly observed through GWs [13, 6, 14, 15, 8, 7, 11]. Both types of BHs naturally occur in binaries: the massive stellar progenitors of stellar-mass BHs are typically formed in binaries, while supermassive BHs form binaries following the mergers of their host galaxies [60]. Gravitational radiation circularizes the orbits of these binaries [415] and causes them to inspiral and eventually merge, making them sources of GWs for current and future GW detectors [13, 228, 517, 491, 429, 345, 346, 261, 295]. The spins of these binary BHs need not be aligned with their orbital angular momentum: stellar-mass BHs may recoil during asymmetric collapses tilting their spins with respect to the orbital plane [264, 252, 204], while the initial orbital plane of supermassive BH binaries reflects that of their host galaxies and is thus independent of their spin. Gravitational effects alone will not align the BH spins with the orbital angular momentum [463, 92], but astrophysical mechanisms exist that drive the BH spins towards alignment in both regimes. The first BH to collapse in stellar-mass BH binaries may accrete in a disk from its as yet uncollapsed companion, while both members of a supermassive BH binary may accrete from a common circumbinary disk. Warps in these accretion disks can align the BH spins with the orbital angular momentum via the Bardeen-Petterson effect (see [55, 367, 211] and Chapter 5), but if the initial misalignment between the BH spin and accretion disk is

greater than 90°, the BH may instead be driven into antialignment [278] (cf. Sec. 5.2.3).

Misaligned spins cause the orbital angular momentum to precess [56, 508, 276], modulating the emitted GWs [31]. Spin misalignment is both a blessing and a curse for GW data analysis: it increases the parameter space of templates needed to detect GWs via matched filtering but also breaks degeneracies between estimated parameters in detected events [139]. Misaligned spins at merger can generate large gravitational recoils [215, 115, 112], ejecting supermassive BHs from their host galaxies (cf. Chapter 4). Spin precession may also be responsible for the observed "X-shaped" morphology of AGN radio lobes [361, 199]. Given the importance of spin misalignment, it is worth investigating the robustness of aligned spin configurations.

In the general case that the BHs have unequal masses, there are four distinct (anti-)aligned configurations, which we refer to as up-up, up-down, down-up, and down-down. The direction before (after) the hyphen describes the more (less) massive BH and up (down) implies (anti-)alignment of the spin with the orbital angular momentum. By symmetry, all four configurations are equilibrium solutions to the orbit-averaged spin-precession equations [276], but are these solutions stable? To answer this question, we investigate how the configurations respond to perturbations of the spin directions using the approach for studying generically precessing systems presented in Chapter 2 [269, 206]. As we will demonstrate below, the up-down configuration is unstable for certain choices of binary parameters, with significant consequences for GW data analysis and astrophysics.

3.1.2 Generic spin precession

This paragraph summarizes the approach to spin precession described in Chapter 2 [269, 206], using natural units $G = c = 1$. Binary BHs with total mass $M = m_1 + m_2$, mass ratio $q = m_2/m_1 \leq 1$, symmetric mass ratio $\eta = q/(1+q)^2$, and spins $\mathbf{S}_i = \chi_i m_i^2 \hat{\mathbf{S}}_i$ evolve on three distinct time scales: the orbital time $t_{\rm orb} \simeq (r^3/M)^{1/2}$ on which their separation $\mathbf{r}$ changes direction, the precession time $t_{\rm pre} \simeq t_{\rm orb}(r/M)$ on which the spins and orbital angular momentum $\mathbf{L}$ change direction, and the radiation-reaction time $t_{\rm RR} \simeq t_{\rm orb}(r/M)^{5/2}$ on which the magnitudes r and L decrease due to GW emission. The relative orientations of the spins are often specified by the two angles $\cos\theta_i = \hat{\mathbf{S}}_\mathbf{i} \cdot \hat{\mathbf{L}}$ and the angle $\Delta\Phi$ between the projections of the two spins onto the orbital plane given in Eqs. (2.2-2.4), all of which vary on $t_{\rm pre}$. The spin orientations can equivalently be specified by the magnitudes of the total spin $\mathbf{S} = \mathbf{S}_1 + \mathbf{S}_2$, the total angular momentum $\mathbf{J} = \mathbf{L} + \mathbf{S}$, and the projected effective spin [141, 431] $\xi \equiv M^{-2}[(1+q)\mathbf{S}_1 + (1+q^{-1})\mathbf{S}_2] \cdot \hat{\mathbf{L}}$. This specification has the advantage that only S evolves on $t_{\rm pre}$, while J evolves on $t_{\rm RR}$ and ξ is conserved throughout the PN

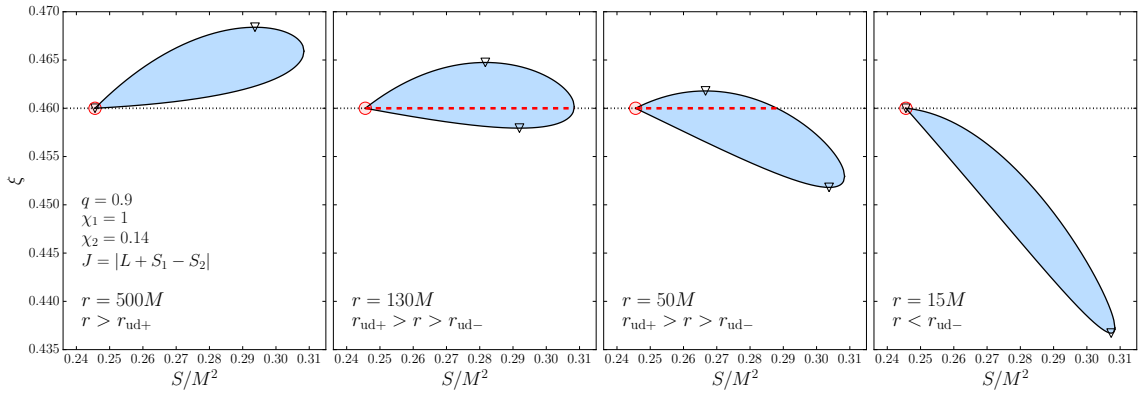

Figure 3.1: Effective-potential loops $\xi_\pm(S)$ for binary BHs with mass ratio $q = 0.9$, dimensionless spins $\chi_1 = 1$, $\chi_2 = 0.14$, and total angular momentum $J = |L + S_1 - S_2|$, corresponding to the up-down configuration. For binary separations $r > r_{\rm ud+} \simeq 337M$ (left panel), the up-down configuration at $S_{\rm min}$ marked by a red circle is also a minimum (marked by the lower triangle). At intermediate separations $r_{\rm ud+} > r > r_{\rm ud-} \simeq 17M$ (middle panels), misaligned binaries with the same value of the conserved ξ exist along the dashed red line. Perturbations δJ, $\delta\xi$ will cause S to oscillate between the points $S_\pm$ where this line intersects the loop, making the up-down configuration unstable. For $r < r_{\rm ud-}$ (right panel), the up-down configuration is again a stable extremum, now a maximum (marked by the upper triangle). An animated version of this figure is available online at [200].

stage of the inspiral ($r \gtrsim 10M$) by orbit-averaged 2PN spin precession and 2.5PN radiation reaction [270]. On the precession time, the spin magnitude S simply oscillates back and forth between the two roots $S_\pm$ of the equation $\xi = \xi_\pm(S)$, where $\xi_\pm(S)$ are the effective potentials for BH spin precession given by Eq. (2.24). Note that S is the only quantity on the right-hand side of Eq. (2.24) changing on $t_{\rm pre}$; in the absence of radiation reaction, the spins return to their initial relative orientation after a time $\tau(L, J, \xi)$ during which $\mathbf{L}$, $\mathbf{S}_1$, and $\mathbf{S}_2$ precess about $\mathbf{J}$ by an angle $\alpha(L, J, \xi)$. The two potentials $\xi_\pm(S)$ form a closed loop in the $S\xi$ plane, implying that the two roots $S_\pm$ coincide at the extrema $\xi_{\rm min,max}(L, J)$ of the loop. At these extrema, also known as spin-orbit resonances [463], S does not oscillate and $\mathbf{L}$, $\mathbf{S}_1$, and $\mathbf{S}_2$ all remain coplanar on the precession time.

3.2 Stability of aligned configurations

In this Section we present the stability analysis of BH binaries with aligned spins. The evolution of aligned binaries on the precessional timescale is described in Sec. 3.2.1. In Sec. 3.2.2 we describe the dynamics of such configurations under the effect of radiation reaction. Technical details are postponed to Appendix 3.A.

3.2.1 Precessional (in)stability

We begin with the up-up and down-down configurations, for which $J = |L \pm (S_1 + S_2)|$, respectively. According to Eq. (2.24), the effective-potential loop reduces to a single point in this limit which is necessarily an extremum: S cannot oscillate consistent with conservation of J and ξ. Now consider the down-up (up-down) configurations for which $J = |L - S_1 + S_2|$ ($J = |L + S_1 - S_2|$). The effective-potential loop $\xi_\pm(S)$ encloses a nonzero area for these values of J, implying that oscillations in S are possible, except at the extrema $\xi_{\rm min,max}$. Since the spins are antialigned with each other in both configurations, S is minimized at $S_{\rm min} = |S_1 - S_2|$ and both configurations sit on the leftmost point of the loop, where $\xi_+(S)$ and $\xi_-(S)$ coincide. Whether this point is also an extremum $\xi_{\rm min,max}$ depends on the slopes of these two functions at that point (cf. Sec. 3.A.1 below). Both slopes are always negative for the down-up configuration, implying that it is a maximum $\xi_{\rm max}$ and thus a spin-orbit resonance like the up-up and down-down configurations. At large binary separations r, the slopes of $\xi_\pm(S)$ are both positive for the up-down configuration, making it a minimum $\xi_{\rm min}$. However, below $r_{\rm ud+}$ given by

$$r_{\rm ud\pm} = \frac{(\sqrt{\chi_1} \pm \sqrt{q\chi_2})^4}{(1-q)^2} M \ , \tag{3.1}$$

the slope of $\xi_-(S)$ becomes negative and up-down is no longer an extremum of the effective-potential loop, as seen in Fig. 3.1. At separations below $r_{\rm ud-}$, the slope of $\xi_+(S)$ also becomes negative and up-down is again an extremum, this time a maximum $\xi_{\rm max}$. Misaligned BHs with the *same* values of J and ξ as the up-down configuration but $S > S_{\rm min}$ exist in the intermediate range $r_{\rm ud-} < r < r_{\rm ud+}$, as shown by the dashed red line. At $r = r_{\rm ud\pm}$, misaligned BHs have an infinite precessional period τ (cf. Sec. 3.A.2): they exponentially approach the up-down configuration on the precession time $t_{\rm pre}$ but never reach it.

The evolving relationship between the up-down configuration and the spin-orbit resonances parameterized by the angles θ_i is seen in Fig. 3.2. The solid curves show the $\Delta\Phi = 0$ resonances $[\xi_{\rm min}(J)]$ for separations $10M \leq r \leq 3000M$, while the dashed curves show the $\Delta\Phi = \pi$ resonances $[\xi_{\rm max}(J)]$. The up-down configuration is located in the bottom right corner of this figure. For $r > r_{\rm ud+}$, the up-down configuration lies on the solid curves and belongs to the $\Delta\Phi = 0$ family, but for smaller separations these curves detach from the bottom right corner, and thus up-down is no longer a minimum of $\xi_\pm(S)$. The dashed curves indicating the $\Delta\Phi = \pi$ family migrate to the right with decreasing separation and reach the bottom right corner, making the up-down configuration a maximum of $\xi_\pm(S)$, for $r < r_{\rm ud-}$. The up-up and down-down configurations (top right and bottom left corners)

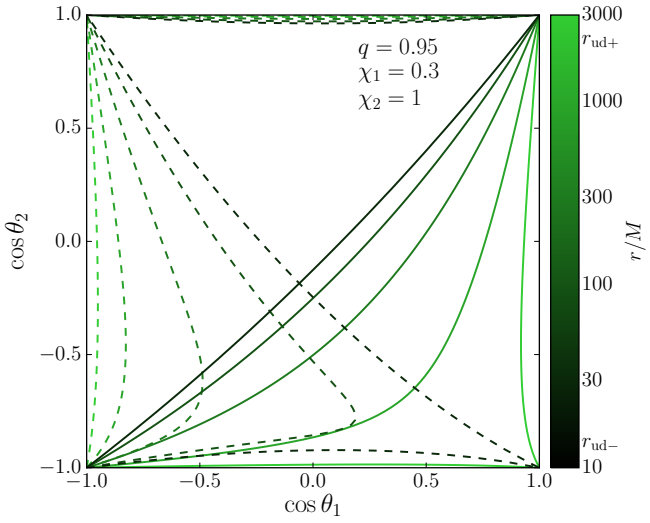

Figure 3.2: The angles $\cos\theta_i = \hat{\mathbf{S}}_\mathbf{i} \cdot \hat{\mathbf{L}}$ for spin-orbit resonances [extrema of $\xi_\pm(S)$] for BHs with $q = 0.95$, $\chi_1 = 0.3$, and $\chi_2 = 1$. The solid (dashed) curves indicate the $\Delta\Phi = 0$ (π) family and the five curves for each family correspond to binary separations $r/M = 3000, 720, 170, 40,$ and 10. The up-down configuration (bottom right corner) belongs to the $\Delta\Phi = 0$ family for $r > r_{\rm ud+} \simeq 2149M$, to the $\Delta\Phi = \pi$ family for $r < r_{\rm ud-} \simeq 13M$, and is unstable for intermediate values $r_{\rm ud-} < r < r_{\rm ud+}$. An animated version of this figure is available online at [200].

belong to both resonant families, reflecting the degeneracy of the effective-potential loop as a single point that is both minimum and maximum. The down-up configuration (top left) always belongs to the $\Delta\Phi = \pi$ family and is thus a maximum $\xi_{\rm max}$.

The stability of a system is determined by its response to perturbations, in this case to the spin angles $(\delta\theta_1, \delta\theta_2, \delta\Delta\Phi)$ or equivalently to the angular momenta $(\delta S, \delta J, \delta\xi)$. After such a perturbation, configurations that are extrema of $\xi_\pm(S)$ (all aligned configurations except up-down for $r_{\rm ud-} < r < r_{\rm ud+}$) will undergo oscillations in S (and thus the three spin angles) that are linear in the perturbation amplitude, and have a period τ that is independent of this amplitude. This is a stable response equivalent to that of a simple harmonic oscillator. The response of the up-down configuration for $r_{\rm ud-} < r < r_{\rm ud+}$ is very different, as seen in the middle panels of Fig. 3.1: S oscillates between the turning points $S_\pm$ independent of the perturbation amplitude, but the period τ of these oscillations – as proved in Sec. 3.A.2– diverges logarithmically as this amplitude approaches zero. This is an unstable response: the time it takes for a zero-energy particle with $dx/dt < 0$ to travel from finite x_0 to δx in the unstable potential $V = -\frac{1}{2}kx^2$ similarly diverges logarithmically with δx.

A perturbative analysis of nearly aligned configurations [283] can identify that perturbations can oscillate at complex frequencies (indicating an instability) in the same region $r_{\rm ud-} < r < r_{\rm ud+}$ found here, but such analysis cannot predict the amplitude of these perturbations or their response to precession-averaged radiation reaction.

3.2.2 Inspiral dynamics

We have shown that for $r_{\rm ud-} < r < r_{\rm ud+}$, spin configurations with J and ξ infinitesimally close to the up-down configuration can experience finite-amplitude oscillations in S and

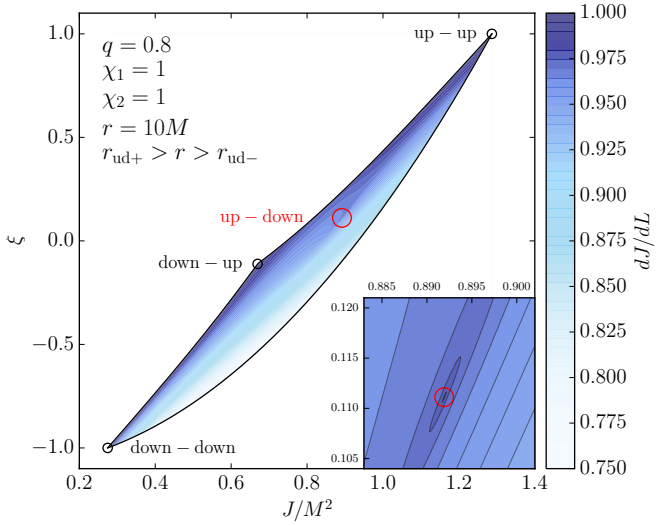

Figure 3.3: Precession-averaged radiation reaction dJ/dL as a function of J and ξ for binaries with $q = 0.8$, $\chi_1 = \chi_2 = 1$, and separation $r = 10M$ in the unstable region $r_{\rm ud-} < r < r_{\rm ud+}$. Spin-orbit resonances including the up-up, down-down, and down-up configurations are extrema of $\xi_\pm(S)$ and constitute the boundary of the allowed region. All four aligned configurations are maxima where $dJ/dL = 1$, but the unstable up-down configuration (shown in the inset) is a cusp. An animated version of this figure is available online at [200].

the angles θ_1, θ_2, and $\Delta\Phi$. We now investigate how these configurations evolve on the longer radiation-reaction time $t_{\rm RR}$. Since ξ is conserved throughout the inspiral and L monotonically decreases at 2.5PN order, the only challenge is to evolve J. In Sec. 2.3.1 we derived a precession-averaged expression for dJ/dL, a contour plot of which is shown in Fig. 3.3. The shaded region shows the allowed values of J and ξ for this mass ratio, spin magnitudes, and binary separation. The spin-orbit resonances, being extrema of $\xi_\pm(S)$, constitute the boundaries of this region. The up-up, down-down, and down-up configurations, being spin-orbit resonances, lie on these boundaries. At $r_{\rm ud+}$, the up-down configuration detaches from the right boundary of this region [it stops being a minimum of $\xi_\pm(S)$] and begins to migrate leftwards through the allowed region, eventually reattaching to the left boundary at $r_{\rm ud-}$ [where it becomes a maximum of $\xi_\pm(S)$]. This is just an alternative visualization of the four panels of Fig. 3.1.

For all four aligned configurations, $\mathbf{J}$ and $\mathbf{L}$ are aligned so $dJ/dL = 1$ is maximized. However, the nature of these maxima is very different for the stable and unstable configurations. For the stable configurations, the partial derivatives of dJ/dL with respect to J and ξ remain finite, implying that neighboring points separated by $(\delta J, \delta\xi)$ slowly drift away at a rate that scales linearly with these infinitesimal quantities. The unstable configuration however is a cusp where these partial derivatives approach $\pm\infty$, depending on whether this point in the $J\xi$ plane is approached from below or above. Neighboring points (experiencing large-amplitude oscillations in S, as seen in the middle panels of Fig. 3.1) rapidly deviate from the up-down configuration as it sweeps across the allowed region. This is an essential point: even if the stability of the up-down configuration is restored in the PN regime ($r_{\rm ud-} > 10M$), radiation reaction during the inspiral between $r_{\rm ud\pm}$ will drive BHs initially in this configuration to large misalignments prior to merger. The migration of the up-down

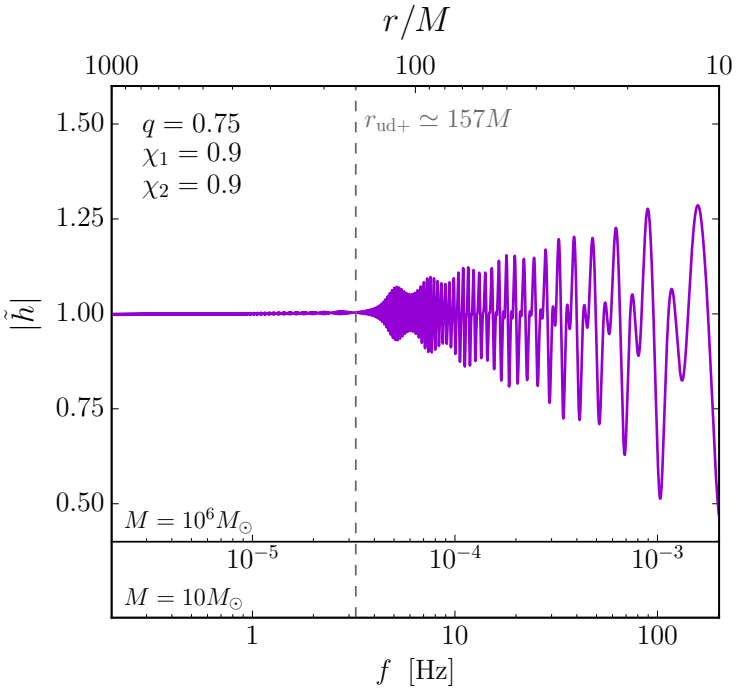

Figure 3.4: GW Fourier amplitude $\tilde{h}$ (normalized to a non-precessing system, cf. [283]) as a function of orbital frequency f and binary separation r during the inspiral of BHs with $q = 0.75$ and $\chi_1 = \chi_2 = 0.9$. At the initial separation $r = 1000M$, the spins are nearly in the up-down configuration, but this configuration becomes unstable below $r_{ud+} \simeq 157M$, after which large precession-induced modulations occur at frequencies accessible to GW detectors.

configuration through the $J\xi$ plane also reconciles the instability with the empirical result that isotropic spin distributions remain isotropic during the inspiral [463, 92]: although nearby binaries may indeed be left behind, the unstable configuration will always encounter a fresh supply, until it is restored to stability at the left edge of the allowed region.

3.3 Binaries may start precessing while being observed

Binaries with separations in the unstable region between $r_{\rm ud\pm}$ emit GWs with frequencies in the range $f_{\rm ud\pm} \simeq 6.4 \times 10^4 {\rm Hz}(M/M_\odot)^{-1}(1-q)^3/(\sqrt{\chi_1} \pm \sqrt{q\chi_2})^6$, within or below the sensitivity band of existing and planned GW detectors. In Fig. 3.4, we show the waveform of one such binary initially near the up-down configuration before entering the unstable region. Once the binary crosses the threshold at $r_{\rm ud+}$, its waveform develops large-amplitude precessional modulation on the precession time $t_{\rm pre}$. The amplitude of this modulation is independent of the initial deviation from the up-down configuration: it is set by the finite-amplitude oscillations in S seen in the middle panels of Fig. 3.1. Modulation occurs on two distinct time scales associated with the precession of $\mathbf{L}$ in a frame aligned with $\mathbf{J}$. In this frame the direction of $\mathbf{L}$ is specified by the polar angle $\cos\theta_L = \hat{\mathbf{L}} \cdot \hat{\mathbf{J}}$ and the azimuthal angle Φ_L in the plane perpendicular to $\mathbf{J}$. The longer of these time scales is τ (the period of oscillations in θ_L), while the shorter time scale is $(2\pi/\alpha)\tau$ (the precession-averaged time for Φ_L to change by 2π) [269, 206]. Measuring this modulation could yield insights into the astrophysical origins of binary BHs [204, 206].

Spin precession could also affect the electromagnetic counterparts to BH mergers [371, 323] and the probability of ejecting a supermassive BH from its host galaxy [215, 115, 112, 271]. We look forward to confronting these predictions with observations in the dawning age of GW astronomy.

Appendix

3.A Details on the stability analysis

In this Appendix we present the derivation of two crucial points entering our analysis of BH binaries with aligned spins: the properties of the derivatives $d\xi_{\pm}/dS$ (Sec. 3.A.1) and the integrability of $|dS/dt|^{-1}$ (Sec. 3.A.2).

3.A.1 Derivatives of the effective potentials

An aligned binary is described by $J = |L \pm S_1 \pm S_2|$ and in particular: $J = L + S_1 + S_2$ for up-up binaries; $J = |L - S_1 - S_2|$ for down-down binaries; $J = |L + S_1 - S_2|$ for up-down binaries; and $J = |L - S_1 + S_2|$ for down-up binaries. We study the initial value problem described by Eq. (2.62) with initial condition $J_0 = |L_0 \pm S_1 \pm S_2|$, corresponding to an aligned binary. Such an aligned configuration is stable if the magnitude J evolves according to $J(L) = |L \pm S_1 \pm S_2|$. This implies via $dJ/dL = 1$ [c.f. Eq. (2.62)] that $\langle S^2 \rangle_{\rm pre} = (S_1 + S_2)^2$ for up-up and down-down binaries, and $\langle S^2 \rangle_{\rm pre} = (S_1 - S_2)^2$ for up-down and down-up binaries.

3.A.1.1 Up-up and down-down

The up-up configuration is defined by $J = J_{\rm max} = L + S_1 + S_2$, which gives $S_{\rm min} = S_{\rm max} = S_1 + S_2$ and

$$\xi_+(S) = \xi_-(S) = \frac{(1+q)S_1 + (1+q^{-1})S_2}{M^2}\,. \tag{3.2}$$

Similarly, down-down binaries have $J = |L - S_1 - S_2|$, $S_{\rm min} = S_{\rm max} = S_1 + S_2$ and

$$\xi_+(S) = \xi_-(S) = -\frac{(1+q)S_1 + (1+q^{-1})S_2}{M^2}\,. \tag{3.3}$$

In both cases, only one value of S is allowed at any separation (because $S_{\rm min} = S_{\rm max}$). These configurations trivially satisfy $\langle S^2 \rangle_{\rm pre} = (S_1 + S_2)^2$ and are therefore stable.

3.A.1.2 Up-down

First, let us recall that one of the A_i's of Eq. (2.20-2.21) vanishes at either $S_{\rm min}$ or $S_{\rm max}$. Generic precessing configurations therefore satisfy

$$\lim_{S\to S_{\rm min}} \frac{d\xi_\pm}{dS} = \pm\infty\,, \qquad \lim_{S\to S_{\rm max}} \frac{d\xi_\pm}{dS} = \mp\infty\,, \tag{3.4}$$

because the A_i's will show up in the denominator of these derivatives. Examples were given in Fig. 2.5, where the effective potential loops are infinitely steep at their left and right edges. However, for some of the aligned configurations, the numerator of $d\xi_\pm/dS$ also vanishes and the limits above may become finite. Ultimately, this point turns out to be the mathematical origin of the precessional instability presented in this Chapter.

Plugging $J = |L + S_1 - S_2|$ into Eq. (2.24) one gets

$$\begin{aligned}\xi_\pm(S) = \frac{1}{4LM^2qS^2}\Big\{&[(L+S_1-S_2)^2 - L^2 - S^2][(1+q)^2S^2 + (-1+q^2)(S_1-S_2)(S_1+S_2)] \\ &\pm (1-q^2)\sqrt{(2L-S+S_1-S_2)(S+S_1-S_2)(2L+S+S_1-S_2)(S-S1+S_2)} \\ &\times \sqrt{(S+S_1-S_2)(S-S_1+S_2)[(S_1+S_2)^2 - S^2]}\Big\}\,.\end{aligned} \tag{3.5}$$

The up-down configuration is realized at $S_{\rm min} = |J - L| = |S_1 - S_2|$, where both cases in the maximum of Eq.(2.13) are simultaneously satisfied. From Eq. (3.5) one obtains

$$\lim_{S\to S_{\rm min}} \frac{d\xi_\pm}{dS} = -\frac{1-q^2}{LM^2q}\left[\frac{(S_1-S_2)(qS_1-S_2)}{1-q} - L(S_1+S_2) \mp 2\sqrt{L}\sqrt{S_1S_2|L+S_1-S_2|}\right]. \tag{3.6}$$

It follows that both limits are positive at large separations:

$$\lim_{L\to\infty}\lim_{S\to S_{\rm min}} \frac{d\xi_\pm}{dS} = \frac{(1-q^2)\left(\sqrt{S_1} \pm \sqrt{S_2}\right)^2}{(M^2q)} > 0\,. \tag{3.7}$$

The upper effective potentials is steeper, but the slope of ξ_- is also positive at $S_{\rm min}$. One example is given in the first panel of Fig. 3.1. Aligned binaries lie at $S_{\rm min}$ and are non-precessing because they are forced to stay in the kink between the two effective potentials, i.e. $S_- = S_+ = S_{\rm min}$. This corresponds to $\langle S^2\rangle_{\rm pre} = (S_1 - S_2)^2$, hence stability. The onset of the instability can be found solving

$$\lim_{S\to S_{\rm min}} \frac{d\xi_-}{dS} = 0 \tag{3.8}$$

as a function of r. A straightforward (although tedious) calculation shows that only one solution exists and it is given by

$$r_{\rm ud+} = \frac{\left(\sqrt{\chi_1} + \sqrt{q\chi_2}\right)^4}{(1-q)^2} M\,. \tag{3.9}$$

As the binary crosses $r_{\rm ud+}$ (central panels of Fig.3.1), configurations with $S \neq |S_1 - S_2|$ become available. Similarly, the equation

$$\lim_{S\to S_{\rm min}} \frac{d\xi_+}{dS} = 0 \tag{3.10}$$

admits a single solution at

$$r_{\rm ud-} = \frac{\left(\sqrt{\chi_1} - \sqrt{q\chi_2}\right)^4}{(1-q)^2} M\,. \tag{3.11}$$

When the derivative of the upper effective potential vanishes at $S_{\rm min}$, a new kink forms at $S_{\rm min}$ (right panel of Fig. 3.1). Up-down binaries at separations smaller than this second threshold are stable because $\langle S^2\rangle_{\rm pre} = |S_1 - S_2|$.

3.A.1.3 Down-up

Down-up configurations are characterized by $J = |L - S_1 + S_2|$ and $S_{\rm min} = |J - L| = |S_1 - S_2|$. At large separations both effective potentials have negative derivative at $S_{\rm min}$:

$$\lim_{L\to\infty}\lim_{S\to S_{\rm min}} \frac{d\xi_\pm}{dS} = -\frac{(1-q^2)\left(\sqrt{S_1} \mp \sqrt{S_2}\right)^2}{(M^2 q)} < 0. \tag{3.12}$$

However, the equations

$$\lim_{S\to S_{\rm min}} \frac{d\xi_\pm}{dS} = 0 \tag{3.13}$$

cannot be solved for any positive r. At all separations, down-up binaries have $S_{\rm min} = S_- = S_+$ and $\langle S^2\rangle_{\rm pre} = (S_1 - S_2)^2$ for any value of q and χ_i.

3.A.2 Precessional period

In this Section we show that up-down binaries at the instability threshold $r = r_{\rm ud\pm}$ have infinite precessional period $\tau \to \infty$. From Eq. (2.49-2.50) one has

$$\tau = 2\int_{S_-}^{S_+} \frac{dS}{|dS/dt|} = \frac{q}{3(1-q^2)}\frac{L^5}{S_1 S_2 (\eta^2 M^3)^3}\left(1-\frac{\eta M^2 \xi}{L}\right)^{-1}\int_{S_-^2}^{S_+^2}\frac{dS^2}{\sin\theta_1 \sin\theta_2 \sin\Delta\Phi}\,. \tag{3.14}$$

The integrand is the inverse of a square root of a third degree polynomial in S^2. Its roots correspond to the solution of the equation $dS/dt = 0$ as given by Eqs. (2.26-2.30) (which, indeed, is a third degree polynomial in S^2). Two of these solutions are S_- and S_+ which mark the extrema of the evolution of the total-spin magnitude S. Let us denote the third solution with S_3, such that

$$\tau \propto \int_{S_-^2}^{S_+^2}\frac{dS^2}{\sqrt{(S^2-S_-^2)(S_+^2-S^2)|S^2-S_3^2|}}\,. \tag{3.15}$$

In Sec. 2.2.2 we proved the third root must be outside the physical regime, i.e. $S_3 \notin (S_{\rm min}, S_{\rm max})$. For a generic precessing binary $S_- \neq S_+ \neq S_3$ and the singularities at $S_\pm$ are integrable.

The spin-orbit resonances $\xi = \max_S(\xi_+)$ and $\xi = \min_S(\xi_-)$ are characterized by $S_- = S_+$ (cf. Sec. 2.2.2). In the limit $S_-, S_+ \to \tilde{S}$ one obtains[1]

$$\tau \propto \frac{1}{\sqrt{|\tilde{S}^2 - S_3^2|}}\int_{S_-^2}^{S_+^2}\frac{dS^2}{\sqrt{(S^2-S_-^2)(S_+^2-S^2)}} = \frac{\pi}{\sqrt{|\tilde{S}^2-S_3^2|}}\,. \tag{3.17}$$

The precessional period τ is finite for the spin-orbit resonances $\xi = \xi_{\rm min}$ and $\xi = \xi_{\rm max}$.

Let us now concentrate on up-down BH binaries. Stable up-down binaries at separations $r > r_{\rm ud+}$ and $r < r_{\rm ud-}$ have $S_- = S_+ = S_{\rm min}$. On the other hand, in the instability region $r_{\rm ud+} > r > r_{\rm ud-}$ binaries have $S_- = S_{\rm min}$ but $S_+ \neq S_{\rm min}$ (cf. Fig. 3.1). Although it is guaranteed that $S_3 \notin (S_{\rm min}, S_{\rm max})$, the equality $S_3 = S_{\rm min}$ may, in principle, be satisfied. There are two possibilities regarding the integration of Eq. (3.15) at S_-:

- the singularity is integrable if $S_3 \neq S_{\rm min} = S_-$;
- the integral diverges if $S_3 = S_{\rm min} = S_-$.

[1] We made use of the following definite integral

$$\int_a^b \frac{dx}{\sqrt{(x-a)(b-x)}} = \pi\,. \tag{3.16}$$

The singularity of $|dS/dt|^{-1}$ at S_- is *not* integrable if $S_{\rm min}$ is a multiple root of the equation $\xi_\pm(S) = \xi$. Let us recall that $x = \tilde{x}$ is a multiple root of a real function $f(x)$ if $f(x = \tilde{x}) = 0$ and $f'(x)|_{x=\tilde{x}} = 0$. Therefore, the configuration $S = S_{\rm min}$ is a multiple root if

$$\lim_{S\to S_{\rm min}} \frac{d\xi_\pm}{dS} = 0\,. \tag{3.18}$$

which are the same conditions (3.8) and (3.10) marking the onsets of the instability. To summarize, the precessional period τ of up-down configurations behaves as follows:

- At separations $r > r_{\rm ud+}$ and $r < r_{\rm ud-}$, one has $S_- = S_+$ and $\lim_{S\to S_{\rm min}} d\xi_\pm/dS \neq 0$. The equation $\xi = \xi_\pm(S)$ has a single root on ξ_- and a single root on ξ_+, which are equal to each other. This case is equivalent to the spin-orbit resonances studied above, for which τ is finite. Note, however, that genuine spin-orbit resonances have both roots $S_\pm$ on the same effective potential.

- At separations $r_{\rm ud+} < r < r_{\rm ud-}$ where up-down binaries are unstable, one has $S_- \neq S_+$ and $\lim_{S\to S_{\rm min}} d\xi_\pm/dS \neq 0$. It follows that $S_- = S_{\rm min}$ is a single integrable root.

- If $r = r_{\rm ud+}$, one has $S_- = S_+$ but $\lim_{S\to S_{\rm min}} d\xi_-/dS = 0$ and $\lim_{S\to S_{\rm min}} d\xi_+/dS \neq 0$. Similarly, if $r = r_{\rm ud-}$, one has $S_- = S_+$ but $\lim_{S\to S_{\rm min}} d\xi_+/dS = 0$ and $\lim_{S\to S_{\rm min}} d\xi_-/dS \neq 0$. In both cases, all three roots all coincides $S_- = S_+ = S_3 = S_{\rm min}$ and the integral of Eq. (3.15) diverges.

Chapter 4

Missing black holes in brightest cluster galaxies

Outlook

In this Chapter we investigate the consequences of superkicks on the population of SMBHs in the Universe residing in Brightest Cluster Galaxies (BCGs). There is strong observational evidence that BCGs grew prominently at late times (up to a factor 2-4 in mass from $z = 1$), mainly through mergers with satellite galaxies from the cluster, and they are known to host the most massive SMBHs ever observed. Those SMBHs are also expected to grow hierarchically, experiencing a series of mergers with other SMBHs brought in by merging satellites. Because of the net linear momentum taken away from the asymmetric GW emission, the remnant SMBH experiences a kick in the opposite direction. Kicks may be as large as $\sim$ 5000 km s^{-1} ("superkicks"), pushing the SMBHs out in the cluster outskirts for a time comparable to galaxy-evolution timescales. We predict, under a number of plausible assumptions, that superkicks can efficiently eject SMBHs from BCGs, bringing their occupation fraction down to a likely range $0.9 < f < 0.99$ in the local Universe. Future 30m-class telescopes like E-ELT (European Extremely Large Telescope) and TMT (Thirty Meter Telescope) will be capable of measuring SMBHs in hundreds of BCGs up to $z = 0.2$, testing the occurrence of superkicks in nature and the strong-gravity regime of SMBH mergers.

Executive summary

This Chapter is organized as follows. In Sec. 4.1 we motivate our study. Sec. 4.2 presents the ingredients of our models: (i) SMBH merger fitting formulas; (ii) galaxy density profiles; (iii) prescriptions for the SMBH return timescales and (iv) the merger events; and (v) finally our evolutionary procedure. We highlight our results in Sec. 4.3 and present our conclusions in Sec. 4.4

The material presented in this Chapter is based on [209].

4.1 Looking for superkicks

The centers of galaxy clusters host the most massive galaxies in the Universe, generally known as BCGs. Their luminosity can easily exceed $10^{12} L_{\odot}$ and, consequently, their estimated masses can be up to few$\times 10^{12} M_{\odot}$. They also host the biggest SMBHs known in the Universe, with masses in the range $10^{9} - 10^{10} M_{\odot}$ [356], tipping the observed SMBH-host relations at the high mass end [355].

In the context of the Λ Cold Dark Matter (ΛCDM) cosmological paradigm, large Dark Matter (DM) halos in the Universe build up hierarchically [541], driving the assembly of galactic structures. Galaxy formation kicks off at high redshifts, as gas starts to cool at the centers of DM halos. Following the halo hierarchy, small protogalaxies merge with each other forming larger ones. This process continues until the present time, resulting in the formation of massive galaxies we see today. Within this framework, also SMBHs grow hierarchically, experiencing a sequence of accretion events and merging with other SMBHs following galaxy mergers [60, 533].

One interesting astrophysical consequence of SMBH binary mergers is the gravitational recoil. Emission of asymmetric GWs in the late inspiral and final coalescence takes away net linear momentum from the binary system, and the remnant SMBH is consequently kicked in the opposite direction. With the advent of numerical relativity [426, 113, 45], it is now possible to simulate SMBH mergers in full GR and assess the magnitude of these kicks. Surprisingly, configurations have been found in which the final kick can reach magnitudes up to ~ 5000km/s [112, 216, 332][1] opening the possibility of SMBH ejection even from the deepest potential wells created by the most massive galaxies [362, 467]. Observationally, few candidate recoiling SMBHs have been recently identified as off-center AGNs [132, 131,

[1] Technically, [112, 216] found recoils up to ~ 4000km/s for systems with spins lying in the binary orbital plane, which they referred to as "superkicks". "Hangup kicks" up to ~ 5000km/s were found by [332] in a different configuration, in which the spins are inclined with respect to the orbital plane of the binary. For simplicity, we will generally refer to high-velocity recoils as "superkicks" throughout this Thesis.

294], and an excellent review of the spatial and kinematical observational signatures of these peculiar systems can be found in [287]. A direct consequence of high velocity kicks is that the SMBH occupation fraction may be altered [464, 532, 531], providing an indirect way to test the strong-gravity physics behind GW kicks. In this Chapter, we explore this possibility by investigating the consequences of gravitational recoils onto SMBH masses and the occupation fraction in BCGs.

Although kicks will naturally eject SMBHs more easily from lighter galaxies (as extensively investigated in [531]), there are at least three good reasons for considering this possibility in BCGs. Firstly, BCGs show the strongest mass evolution from $z \approx 1.5$ up to now. In general, both detailed numerical simulations of galaxy formation [151, 397, 300] and observations of BCGs at different z [515, 310, 309], show an average mass doubling from $z = 1$ to the present time. Though it is difficult to assess observationally what is the cause of this mass growth, it appears in simulations to be driven primarily by galaxy mergers [327, 303]. This is also consistent with close galaxy pair counts at $z < 1$ [65, 103, 152, 445, 549, 325], which imply a prominent merger activity for these systems. In contrast with all other types of galaxies, very massive ellipticals (and BCGs in particular) are expected to have undergone several mergers in the last 10 Gyr, some of which 'major' (i.e. with satellite to primary galaxy mass ratio $M_2/M_1 > 1/4$). It is therefore possible that they also experienced a few SMBH binary coalescences, with consequent gravitational recoils. Secondly, SMBHs of mass $> 10^9 M_\odot$ in the relatively low-density environment of BCG nuclei have the largest impact on the dynamics of the surrounding stars [356]. The influence radius of the SMBH can be up to few hundred parsecs, making them ideal targets for direct dynamical measurements of SMBH masses. With angular resolutions of ≈ 0.1arcsec, it is today possible to confidently measure SMBH masses in BCGs up to $z \approx 0.03$. A factor of ten improvement in the instrumentation, expected with the TMT and the E-ELT, will dramatically increase this range. As an example, Do et al. [159] estimated that 50 masses of SMBHs residing in BCGs up to $z = 0.05$ can be measured with a relatively cheap program of 14 observing nights on the TMT. Moreover, they show that the TMT potential will be much greater than that, making mass measurement possible in hundreds of BCGs up to $z \approx 0.2$. Conversely, in Milky Way-type galaxies with SMBH sphere of influence of the order of few parsecs, even with E-ELT precision dynamical measurements will be restricted to our local neighborhood ($D < 30$ Mpc, $z < 0.01$). Lastly, according to our galaxy formation knowledge, the SMBH occupation fraction f (i.e., the fraction of galaxies hosting a SMBH) is an increasing function of the galaxy mass. Although already at dwarf galaxy scales f might be around unity [66], observations of galaxies in

Virgo cluster shows a sudden drop in the X-ray activity at stellar masses around $10^{10} M_\odot$ [366]. Although this cannot be taken as evidence of lack of nuclear SMBHs, there is no observational confirmation of a large f for galaxies on those small scales.

Some tentative candidates of SMBH ejections from BCGs have already been identified: the BCG in the A2261 cluster shows an exceptionally large core of 3.2 kpc consistent with the absence of a scouring SMBH [420]; the small $1.2 \times 10^{11} M_\odot$ lenticular galaxy NCG 1277 in the Perseus cluster hosts an exceptionally heavy SMBH of $1.7 \times 10^{10} M_\odot$ [519] which may have been grown in the close BCG NCG 1275, ejected by a superkick and finally captured by NCG 1277 [487].

Summarizing, BCGs, being the most massive galaxies in the Universe, (i) are expected to have $f = 1$ (pending, of course, the occurrence of superkicks); (ii) have possibly experienced multiple mergers at low redshift; (iii) are the easiest targets for nuclear SMBH mass measurements. These facts make them ideal targets for observing the effects of extreme recoils: any observational confirmation of a missing nuclear SMBH would provide strong evidence for the occurrence of superkicks.

Throughout this Chapter, we use a ΛCDM cosmological model with $\Omega_M = 0.27$, $\Omega_\Lambda = 0.73$ and $H_0 = 100h\,\mathrm{km/s\,Mpc^{-1}} = 70\,\mathrm{km/s\,Mpc^{-1}}$ (cf. [242]). Following the convention mostly used in the astrophysics literature, we use physical units where the fundamental constants G and c are explicitly indicated.

4.2 BCG merger modeling

A thoughtful modeling of the recoil effect on the SMBH occupation fraction in BCGs requires to put together in a coherent framework four main ingredients:

1. the recoil magnitude as a function of the SMBH binary parameters (binary mass ratio, magnitude and orientation of the individual SMBH spins);

2. the gravitational potential in which the recoiled SMBH evolves;

3. the return timescale for SMBHs suffering kicks below the escape velocity of their hosts;

4. the number of mergers experienced by BCGs as a function of z and of the galaxy mass ratio.

We will describe each item separately in the following subsections, providing in Sec. 4.2.5 a description of the 'coherent framework' that brings them together.

4.2.1 BH final mass, spin and kick velocity

We start by modelling the properties of the remnant SMBH as a function of the properties of the progenitor merging holes. We use a standard notation in which m_1 and m_2 denote the individual masses of the merging SMBHs (with $m_1 > m_2$), $M = m_1 + m_2$ is the total mass, $q = m_2/m_1 \leq 1$ is the mass ratio and $\eta = m_1 m_2/M^2$ is the symmetric mass ratio. The SMBH spin vectors are (with $i = 1, 2$)

$$\mathbf{S_i} = \chi_i \frac{G m_i^2}{c} \hat{\mathbf{S}}_\mathbf{i}, \tag{4.1}$$

where $0 \leq \chi_i \leq 1$ is the dimensionless-spin parameter and hats denote unit vectors. We describe the directions of the spins $\hat{\mathbf{S}}_\mathbf{i}$ with three angles θ_1, θ_2 and $\Delta\Phi$ as defined in Eqs. (2.2-2.4) and Fig. 2.1. It is also useful to define the following quantities

$$\boldsymbol{\Delta} = \frac{q\chi_2 \hat{\mathbf{S}}_\mathbf{2} - \chi_1 \hat{\mathbf{S}}_\mathbf{1}}{1+q}, \tag{4.2}$$

$$\tilde{\boldsymbol{\chi}} = \frac{q^2 \chi_2 \hat{\mathbf{S}}_\mathbf{2} + \chi_1 \hat{\mathbf{S}}_\mathbf{1}}{(1+q)^2}, \tag{4.3}$$

and to introduce the subscripts $\parallel$ and $\perp$ for vector components along/perpendicular to the orbital angular momentum of the binary $\mathbf{L}$: $\tilde{\chi}_\parallel = \tilde{\boldsymbol{\chi}} \cdot \hat{\mathbf{L}}$, $\tilde{\chi}_\perp = |\tilde{\boldsymbol{\chi}} \times \hat{\mathbf{L}}|$, $\Delta_\parallel = \boldsymbol{\Delta} \cdot \hat{\mathbf{L}}$, $\Delta_\perp = |\boldsymbol{\Delta} \times \hat{\mathbf{L}}|$. The following fitting formulae are implemented in the numerical code PRECESSION described in Sec. 2.A.

The energy radiated during the inspiral and merger phase $E_{\rm rad}$ reduces the post-merger mass to $M_f = M - E_{\rm rad} c^{-2}$. The dependence of $E_{\rm rad}$ on the initial parameters (namely the masses and the spins) can be derived analytically in the test-particle limit $q \to 0$ [268], while the comparable-mass regime $q \simeq 1$ can only be estimated using full numerical relativity simulations [72, 509, 328]. Here we use the expression recently provided in [51], where the two regimes are interpolated

$$\frac{E_{\rm rad}}{M} = 1 - \frac{M_f}{M} = \eta \left[1 - E'_{\rm ISCO}\right] + 4\eta^2 \left[4p_0 + 16 p_1 \tilde{\chi}_\parallel \left(\tilde{\chi}_\parallel + 1\right) + E'_{\rm ISCO} - 1\right], \tag{4.4}$$

where $c^2 E'_{\rm ISCO}$ is the energy per unit mass at the Innermost Stable Circular Orbit (ISCO) in

the test-particle limit generalized to inclined orbits and evaluated at the effective spin $\tilde{\boldsymbol{\chi}}$ [54]

$$E'_{\rm ISCO} = \sqrt{1 - \frac{2}{3r'_{\rm ISCO}}}\,, \tag{4.5}$$

$$r'_{\rm ISCO} = 3 + Z_2 - {\rm sign}(\tilde{\chi}_\parallel)\sqrt{(3-Z_1)(3+Z_1+2Z_2)}\,, \tag{4.6}$$

$$Z_1 = 1 + \left(1-\tilde{\chi}_\parallel^2\right)^{1/3}\left[\left(1+\tilde{\chi}_\parallel\right)^{1/3} + \left(1-\tilde{\chi}_\parallel\right)^{1/3}\right]\,, \tag{4.7}$$

$$Z_2 = \sqrt{3\tilde{\chi}_\parallel^2 + Z_1^2}. \tag{4.8}$$

The parameters p_0 and p_1 in Eq. (4.4) were fitted in [51] using the numerical relativity data published at the time (see references therein): they report $p_0 = 0.04827$ and $p_1 = 0.01707$.

The final spin magnitude χ_f has been predicted either by calibrating fitting formulas with numerical relativity simulations [509, 441, 53, 328], or by extrapolating test-particle results [107, 268]. Here we use the expression developed in [53], which has been shown to reproduce the available numerical relativity data with 8% precision in χ_f for every value of q:

$$\chi_f = \left|\tilde{\boldsymbol{\chi}} + \frac{q}{(1+q)^2}\ell\,\hat{\mathbf{L}}\right|\,, \tag{4.9}$$

$$\ell = 2\sqrt{3} + t_2\eta + t_3\eta^2 + s_4\frac{(1+q)^4}{(1+q^2)^2}\tilde{\chi}^2 + (s_5\eta + t_0 + 2)\frac{(1+q)^2}{1+q^2}\tilde{\chi}_\parallel\,. \tag{4.10}$$

The remaining free parameters are fitted to numerical relativity simulations (see [53] for details): $t_0 = -2.8904$, $t_2 = -3.51712$, $t_3 = 2.5763$, $s_4 = -0.1229$ and $s_5 = 0.4537$. We assume $\chi_f = 1$ whenever the fitting formula (4.9) predicts higher unphysical values.

GW recoils generally arise from asymmetries in the merging binary, that could be either in the masses or in the spins. Fitting formulas for the recoil velocity $\mathbf{v_k}$ are typically broken down into a mass asymmetry term v_m, and two spin asymmetry terms $v_{s\parallel}$ and $v_{s\perp}$ [112]

$$\mathbf{v_k} = v_m\hat{\mathbf{e}}_{\perp\mathbf{1}} + v_{s\perp}(\cos\xi\hat{\mathbf{e}}_{\perp\mathbf{1}} + \sin\xi\hat{\mathbf{e}}_{\perp\mathbf{2}}) + v_{s\parallel}\hat{\mathbf{L}}\,, \tag{4.11}$$

where $\hat{\mathbf{e}}_{\perp\mathbf{1}}, \hat{\mathbf{e}}_{\perp\mathbf{2}}$ are two orthogonal unit vectors in the orbital plane (such that the mass term of the kick lies along $\hat{\mathbf{e}}_{\perp\mathbf{1}}$) and ξ is the angle between the mass term and the orbital-plane spin term. Expressions for $v_m, v_{s\parallel}$ and $v_{s\perp}$ are available as fitting formulas to numerical

relativity simulations. In this work we implement the following expressions

$$v_m = A\eta^2 \frac{1-q}{1+q}(1+B\eta)\,, \tag{4.12}$$

$$v_{s\perp} = H\eta^2 \Delta_\parallel\,, \tag{4.13}$$

$$v_{s\parallel} = 16\eta^2[\Delta_\perp(V_{11}+2V_A\tilde{\chi}_\parallel+4V_B\tilde{\chi}_\parallel^2+8V_C\tilde{\chi}_\parallel^3)+\tilde{\chi}_\perp\Delta_\parallel(2C_2+4C_3\tilde{\chi}_\parallel)]\cos\Theta\,. \tag{4.14}$$

The term proportional to V_{11} in Eq. (4.14) arises from the superkick formula [215, 112], the terms in $V_{A,B,C}$ have been called "hangup-kick" effect [332], while the ones proportional to $C_{2,3}$ model the more recently discovered "cross-kick" effect [333]. The parameters in the equations above are currently estimated to be: $A = 1.2\times10^4$ km/s, $B = -0.93$ [216], $H = 6.9\times10^3$ km/s [330], $V_{11} = 3677.76$ km/s, $V_A = 2481.21$ km/s, $V_B = 1792.45$ km/s, $V_C = 1506.52$ km/s [335], $C_2 = 1140$ km/s, $C_3 = 2481$ km/s [333], $\xi = 145°$ [330]. The value of the angle Θ actually depends on the initial separation of the binary in the numerical simulations: as in previous studies [335, 76], we deal with this dependence by sampling over a uniform distribution in Θ.

Since the spin angles θ_1, θ_2 and $\Delta\Phi$ evolve during the inspiral (see Chapter 2), the recoil fitting formula provided above can only by applied close to merger, at separations $r \sim 10M$ where numerical relativity simulations typically start[2]. Kesden et al. [271] pointed out that substantial recoil suppression/enhancement could occur due to spin-orbit resonances [463] in the PN regime of the inspiral. In light of our findings presented in Chapter 2, this effect can actually be revisited in terms of morphological phase transitions towards the librating morphologies during the PN inspiral. Phase transitions mostly affect binaries with asymmetric spin directions at large separation ($\theta_1 \neq \theta_2$), while symmetric configurations ($\theta_1 \simeq \theta_2$) are generally unaffected (Sec. 2.4.2). Both effects are generally present for isotropic distributions of the spin angles, that are therefore maintained qualitatively isotropic by the PN evolution [92, 270] (see also Fig. 2.9, top panels). Resonant effects are therefore strongly dependent on early-time alignment processes, such those arising from accretion-disk interactions (Chapter 5 and [413, 167, 317, 367]).

In this astrophysical application to BCG galaxies, we assume isotropic distributions of both the spin vectors, taking the spin angles uniformly distributed in $\cos\theta_1, \cos\theta_2$ and $\Delta\Phi$. This is a delicate point because the misalignment distribution (also needed to properly initialize the late-time PN inspiral) has a strong impact on the recoil velocities. Although spin alignment is expected to occur when a SMBH binary is surrounded by a cold massive

[2]The effect of PN resonances is critical to compute the kick velocity, but not so critical in the case of the final mass – Eq. (4.4) – and the final spin – Eq. (4.9) –: see [53] for a discussion of this point.

circumbinary disk, the relative cold gas content of galaxies is a decreasing function of their mass [121] and BCGs are extremely gas-poor systems. Fresh cold gas can be naturally brought in by the merging satellite; however, most of the companions of massive elliptical galaxies in observed galaxy pairs are red (up to about 70%, [325]), making dry mergers the more common mass growth channel for BCGs. Nonetheless, a fraction of mergers can still result in significant accretion onto the central SMBH; in fact, BCGs are known to power luminous radio jets [80] creating X-ray cavities in a number of clusters [450, 243]. However, as a result of the 'anti-hierarchical' behavior of AGNs, only about one in a thousand of the SMBHs with $M > 3 \times 10^8 M_\odot$ is accreting at more than 1% of the Eddington rate at low redshift [236]. This is despite the fact very massive galaxies experience (as we will see below) a prominent merger activity at $z < 1$. Assuming one merger per BCG since $z = 1$, the numbers above imply that BCGs are, on average, accreting at about 1% of the Eddington rate for $\sim 10^7$ yr, resulting in a mass growth $< 1\%$. This is generally insufficient to align the spins of a putative SMBH binary even if the gas is accreted from a coherent circumbinary pool [167]. Moreover, accretion might occur in a series of subsequent episodes with incoherent angular momenta orientations [279, 474], and disk spin alignment might be less effective than generally assumed in simple α-disks models [317]. Therefore, disk-driven alignment processes should be less important for the systems relevant to this investigation[3], and random spin orientation is a sensible working hypothesis for the majority of them. In this case, the kick distribution is only weakly modified by the PN inspiral (cf. [76], their Fig. 2) and can therefore be neglected. We checked and confirmed this conclusion using orbit-averaged PN inspirals computed with the code presented in Sec. 2.A. For reasonably large samples (~ 1000 BCGs), uncertainties in the occupation fraction are still dominated by Poisson counting errors, rather than the PN influence on the kicks.

4.2.2 BCG mass-density and potential profile

BCGs sit at the center of their host cluster. The relevant potential is therefore given by the spheroidal component of the BCG plus the whole cluster DM halo.

A simple analytic model to describe the spheroidal component is given by the Hernquist mass-density profile ([238, 513], see [303] for a specific application to BCGs)

$$\rho_{\rm BCG}(r) = \frac{M_{\rm BCG}}{2\pi}\frac{r_H}{r}\frac{1}{(r+r_H)^3}, \tag{4.15}$$

where $M_{\rm BCG}$ is the mass of the spheroid and r_H is a scale radius. The scale radius r_H can be related to the typical cusp radius r_γ observed in the luminosity profiles of elliptical galaxies

[3] Disc-spin alignment processes in gas-rich galaxies is the main topic addressed in Chapter 5.

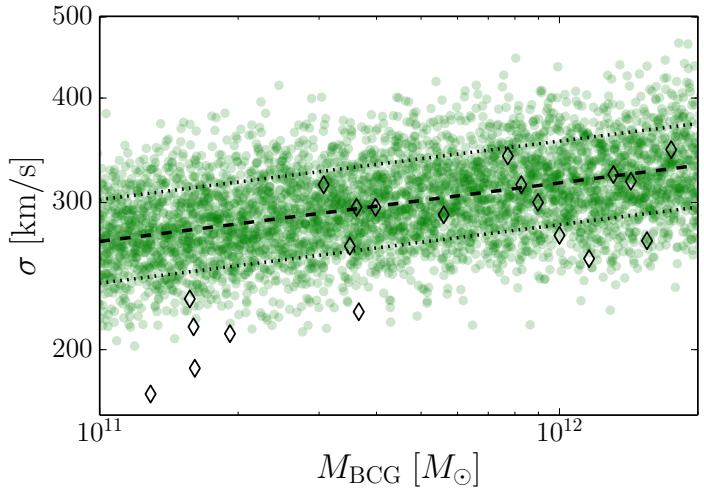

Figure 4.1: BCG kinematical properties, modeled using the Hernquist profile. The velocity dispersion values predicted from our model are compared with the sample of observations reported by [355] (black diamonds). Green circle points are computed sampling Eq. (4.16) with a Gaussian error of 0.1 dex and then considering $\sigma \approx 0.3\sqrt{GM_{\rm BCG}/r_H}$ [238]; black dashed and dotted lines show the average and the 1-σ interval of the same distribution.

[118, 306]. We match cusp-radius measurements from [306] and galaxy-mass measurements from [355], obtaining a final sample of 14 BCGs. We fit these values using a log-log relation, obtaining

$$\log\left(\frac{r_\gamma}{\rm pc}\right) = -7.73 + 0.857\log\left(\frac{M_{\rm BCG}}{M_\odot}\right), \tag{4.16}$$

with dispersion of 0.1 dex. The central densities of elliptical cores typically lie in the range $10^3 - 10^4 M_\odot/{\rm pc}^3$ [see, e.g., 503]; these values are reproduced by scaling the cusp radius by an order of magnitude, i.e. taking $r_H = 10 r_\gamma$. This choice gives acceptable results in terms of the kinematical properties of BCGs, especially at typical BCG masses $\sim 10^{12} M_\odot$: Fig. 4.1 shows the velocity dispersion of the BCG $\sigma \approx 0.3\sqrt{GM_{\rm BCG}/r_H}$ [238] compared[4] to the measurements in the sample of large elliptical galaxies collected by [355].

Self-consistent (and therefore more realistic) models have also been developed to describe photometric and kinematical data in elliptical galaxies (see e.g. [77]) but we opted for the Hernquist profile because it reproduces the kinematical properties quite well despite its analytical simplicity. We model the cluster DM halo with a Navarro-Frenk-White (NFW) profile [378, 379], which has been found to be in good agreement with galaxy cluster data [520]. The NFW mass-density profile is

$$\rho_{\rm DM}(r) = \frac{c^3 g_c \Delta_v(z)}{3}\rho_c(z)\frac{1}{(cr/r_v)\,(1+cr/r_v)^2}, \tag{4.17}$$

where r_v is the virial radius; $\Delta_v(z)$ is the virial overdensity (see below); c is a concentration

[4] Since the baryonic structure is much more concentrated than the DM halo (i.e. $r_H \ll r_v$), considering the stellar component only is sufficient in a comparison with stellar-velocity data. The definition of σ used by [355] involves measurements of velocity dispersion and radial velocity averaged up to some effective radius [their Eq. (1)]. We compare their estimates with values of σ evaluated close to r_H, where the Hernquist profile is expected to give the largest contribution to their averaged estimations.

parameter[5]; the function g_c is given by

$$g_c = \frac{1}{\ln(1+c) - c/(1+c)}; \tag{4.18}$$

and $\rho_c(z)$ is the critical density of the Universe at the redshift under consideration,

$$\rho_c(z) = \frac{3H^2(z)}{8\pi G}, \tag{4.19}$$

where

$$H(z) = H_0\sqrt{(1+z)^3\,\Omega_M + \Omega_\Lambda}. \tag{4.20}$$

The virial radius r_v is defined as the distance from the center of the halo within which the mean density is $\Delta_v(z)\rho_c(z)$. The halo mass $M_{\rm DM}$ is then simply defined to be the DM mass within r_v:

$$M_{\rm DM} = \frac{4}{3}\pi r_v^3 \Delta_v(z)\rho_c(z)\,. \tag{4.21}$$

Under the assumption that the cluster has just virialized[6], perturbative calculations [409] yield $\Delta_v \simeq 18\pi^2 \sim 178$, but the actual value depends on the cosmological model through [299, 102, 286]

$$\Delta_v(z) = 18\pi^2 - 82\Omega_\Lambda(z) - 39\Omega_\Lambda^2(z), \tag{4.22}$$

where

$$\Omega_M(z) = \frac{(1+z)^3\,\Omega_M}{(1+z)^3\,\Omega_M + \Omega_\Lambda}\,, \tag{4.23}$$

$$\Omega_\Lambda(z) = 1 - \Omega_M(z). \tag{4.24}$$

The virial radius as a function of the halo mass reads

$$r_v = \left(\frac{M_{\rm DM}}{10^{14}M_\odot}\right)^{1/3}\left(\frac{\Omega_M}{\Omega_M(z)}\frac{\Delta_v(z)}{18\pi^2}\right)^{-1/3}\frac{1\,{\rm Mpc}}{1+z}. \tag{4.25}$$

[5]We use the same symbol c to indicate the speed of light and the halo concentration parameter. The difference should be evident from the context.

[6]For simplicity, we do not truncate the NFW halo at the virial radius, which is expected under such virialization assumption (e.g. [408, 47]). Our predictions of the final occupation fractions are independent of this assumption: SMBHs kicked at $r_{\rm max} > r_v \sim$ few Mpc in general do not find their way back to the galactic center within a Hubble time.

In the regime considered here ($z < 1$), the virial overdensity Δ_v is roughly $0.7 \times 18\pi^2 \simeq 124$ with a rather weak dependence on z; typical sizes of DM halos with the same mass may differ by a factor ~ 1.5 if placed at different redshifts.

Stott et al. [497] relate the BCG visible mass to the halo mass measured at r_{500}, defined to be the radius at which the mean density is 500 times the critical density of the *present* Universe

$$M_{500} = \frac{4}{3}\pi r_{500}^3 \, \rho_c(z=0) \times 500. \tag{4.26}$$

Their observational relation reads [497]

$$\log\left(\frac{M_{500}}{10^{14} M_\odot}\right) = -14.29 + 1.28 \log\left(\frac{M_{\rm BCG}}{M_\odot}\right), \tag{4.27}$$

with dispersion $\sigma \approx 0.3$ dex. The concentration parameter c is related to the halo mass and in general depends on the redshift and the underlying cosmological model [381, 341, 337]. Those dependencies are however rather weak in the BCG range ($M_{200} \sim 10^{13-16} M_\odot$), in which theoretical predictions by different authors tend to agree (see Fig. 10 in [337]). Here we implement the relation reported by [381]

$$\log c = 5.26 - 0.1 \log\left(\frac{M_{200}}{10^{14} M_\odot} h^{-1}\right), \tag{4.28}$$

with a dispersion of 0.05 dex. In analogy with Eq. (4.27), M_{200} is defined to be the mass of the halo inside a radius r_{200} at which the mean density is 200 times the critical density

$$M_{200} = \frac{4}{3}\pi r_{200}^3 \, \rho_c(z=0) \times 200. \tag{4.29}$$

The value of M_{500} and M_{200} can also be obtained by integrating $\rho_{\rm DM}(r)$ from Eq. (4.17). This gives the following constraints on r_{200}, r_{500} and r_v:

$$\frac{500}{\Delta_v}\frac{H_0^2}{H^2(z)} = g_c \left(\frac{r_v}{r_{500}}\right)^3 \left[\ln\left(1 + \frac{c r_{500}}{r_v}\right) - \frac{c r_{500}/r_v}{1 + c r_{500}/r_v}\right]; \tag{4.30}$$

$$\frac{200}{\Delta_v}\frac{H_0^2}{H^2(z)} = g_c \left(\frac{r_v}{r_{200}}\right)^3 \left[\ln\left(1 + \frac{c r_{200}}{r_v}\right) - \frac{c r_{200}/r_v}{1 + c r_{200}/r_v}\right]. \tag{4.31}$$

We implement an iterative procedure to find r_v and c simultaneously; results are presented in Fig. 4.2. For each BCG stellar mass, $M_{\rm BCG}$, we compute M_{500} through Eq. (4.27) assuming a Gaussian error of 0.3 dex, and then r_{500} using Eq. (4.26). Given the initial guess $c = 5$, the constraint (4.30) is used to obtain numerically r_v. Eq. (4.31) is then solved

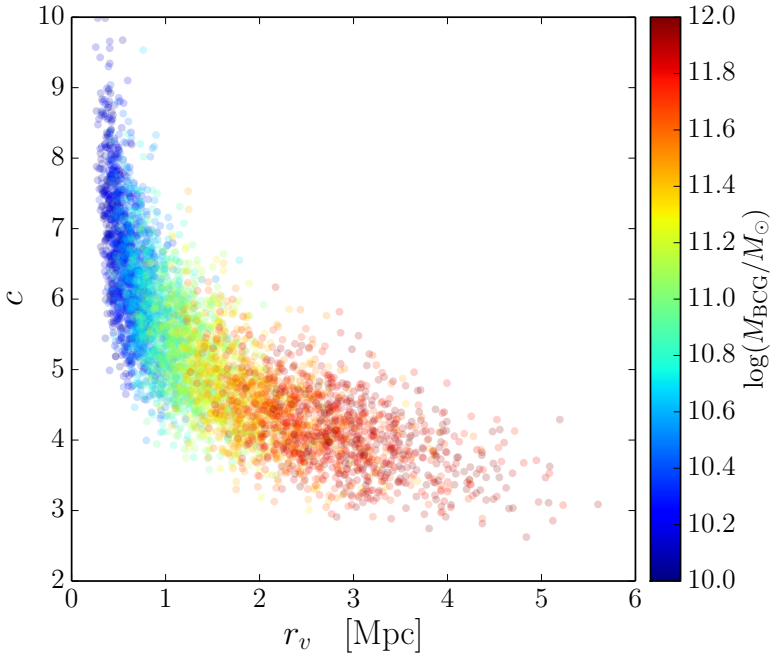

Figure 4.2: Observationally based relation between the halo virial radius r_v and the concentration parameter c. Fitting formulas provided by [497] and [381] are solved using the iterative procedure described in the main text. $M_{\rm BCG}$ is reported on the color scale. Massive galaxies (lighter points on the right) correspond to larger halos and to lower values of c; on the other hand, lighter BCGs (darker points on the left) are hosted in smaller halos and present a wider range of concentrations up to $c \simeq 10$. This figure is obtained with a uniform distribution in $\log M_{\rm BCG}/M_\odot \in [10, 12]$ at $z = 0$.

to find r_{200}, and M_{200} is obtained using Eq. (4.29). An updated value of c can now be computed through the observational relation (4.28). The whole procedure is then iterated. When convergence is reached[7], we add a Gaussian error of 0.05 dex to the final value of c. Once r_v and c are obtained, the halo mass, $M_{\rm DM}$, is given by Eq. (4.21). As a consistency test, the BCG/DM-halo relation is shown in Fig. 4.3, where our Monte Carlo sample is contrasted to observational data from [310].

To summarize: we model the BCG mass density from Eqs. (4.15) and (4.17) as $\rho = \rho_{\rm BCG} + \rho_{\rm DM}$, while the associated gravitational potential is given by $\Phi = \Phi_{\rm BCG} + \Phi_{\rm DM}$, with

$$\Phi_{\rm BCG}(r) = -\frac{GM_{\rm BCG}}{r + r_H}, \tag{4.32}$$

and

$$\Phi_{\rm DM}(r) = -g_c \frac{GM_{\rm DM}}{r_v} \frac{\ln(1 + cr/r_v)}{r/r_v}. \tag{4.33}$$

[7]Convergence down to $|\Delta c| < 10^{-6}$ is typically obtained after 5 iterations.

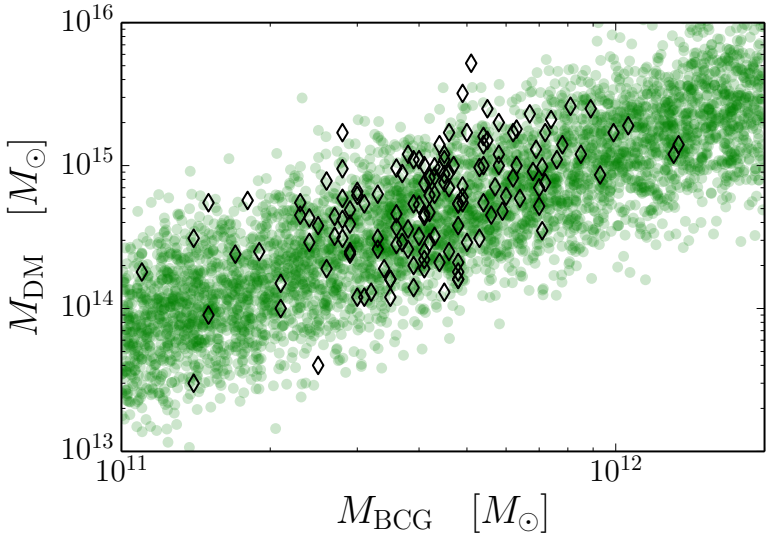

Figure 4.3: Relation between $M_{\rm BCG}$ and $M_{\rm DM}$ as implemented in our model. Our Monte Carlo realization (green circles) is statistically consistent with the observational catalog of 160 BCGs collected by [310] (black diamonds). This figure is obtained with uniform distributions in $\log M_{\rm BCG}/M_\odot \in [11, 12.3]$ and $z \in [0, 1.5]$, which are the same ranges covered by the data sample of [310].

4.2.3 Recoiled SMBH return timescales

Following the binary merger, the remnant SMBH recoils because of asymmetrical GW emission which may result in its ejection from the BCG core. The recoiling SMBH transfers its orbital energy into random motions of the surrounding stars through collisions, and may sink back to the galactic center. Here we develop two physical models to predict the return timescale of this process.

The remnant SMBH is initially kicked out on a radial trajectory. Detailed N-body simulations of the process have been performed by Gualandris and Merritt [219], who detect strong damping during each passage of the SMBH though the galactic core. It is therefore critical to know whether the recoiling SMBH orbit crosses the galactic core, since damping happens mainly in those quick passages. Repeated core passages cannot be prevented in a spherically symmetric potential. However, post-merger galactic potentials are expected to be triaxial [425, 272]: the SMBH orbit will not in general remain exactly radial and in particular the core may not be crossed [527]. Moreover, especially for extreme kicks, the SMBH can travel further than a Mpc from the BCG core. At this point, its trajectory is likely to be perturbed by the clumpy potential of other galaxies and DM subhalos within the main cluster halo, and return to the BCG core is unlikely. Missing the core would result in a much longer inspiral timescale because only low-density regions contribute to the frictional force. This difference is critical to our purposes, particularly if this timescale gets comparable with the timescale between two galactic mergers: less efficient sinking may result in "empty" galactic centers when the next satellite galaxy merges into the BCG. The full complexity of the problem cannot be solved within our spherically symmetric model; therefore, we developed two extreme approaches bracketing the uncertainties related to the

dynamics describe above.

1. In the first model, we assume that the SMBH orbit is "quasi-circular" and we compute the sinking timescale using Chandrasekhar's [123] Dynamical Friction. This is meant to be the extreme case for a strongly perturbed potential for which the SMBH never crosses the galactic core.

2. In the second scenario, we consider repeated SMBH-core bounces by fitting the N-body simulations reported by [219]. This model is appropriate for BCG and cluster potentials which exhibit small deviations from spherical symmetry.

4.2.3.1 Dynamical-friction model

Let us consider a SMBH with mass $M_{\rm BH}$ kicked with velocity v_k from the galactic center ($r = 0$). The SMBH will be ejected from the galactic halo if v_k exceeds the escape velocity of the system

$$v_{\rm esc} = \sqrt{2G\left(\frac{M_{\rm BCG}}{r_H} + c\, g_c \frac{M_{\rm DM}}{r_v}\right)}\,. \tag{4.34}$$

If $v_k < v_{\rm esc}$, the SMBH will stop at a distance $r_{\rm max}$ from the center. Gualandris and Merritt [219] showed that the maximum displacement $r_{\rm max}$ can be estimated simply through energy conservation neglecting star friction (see their Fig. 2)

$$\frac{1}{2}v_k^2 + \phi(0) = \phi(r_{\rm max})\,. \tag{4.35}$$

The initial displacement is reached in a time which is typically 100 times smaller than the sinking timescale [219] and will be therefore neglected. Here we estimate the time needed to sink back to $r = 0$ integrating the DF equation on quasi-circular orbits. The frictional force exerted onto the BH is given by (e.g. [84])

$$F(r) = \frac{4\pi G^2 M_{\rm BH}^2 \rho(r)\, \xi(r) \ln\Lambda}{v_c^2(r)}\,, \tag{4.36}$$

where $v_c(r) = \sqrt{r\, d\phi/dr}$ is the circular velocity, $\ln\Lambda$ is the Coulomb logarithm and the factor $\xi(r)$ depends on the stellar velocity distribution. We take $\ln\Lambda = 2.5$, as observed in [219] in the very first phase of their simulated orbits (see also [177]). We assume the velocity distribution to be locally Maxwellian, with velocity dispersion $\sigma(r)$. Although not exact, the Maxwellian distribution is approached as a consequence of collisionless relaxation

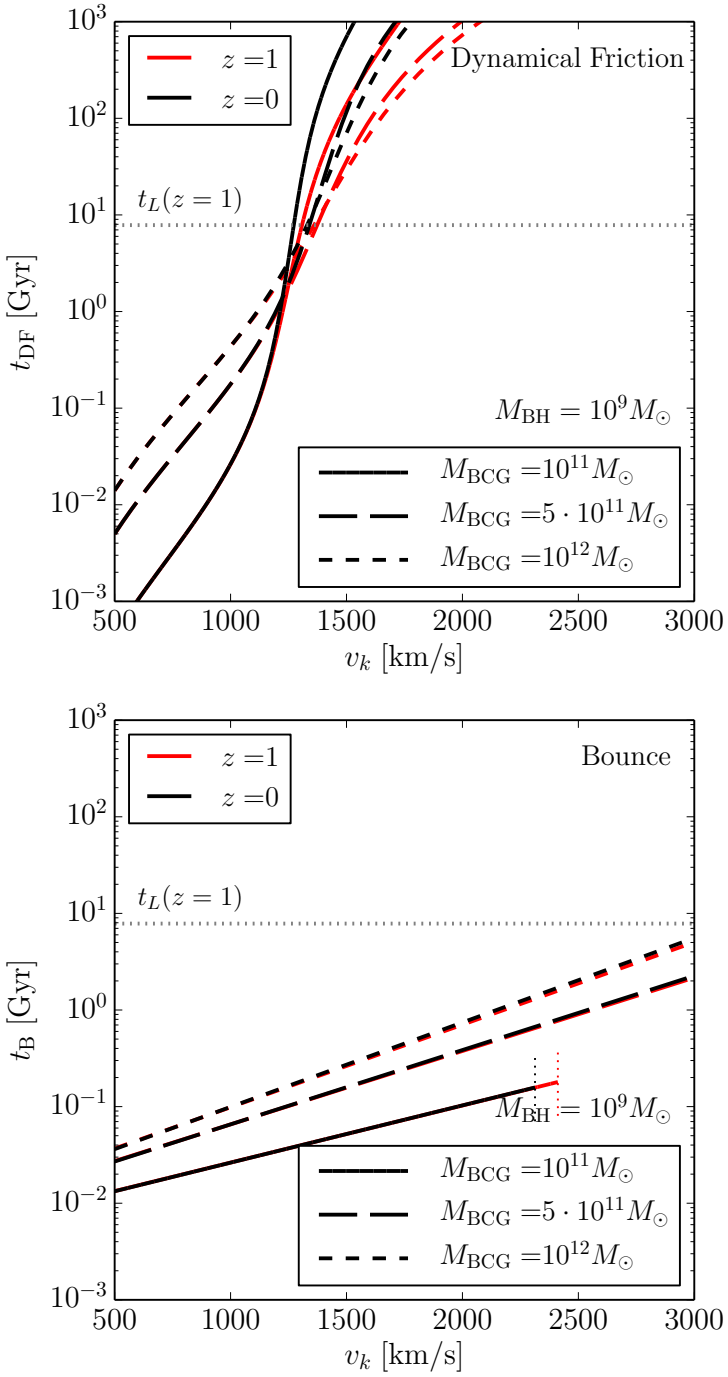

Figure 4.4: SMBH return timescales, in both the DF (top) and the bounce model (bottom), as a function of the kick velocity v_k. We consider recoiling SMBHs with $M_{\rm BH} = 10^9 M_\odot$ and BCGs with stellar mass $M_{\rm BCG} = 10^{11} M_\odot$ (solid), $5 \cdot 10^{11} M_\odot$ (long-dashed) and $10^{12} M_\odot$ (short-dashed). The remaining galaxy parameters (such as r_H, $M_{\rm DM}$, r_v and c) are estimated using the prescriptions presented in Sec. 4.2.2. To facilitate comparisons, here we set variances in Eqs. (4.16), (4.27) and (4.28) to zero. In order to bracket the effects of cosmological evolution we carry out the analysis at both $z = 0$ (darker, black lines) and $z = 1$ (lighter, red lines). BHs are effectively ejected from the BCGs when the sinking timescale (either $t_{\rm DF}$ or $t_{\rm B}$) gets larger than the lookback time at the merger redshift, which in turn is always smaller than the one computed at $z = 1$ (~ 7.8 Gyr, shown with a dotted horizontal line). Dotted vertical lines in the right panel are placed at the escape velocity $v_{\rm esc}$, at which Eq. (4.41) must be truncated.

processes [339]. Under this assumption, the ξ factor in Eq. (4.36) reads [84]

$$\xi(r) = \mathrm{erf}\left[\frac{v_c(r)}{\sqrt{2}\sigma(r)}\right] - \sqrt{\frac{2}{\pi}}\frac{v_c(r)}{\sigma(r)}\exp\left[-\frac{v_c^2(r)}{2\sigma^2(r)}\right] . \tag{4.37}$$

The velocity dispersion $\sigma(r)$ is computed from our galactic potential using the expression provided in [83] when isotropy is assumed. The frictional force $F(r)$ is tangential and directed opposite to the SMBH velocity. The SMBH angular momentum $L(r) = M_{\rm BH} r v_c(r)$ is lost at the rate $dL(r)/dt = -rF(r)$ by Newton's third law, causing the SMBH to slowly inspiral while remaining on a quasi-circular orbit. The DF timescale, over which the SMBH sinks back to the galactic center $r = 0$ from its initial position $r_{\rm max}$, is thus given by[8]

$$t_{\rm DF} = -\int_{r_{\rm max}}^{0} \frac{dL(r)}{dr}\frac{1}{rF(r)}dr\,. \tag{4.38}$$

DF timescales for typical systems are reported in Fig. 4.4 (top panel) as a function of the kick velocity v_k. A recoiling SMBH is strictly ejected only if $v_k > v_{\rm esc}$, which is unlikely since we are considering the whole cluster potential for which $v_{\rm esc}$ may be as large as ~ 6000 km/s for the typical values $M_{\rm BCG} = 10^{12} M_\odot$ and $M_{\rm BH} = 10^9 M_\odot$. However, SMBHs are effectively ejected if their return timescales are larger than the lookback time at the merger redshift z_m (e.g. [410])

$$t_L(z_m) = \int_0^{z_m} \frac{dz}{(1+z)H(z)}\,, \tag{4.39}$$

which corresponds to the time the Universe needs to evolve from z_m to now. In this case, the SMBH remains outside the BCG, wandering in the intracluster medium. Our systems are evolved from $z = 1$ to $z = 0$, which sets a (conservative) effective escape condition $t_{\rm DF} > t_L(z = 1)$ for which SMBHs will never come back to the BCG center. As shown in the top panel of Fig. 4.4, this condition is fulfilled for achievable kicks $v_k \sim 1500$ km/s, opening the possibility of several (effective) ejections from typical BCGs. When this occurs, the distance between the SMBH and the galaxy center (offset) can be estimated by numerically inverting Eq. (4.38). At $z = 0$, the SMBH needs the additional time $t_{\rm DF} - t_L(z_m)$ to sink to the center. The offset $r_{\rm z=0}$ is given by the displacement resulting

[8] Because of the intrinsic divergence in the density profile (4.15-4.17), this integral cannot be computed up to $r = 0$: hereafter, we implement a lower threshold at $10^{-3} r_H \sim 1$ pc. We also neglect the dependence on the redshift while computing the integral (4.38). In both models, the sinking times are computed fixing the redshift the initial value (i.e. when the kick is imparted to the SMBH). As shown in Fig. 4.4, differences between timescales computed at different redshifts are negligible in the interesting region $t_{\rm DF} < t_L(z = 1)$.

in a such time[9], i.e.

$$t_{\rm DF} - t_L(z_m) = -\int_{r_{z=0}}^{0} \frac{dL(r)}{dr}\frac{1}{rF(r)}dr\,. \tag{4.40}$$

4.2.3.2 Bounce model

To describe recoiling SMBHs on radial orbit, we rely on the N-body simulations performed by Gualandris and Merritt [219]. They study the motion of a SMBH recoiling from the center of an initially spherically symmetric galaxy. The SMBH motion can be divided into three distinct stages: (i) firstly, a short DF phase damps the radial oscillations as predicted by Chandrasekhar's [123] formula with $2 \lesssim \ln\Lambda \lesssim 3$; (ii) once the amplitude of the motion is smaller than the core radius, the SMBH and the galactic core exhibit oscillations about their common center of mass; (iii) finally, the SMBH and the core reach thermal equilibrium when the SMBH kinetic energy equals the mean kinetic energy of the stars in the core. Orbital energy dissipation occurs mostly during core-SMBH encounters. Here we are interested in estimating the timescale $t_{\rm B}$, given by the sum of the first and the second phase.

The duration of the first two phases is listed in [219] for 18 simulations in total, 6 in each of their 3 different models. As suggested by the authors themselves [their Eq. (18)], the second-phase times originally reported must be corrected, since the number of N-body particles used is smaller than the actual number of stars in a galaxy. They implement the galaxy profile firstly proposed by [503] to describe binary-depleted galactic cores which present a well defined profile transition at the core radius r_c. Oscillations damp only during passages through the galaxy core, whose properties are expected to strongly influence the damping time. For a given $M_{\rm BCG}$, we firstly compute the SMBH mass $M_{\rm BH}$, the velocity dispersion σ_c and the mass density ρ_c at r_c for each of their three models using the density profile of [503]. Even if DF cannot fully describe such core-passage dynamics, the return time appears to satisfy the same scaling relation as if DF would be fully responsible for the sinking process [219]. We therefore scale the simulated kick velocities with σ_c and the reported return timescales $t_{\rm B}$ with $\sigma_c^3/G^2\rho_c M_{\rm BH}$.

Once reduced to a dimensionless problem, we fit their 18 simulated timescales with the ansatz

$$t_{\rm B} = \frac{\sigma_c^3}{G^2\rho_c M_{\rm BH}}\,\exp\left(a\frac{v}{\sigma_c}+b\right)\,, \tag{4.41}$$

truncated at the escape velocity $v_{\rm esc}$. Here a and b are best fit coefficients. They only

[9] In both scenarios, offsets are computed with the galaxy properties at $z = 0$.

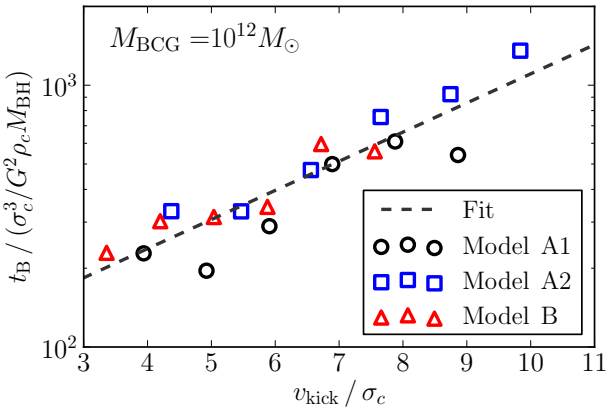

Figure 4.5: Fitting curve employed to compute the return timescale in the bounce model $t_{\rm B}$ as a function of the kick velocity $v_{\rm kick}$. Markers show predictions computed by [219] in each of their models, namely *A1*, *A2* and *B*. Once reduced to dimensionless quantities with the expected scaling, all three models appear to lie on the same lin-log relation, which however must be truncated at the escape velocity $v_{\rm esc}$. The dimensionless-scaled points and the fitting curve (dashed black line) depend only weakly on the galaxy mass $M_{\rm BCG}$. This figure is produced with $M = 10^{12}M_\odot$; the resulting fitting coefficients are $a = 0.26$ and $b = 4.44$.

depend (weakly) on the galactic mass $M_{\rm BCG}$ which enters in the correction factor to $t_{\rm B}$ due to the limited number of N-body particles. Fig. 4.5 shows the results of our fit for a fiducial mass $M_{\rm BCG} = 10^{12}M_\odot$. The dimensionless fit can be converted into physical units by computing σ_c and ρ_c for our galactic profiles (Hernquist+NFW) at a fiducial core radius

$$\log\left(\frac{r_c}{\rm pc}\right) \simeq 1.1 + 0.09\log\left(\frac{r_H}{\rm pc}\right), \tag{4.42}$$

as obtained by matching the mass dependencies in Eq. (4.16) with the analogous estimate for the core radius used in [219]. Results of our procedure are reported in the bottom panel of Fig. 4.4. This second model predicts longer return timescales for kicks smaller than $\sim$ 1000 km/s; while large kicks make SMBHs return very quickly ($\sim$ 100 Myr) to their galactic centers. If the SMBH does not escape from the cluster ($v < v_{\rm esc}$), there will always be a first core passage causing enough dissipation to trigger more and more passages leading to a quick comeback.

The SMBH offset at $z = 0$ can be computed by iterating the fit procedure described above. We numerically look for the hypothetical kick velocity $\tilde{v}_k$ which would result in a return time equal to $t_B - t_L(z_m)$, i.e. the time left to the SMBH at $z = 0$ to finally reach the galactic center. Assuming the SMBH motion to be approximately oscillatory, we compute the amplitude of the oscillations $\tilde{r}_{\rm z=0}$ from energy conservation [cf. Eq. (4.35)] and we finally estimate the offset to be $r_{z=0} = \tilde{r}_{\rm z=0}\sin\varphi$, with φ uniformly distributed in $[0, \pi]$.

4.2.4 BCG merger rates

In the last few years, strong observational evidence for a prominent growth of BCGs from $z = 1$ came about. Among other studies, [515] observes that early-type galaxies grew by a factor 5-10 in size and 2-4 in mass since $z = 1$, and [310] finds that BCGs grow in mass by a factor of ≈ 2 in the redshift range $0.9 - 0.2$ (see also [109, 40]). BCG mass growth is naturally explained by frequent mergers in the hierarchical build-up scenario, and several dedicated simulations and theoretical studies find that major and minor mergers can account for it [151, 397, 300, 303]. However, there are claims that size growth cannot be ascribed to mergers, and might be related to the redshift evolution of the properties of the underlying DM halos [493, 419]. In general, the merger-driven mass-growth scenario is consistent with observations of close galaxy pairs [315, 103, 152, 445, 549, 325], and both observations and simulations point toward high merger rates for early-type galaxies [245, 327], that can be up to 0.4/Gyr at $z \sim 1$ for BCGs [309].

Here we exploit the observationally based approach put forward by Sesana [472]. We are not interested in a global galaxy-merger rate, but rather in the distribution of mergers experienced by the typical BCG. Building on the same formalism as in [472], the galaxy merger rate per unit mass ratio[10] and redshift experienced by a galaxy of a given mass can be written as:

$$\left.\frac{d^2N}{dzdQ}\right|_M = \left.\frac{df}{dQ}\right|_{M,z} \frac{1}{\tau(z, M, Q)} \frac{dt_L}{dz}. \tag{4.43}$$

Here, $df/dQ|_{M,z}$ is the differential fraction of galaxies with mass M at redshift z paired with a secondary galaxy having a mass ratio in the range $[Q, Q + \delta Q]$; $\tau(z, M, Q)$ is the typical merger timescale for a galaxy pair with a given M and Q at a given z; and dt_L/dz is the integrand in Eq. (4.39). df/dQ can be directly measured from observations, whereas τ can be inferred by detailed numerical simulations of galaxy mergers. The number of mergers experienced from $z = 1$ to $z = 0$ by a galaxy starting with mass $M_{\rm BCG} = M_{\rm z=1}$ at $z = 1$ can be therefore written as

$$N(M_{\rm z=1}) = \int_1^0 dz \int_{Q_{\rm min}}^1 dQ \int dM \left.\frac{d^2N}{dzdQ}\right|_M \delta[M - M(z)], \tag{4.44}$$

where the integral is consistently evaluated at the redshift-evolving galaxy mass $M(z)$ through the Dirac delta function.

To estimate the mass growth of BCGs, we consider the fraction f of galaxies with a companion in the range $Q_{\rm min} = 0.25 < Q < 1$, which corresponds to the standard definition of major mergers. f is estimated in several observational studies, and it is generally fitted

[10] We indicate galaxy mass ratios with Q, to differentiate with black-holes mass ratios q.

with a function of redshift of the form

$$f = a(1+z)^b. \tag{4.45}$$

The parameters a and b are, in general, functions of the primary galaxy mass. Since we are concerned with BCGs, we consider fits to Eq. (4.45) corresponding to primaries with mass $M > 10^{11} M_\odot$. We construct three models, to which we will refer as "Optimistic", "Fiducial" and "Pessimistic". In the "Fiducial" model we take the best fit to the observations of [103], yielding $a = 0.035$, $b = 1.3$. Those data are consistent with a larger fraction described by $a = 0.07$, $b = 0.7$, which we take as "Optimistic" model. A smaller pair fraction with a stronger redshift dependence is found in [325], corresponding to $a = 0.02$, $b = 1.8$, which we take as "Pessimistic" model. Pairs are then distributed across the allowed mass ratio range according to $df/dQ|_{M,z} \propto Q^{-1}$ [324]. Ref. [325] additionally provides the pair fraction in the range $0.1 < Q < 0.25$, corresponding to minor mergers. This is found to be $f \approx 0.06$ independent of redshift. We add those to the "Pessimistic" model to construct the "Pessimistic-Minor" model, which we use to assess the impact of minor mergers on our findings (see below).

The function τ is then specified by [280]

$$\tau = 1.32\,\mathrm{Gyr}\left(\frac{M_*}{4\times 10^{10} h^{-1} M_\odot}\right)^{-0.3}\left(1+\frac{z}{8}\right), \tag{4.46}$$

where M_* is the total mass of the pair[11]. We shall stress here that Eq. (4.46) provides the *galaxy* merger timescale, which can be regarded as the timescale over which a bound SMBH binary forms. The actual coalescence of the binary might be further delayed because the system needs to get rid of its energy and angular momentum in order to get to the efficient GW emission stage. This is known as the "final parsec problem" [370]; we will return on this potential caveat in the next Section. The galaxy merger rate is finally obtained by inserting Eq. (4.45) –distributing the pairs according to Q^{-1}– and Eq. (4.46) into Eq. (4.43).

Fig. 4.6 compares the predicted mass growth and average number of mergers suffered by BCGs as a function of their mass at $z = 1$ to a number of observations and theoretical models. When corrected for the expected contribution of minor mergers[12], the "Fiducial" model predicts a mass growth in line with observations by [310]. The "Optimistic" one has a larger growth, consistent with theoretical modelling of [151] and [303], whereas the

[11] We fixed $r_p = 30$ kpc in Eq. (10) of [280], because this is the projected separation of the samples we use.

[12] This correction is only implemented to perform this sanity test. The "Fiducial" and "Optimistic" models do not include minor mergers.

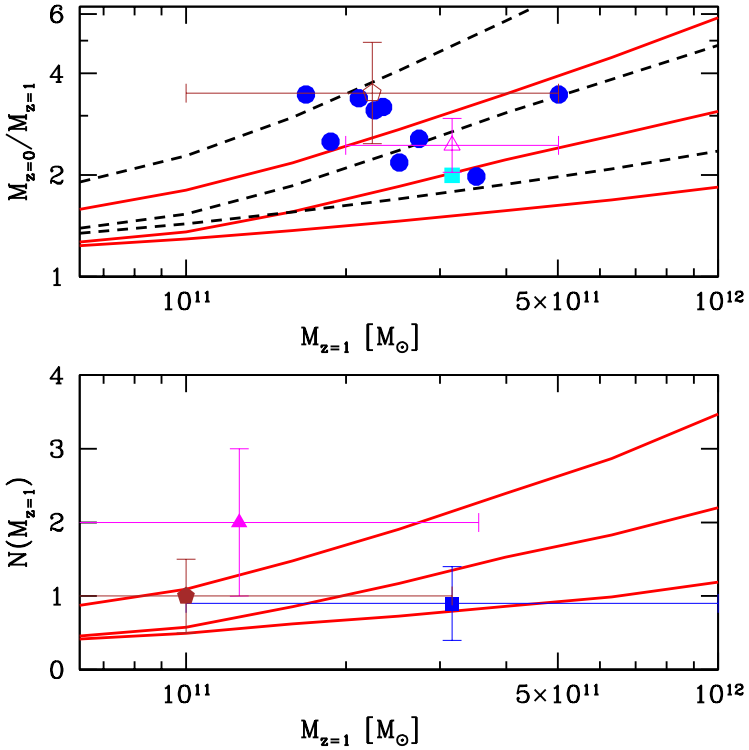

Figure 4.6: BCG mass growth (top panel) and average number of major mergers (bottom panel) as a function of the initial mass at $z = 1$. In both panels, red solid curves are predictions of our observation-based semianalytic models; from bottom to top: "Pessimistic", "Fiducial" and "Optimistic". In the top panel, the additional black–dashed lines are (in the same order) growth factors corrected for the contribution of minor mergers (the lower one corresponds to the "Pessimistic–minor" model, whereas the same fractional growth correction factor is applied to get the other two curves). The magenta triangle is the average mass growth predicted by [310], the brown pentagon is derived from [151], the blue circles are a selected sample of BCGs from [303], and the cyan square is a simulation from [397]. In the bottom panel, only the number of major mergers is considered, and we additionally plot the average number of mergers found by [65] (magenta triangle), [549] (brown pentagon) and [245] (blue square).

"Pessimistic" is marginally consistent with the data, and tends to slightly underpredict the BCG mass growth (still yielding to mass doubling since $z = 1$). We will consider all models in the following, and we stress that our main results do not qualitatively depend on the details of the growth history of BCGs, so long as most galaxies experience at least one merger at $z < 1$.

A small fraction of our galaxies can grow up to $10^{13} M_\odot$ (in the "Optimistic" scenario in particular), which might be at odds with the sharp cutoff in the galaxy mass function observed around $10^{12} M_\odot$ [64]. However, determinations of the mass function are typically obtained by converting luminosities to stellar masses. This results in large systematic uncertainties (especially at the high-mass end) due to the assumptions on the stellar mass-to-light ratio, as well as the different possible light profile fitting procedures [70], which can extend the high mass tail of the galaxy mass function by 0.5 dex [69]. Moreover, extreme

cases of BCGs with masses possibly in excess of $5 \times 10^{12} M_\odot$ have been reported, the most notable case being ESO 146-IG 005 [119].

4.2.5 Putting the pieces together

We select the initial BCG mass at $z = 1$ using the high-redshift sample collected in [310], consisting in 32 observed BCGs with redshift between 0.8 and 1.6. For each initial galaxy of mass $M_{\rm BCG} = M_{\rm z=1}$, we assign a number of mergers drawn from a Poissonian distribution with average $N(M_{\rm z=1})$; mass ratios and redshifts of galactic mergers are distributed according to $dN/dzdQ$ as reported in Eq. (4.43)[13]. Both BCG and each satellite galaxy, are then populated with SMBHs using the SMBH-bulge relation of [355]

$$\log\left(\frac{M_{BH}}{M_\odot}\right) = 8.46 + 1.05 \log\left(\frac{M_{BCG}}{10^{11} M_\odot}\right) , \tag{4.47}$$

with a dispersion of 0.34 dex. In particular, McConnell and Ma [355] detect steeper slopes in the galaxy scale laws when BCG data are included in the fitted sample (cf. also [292]). When a BCG merges with a satellite galaxy, we assume that the satellite mass is fully accreted by the BCG

$$M'_{\rm BCG} = (1 + Q) M_{\rm BCG}. \tag{4.48}$$

and we compute the stellar and DM profile from $M'_{\rm BCG}$ using the procedure described in Sec. 4.2.2. No SMBH remnant can be present in the post-merger BCG if both the parent BCG and satellite did not host any SMBH at their centers; a single SMBH is assumed to lie in the newly formed BCG if only one of the parents carried a SMBH; finally, if both the BCG and the satellites had a SMBH, we assume that the two SMBHs also merge at the same time (redshift) as the galaxies merge. At each SMBH merger, we compute the remnant mass, spin and recoil as presented in Sec. 4.2.1. From the kick velocity and the galactic potential of the newly formed BCG, we compute the return time t_R using either $t_{\rm DF}$ from Eq. (4.38) or t_B from Eq. (4.41) in each of our two models. In practice, the SMBH is removed from the simulation and placed back to the galactic center after a time t_R. If t_R is smaller than the time between two galactic mergers, the SMBH will simply settle back at the center of its BCG; if instead a subsequent galactic merger happens before, the BCG

[13] We bin mass and merger distributions and generate our Monte Carlo samples accordingly. Bin widths have been determined through numerical experiments: 10 bins have been used to map the BCG mass distribution from the [310] data; 5 bins have been considered to obtain the average merger numbers $N(M_{\rm z=1})$ (a Poissonian dispersion is then applied), while for $dN/dzdQ$ we used 4 bins in the mass ratio and 37 bins in the redshift (bin widths are smaller for $z < 0.3$, where redshifts get closer to the end of the simulations $z = 0$).

center may already contain a SMBH (coming from one of the satellites). A new binary merger is computed, possibly resulting in another ejection from the BCG.

4.2.6 Possible caveats

A few simplifying assumptions have been made in the implementation of this procedure, which we justify in the following.

Firstly, we assume that all SMBH binaries merge, thus circumventing the so-called *final-parsec problem* [370]. The bottleneck to SMBH binary evolution [60] is believed to occur on the parsec scale, where intersecting-orbit stars have all been ejected but GWs are still not efficient enough to finally drive the inspiral. In principle, the relatively low-density gas-poor galaxy cores of BCGs are the most exposed to SMBH binary stalling. It has been found that triaxial potentials might alleviate the problem by increasing the number of orbits that cross the binary's loss-cone, therefore providing a way to get rid of additional binary energy and angular momentum [363]. However, recent investigations [524] called this result into question by showing that triaxiality alone might not be enough. Nonetheless, in real mergers, other factors such as rotation, bar-like instabilities and an unrelaxed time evolving potential might significantly enhance the flux of stars into the loss cone [68], and recent ab-initio N-body simulations of merging stellar bulges succeeded in driving the SMBH binary to final coalescence [425, 272]. If some gas is present, this may provide additional help in hardening the binary (see, e.g., [35, 178, 162] for gas driven binaries), even though it has been also argued that gas might indeed be unable to absorb significant angular momentum from the binary if the gaseous-disk mass is limited by self-gravity and fragmentation [319]. Gas-driven inspiral of SMBH binaries is studied in detail in Chapter 5 of this Thesis.

Secondly, we only update SMBH masses and spins during merging events, thus neglecting any accretion mechanism. Giant ellipticals are gas-poor systems, generally unable to supply large amounts of material to feed the central SMBH. It is observationally well known that the accretion activity of the most massive BHs peaks at $z \approx 2$ (e.g. [246]), rapidly declining at lower redshifts. This trend has been reproduced by state of the art theoretical models, which find that the most massive SMBHs at low z grow primarily via mergers [344, 180], with little contribution from gas accretion. The change of the SMBH spin magnitude due to accretion can also be safely neglected: momentum-conservation arguments [504] imply that the spin magnitude is modified significantly only if the accreted mass is of the order of the SMBH mass itself. This assumption is coherent with taking isotropic spin directions neglecting further spin-alignment processes (see discussion in Sec. 4.2.1).

Thirdly, we neglect any delay between galactic and SMBH binary mergers, thus assuming that they take place simultaneously. In reality, binary formation and inspiral will postpone the SMBH merger even if the *final-parsec problem* is solved efficiently. In dense stellar environments, if there is a continuous supply of stars interacting with the binary (technically, a full loss cone) SMBHs generally inspiral for $> 3 \times 10^7$yr before merging with each other [471], and similar timescales apply to gaseous environments [165]. This delay will likely be longer for low density ellipticals [272]; however, BCGs generally experience at most 2-3 major mergers since $z = 1$, therefore delayed SMBH binary mergers could have a substantial impact on our results only if binaries typically survive for Gyrs (in which case, the distinction between delayed merger and stalling becomes blurry). We try here to critically assess the impact on delayed mergers on our results. We consider the longest merger timescales found in N-body simulations of merging galaxies performed in [425, 273]. When scaled to massive ellipticals, the results of [273] give coalescence times that can be as long as $\sim$ 1Gyr (see their Table 5), whereas [425] provide shorter timescales (see their Figure 4). We therefore count a posteriori the fraction of subsequent mergers separated by less than 1Gyr. This fractions turned out to be:

- $\sim$0.2 in the "Fiducial" scenario;
- $\sim$0.3 in the "Optimistic" scenario;
- $\sim$0.12 in the "Pessimistic" scenario;
- $\sim$0.25 in the "Pessimistic–Minor" scenario (here the number of mergers is larger).

We see that delayed mergers can produce triple interaction in 30% of the cases at most (considering only the major merger statistics). When a triplet forms, either (i) a strong triple interaction occurs, causing the ejection of the lightest of the three SMBHs (and possibly accelerating the coalescence of the binary left behind), or (ii) a hierarchical system forms, possibly exciting Kozai resonances in the inner binary, again driving it to rapid coalescence. The outcome of the two processes is generally different, and the occurrence of one or the other depends on how far has the SMBH binary already gone into the hardening process, on how shallow has the galaxy core became, etc. We notice, however, that in case (i) the number of coalescences decreases at most proportionally to the fraction of triplets that form, whereas in case (ii), the number of coalescences is basically unaffected, since each triplet formation leads to the coalescence of the binary that was already in place. Extensive numerical experiments performed by [244] showed that triple interactions generally lead to at least one binary coalescence (in 85% of the cases), usually on a timescale shorter than 1 Gyr (Fig. 8 in [244]). Therefore, triple interactions might cause a fractional change of our

ejection fractions of 0.3 at most. In any case, it might be interesting to track consistently triplets in our simulations, and this point may be the subject of future improvements of our model. This effort is currently being carried out in [96]. We also note that similar assumptions are often made in more elaborate galaxy-evolution models (see e.g. [47] for a critical discussion).

We are also neglecting the previous merger history of the BCGs. BCGs will generally reach $z = 1$ after multiple merger events. The inspiral of a SMBH binary preceding a merger is expected to leave an imprint on the host galaxy in the form of a core scouring in the BCG center (especially if little nuclear star formation occurs). At each merger, the mass ejected in stars is of the order of $\sim 0.5M$ (where M is the total mass of the binary) [360]. The effect may be important after many merger generations and it leads to strong modification of the galactic potential in the core region. This effect is absent in our simplified model, but we note that the core properties are only important when estimating the SMBH return time in the bounce model (Sec. 4.2.3). The fitting procedure developed here is built on the results obtained by [219], which in turn consider an elaborate galaxy model [503] where core depletion is taken into account.

4.3 Results and discussion

We combine different prescriptions for two main processes

- the return time: "Dynamical Friction" (DF) or "Bounce" (Sec. 4.2.3);
- the merger distribution: "Fiducial", "Optimistic" or "Pessimistic" (Sec. 4.2.4).

This results in a set of six models that we use as an investigation playground: "Fiducial-DF", "Fiducial-Bounce", "Optimistic-DF", "Optimistic-Bounce", "Pessimistic-DF", "Pessimistic-Bounce". In each model, the evolution of the SMBH population is characterized by the following input parameters:

- initial BCG occupation fraction $f_{\rm z=1}$;
- occupation fraction of the satellite galaxies f_s;
- initial SMBH spin magnitudes in the BCGs $\chi_{z=1}$;
- SMBH spin magnitudes in the satellites χ_s.

We discuss in the following the results of our simulations, separating the effect of each individual parameter. The main observables are:

- final BCG occupation fraction $f_{\rm z=0}$ (later splitted between those galaxies which underwent a SMBH replenishment $f^{\rm R}_{\rm z=0}$ and those which keep their original SMBH $f^{\rm NR}_{\rm z=0}$);
- fraction of BCG that do not host a nuclear SMBH at $z = 0$, simply defined by $1 - f_{\rm z=0}$;
- distance from the BCG center (offset) of the ejected SMBH at the present time $r_{\rm z=0}$.

For any given set of parameters we simulate 1000 BCGs (with the exception of the runs presented in Figs. 4.9 and 4.11 which contain 10000 BCGs): typical Poisson counting errors on the final occupation fractions are therefore $\sim 3\%$. Most of the results presented here are computed assuming $f_{\rm z=1} = 1$ as a simplifying assumption, cf. Sec. 4.1 (with the exception of Sec. 4.3.2.2 where such issue is explicitly investigated).

4.3.1 Host properties: cluster shape and BCG merger rate

The six models described above are defined by distinct 'environmental properties' which are not directly related to the SMBH population itself; namely the merger history of BCGs (determining the number of SMBH binary mergers) and the shape of the cluster potential (governing the typical return timescales of ejected SMBHs). We describe their impact on the results first (fixing $f_{z=1} = f_s = 1$), turning to the properties of the SMBH population in the next subsection.

4.3.1.1 Bounce and DF models

The detailed shape of the cluster potential affects the trajectory of the recoiling SMBH. If all gravitational potentials were spherically symmetric, then SMBHs would always get back to the core of BCGs, and the Bounce model would provide a complete description of the dynamics. However, cluster density profiles are often triaxial, unrelaxed, and 'clumpy'. In a triaxial potential orbits do not conserve angular momentum, implying that the SMBH will miss the BCG core at subsequent passages; additionally, gravitational perturbations due to sub-halos and other galaxies can easily deflect the SMBH out of its initially radial orbit. The DF model is taken as an extreme (and admittedly unrealistic) case in which the SMBH returns on a circular orbit. Both the DF and the Bounce models are idealizations meant to bracket the range of possible outcomes. As shown in Fig. 4.4 for three selected systems, return timescales can easily exceed the Hubble time in the DF model. This is better seen in Fig. 4.7 where the distributions of recoil velocities v_k and return times t_R are computed along the evolution of the BCG population for our four default models. For

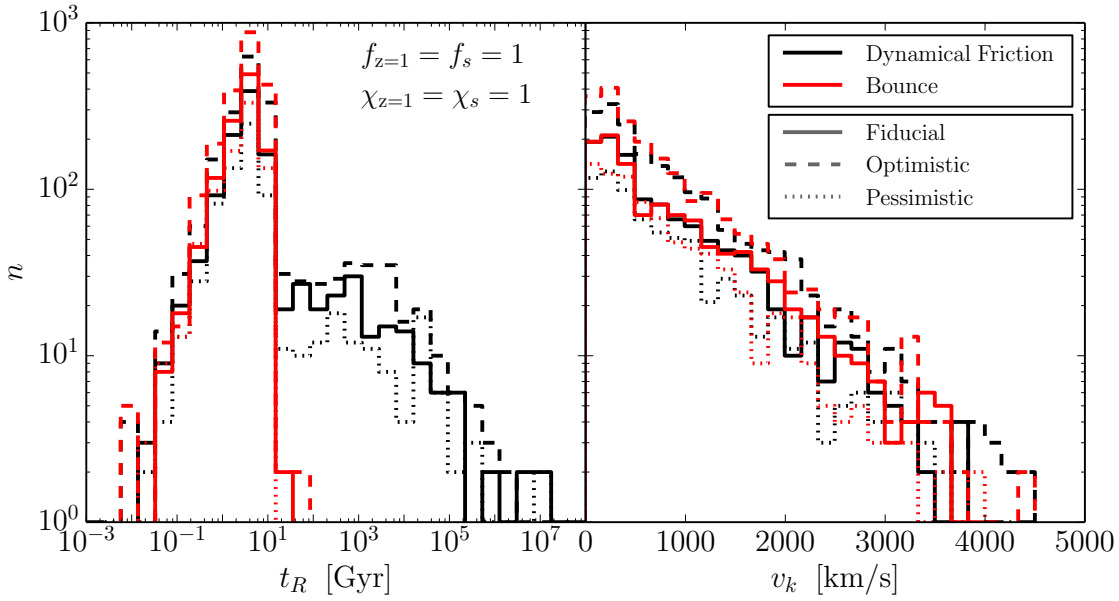

Figure 4.7: Return time distribution t_R (left) and recoil velocity distribution v_k (right) of all kicked SMBH in a 1000-events Monte Carlo realization of our four fiducial models. Red (black) curves are for the Bounce (DF) models, whereas solid, dashed and dotted curves correspond to the Fiducial, Optimistic and Pessimistic scenarios respectively, as labeled in figure. All distributions are computed assuming unit occupation fractions at $z = 1$ and $\chi_{z=1} = \chi_s = 1$.

all of them, the recoil distribution presents a high velocity tail extending to about 4000 km s^{-1}, with a median value of about 600 km s^{-1}. The difference between the Bounce and the DF models is clearly shown in the return time distribution. As expected, the rise of the distribution at $t_R < 1$ Gyr (corresponding to small kick velocities) is similar because the bounce dynamics is basically equivalent to a DF process when the SMBH does not leave the galaxy core. However, in the DF scenario, about 10% of the SMBHs are ejected outside the host BCG and interact only with the low-density dark-matter background outside the galaxy, with resulting return times longer than 10 Gyr (cf. the wider extent of the black distributions in the left panel of Fig. 4.7). As a result, BCG occupation fractions $f_{z=0}$ can be as low as 85% in the case $\chi_{z=1} = \chi_s = 1$, as reported in the upper panels of Fig. 4.8. Conversely, in the Bounce model, only few SMBHs do not make it back to the galaxy core following a kick, resulting in occupation fractions of 98% or higher. The two models are best compared in terms of 'depleted fraction', i.e. the fraction of BCGs that do not host a SMBH at $z = 0$, which is simply $1 - f_{z=0}$. This is shown in the lower panels of Fig. 4.8; it is clear that the DF model depletes BCGs of their central SMBH 10 times more efficiently than the Bounce model.

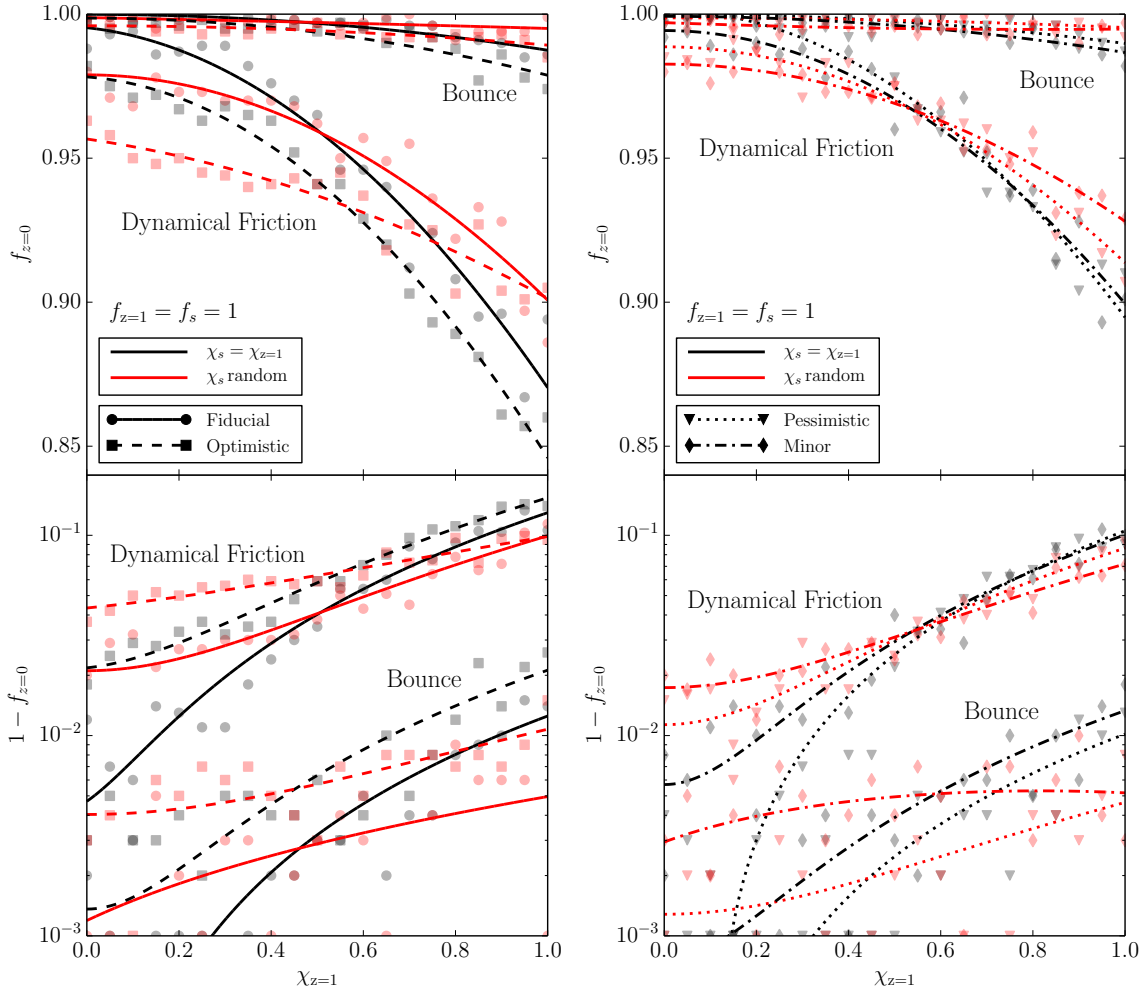

Figure 4.8: BCG occupation fractions. The left plot shows the "Fiducial" and the "Optimistic" models, whereas the right plots compares the "Pessimistic" and the "Pessimistic-Minor" models, to assess the impact of minor mergers. In each plot, the top panel shows the dependence of the $z = 0$ occupation fraction $f_{z=0}$ on the initial BCG spin magnitude $\chi_{z=1}$. To highlight the peculiarities of each individual model, the lower panel shows the corresponding depletion fraction $1 - f_{z=0}$, in logarithmic scale. Runs have been performed with two prescriptions on the spin magnitude of the satellite galaxy SMBHs χ_s, taken either to be equal to the spins of the BCG SMBHs (black curves) or uniformly distributed in $[0, 1]$ (red curves). A quadratic interpolation is presented in both cases. While final fractions as low as ~ 0.85 are detected in the DF scenario, only $f_{z=0} \sim 0.98$ can be achieved in spherically symmetric (Bounce) galaxies even for maximally spinning SMBHs.

4.3.1.2 Fiducial, Optimistic and Pessimistic models

Conversely, the adopted merger rate does not have a strong impact on $f_{z=0}$, and the difference between Fiducial, Optimistic and Pessimistic models is only modest, being at most a factor of ~ 2 in terms of depleted fractions, as shown in Fig. 4.8. For example, for $\chi_{z=1} = \chi_s = 1$, $1 - f_{z=0}$ varies between 0.1 and 0.15 for the DF model. The impact of minor mergers is also small, as shown in the left panels of Fig. 4.8.

Although apparently counter intuitive, this result is in fact expected because a higher BCG merger rate implies also a higher probability of multiple mergers. While it is true that each SMBH has a larger chance to be kicked out of its host, it is also true that there is a higher probability that it is replaced by another (possibly undermassive) SMBH brought in by a subsequent merger. Enhanced ejections and replenishments nearly cancel out making $f_{z=0}$ only weakly dependent on the details of the merger history. This is illustrated in Fig. 4.9, where the extreme case $\chi_{z=1} = \chi_s = 1$ is considered. In the Fiducial-DF model, 87% of the BCGs host a SMBH at $z = 0$ ($f_{z=0} = 0.87$); however, only 79% of them retained their original $z = 1$ SMBH, while ∼9% are depleted of their original SMBH and 'replenished' in a subsequent merger with a satellite galaxy hosting a SMBH. In the Optimistic-DF model those percentages become 69% and 16%, respectively: more SMBH are ejected (only 69% of original SMBHs retained), but a larger fraction of BCGs is replenished (16%) by virtue of the higher merger rate (causing a higher probability of multiple mergers). The opposite behavior is detected when the Pessimistic-DF scenario is considered. The balance is almost perfect in the Bounce models (also shown in Fig. 4.9). All three scenarios show $f_{z=0} \simeq 0.98$, but the probability of replenishment increases from the Pessimistic to the Fiducial and Optimistic models following a larger number of SMBH ejections.

As expected, the SMBH-mass distributions are different for replenished and non- replenished galaxies. Non-replenished galaxies reflect the injected correlation law (4.47) with lower scattering at $z = 0$, while the replenished samples tend to host undermassive SMBHs which have grown within smaller satellite galaxies in the cluster.

4.3.2 SMBH properties: spin magnitude and initial occupation fraction

Having explored the impact of the physics governing the evolution of the SMBH environment, we turn now to a description of the effect of the parameters related to the SMBH population itself; in particular SMBH spins and initial occupation fraction.

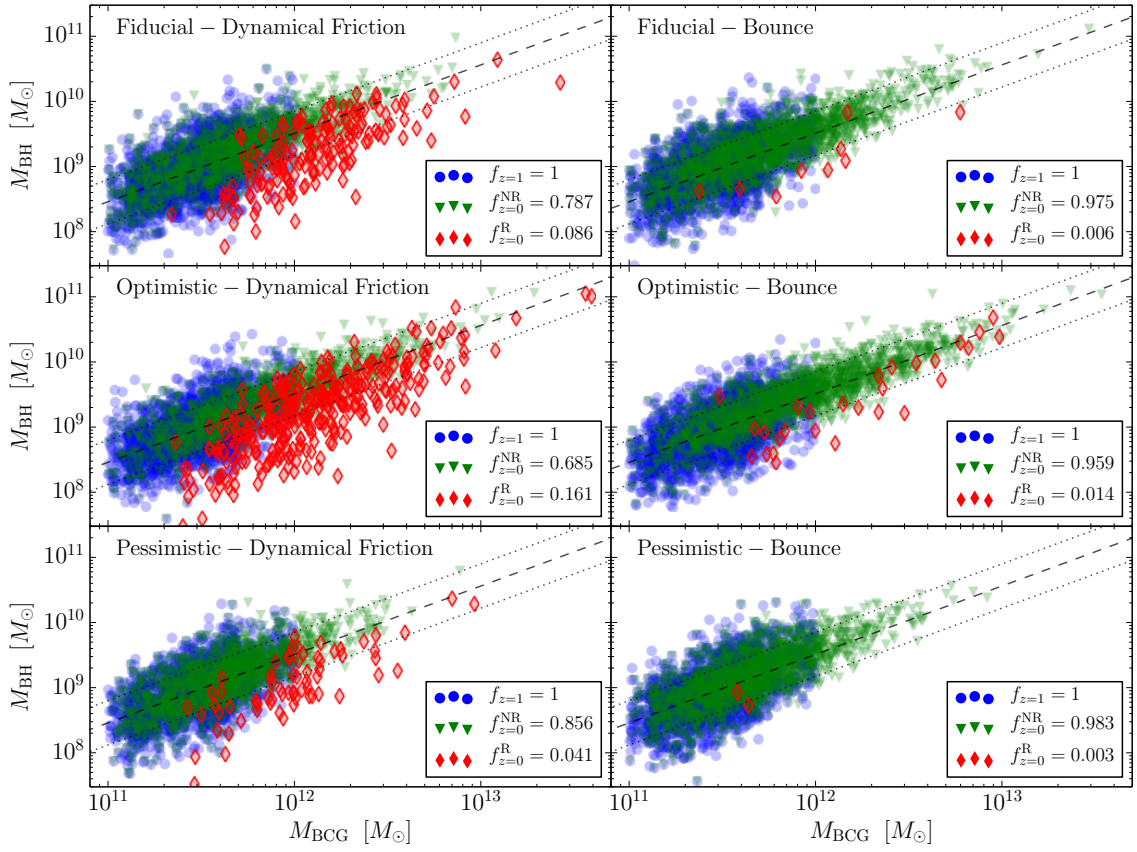

Figure 4.9: Deviations from the SMBH/host relation in replenished galaxies, and final occupation fractions. We show the distributions of the SMBH mass M_{BH} and the galaxy mass M_{BCG} in our six different models, assuming $f_{\rm z=1} = f_s = 1$ and $\chi_{\rm z=1} = \chi_s = 1$. Dashed and dotted lines show the average and the standard deviation of the initial correlation (4.47). Blue circles show the initial $z = 1$ sample. We track those systems where a replenishment occurred (R, red diamonds) and those which just underwent a plain evolution to $z = 0$ (NR, green triangles). While the evolved NR sample still lies on the $z = 1$ correlation but with lower scatter, replenished galaxies clearly exhibit deviations towards lower $M_{\rm BH}$ values. Occupation fractions for each sample are reported in the legends and are computed considering 10000 initial BCGs; points are shown for only 2000 initial BCGs to avoid cluttering.

4.3.2.1 Spin magnitude

The magnitude of the SMBH spin vectors in BCGs is essentially unknown, since most of the direct measurements from Kα iron lines involve local Seyfert galaxies [99, 440] and it is difficult to derive clear constraints through indirect arguments related to jet production, AGN spectra energy distribution fitting, or the evolution of the SMBH accretion efficiency with mass and redshift (see, e.g., [535, 477, 382]). However, we know that spins are crucial in the physics of gravitational recoils, because highly spinning SMBHs are likely to experience stronger recoils [see Eq. (4.14)]. We therefore need to investigate the SMBH parameter space carefully, to cover the full range of possibilities predicted by our models.

For each of our four models, we initialize $\chi_{z=1}$ at a fixed value, running between zero and one. As stated in Sec. 4.2.1, the spin orientations are assumed to be isotropic. For each case, we consider two different χ_s distributions: i) $\chi_s = \chi_{z=1}$ in each individual merger tree, and ii) χ_s random in the range $[0, 1]$. As shown in the upper panels of Fig. 4.8, $f_{z=0}$ is always a decreasing function of $\chi_{z=1}$, and is fairly well described by a quadratic function. Trends are best seen in the lower panels of Fig. 4.8, where we plot the depleted BCG fraction $1 - f_{z=0}$. In terms of the depleted fraction, spins have an order of magnitude impact on the results. In the DF model, only ≈1-4% of the BCGs are depleted at $z = 0$ (i.e., $1 - f_{z=0} = 0.01 - 0.04$) for $\chi_{z=1} = 0$, whereas up to ≈10-15% of the BCGs lost their SMBH at $z = 0$ (i.e., $1 - f_{z=0} = 0.1 - 0.15$) for $\chi_{z=1} = 1$. Similar trends hold for the Bounce model, but in that case only ≈0.1% to ≈2% of the SMBHs are lost at $z = 0$. It is interesting to notice that even for $\chi_{z=1} = 0$, we get $0.01 < 1 - f_{z=0} < 0.04$ in the DF models. This is, again, because of multiple mergers: a Schwarzschild SMBH can acquire a spin $\chi \approx 0.5 - 0.6$ in a single merger event [see Eq. (4.9)], which significantly enhances the probability to experience a superkick if a subsequent merger occurs. The different χ_s prescriptions [case i) and ii) above] show the same qualitative feature. The fits to the depleted fractions (lower panels of Fig. 4.8) intersect around $\chi_{z=1} = 0.5$ as expected: for lower values, the average χ_s in case ii) is larger, resulting in more superkicks and more SMBH ejections, while the opposite is true in case i).

4.3.2.2 Initial BCG occupation fraction

All theoretical models developed to reproduce the SMBH cosmic evolution (including present number density, and quasar luminosity function up to high redshift) require an amount of SMBHs that guarantees an occupation fraction $f = 1$ for massive galaxies [344, 66, 220, 275], pending, of course, the occurrence of superkicks. There is always the possibility that a superkick occurs at $z > 1$, even though galaxies at higher redshift are generally richer of cold gas, which will likely promote SMBH spin alignment during mergers [92, 167], ultimately suppressing superkicks [271]. Nonetheless, this might introduce some uncertainty on $f_{z=1}$ and, although we do not expect it to be far from unity, we study the sensitivity of our models to this parameter for completeness.

Fig. 4.10 shows $f_{z=0}$ as a function of $f_{z=1}$ for 240 different merger trees. The main evidence is that $f_{z=1}$ scales linearly with $f_{z=0}$. The slopes and the intercepts of the linear relation mostly depend on the occupation fraction of the satellite galaxies $f_{\rm s}$, i.e. on how many SMBHs are injected in the simulations between $z = 0$ and $z = 1$. The linear relationship between $f_{z=1}$ and $f_{z=0}$ can be easily understood using a simple analytic model

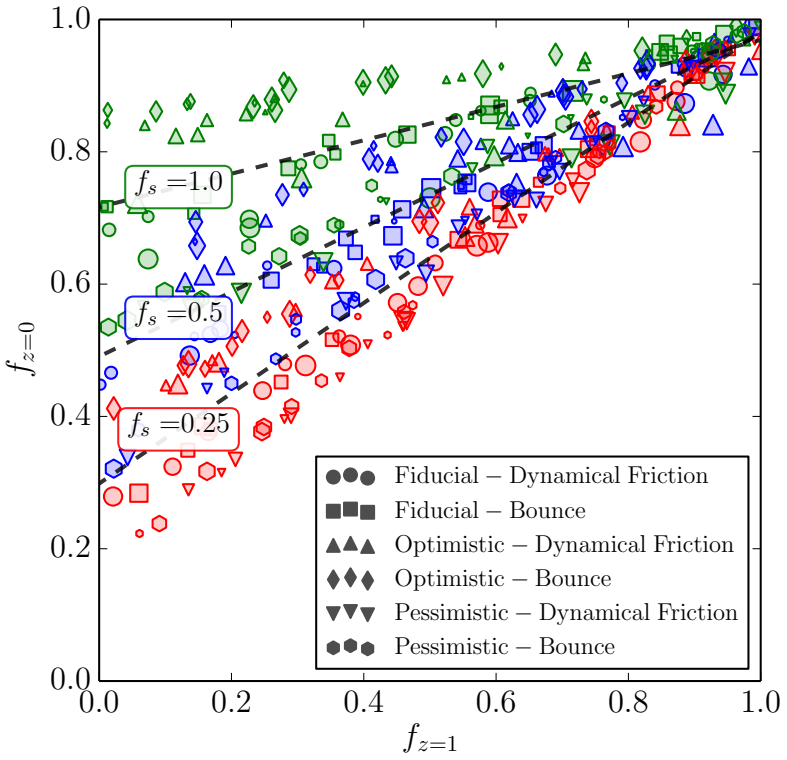

Figure 4.10: Dependence of the final BCG occupation fraction ($f_{z=0}$) on the initial occupation fraction of BCGs ($f_{z=1}$) and satellites (f_s). Each point represents a simulation of 1000 clusters where both the initial BCG and the satellite galaxies have the same initial spin $\chi_{z=1} = \chi_s$ (indicated with symbol size, where small symbols stand for slowly rotating SMBHs and large symbols for high spins) and model prescriptions (indicated with different symbol shapes, as detailed in the legend). Each sample (clustered along the dashed lines, with different colors) is computed with a different value of f_s. As confirmed analytically, the final BCG occupation fraction scales linearly with the initial occupation fraction; slopes and intercepts are mainly determined by f_s.

(built along the lines of [464]). The probability f_i of a BCG to have a SMBH at the i-th merger generation consists in the sum of (i) the probability that only the BCG had a SMBH at the previous generation $f_{i-1}(1 - f_s)$, (ii) the probability that only the satellite had a SMBH $f_s(1 - f_{i-1})$ and (iii) the probability that there has been a merger but the SMBH has not been ejected $f_s f_{i-1}(1 - P_{\rm ej})$ (where $P_{\rm ej}$ is the ejection probability). This yields

$$f_i = f_s + f_{i-1} - f_s f_{i-1}(1 + P_{\rm ej})\,. \tag{4.49}$$

Using the convergence limit $f_\infty = 1/(1 + P_{\rm ej})$, and fixing $f_{z=1}$ as initial condition, we can write down the previous expression as a geometric progression

$$f_i - f_\infty = (f_{z=1} - f_\infty)\left(1 - \frac{f_s}{f_\infty}\right)^i\,. \tag{4.50}$$

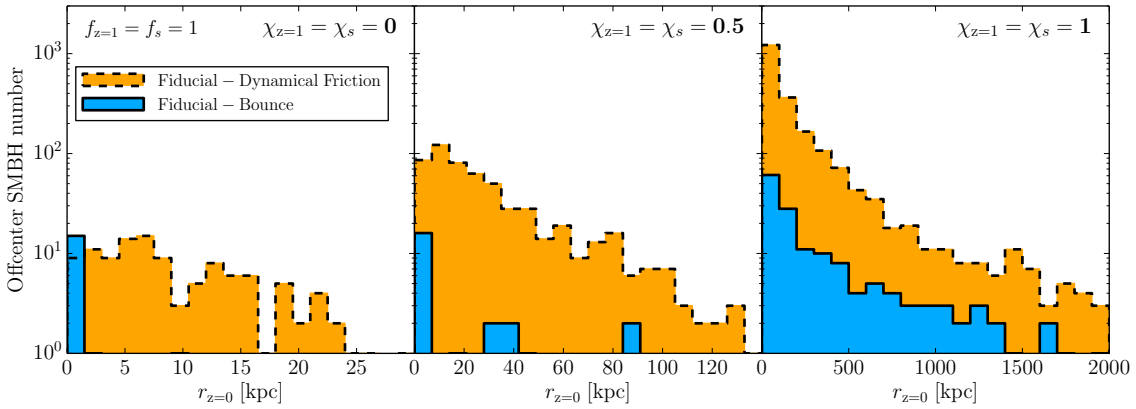

Figure 4.11: Number of wandering, off center, SMBHs as a function of their present distance from the galactic center (offset) $r_{z=0}$. The DF models (suited for non-spherical potentials) present at least a factor ~ 10 more wandering SMBHs than the Bounce models. SMBH detection through off nuclear quasar signatures or compact stellar systems may therefore distinguish between the two scenarios. Each run presented in this figure contains 10000 BCGs, which sets the absolute scale of the SMBH number; three different spin-magnitude values $\chi_{z=1} = \chi_s = 0$ (left panel), 0.5 (middle panel) and 1 (right panel) are considered; initial occupation fractions are fixed as $f_{z=1} = f_s = 1$.

With the further (strongly idealized) assumption that $P_{\rm ej}$ is constant over different merger generations, we can estimate the final occupation fraction in our samples to be

$$f_{z=0} - f_\infty = (f_{z=1} - f_\infty) \sum_{j=0} \epsilon_j \left(1 - \frac{f_s}{f_\infty}\right)^j , \tag{4.51}$$

where ϵ_j is the fraction of BCGs in which j mergers occur between $z = 1$ and $z = 0$. The above expression confirms the main trends observed in the simulations presented in Fig. 4.10, namely the linear relationship between $f_{z=0}$ and $f_{z=1}$, with slope and intersect mainly depending on f_s. The initial occupations $f_{z=1}$ and f_s are physically determined by cosmic history at early times ($z > 1$), whose modeling is outside the scope of the present analysis. However, as discussed before, we expect any deviation of $f_{z=1}$ from unity to be also related to the occurrence of superkicks.

4.3.3 Triaxiality and wandering SMBHs

Our results show that superkicks likely have very interesting and potentially observable astrophysical consequences, most notably, a decrease of the SMBH occupation fraction in BCGs down to 0.9 or lower, under specific assumptions. At the time of writing, secure SMBH mass measurements have been performed in about 10 BCGs [356], an insufficient number to empirically constrain the models presented here. As described in the introduction, future 30m-class telescopes like E-ELT and TMT can easily boost those figures by a factor of 10 or more. With $\mathcal{O}(100)$ SMBH mass measurements, significant deviations

from $f_{z=0} = 1$ can be measured, making it possible to directly test our superkick models, and possibly providing insights on the BCG SMBH spin distribution. As shown in the previous Section, $f_{z=0}$ strongly depends on both spin magnitudes and the detailed shape of the cluster potentials. The effect of the two ingredients is somewhat degenerate, since both high spins and non spherical potentials tend to reduce the occupation fraction. The degeneracy is, however, only partial. For example, $f_{z=0} < 0.9$ is possible only if cluster potentials are highly non-spherical *and* typical spins are higher than 0.8. A measurement of such low BCG occupation fraction will therefore provide valuable information on both the dynamics of the kicked SMBHs and their spins. Conversely, an occupation fraction of, say, 0.98 can be due to a combination of extremely low spins and non spherical potentials *or* very high spins and almost spherical potentials, as demonstrated in the lower panel of Fig. 4.8. In this case, degeneracy might be broken via independent measurements of the cluster mass distribution derived, for example, by lensing. Those allow us to reconstruct the shape of the cluster potential, thus providing an estimate of how likely/unlikely it is for an ejected SMBH to return on a radial orbit.

We note that the Bounce and DF prescriptions have been taken as extreme cases of a continuum range of possibilities. Since those prescriptions have a strong impact on the results, we can try to assess which of the two might be closer to reality on the basis of qualitative theoretical arguments. In the Bounce model, subsequent passages of the SMBH across the BCG core are crucial for damping the radial oscillations, critically shortening the return time. As a matter of fact, the clumpiness of a typical galaxy cluster mass distribution might easily cause a SMBH kicked to a few hundred kpc to miss a galaxy core which is smaller than 10 kpc across [306]. A simple estimate of the deviation from the radial path can be done by considering close encounters between the kicked SMBH and other cluster galaxies at apoastron. Consider a SMBH ejected to $r \approx 100$ kpc in a typical cluster of $M_{\rm DM} = 5 \times 10^{14} M_\odot$. The typical time it spends close to apoastron is $\delta t \approx 0.1$ Gyr. The gravitational pull of a galaxy with mass M at a distance d from the SMBH, will cause a velocity change

$$\delta v \approx \frac{GM}{d^2}\delta t \approx 50 \left(\frac{M}{10^{10} M_\odot}\right)\left(\frac{d}{10^4 pc}\right)^{-2} \text{ km s}^{-1}. \tag{4.52}$$

In a galaxy cluster like Coma, the galaxy density at 100kpc from the center is a few$\times 10^3$ galaxies Mpc^{-3} [539], implying that the presence of at least one perturber at $d < 10$ kpc is guaranteed. Considering a circular velocity of $v_c \approx 10^3$ km s^{-1}, it is therefore very likely that SMBHs kicked at $r > 100$ kpc will acquire a tangential velocity component $\approx 0.1 v_c$ because of interactions with nearby cluster galaxies (and clumpiness of the DM

halo). We performed a simple test of the DF return timescales for non circular orbits by numerically integrating the DF equations in a Hernquist+NFW potential. We placed the sinking SMBH at a distance R from the center, and we gave it an initial tangential velocity $v = v_c(R)$ and $v = 0.1v_c(R)$. The first case corresponds to a circular orbit, while the second implies a nominal eccentricity of $e \approx 0.98$ (if the orbit was Keplerian). Despite an almost radial orbit, the return timescale in the latter case was only approximately 5 times shorter. We tested that reducing $t_{\rm DF}$ in Eq. (4.38) by a factor 5 may cause a maximum variation of $f_{z=0}$ by ~ 0.07 in the extreme case $\chi_s = \chi_{z=1} = 1$, which still implies $f_{z=0} \approx 0.9$. This suggests that small deviations from a perfectly radial orbit result in return timescales just a factor of a few smaller than our DF computation, but two orders of magnitude longer than the Bounce model prediction, which is therefore relevant only for almost spherical potentials. We conclude that the DF scenario provides a better approximation for the return timescales in realistic potentials implying interesting observational prospects. As shown in Fig. 4.8, a DF-like dynamics results in $f_{z=0} < 0.99$ for basically any choice of other relevant parameters, and the superkick effect should be detected with a sample of $\mathcal{O}(100)$ SMBH mass measurements.

Besides the lower BCG occupation fraction, another interesting phenomenon is BCG replenishment. We saw in the previous Section that depleted BCGs can be replenished in a subsequent merger with another SMBH carried by the satellite galaxy. In this case, the new SMBH will most likely be undermassive with respect to the BCG mass. This is shown by the red diamonds in Fig. 4.9, which lie ≈ 0.3 dex below the SMBH-bulge relation defined by the green triangles. However, the net effect of replenishment is just to produce a slightly lower normalization and larger scatter in the SMBH-bulge relation, which would be hard to identify observationally.

The implications of superkicks on the BCG occupation fraction are directly mirrored in the presence of a complementary population of wandering SMBHs. In fact, as already noted, full ejections from galaxy clusters are extremely unlikely because of the high escape speeds. As a natural consequence, some recoiled SMBHs are still sinking back to the BCG center today, and can potentially be detected as off center objects, adding evidence to the superkick scenario. Because of the longer return timescales, off center SMBHs are expected to be at least 10 time more likely in the DF than in the Bounce models. The offset distribution is shown in Fig. 4.11 for three values of the spin magnitudes $\chi_{z=1} = \chi_s = 0, 0.5, 1$, assuming the "Fiducial" model (other models, not shown, yield similar results). The absolute number of recoiling SMBHs in each panel is directly related to the average kick velocity imparted during SMBH mergers, which reflects the average spin magnitude.

Distributions are generally monotonically decreasing functions of the offset $r_{z=0}$, meaning that many of these wandering SMBHs are concentrated in a few central kpc. However, in the maximally spinning case (right panel) about 50% of the ejected SMBHs are located well outside the central BCG, with an offset between 100 kpc and 1 Mpc. Moreover, a tail extending to few Mpc is present, implying that a few SMBHs might even lurk in the outskirts of galaxy clusters. For this favorable configuration, we predict that between 0.5% and 5% of massive galaxy clusters should host a wondering BCG SMBH with an offset of a few hundred kpc from the cluster center. The situation is less promising for lower spin values, even though in the intermediate case (central panel) for the DF model, about 1% of the BCGs might host a SMBH lurking at few tens of kpc from their centers.

Several observational signatures of recoiling SMBHs have been proposed in the literature, ranging from off center AGNs [88] and tidal disruptions [289, 308], to intracluster ultracompact stellar systems [364]. All of them rely on the fact that the recoiling SMBH is carrying with it a significant amount of nuclear gas and stars, which is not likely in our case. Firstly, BCGs are mostly gas poor systems with shallow stellar cores; little cold gas should be available in the surrounding of the merger remnant, disfavoring off–nuclear AGN activity. Secondly, the SMBH can carry away only material that is orbiting around it with a velocity greater than the kick velocity v_k. Ejections to a few hundred kpc require $v_{\rm k} > 1500$ km s$^{-1} \gg \sigma$, implying that the mass in stars and gas that can be carried away is likely $< 1\%$ of the SMBH mass. Lastly, because of their high mass, those SMBHs will simply swallow stars without tidally disrupting them, inhibiting the tidal disruption channel as a possible observational signature. The only possibility seems therefore to be the challenging detection of a faint ultracompact cluster with extremely high velocity dispersion, which might be feasible in nearby galaxy clusters [364]. Alternatively, also 'naked' SMBHs still interact with the diffuse hot intracluster gas. This can produce X-ray emission potentially observable at nearby galaxy cluster distances (see [154] for details).

4.4 Strong gravity in BCGs

We investigated the consequences of superkicks for the population of the most massive SMBHs in the Universe residing in BCGs. The choice of BCGs as study targets follows from a number of theoretical and observational arguments: i) compared to other types of galaxies, BCGs have the richest merger history, especially at low redshift, ii) future 30m-scale telescopes will have the resolution to easily reveal SMBHs in hundreds of BCGs up to $z \approx 0.2$, iii) theoretically, BCGs are expected to have unit SMBH occupation fraction, and even a single depleted system would be a smoking gun of superkick occurrence in nature.

We demonstrate that, under plausible astrophysical assumptions, SMBHs can be ejected from BCG cores, potentially resulting in an occupation fraction substantially lower than one in the local Universe (say, $z < 0.1$).

Starting from the observational fact that BCGs have doubled their mass since $z = 1$ – and that this mass growth is consistent with their merger activity as inferred from galaxy pair counts, and as found in simulations of galaxy formation – we have constructed a simple semianalytical model to track their evolution to the present time. Our model reconstructs the dynamics of each single major merger, including a self-consistent computation of the gravitational recoil and of the return time of the kicked SMBHs. We considered six classes of models combining two BCG major merger history models ("Fiducial", "Optimistic" and "Pessimistic", covering the range consistent with observations and simulations) and two specific prescriptions for the return times ("Bounce" and "DF"). Minor merger rates were also available for the "Pessimistic" scenario, we investigated their impact by including them in the "Pessimistic-Minor" model. Since the magnitude of the spins of SMBHs in BCGs is basically unknown, for each model we considered a range of spin distributions for the SMBHs residing in the BCGs, χ, and in the merging satellites, χ_s. We ran several sets of simulations varying all the relevant parameters, we studied their impact on the final BCG occupation fraction $f_{z=0}$, and we investigated possible observational consequences.

Our main results can be summarized as follows:

1. superkicks can efficiently deplete BCGs of their central SMBHs. The occupation fraction at $z = 0$ can be as low as $f_{z=0} = 0.85$ for the most favorable scenarios;

2. $f_{z=0}$ is quite insensitive to the BCG merger history, so long as those experience at least ≈ 1 merger since $z = 1$;

3. only small quantitative differences were found when comparing the "Pessimistic" and the "Pessimistic-Minor" models, implying that the poorly constrained distribution of minor mergers is not a significant caveat to our findings;

4. $f_{z=0}$ is very sensitive to the dynamics of the ejected SMBHs in the galaxy cluster potential well. The fraction of depleted BCGs (i.e. $1 - f_{z=0}$) is of the order of 0.01 only for the Bounce models, but it is typically 0.05-0.1 for the DF models;

5. the intial value of the SMBH spins has an order of magnitude influence on the depleted BCG fraction. In the DF models, this varies from ≈ 0.02 for non spinning SMBHs, up to ≈ 0.15 for maximally spinning SMBHs;

6. we predict that a few percent of the galaxy clusters host an offset BCG SMBH

inspiralling at a few hundred kpc from the dynamical center, although they might be difficult to detect;

7. for a large variety of physically plausible scenarios, we predict $f_{z=0} < 0.99$, that can be directly tested with measurements of SMBHs in the center of $\mathcal{O}(100)$ BCGs with future 30m telescopes.

As detailed in Sec. 4.2.5, we made a number of simplifying assumptions in our calculation. In particular we neglected any possible mass and spin evolution due to gas accretion, and we assumed SMBH binaries always merge following galaxy mergers (i.e., we by-passed the *final parsec problem*). Moreover, we assumed random spin orientations when computing kick velocities. We showed that all these assumptions are well justified at least for the majority of mergers involving BCGs, but refinement of some of them might be considered for future work.

Although current statistics of SMBH mass measurements in BCGs is insufficient to empirically constrain the models presented here, prospects look promising for the next generation of 30m-class optical telescopes. Any measurement of a BCG occupation fraction lower than unity will provide observational evidence for the occurrence of superkicks in nature, bringing the extreme dynamical effects of strong-field GR to the realm of observational astronomy.

Chapter 5

Differential disc accretion and black-hole spin alignment

Outlook

Interactions between a SMBH binary and the surrounding accretion disc can both assist the binary inspiral and align the BH spins with the disc angular momentum. While binary migration is due to angular-momentum transfer within the circumbinary disc, the spin-alignment process is driven by the mass accreting onto each BH. Mass transfer between different disc components thus couples the inspiral and the alignment process together. Mass is expected to leak through the cavity cleared by the binary, and preferentially accretes onto the lighter (secondary) BH which orbits closer to the disc edge. Low accretion rate onto the heavier (primary) BH slows down the alignment process. We revisit the problem and develop a semi-analytical model to describe the coupling between gas-driven inspiral and spin alignment, finding that binaries with mass ratio $q \lesssim 0.2$ approach the GW driven inspiral in differential misalignment: light secondaries prevent primaries from aligning. Binary BHs with misaligned primaries are ideal candidates for precession effects in the strong-gravity regime and may suffer from moderately large (~ 1500 km/s) kick velocities.

Executive summary

This Chapter is organized as follows. In Sec. 5.1 we review previous studies which tackled the disc-spin alignment process. Our model to compute the relevant timescales is introduced in Sec. 5.2, where both the inspiral and the alignment problems are treated. Sec. 5.3 describes our main findings, namely the role of the binary mass ratio in the spin-alignment process, and its relevance for cosmologically motivated binary distributions and kick predictions. Finally, in Sec. 5.4 we draw our conclusions and stress the possible caveats of our analysis.

The material presented in this Chapter is based on [211].

5.1 Gas interactions: inspiral and alignment

Following a galaxy merger, the SMBHs hosted [293] by the two merging galaxies sink towards the centre of the newly formed stellar environment through DF, forming a binary [60, 352]. Binary BHs can merge if the astrophysical environment provides a way to dissipate their angular momentum in less than a Hubble time. Scattering from stars can bring the binary only down to parsec scales [191], below which the available phase space is quickly depleted, thus stalling the inspiral process (*final-parsec problem* [369, 552]). While triaxiality in the stellar potential may help driving the inspiral in elliptical gas-poor galaxies [363, 68], the interaction with gaseous disc(s) may actually solve the final-parsec problem in gas-rich galaxies [35, 138]. Indeed, DF against a gaseous background can help reduce the binary separation to distances of the order of 0.1 pc within a timescale of 10-50 Myrs [178, 162, 165]. Further shrinking of the binary can proceed through what is known as type II migration in the context of planet-disc interaction. However, such disc-assisted migration can only be effective at separations smaller than ~ 0.01 pc, beyond which the disc becomes self-gravitating and will likely fragment and form stars [319]. Finally, if the binary reaches separations close to $\simeq 10^{-3}$pc, GWs quickly become an extremely efficient way to drive the binary to a merger [415, 414]. Asymmetric emission of GWs in the late inspiral and merger may impart recoil velocities to the remnant BHs [437] which can be as high as 5000 km/s [115, 215, 332], possibly larger than the escape speed of the host galaxies [362].

A variety of electromagnetic signatures has been proposed to detect SMBH binaries, which however remain elusive [166, 466, 91]. The most convincing evidence comes from double AGN imaging, with the notable example of the radio galaxy 0402+379 showing two compact cores with estimated separation of 7.3 pc [446]. Indirect evidence for SMBH

binaries at sub-parsec scales suffers from higher uncertainties; we mention in particular the case of the blazar OJ287 [518], where ~ 12 yr periodic outbursts have been interpreted as signature of a BH binary orbital motion. Identifying recoiling BHs through observations is even more challenging [287], but tentative candidates are nonetheless present [290, 131, 153, 294]. Direct measurements of SMBH inspirals and mergers are the main target of all future space-based GW observatories and PTA experiments. The eLISA mission is expected to detect hundreds merging binaries per year casting new light on our understating of such systems [469, 48].

Hydrodynamical interactions can not only assist the binary inspiral, but are responsible for the reorientation of the two BH spins. BH spin alignment has a crucial impact on the merger dynamics and on the cosmic growth history of SMBHs. Strong recoil velocities can only be achieved if the merging BHs are highly spinning and the two spin vectors are strongly misaligned with each other. As we already saw in Chapter 4, highly recoiling BHs can be significantly displaced from the galactic nucleus or even ejected from it. This has strong consequences for the coevolution of SMBHs and their host galaxies, with mild recoil regulating the BH growth and large kick velocities strongly affecting the feedback process [89]. If large recoils causing BH ejections are present, this affects the fraction of galaxies hosting SMBHs[1] [464, 531, 209] and consequently the predicted (e)LISA event rates [470]. As carefully addressed in Chapters 2 and 3, spin misalignments are crucial for GW astronomy and data analysis. Spin misalignments introduce a richer structure to the expected signals that carries precious information on the binary dynamics [525, 285, 400] which can improve the parameter estimation process by up to an order of magnitude [125]. At the same time, since accurate waveform modelling is required for GW searches, spin precession makes the waveform generation more challenging [411, 284], dramatically increasing the parameter-space dimensionality that needs to be explored.

It is thus important for both electromagnetic and GW observations to understand in which region of the BH-binary parameter space we expect significant spin misalignment. The physical process responsible for the reorientation of BH spins during the long gas-driven inspiral is the so-called Bardeen-Petterson effect [55], where the general relativistic Lense-Thirring torque between the BH and a misaligned disc warps the accretion disc and secularly aligns the BH spin with the disc angular momentum. The Bardeen-Petterson effect does not just affect the binary dynamics during the gas-driven phase, but leaves a deep imprint in the subsequent GW-driven inspiral, where precession effects are strongly dependent on the residual misalignments left by the astrophysical environment [270, 271,

[1] The analysis presented in Chapter 4 tackles this problem in gas-poor galaxies, where disc-assisted inspiral and alignment are not crucial (cf. our discussion in Sec. 4.2.1).

204]. It is therefore an essential ingredient for predicting the spin configuration at merger.

The efficiency of the Bardeen-Petterson effect in aligning the spins with the binary angular momentum within the timescale of the merger has recently been investigated by multiple authors. Bogdanović et al. [92] first made some order-of-magnitude estimates of the alignment time for a single BH with its own disc and found that it is much smaller than the merger time concluding that alignment is likely in a gaseous environment. A similar conclusion was obtained by Dotti et al. [167], who found short alignment timescales of $\sim 2 \times 10^6$ yr. One notable achievement of the study performed by Dotti et al. [167] is combination of Smoothed-Particle Hydrodynamics (SPH) simulations and a semi-analytical treatment of the Bardeen-Petterson effect [413], through which they have been able to quantify the residual misalignment to either 10° or 30° depending on the gas temperature. In previous work [317], we revisited these estimates considering the previously neglected effects of non-linear warps. We found that the alignment time can be significantly longer than 10^7 yr if the initial misalignments are large, thus casting doubts on the ability of the disc to align the binary. Miller and Krolik [367] made a step forward, pointing out that the spin alignment process in BH binaries may actually be sensibly faster than for isolated BHs, because of the stabilizing effect of the companion that increases the degree of disc warping close to the holes.

Here we argue that the binary mass ratio plays a key role in estimating the spin-alignment likelihood in merging BH binaries. We present a semi-analytical model to compute the inspiral and alignment processes from the properties of the circumbinary disc. On the one hand, the mass ratio strongly affects the binary inspiral rate, marking the onset of different disc-morphology regimes when either a gap or a proper cavity can be opened. On the other hand, and perhaps most importantly, the binary mass ratio sets the amount of differential accretion onto the two components of the binary system. The Bardeen-Petterson effectiveness in aligning the spins depends sensitively on the mass accretion rate through each single disc. We quantify this rate constructing prescriptions based on results of hydrodynamical simulations. Gas is expected to preferentially accrete onto the lighter binary member that therefore aligns faster. Accretion rates onto the heavier BH is consequently smaller and may prevent it from aligning.

5.2 Binary and disc modelling

We model the gas environment surrounding merging BH binaries through three different accretion discs: mass may reach the binary from galactic scales forming a *circumbinary* disc, and later be accreted onto the individual BHs from *circumprimary* and *circumsecondary*

discs respectively[2]. We define[3] R to be the binary separation, M_1 and M_2 to be the two BH masses (with $M_1 \geq M_2$), $M_{\rm bin} = M_1 + M_2$ to be the total mass of the binary, $q = M_2/M_1 \leq 1$ to be the binary mass ratio and $S_i = \chi_i G M_i^2/c$ to be the spin of any of two BHs (where $i = 1, 2$ and dimensionless spin $0 \leq \chi_i \leq 1$). Following [499], we also define a measure of the local circumbinary-disc mass at a generic radius r as $M(r) = 4\pi\Sigma(r)r^2$ and finally $q_{\rm disc}(r) = M(r)/M_{\rm bin}$ to be the disc-to-binary mass ratio. For typical profiles of the surface density $\Sigma(r)$, this is a reasonable estimate of the rigorous value obtained by radially integrating the surface density [476]. In addition, the migration rates are set by the properties of the disc in the vicinity of the secondary, and the local nature of this parameter is thus more relevant than the total disc mass. When studying the spin alignment, we will refer to the mass of the aligning BH as M (meaning either M_1 or M_2) and the mass of the other binary member as $M_{\rm c}$. While the accretion rate of the circumbinary disc $\dot{M}_{\rm bin}$ determines the inspiral process, the alignment timescales are only determined by the rates $\dot{M}_1$ and $\dot{M}_2$ at which mass reaches the circumprimary and circumsecondary discs respectively. It is also useful to define f to be the dimensionless value of $\dot{M}_{\rm bin}$ in terms of the Eddington accretion rate

$$\dot{M}_{\rm bin} = f \frac{M_{\rm bin}}{t_{\rm Edd}} \,, \tag{5.1}$$

where $t_{\rm Edd} = \kappa_{\rm e} c/4\pi G \simeq 4.5 \times 10^8 {\rm yr}$ is the Salpeter time [453], and $\kappa_{\rm e}$ is the opacity for Thomson electron scattering.

In this Section, we first present a new estimate for the inspiral timescale by interpolating estimates computed in different regimes and we discuss the circumbinary disc self-gravity condition to evaluate the inspiral timescale. Secondly, we summarize the main findings of [317] on the spin-alignment timescale and we explore the effect of the companion on the individual-discs structure. We finally model mass transfer and differential accretion onto the different discs.

5.2.1 Gas-driven inspiral

If SMBH mergers do happen in nature, it is likely that the gas-driven phase is the bottleneck of the whole binary evolutionary track. Therefore, the time spent by the binary in this phase gives us an estimate of the total time available to align the BH spins through environmental processes before merger. Although gas-driven inspiral is mediated by the

[2]The name *minidiscs* can also be found in the literature to indicate circumprimary and circumsecondary discs.

[3]We opt here for the standard notation used in the accretion-disc literature. Consequently, the notation used in this Chapter is slightly different than the one used in any other Chapter of this Thesis.

torques exerted by the disc on the binary, a detailed description of the torques is not necessary to correctly derive the migration rates. Ultimately, the migration rate is controlled by the rate at which the disc is able to redistribute the angular momentum gained from the binary, and the torques will adjust to give the correct rate (e.g., [34]). This same mechanism is called type II migration in the context of protoplanetary discs [312]. Depending on the ratio between the BH and the circumbinary disc masses, we identify three possible regimes:

1. For small mass ratios ($M_2 \ll M(R) \ll M_1$), the secondary BH perturbs the disc of the primary, which reacts by opening a gap[4] at the binary separation [311, 36]. Tidal interactions between gas particles and the secondary BH transfer angular momentum to the disc, thus decreasing the binary separation. The secondary BH behaves like a fluid element in the disc, evolving at the viscous rate [35]

$$t_{\rm in} = t_\nu(R) \simeq \frac{R^2}{\nu} \,, \tag{5.2}$$

   where $\nu = \alpha c_s H$ is kinematic viscosity coefficient of the disc, usually [476] rescaled to a dimensionless coefficient α with the speed of sound c_s and the disc height H.

2. If the secondary BH mass becomes comparable to the disc mass ($M_2 \sim M(R) \ll M_1$), the disc cannot efficiently redistribute the momentum acquired from the binary. The shrinking rate consequently decreases. An analytical expression for the inspiral timescale in this regime can be computed directly from the angular-momentum conservation equation in the thin-disc approximation [499, 255, 319, 57] and reads

$$t_{\rm in} = \frac{M_2 + M(R)}{M(R)} t_\nu(R) \,, \tag{5.3}$$

   which correctly reduces to $t_\nu(R)$ in the limit $M_2 \ll M(R)$.

3. For comparable mass binaries ($M_1 \lesssim M_2$), the secondary-BH potential cannot be neglected. The gap at the secondary location now becomes a proper cavity in the disc with radius $\sim 2R$ cleared by both BHs [342]. A rich phenomenology may be present, including disc asymmetry and growing eccentricity, and can only be captured using hydrodynamical simulations [138, 447, 448, 484]. An approximate expression for the inspiral timescale in the comparable mass regime has been presented by Rafikov [434], assuming the binary potential to be represented by a Newtonian potential produced

[4] Binaries with very small mass ratios ($q \lesssim 10^{-4}$, see [34]) cannot open a gap; however, such low mass ratios are not expected to be relevant in the SMBH context.

by the binary total mass. He obtains

$$t_{\rm in} = \frac{M_1 M_2}{M_{\rm bin}\, M(R)} t_\nu(R) \,, \tag{5.4}$$

where the correction factor $M_1/M_{\rm bin}$ models the expected speed up due to the higher angular momentum flux induced by the binary mass. The same mass-ratio dependence has been recently obtained in [164] integrating the torque at the edge of a $2R$-wide cavity.

Here, we propose a smooth analytical interpolation between the timescales obtained in the different regimes given by

$$t_{\rm in} = \frac{M_1}{M_{\rm bin}} \frac{M_2 + M(R)}{M(R)} t_\nu(R) \,, \tag{5.5}$$

which correctly reduces to either Eq. (5.2), (5.3) or (5.4) in the relevant limits. Various numerical factors in Eq. (5.4) –as already acknowledged in [434]– and different possible definitions of the viscous timescale may modify this estimate by a factor ∼few. The accretion rate of the circumbinary disc $\dot{M}_{\rm bin}$ only enters in the merger timescale through the viscous timescale, which can be rewritten as

$$t_\nu(R) = \frac{3}{4} \frac{M(R)}{\dot{M}_{\rm bin}} \,, \tag{5.6}$$

since both $M(R) = 4\pi R^2 \Sigma(R)$ and $\dot{M}_{\rm bin} \simeq 3\pi\nu\Sigma(R)$ are related to the surface density Σ of the circumbinary disc in the stationary limit. Combining Eqs. (5.1), (5.5) and (5.6), we obtain our final estimate of the inspiral timescale, to be compared to the individual alignment timescales,

$$t_{\rm in} = \frac{3}{4} \frac{(1+q)\, q_{\rm disc}(R) + q}{(1+q)^2} \frac{t_{\rm edd}}{f} \,. \tag{5.7}$$

While the low mass ratio regime is relatively well tested by the planetary community (e.g. [380, 58], but see below for possible caveats), the regime of high mass ratios has not been explored extensively. At the moment only few simulations of disc driven migration of a binary have been conducted [342, 138, 484], which test only a small part of the parameter space. For example, for a ratio $q = 1/3$, Cuadra et al. [138] find in 3D SPH simulations a migration rate of $\dot{R}/R = -2 \times 10^{-5}\ \Omega$, where $\Omega = (GM_{\rm bin}/R^3)^{1/2}$ is the orbital frequency of the binary. They compare this value with the analytical formula of [255], our Eq. (5.3), which yields $\dot{R}/R = -3 \times 10^{-5}\ \Omega$, yielding very good agreement. MacFadyen and Milosavljević [342] find in 2D grid-based simulations of $q = 1$ binaries

that the inspiral timescale is roughly equal to the viscous timescale, reduced by $q_{\rm disc}$, which is consistent with Eq. (5.7). The simulations described so far neglect the details of the angular momentum redistribution mechanism, which in the standard picture is the magneto-rotational instability [46], and typically adopt the α parametrization [476] (e.g., [342]) in order to reduce the computational cost. Only recently Shi et al. [484] have performed global numerical simulations of migrating binaries including the magneto-rotational instability. They found that magnetohydrodynamics effects slightly enhance the migration rate with respect to the purely hydrodynamical case (a factor of ~ 3 when compared to [342]). They also observed that the accretion of material with a higher specific angular momentum than the binary can make the binary *gain* angular momentum, which however is offset by the higher torques they measure from the disc. Given the number of other uncertainties present in the model, we are thus satisfied that our expressions can be used reliably.

Recent numerical simulations [169, 170] by the planetary community have questioned the validity of type II migration, casting doubts that a regime where the satellite behaves like a test particle exists at all. In particular, the simulations show that it is possible to achieve faster (up to a factor of 5) migration rates than what expected from Type II theory. These simulations have only been run for a fraction of a viscous time, and it is still unclear if this result holds on the timescale of the merger. For this reason we neglect these results in what follows, and note that this makes our estimates an upper limit for the merger timescales.

Finally, we note that the simulations conducted so far, to the best of our knowledge, have explored relatively thick discs, with an aspect ratio ranging from 0.05 to 0.1 [e.g., 342, 138, 448, 484]. This is significantly thicker than the value we derive in the next Section and it is not clear how the results would change with more realistic values (cf. Sec. 5.4).

5.2.2 Self-gravity condition

The inspiral timescale reported in Eq. (5.7) depends on the binary separation R. For typical disc structures [476, 217], $t_{\rm in}$ is a steep monotonically increasing function of R [223]. Most time will be spent by the binary at large separations, while the remaining inspiral is completed rather quickly. The time available to align the spins –which the spin-alignment time must be compared to– is roughly the inspiral timescale $t_{\rm in}$ evaluated at the largest separation of the disc-driven evolution.

A natural physical limit on the size of the circumbinary disc is set by the disc's self

gravity. Local gravitational stability under axisymmetric disturbances is guaranteed up to the fragmentation radius $R_{\rm f}$ where the Toomre's [511] parameter equals unity:

$$Q \equiv \frac{c_s \Omega}{\pi G \Sigma} = 1 \,. \tag{5.8}$$

At separation $R > R_{\rm f}$, self gravity cannot be neglected and the disc is gravitationally unstable (cf. [316] for a review). The evolution of gravitationally unstable discs has been investigated in great detail in recent years [322, 443, 137]. If the cooling time is smaller or of the order of the dynamical time [198], the disc will fragment into gravitationally bound clumps, although the actual fragmentation threshold is debated [365]. For values appropriate for AGN discs, the disc is expected to fragment, create stars and thus deplete the area surrounding the binary of gaseous material, possibly halting the inspiral [319]. Using the vertical-equilibrium equation $c_s/\Omega = H$, the self-gravity stability condition $Q = 1$ can be rewritten as

$$q_{\rm disc}(R) = \frac{M(R)}{M_{\rm bin}} \simeq 4\frac{H}{R} \,, \tag{5.9}$$

evaluated at $R = R_{\rm f}$. The fragmentation radius is likely to lie in the outer region of the circumbinary disc, dominated by gas-pressure and electron-scattering opacity [476]. Assuming viscosity to be proportional to the gas pressure (β-disc) and setting the mass of the accreting object to $M_{\rm bin}$, one gets for the fragmentation radius [476, 217, 223]

$$\begin{aligned} R_{\rm f} &\simeq 10^5 \frac{G M_{\rm bin}}{c^2} \left(\frac{M_{\rm bin}}{10^7 M_\odot}\right)^{-26/27} \left(\frac{f}{0.1}\right)^{-8/27} \left(\frac{\alpha}{0.2}\right)^{14/27} \\ &\simeq 0.05 \left(\frac{M_{\rm bin}}{10^7 M_\odot}\right)^{1/27} \left(\frac{f}{0.1}\right)^{-8/27} \left(\frac{\alpha}{0.2}\right)^{14/27} \ {\rm pc} \,. \end{aligned} \tag{5.10}$$

For a separation r in such a region, the disc aspect ratio reads

$$\frac{H}{r} = 0.001 \left(\frac{r}{G M_{\rm bin}/c^2}\right)^{1/20} \left(\frac{M_{\rm bin}}{10^7 M_\odot}\right)^{-1/10} \left(\frac{f}{0.1}\right)^{1/5} \left(\frac{\alpha}{0.2}\right)^{-1/10} \,. \tag{5.11}$$

We evaluate the inspiral timescale of Eq. (5.7) at the fragmentation radius: $R = R_{\rm f}$. This is a rather conservative assumption because $t_{\rm in}$ is monotonically increasing with R [223] and $R_{\rm f}$ is the largest separation at which gas can be found under the form of a circumbinary disc. We are therefore assuming –somehow ignoring the final parsec problem– that some previous mechanisms are efficient enough to shrink the binary separation down to $R_{\rm f}$.

From Eqs. (5.7-5.11) we find that the inspiral time $t_{\rm in}$ scales only mildly with the

viscosity α and the binary total mass $M_{\rm bin}$. As for the accretion rate f, the implicit dependence of Eq. (5.11) and (5.10) is also mild; the explicit dependence $1/f$ in Eq. (5.7) is still present but will cancel when compared to the spin-aligment time (Sec. 5.3.1). On the other hand, the dependence on q plays a crucial role when comparing each spin-alignment time with the inspiral timescale, and is therefore the main subject of this study.

5.2.3 BH spin alignment

The circumprimary and cirbumsecondary discs interact with the BHs through the Bardeen-Petterson effect. Bardeen and Petterson [55] first showed that a viscous disc initially misaligned with the equatorial plane of a spinning BH naturally relaxes to a coplanar state in the inner regions, while the outer disc may retain its original misalignment. Rees [438] realized that, by Newton's third law, the outer disc must react by pulling the BH towards complete alignment (or antialignment) of the spin with the orbital angular momentum of the outer disc itself.

Angular momentum is initially transferred from the spin to the inner disc through relativistic Lense-Thirring precession and finally to the outer disc by the propagation of warps, i.e. vertical shearing by close, misaligned, gas rings [459, 321, 348]. Warp propagation is ruled by a vertical viscosity coefficient ν_2, which generally differs from the kinematic viscosity coefficient ν introduced above. As done for α, let us introduce a vertical-viscosity coefficient α_2 such that $\nu_2 = \alpha_2 c_s H$ [407]. In the small-warp –which in our case actually means small-misalignment– limit, the warp-propagation coefficient is related to the kinematic viscosity by [427, 393]

$$\alpha_2 = \frac{1}{2\alpha}\frac{4(1+7\alpha^2)}{4+\alpha^2}\,, \tag{5.12}$$

and, in particular, it is independent of the misalignment φ between the inner disc and the outer disc. A full non-linear theory of warp propagation has been computed in [393] and later verified numerically [320]. Non-linearities introduce a qualitatively new dependence[5] on φ, which can lower the value of α_2 by a factor of ~ 7 for large misalignment angles (see Fig. 1 in [317]). We consider the full non-linear expression $\alpha_2(\alpha,\varphi)$ as derived by [393], which reduces to Eq. (5.12) for $\varphi \ll 1$.

Lense-Thirring precession efficiently aligns the disc up to the Bardeen-Petterson radius R_{BP}, defined to be the disc location where the inverse of the Lense-Thirring precession

[5]The warp-propagation coefficient actually depends on the radial derivative of the local inclination of the disc ψ, see Eq. (1) in [320]. Here we implement the approximation $\psi \sim \varphi$ as already done by [317].

frequency [542]

$$\Omega_{LT}(r) = 2\frac{G^2M^2\chi}{c^3r^3} \tag{5.13}$$

equals the warp propagation time $t_{\nu_2}(r) = r^2/\nu_2$, i.e

$$R_{\rm BP} = 2^{2/3}\left(\frac{\chi}{\alpha_2}\right)^{2/3}\left(\frac{H}{r}\right)^{-4/3}\left(\frac{GM}{c^2}\right) . \tag{5.14}$$

For a single BH-disc system, R_{BP} coincides with the maximum warp location (*warp radius*) R_W and marks the boundary between the (quickly aligned) inner disc and the (still aligning) outer disc. The timescale over which the outer disc finally aligns the BH spin can be found by computing the torque acting on the disc at R_W [377]. A single BH of mass M and dimensionless spin χ aligns with the angular momentum of the surrounding accretion disc within [459, 377, 317]

$$t_{\rm al} \simeq 3.4\,\frac{M}{\dot{M}}\,\alpha\,\left(\frac{\chi}{\alpha_2}\frac{H}{r}\right)^{2/3} , \tag{5.15}$$

where $\dot{M}$ is the accretion rate of the circumprimary/circumsecondary disc and H/r its aspect ratio evaluated at the warp radius. We note here that the alignment time $t_{\rm al}$ is sensibly smaller than the growth time $M/\dot{M}$ for reasonable viscosities $\alpha \sim 0.1$ and aspect ratios $H/r \sim 0.001$. BH mass and spin magnitude can therefore be considered fixed during the alignment process ([277]; see Sec. 5.4).

The Bardeen-Petterson effect can drive the BH spin towards either alignment or antialignment with the outer disc. The system antialigns if [278]

$$\theta > \pi/2 \quad \text{and} \quad L(R_W) < 2S\,, \tag{5.16}$$

where θ is the angle between the BH spin and the angular momentum of the outer disc, $L(R_W)$ is the angular momentum of the inner disc (i.e. inside the warp radius) and S is the BH spin. The BH spin aligns with the outer disc if any of the two conditions above is not satisfied. Once θ is provided (cf. Sec. 5.3), the misalignment φ between the inner-disc angular momentum and the outer-disc angular momentum is given by $\varphi = \theta$ in the aligned case, while $\varphi = \pi - \theta$ if the system tends towards antialignment.

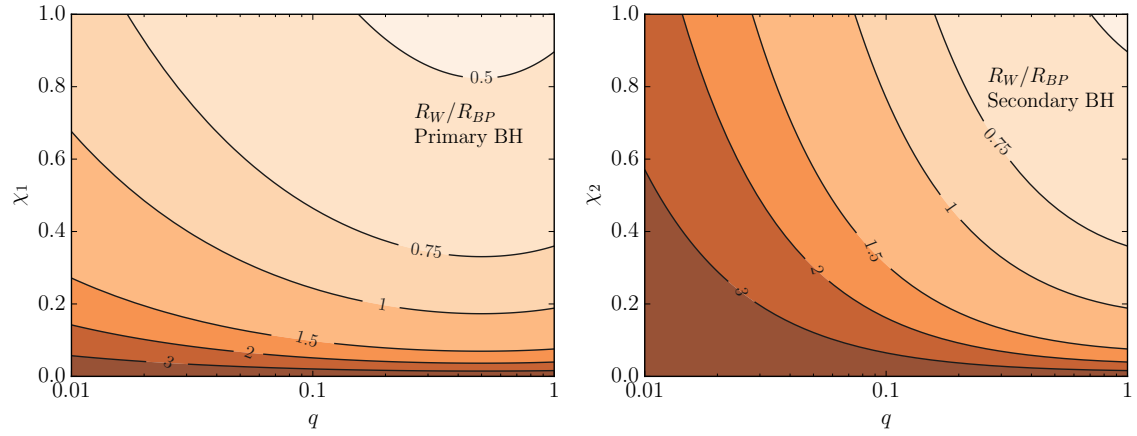

Figure 5.1: Effect of the companion on the location of the warp radius. Primary and secondary BHs are considered on the left-hand and right-hand panel respectively. Contours map the ratio between the maximum-warp location R_W (where the external torque from the companion matches the Lense-Thirring torque) and the Bardeen-Petterson radius R_{BP} (where the Lense-Thirring time equals the warp propagation time) derived for an isolated BH. The dependence on the binary mass ratio q and the spin of the aligning BH (either χ_1 or χ_2) is reported on the x and y axes. A companion BH is expected to speed up the alignment process up to a factor of ~ 2 in most of the parameter space, meaning a $\mathcal{O}(1)$ uncertainty in the estimate of the alignment time. This figures have been produced taking $M_{\rm bin} = 10^7 M_\odot$, $H/r = 0.001$, $f = 0.1$, $\alpha = 1/2\alpha_2 = 0.2$, $\beta = 1$ and $R = R_{\rm f}$ [see Eq. (5.19)].

5.2.4 Effect of the companion on disc-spin alignment

So far we have only considered the alignment of a single BH with its surrounding accretion disc. Here we discuss the effect of a far ($R \gg R_W$) companion on the alignment process. This effect –neglected in our previous study [317]– has been recently pointed out by Miller and Krolik [367] in the SMBH binary case, while [349] have previously considered the same interaction for stellar-mass BHs with stellar companions. For a further study, see [512].

If the aligning BH is part of a binary system, the gravitational potential felt by an orbiting gas ring is perturbed by the presence of the companion [336, 394]. The binary gravitational potential can be expanded in a series of r/R (where r is the distance of the gas ring from the BH and R is the binary separation; see e.g. [265]): to leading order, the resulting torque is perpendicular to the angular momentum of the gas ring $\mathbf{L}$, causing precession about the angular momentum of the binary $\mathbf{L}_{\rm bin}$. The precessional frequency can be obtained by averaging the torque over the binary orbital period and reads[6] [416]

$$\Omega_C(r) = \frac{3}{4}\frac{GM_{\rm c}}{R^3}\left(\frac{r^3}{GM}\right)^{1/2}\beta\,, \tag{5.17}$$

[6]We do not quote the sign of the precession frequency, because it only sets the precession direction about $\mathbf{L}_{\rm bin}$ which is not important for our order-of-magnitude estimate.

where $\beta = |\hat{\mathbf{L}}_{\rm bin}\cdot\hat{\mathbf{L}}|$, M is the mass of the aligning BH and $M_{\rm c}$ is the mass of the companion. Note that in our notation $M_{\rm c} = qM$ in the case of the primary BH, but $M_{\rm c} = M/q$ when the alignment of the secondary is considered.

If a spinning BH is part of a binary system, both Lense-Thirring and companion-induced precession are present. The companion drives the system towards alignment with the angular momentum of the binary, which tracks the plane of the circumbinary disc (see Sec. 5.4 on this point). At the same time, the inner disc is being aligned with the BH spin by Lense-Thirring precession. In practice, the companion reduces the frame-dragging efficiency: material could stay misaligned with the BH spin at closer locations, thus speeding the alignment process up [367]. This effect can be quantified by computing the locations at which the two contributions are equally important. The Lense-Thirring time Ω_{LT}^{-1} equals the warp propagation time t_{ν_2} at R_{BP}, as given by Eq. (5.14). On the other hand, the disc is now expected to be maximally warped at the warp radius R_W, where the Lense-Thirring contribution matches the companion one $\Omega_{LT} = \Omega_C$ [349]. From Eq. (5.13) and (5.17) one gets [349, 367]

$$R_W = \left(\frac{8\chi}{3\beta}\frac{M}{M_{\rm c}}\right)^{2/9} R^{2/3}\left(\frac{GM}{c^2}\right)^{1/3} . \tag{5.18}$$

If $R_W \gtrsim R_{BP}$, the companion term can be neglected and the closer location at which misaligned material can be found is still $\sim R_{BP}$. The alignment speed-up discussed in [367] is relevant if $R_W \lesssim R_{BP}$, because warped regions are present closer to the hole. At $R = R_{\rm f}$ (cf. Sec. 5.2.2), we find

$$\begin{aligned}\frac{R_W}{R_{BP}} \simeq 0.48\ \beta^{-2/9} a^{-4/9}\left[\frac{M+M_{\rm c}}{2\,M_{\rm c}^{1/3}M^{2/3}}\right]^{2/3}\left(\frac{M+M_{\rm c}}{10^7 M_\odot}\right)^{-52/81} \\ \times\left(\frac{H/r}{0.001}\right)^{4/3}\left(\frac{f}{0.1}\right)^{-16/81}\left(\frac{\alpha}{0.2}\right)^{-26/81}\left(\frac{\alpha_2}{1/2\alpha}\right)^{2/3} .\end{aligned} \tag{5.19}$$

Fig. 5.1 shows the dependences of R_W/R_{BP} on the binary mass ratio and the spin magnitude of the aligning BH, both for primaries and secondaries. Slowly rotating BHs are less affected by the presence of a companion because the spin set the magnitude of the frame-dragging term. For fixed total mass $M_{\rm bin} = M + M_{\rm c}$, primaries are more sensitive to the companion than secondaries, because their gravitational radius is larger and Lense-Thirring precession can be matched more easily by the additional precession term.

Here we use the simple expression reported in Eq. (5.15) to compute the spin-alignment time, as formally obtained for an isolated BH-disc system. Our analysis [Eq. (5.19) and

Fig. 5.1] shows that the position of the warp radius can be modified by a factor of ~ 2 if the BH is part of a binary system. The alignment time $t_{\rm al} \propto R_W^{11/10}$ [377, 367] can therefore only be lowered by a factor of ∼few. From Eq. (5.19), this assumption may not be valid if (i) the binary is very massive $M_{\rm bin} \gtrsim 10^7 M_\odot$, (ii) the individual discs are thinner than the circumbinary disc at the fragmentation radius $H/r \lesssim 0.001$, (iii) the binary accretion rate is close to the Eddington limit $f > 0.1$. A more complete understanding of the alignment process in BH binary systems requires explicit integrations of the angular momentum equation [349]. This goes beyond the scope of this work, which instead focuses on getting an estimate for the alignment timescale.

5.2.5 Cavity pile-up and differential accretion

The accretions rates of the individual discs $\dot{M}_1$ and $\dot{M}_2$ depend on the circumbinary-disc accretion rate $\dot{M}_{\rm bin}$, since the formers are fed by the latter. Here we develop a simple prescription to link these three quantities.

Accretion from the outermost regions of the circumbinary disc onto the binary BH is suppressed because of either the perturbation of the secondary (low-q regime) or the two-body central potential (high-q regime). Therefore, the binary may only accrete at a lower accretion rate $\dot{M}_1 + \dot{M}_2 \leq \dot{M}_{\rm bin}$. Mass tends to pile up at the outer edge of the cavity created by the binary itself: accretion –and therefore spin alignment– is still possible if gas streams can penetrate the cavity and reach the BHs. We call $\dot{M}_{\rm gap}$ the mass accretion rate that overcomes the cavity pile-up: this gas will sooner or later accrete onto either the primary or the secondary BH, i.e.

$$\dot{M}_{\rm gap} = \dot{M}_1 + \dot{M}_2 \ . \tag{5.20}$$

Gas-stream propagation is an intrinsically multi-dimensional non-linear phenomenon that requires dedicated hydrodynamical simulations to be studied in detail. In particular, the dynamics of gas accretion through the cavity is strongly dependent on the binary mass ratio q, since qualitatively different regimes are present. Equal-mass binary simulations were first performed in [342], while the $q = 1/2$ case has been presented in [234] and extended to $q = 1/3$ in [138, 448]. A recent major improvement has been made by D'Orazio et al. [161] and Farris et al. [183] who extensively studied the dependence on q of the mass rate overcoming the cavity pile-up.

D'Orazio et al. [161] present 2D hydrodynamical simulations in the range $0.003 \leq q \leq 1$ assuming fiducial values $\alpha = 0.01$ and $H/r = 0.1$. Accretion onto the binary is indeed limited to narrow gas streams and it is typically suppressed by a factor of 2-5 when

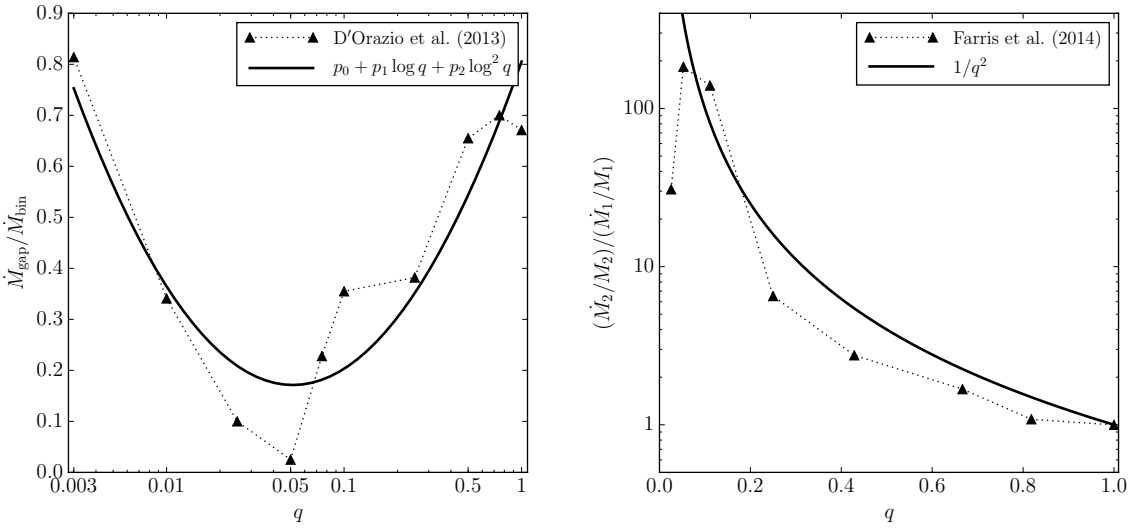

Figure 5.2: Numerical fits to hydrodynamical simulations to compute the accretion rates of the two members of a BH binary. Left-hand panel shows the fraction of the accretion rate $\dot{M}_{\rm gap}/\dot{M}_{\rm bin}$ that penetrates through the disc cavity and reaches one of the two binary members. A quadratic interpolation is performed to numerical results by [161] here reported in Eq. (5.21). On the right-hand panel, the binary accretion rates is broken down between the primary and the secondary BHs. The ratio of the accretion times in the systems simulated in [183] appears to be described by the simple prescription $(\dot{M}_2/M_2)/(\dot{M}_1/M_1) = 1/q^2$ in Eq. (5.22).

compared to a single-BH disc of the same mass. They detect the presence of two physical regimes:

1. For high mass ratios $0.05 \lesssim q \leq 1$, the presence of the binary strongly modulates the streams. Streams are generated by deviations from spherical symmetry in the binary potential: more asymmetry is present for equal mass binaries that therefore show less mass pile-up at the cavity edge and more binary accretion. In such a regime, the ratio $\dot{M}_{\rm gap}/\dot{M}_{\rm bin}$ is expected to increase with q.

2. In the low-mass ratio regime $q \lesssim 0.05$, the secondary BH quickly swipes through the disc accreting most of the material coming from large distances: a single gas stream is present feeding the secondary BH. This effect gets more pronounced when the mass ratio is lower and consequently the ratio $\dot{M}_{\rm gap}/\dot{M}_{\rm bin}$ decreases with q.

These results are shown in the left-hand panel of Fig. 5.2, were the "MidΔr-Lo$\Delta\phi$" simulations of [161] are considered. The minimum in $\dot{M}_{\rm gap}/\dot{M}_{\rm bin}$ separates the two physical regimes just described above. We interpolate the results of their simulations with the ansatz

$$\frac{\dot{M}_{\rm gap}}{\dot{M}_{\rm bin}} = p_0 + p_1 \log(q) + p_2 \log^2(q) \tag{5.21}$$

and best-fitting coefficients $p_0 = 0.8054$, $p_1 = 0.9840$ and $p_2 = 0.3818$. For a given circumbinary-disc accretion rate $\dot{M}_{\rm bin}$, Eq. (5.21) specifies the mass rate $\dot{M}_{\rm gap}$ which overcomes the cavity pile-up and accretes onto *either* the primary *or* the secondary BH. The subsequent study [183] found that the ratio between the total accretion rate onto either one of the two BHs and the accretion rate onto a single BH of the same total mass may exceed unity, thus casting doubts on whether such fraction can be interpreted as $\dot{M}_{\rm gap}/\dot{M}_{\rm bin}$. To bracket this uncertainty, we use Eq. (5.21) as our reference model but we also study an additional variation where we fix $\dot{M}_{\rm gap} = \dot{M}_{\rm bin}$ (cf. Sec. 5.3.1).

Farris et al. [183] performed 2D grid simulations (assuming $H/R = 0.1$ and $\alpha = 0.1$), specifically addressing the feeding of the individual discs from streams penetrating the cavity. They systematically find that the secondary BH accretes faster than the primary, mainly because the former orbits closer to the cavity edge. Their results are here reported in the right-hand panel of Fig. 5.2, where the ratio of the accretion times $\dot{M}_i/M_i$ $(i = 1, 2)$ is showed as a function of the binary mass ratio q. Symmetry implies $\dot{M}_1 \sim \dot{M}_2$ for binaries with high mass ratios, while lower values of q show pronounced differential accretion in favour of the secondary. A qualitatively different regime is detected for the lowest of their simulated cases $q = 0.025$: the cavity is not efficiently cleared by the secondary BH, and mass from the circumbinary disc directly flows inwards forming a large circumprimary disc. As pointed out in Sec. 5.2.1, such a change in the dynamics of the system is expected for lower mass ratios, where the disc should form a small annular gap rather than a large hollow cavity. To directly reach the circumprimary disc, gas should be able to flow past the secondary escaping its gravitational attraction. As already pointed out in [183], the actual turning point in q is likely to be highly dependent on the thickness of the disc and possibly on the viscosity. As shown recently [550] in the context of binary stars, direct flow from the circumbinary to the circumprimary disc is easier for thicker discs, where the stronger pressure forces can make part of the material "skirt" the Roche lobe of the secondary, eventually reaching the primary Roche lobe and being captured by its gravitational attraction. Due to such uncertainties, in this work we deliberately ignore the onset of such effects in the low-q regime when considering differential accretion. The growth-time ratio presented in [183] appear to be well approximated by (see Fig. 5.2, right panel)

$$\frac{\dot{M}_2/M_2}{\dot{M}_1/M_1} = \frac{1}{q^2} \,. \tag{5.22}$$

Due to such a pronounced differential accretion, the prescription presented here may formally predict super-Eddington rates for the secondary BHs in the low-q regime. This

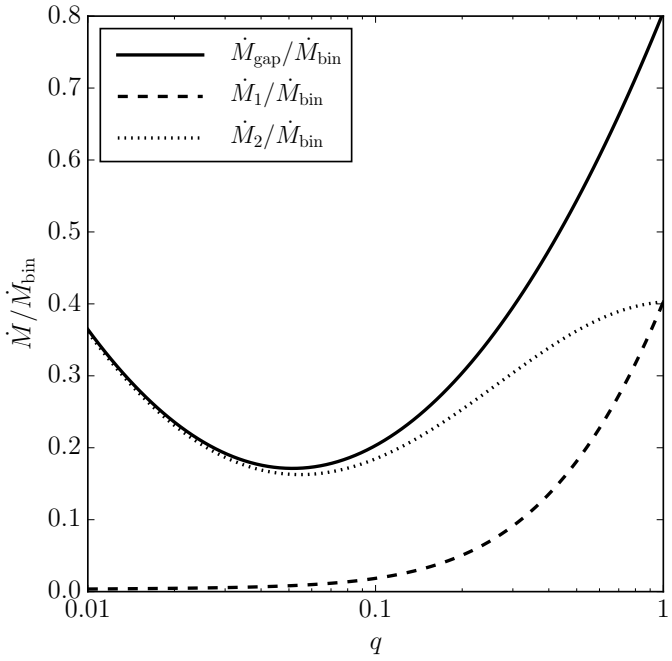

Figure 5.3: Combined effect of mass pile-up at the edge of the disc cavity and differential accretion in unequal-mass binaries. Prescriptions for the accretion rates presented in Eqs. (5.21-5.23) and Fig. (5.2) are summarized here. As a function of q, we show the following fractions of the accretion rate of the outer circumbinary disc $\dot{M}_{\rm bin}$: (i) $\dot{M}_{\rm gap}$ which overcomes the cavity-pile up and accretes onto the binary (solid); (ii) $\dot{M}_2$ which is captured by the secondary BH (dashed); (iii) $\dot{M}_1$ which finally accretes onto the primary BH (dotted).

has no relevant impact on our model: if we define the secondary Eddington ratio to be $f_2 = \epsilon t_{\rm Edd}\dot{M}_2/M_2 = (1+q)\dot{M}_2\epsilon f/q\dot{M}_{\rm bin}$, the Eddington limit $f_2 = 1$ is only marginally reached for very high circumbinary-disc accretion rates ($f \sim 1$) and low mass ratio $q \lesssim 0.05$ (assuming a typical accretion efficiency $\epsilon \sim 0.1$). Lower values of f shift the critical mass ratio at which the Eddington limit is formally reached to even lower values. Finally, we note that, as in Sec. 5.2.1, the thickness values explored by the simulations considered in this Section are significantly higher than those expected for massive-BH binaries (Sec. 5.2.2).

From Eq. (5.20) and (5.22) one gets

$$\dot{M}_1 = \frac{q}{1+q}\dot{M}_{\rm gap}\ , \qquad \dot{M}_2 = \frac{1}{1+q}\dot{M}_{\rm gap}\ . \tag{5.23}$$

Fig. (5.3) combines the results presented in Eq. (5.21) and Eq. (5.23). For equal-mass binaries, $\sim 80\%$ of the incoming mass may accrete onto the binary and it is equally distributed between the two binary members. Unequal-mass binaries present differential accretion and consequently the inequality $\dot{M}_1 < \dot{M}_2$ grows stronger as q is decreased. When q is increased from $q \sim 0.2$ to unity, gas streams start to flows towards the primary and $\dot{M}_2/\dot{M}_{\rm bin}$ consequently flattens. On the other hand, if q is decreased from $q \sim 0.05$ to 0.001, the secondary orbit gets closer to the inner edge of the cavity [161]: more mass can overcome the cavity pile-up and it is almost entirely accreted by the secondary.

Parameter	Fiducial model	Synthetic distributions
q	Free parameter	Power-law distributions
$M_{\rm bin}$	Not relevant	Not relevant
χ_1, χ_2	1	Either 1 (E) or 0.1 (C)
θ_1, θ_2	Extremize over	Random variables
R	$R_{\rm f}$ (fragmentation)	$R_{\rm f}$ (fragmentation)
H/r	0.001	0.001
α	0.2	0.2
f	Not relevant	Not relevant
$\dot{M}_1$, $\dot{M}_2$	Eqs. (5.21) and (5.23)	Eqs. (5.21) and (5.23)

Table 5.1: Choice of the binary and disc parameters in our timescale comparison for both the fiducial case (Sec. 5.3.1) and the cosmologically motivated distributions (Sec. 5.3.2).

5.3 Results: differential misalignment

In this Section we compare the spin-alignment time and the inspiral time. We first outline the regions of the parameter space where misalignments are foreseen (Sec. 5.3.1); secondly, we fold our model into synthetic SMBH binary populations (Sec. 5.3.2); and we finally present a preliminary study to address the impact of our findings on the occurrence of large post-merger kicks (Sec. 5.3.3).

5.3.1 Misaligned primary BHs

5.3.1.1 Fiducial values of the parameters

The circumbinary disc properties enter the inspiral time $t_{\rm in}$ while the primary/secondary alignment times $t_{\rm al}$ are set by individual-disc parameters. The ratio $t_{\rm al}/t_{\rm in}$ in general depends on the binary separation R, the three disc aspect ratios H/r, the gas viscosity α, the accretion rates of the circumbinary $\dot{M}_{\rm bin}$ and the individual discs $\dot{M}_{1,2}$, the BH masses M_1 and M_2 (or equivalently q and $M_{\rm bin}$), the orientation angles θ_1 and θ_2, and the BH spin magnitudes χ_1 and χ_2. We first specify a fiducial model by taking likely values of all these parameters and we later perform a small parameter study around this model. Table 5.1 summarizes the values we assume for the parameters, highlighting the differences with the next Section. We summarize our choices as follows.

- As detailed in Sec. 5.2.2, a rather conservative assumption can be made by evaluating the inspiral time at the fragmentation radius $R_{\rm f}$. This is determined by the largest separation where the inspiral can be driven by interaction with a gaseous environment and is typically believed to be the bottleneck of the whole binary evolution.

- In our fiducial model we fix the aspect ratios of all discs to $H/r = 0.001$. As reported

in Eq. (5.11) for the circumbinary disc, the aspect-ratio dependence on the other parameters (namely the viscosity, the accreting mass and the accretion rate) is not crucial to evaluate the inspiral timescale, and will be neglected here for simplicity. For the same reason, we assume the individual discs to share the same aspect ratio of the circumbinary disc (cf. the analogous assumption made in [367]).

- Unless specified otherwise, we fix $\alpha = 0.2$. A parametric study on the viscosity has been presented in [317] and the alignment process has been found to be overall quite independent of α. Negative azimuthal viscosities are formally predicted by the non-linear warp propagation theory for $\alpha \lesssim 0.1$ and large misalignments φ [393, 317]: the evolution of the disc in these cases is unclear and beyond the scope of this study (see [385, 384] for extensive discussions).

- As described in Sec. 5.2.5, the BH accretion rates $\dot{M}_1$ and $\dot{M}_2$ are related to the circumbinary disc accretion rate $\dot{M}_{\rm bin}$, conveniently expressed in terms of the dimensionless quantity f in Eq. (5.1). In our fiducial model we implement Eqs. (5.21) and (5.23). Once H/r is fixed, the alignment likelihood $t_{\rm al}/t_{\rm in}$ is independent of f because both times scale as $1/f$ [cf. Eqs. (5.7) and (5.15)]. This is a point of improvement over our previous estimate [317], where an effective dependence on f was introduced when decoupling the inspiral and the alignment processes. For concreteness, the overall scale of Fig. 5.4 below is computed assuming $f = 0.1$.

- Within our assumptions, both the inspiral and the alignment times are independent of the binary total mass $M_{\rm bin}$. This is compatible with [223] where $t_{\rm in}$ is evaluated at the fragmentation radius.

- The orientation angles θ_1 and θ_2 set the warp efficiency α_2 (Sec. 5.2.3) and their effect is the main point raised in [317]. In the following, we bracket such uncertainties extremizing $t_{\rm al}$ over all possible orientations.

- For simplicity, we consider maximally spinning BHs ($\chi_1 = \chi_2 = 1$) unless specified otherwise. The status of SMBH spin measurements has been recently reviewed by [439]: some highly spinning BHs are found, but the current statistic is too low to provide a complete picture of the spin magnitude distributions. The effect of the spin magnitude on the alignment likelihood can however be easily predicted, because the alignment time scales as $t_{\rm al} \propto \chi^{2/3}$, cf. Eq. (5.15).

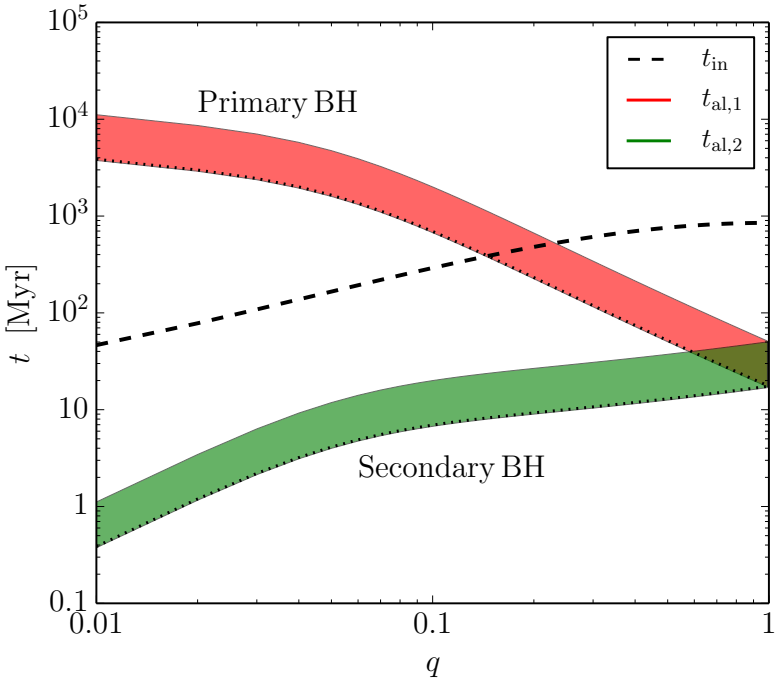

Figure 5.4: Comparison between the alignment times and the inspiral time as a function of the binary mass ratio q. Gas interactions have time to align the BH spins with the orbital angular momentum of the binary if the alignment time $t_{\rm al}$ (shaded areas) is smaller than the inspiral time $t_{\rm in}$ (dashed line). While secondary BHs (lower, green area) aligns for all mass ratios, this is not the case for the primary members (upper, red area) which retain their initial misalignments if q is low enough. Our fiducial model is assumed here: $H/r = 0.001$, $\alpha = 0.2$, $f = 0.1$, and maximally spinning BHs $\chi_1 = \chi_2 = 1$. Warp non-linear propagation theory introduces uncertainties (thus the shaded areas) of a factor of $\sim$ 2.5 in the alignment times. The corresponding times obtained with the linear theory are shown with dotted lines for comparison and always underestimate the non-linear result.

5.3.1.2 Predicted timescales

The key dependence of the spin-alignment problem in SMBH binaries is the one on the binary mass ratio q, which both controls the onset of different inspiral regimes and determines the importance of differential accretion. Fig. 5.4 shows the inspiral and the alignment times as functions of q for our fiducial set of parameters. The uncertainty in the initial misalignments θ_i causes the alignment times to appear as stripes in the figure, rather than lines. For comparison, we also show (dotted lines) the behaviour predicted by the linear warp-propagation of Eq. (5.12) where $t_{\rm al}$ is independent of θ_i. The linear theory underestimates the alignment time by up to a factor of ~ 2.5 [317]. Fig. 5.4 illustrates the main result of this analysis: while secondaries are found aligned ($t_{\rm al,2} \ll t_{\rm in}$) for every value of q, primary BHs only align if $q \gtrsim 0.2$. Light secondaries may prevent primaries from aligning. If such BHs were misaligned before the disc interactions, these misalignments are carried over to the next stages of the binary evolution. As explored in Sec. 5.3.3 this *differential*

Variation	Primary BH		Secondary BH	
Fiducial	[0.14 - 0.23]	(0.14)	[n-n]	(n)
$\alpha = 0.3$	[0.17 - 0.28]	(0.18)	[n-n]	(n)
$\alpha = 0.4$	[0.19 - 0.32]	(0.21)	[n-n]	(n)
$\alpha = 0.5$	[0.21 - 0.35]	(0.23)	[n-n]	(n)
$H/r = 10^{-4}$	[0.07 - 0.12]	(0.07)	[n-n]	(n)
$H/r = 10^{-2}$	[0.28 - 0.48]	(0.29)	[n-n]	(n)
$H/r = 10^{-1}$	[0.60 - 1]	(0.61)	[0.02 - n]	(n)
$\chi_i = 0.2$	[0.09 - 0.14]	(0.09)	[n-n]	(n)
$\chi_i = 0.5$	[0.12 - 0.19]	(0.12)	[n-n]	(n)
$\chi_i = 0.8$	[0.14 - 0.22]	(0.14)	[n-n]	(n)
$\dot{M}_{\rm bin} = \dot{M}_{\rm gap}$	[0.07 - 0.12]	(0.07)	[n-n]	(n)

Table 5.2: Binary mass ratios marking the transition between aligned and misaligned spins. For any variation from our fiducial model [$a_i = 1$, $\alpha = 0.2$, $H/r = 10^{-3}$, $\dot{M}_{\rm gap}$ given by Eq. (5.21)], we report values $\bar{q}$ such that BH spins in binaries with $q < \bar{q}$ are expected to be left misaligned (i.e. $t_{\rm al} > t_{\rm in}$) by gaseous interactions. Values in square brackets refer to the lower and upper limit of $\bar{q}$ due to the initial-misalignment uncertainty foreseen using non-linear warp propagation. Values in round brackets show the analogous result when the linear theory is considered, and notably underestimates the value of $\bar{q}$. Misaligned secondaries are typically not present (as indicated with "n") unless some of the parameters are cranked up to unrealistic values (as for example H/r in this table).

alignment between the two binary members will affect the subsequent GW-driven inspiral, the merger phase and the properties of the remnant BHs allowing for the possibilities of large kicks.

A short parametric study around our fiducial model is shown in Table 5.2, where we compute the values of q which mark the onset of the misaligned regime (i.e. where $t_{\rm al} = t_{\rm in}$). As expected [317], the alignment process is rather independent of α with thresholds varying from $q \sim 0.17$ to 0.35 if α is increased from 0.2 to 0.5. Notably, the alignment likelihood is also rather independent of the spin magnitudes χ_1 and χ_2, because of the mild scaling of $t_{\rm al}$ [cf. Eq. (5.15)]. Alignment times are longer for maximally spinning BHs $\chi_1 = \chi_2 = 1$ chosen for our fiducial model, but misaligned primaries are predicted for mass ratios $q \sim 0.15$ even when moderately spinning BHs are considered. Perhaps more surprisingly, the alignment process appear to be strongly dependent on the disc aspect ratio H/r which enters linearly in $t_{\rm in}$ and with a lower power in $t_{\rm al}$. Only primaries with $q > 0.6$ have enough time to align their spins in thicker discs with $H/r \sim 0.1$, even when maximally rotating BHs are considered. Moreover, if H/r is large enough, the inspiral time may become comparable to the secondary alignment time within the physical uncertainty due to initial spin orientation. As already pointed out (Sec. 5.2.1, se also Sec. 5.4 below), the disc thickness is one of the main uncertainties in the current modelling of binary-disc interactions. Details of the gas streams leaking through the disc cavity also have a notable

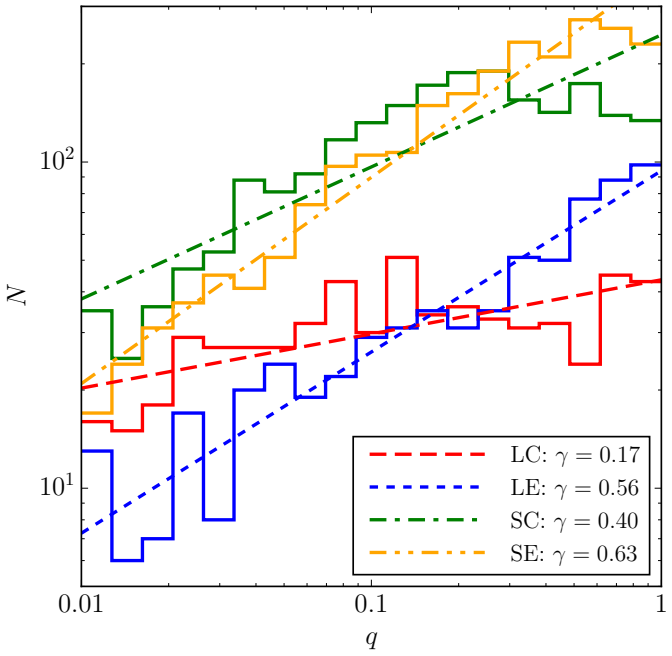

Figure 5.5: Mass ratio distributions in the synthetic SMBH binary populations developed by [37]. Four models are available, for different prescriptions of the accretion geometry (**E**fficient versus **C**haotic) and the BH seeds (**L**arge versus **S**mall). Data sets are binned within the range $q \in [0.01, 1]$ and fitted with power laws $N \propto q^{\gamma}$. The best-fitting spectral indices γ are reported in the legend for each model. The histogram normalization has been inherited from the original models and is irrelevant for our purposes.

effect: the largest value of q where misalignment is foreseen drops down to ~ 0.12 if all of the gas of the circumbinary disc ends up being accreted by either one of the two BHs (i.e. if $\dot{M}_{\rm bin} = \dot{M}_{\rm gap}$, cf. [183]).

5.3.2 Cosmologically-motivated distributions

Our findings are relevant if SMBH binaries with spins and mass ratios in the misaligned regime are present in nature and detectable. While electromagnetic observations already constrain almost a hundred SMBH masses [355] and a handful of BH spins [439], the measurements of the global properties of the SMBH binary population is the main goal of future space-based GW observatories. eLISA [469] will detect hundreds of binaries per year up to redshift $z \leq 10$ with sufficient signal-to-noise ratio $\mathcal{O}(10 - 100)$ to measure accurately both individual-source parameters and their statistical distribution [48].

Here we present a simplified analysis to address whether the misaligned-spin regime highlighted above is relevant in this context. Publicly available [530] synthetic distributions of merging BH binaries have been developed by the LISA collaboration in the context of the LISA Parameter Estimation Taskforce [37] and later updated in [475]. The authors developed four merger-tree models of BH evolution, varying over only two ingredients, considered to be the main sources of uncertainty.

1. *The mass of the BH seeds.* In the small seed scenario (**S**), BHs are initialized as remnants of Population III stars at $z \sim 20$ with mass $\sim 100 M_{\odot}$ and evolved according to the model of [533]. In the large seed scenario (**L**), BH with mass $10^5 M_{\odot}$ are formed

from gaseous protogalactic discs at $z \sim 15$ to ~ 10 as described by [61] (see also [318])

2. *The accretion geometry.* If accretion efficiently (**E**) occurs during a few long episodes, the BHs will generally be spun up during their cosmic evolution [504]. On the other hand, accretion may also happen to be chaotic (**C**), in the form of many short episodes [279]. In this case, lumps of material accreted in random directions on average spin the holes down.

This approach results in four models, referred to as SE, SC, LE and LC. Fig. 5.5 shows the extracted mass ratio distributions, together with power-law fits $N \propto q^{\gamma}$ in the range $q \in [0.01, 1]$. We obtain $\gamma = 0.17$ for LC, $\gamma = 0.56$ for LE, $\gamma = 0.40$ for SC and $\gamma = 0.63$ for SE. The spin-magnitude distributions of [37] are strongly peaked towards slowly spinning BHs for the C models and $a \sim 1$ for the E models. This is a direct consequence of their simplified accretion treatment, which is either completely coherent or completely chaotic; broader distributions are predicted for more realistic evolutionary models where this assumption is relaxed [47, 163, 474]. Spin orientations are not tracked during the cosmic evolution by [37]: spins are assumed to efficiently align in models E, while their directions are kept isotropic in models C.

Fig. 5.6 shows the cumulative fraction of aligned BHs using these four synthetic BH-binary populations[7]. We sample the mass ratio q over the fitted power-law distributions from Fig. 5.5; spin magnitudes are set to $\chi_1 = \chi_2 = 0.1$ in the C models and $\chi_1 = \chi_2 = 1$ in the E models, to mimick the strongly peaked distributions of [37]. For simplicity, we fix the disc properties to our fiducial values [$H/r = 0.001$, $\alpha = 0.2$, $\dot{M}_{\rm gap}$ given by Eq. (5.21)] and we sample over a uniform distribution in $\cos\theta_i$ to extract values of the alignment time within the initial-orientation uncertainty presented in Sec. 5.3.1. Fig. 5.6 shows, for each value of τ, the fraction of binaries P for which $t_{\rm al} < t_{\rm in}\tau$. Sections at $\tau = 1$ correspond to our current model: while all secondaries align during the inspiral, up to $\sim 8\%$ of the primaries may not have time to align their spins before merger. This statement appears to be rather independent of the population synthesis model chosen. In particular we find $P(t_{\rm al,1} < t_{\rm in}) = 0.93$ for LC, $P(t_{\rm al,1} < t_{\rm in}) = 0.96$ for SC, $P(t_{\rm al,1} < t_{\rm in}) = 0.92$ for LE and $P(t_{\rm al,1} < t_{\rm in}) = 0.93$ for SE. Here two main effects are combined: while the E models present higher spin magnitudes (hence longer alignment times) than the C models, they also predict a steeper profile in the mass ratio (Fig. 5.5), with fewer small-q binaries (hence, on average, shorter alignment times). The misaligned, rapidly rotating, primary

[7] We are aware of the inconsistency of our procedure: the binary mass ratio distributions used here are coupled to the spin orientations; at each merger tree level, the properties of the daughter BHs do depend on the spin orientations of their progenitors (cf. Sec. 4.2.1 and references therein).

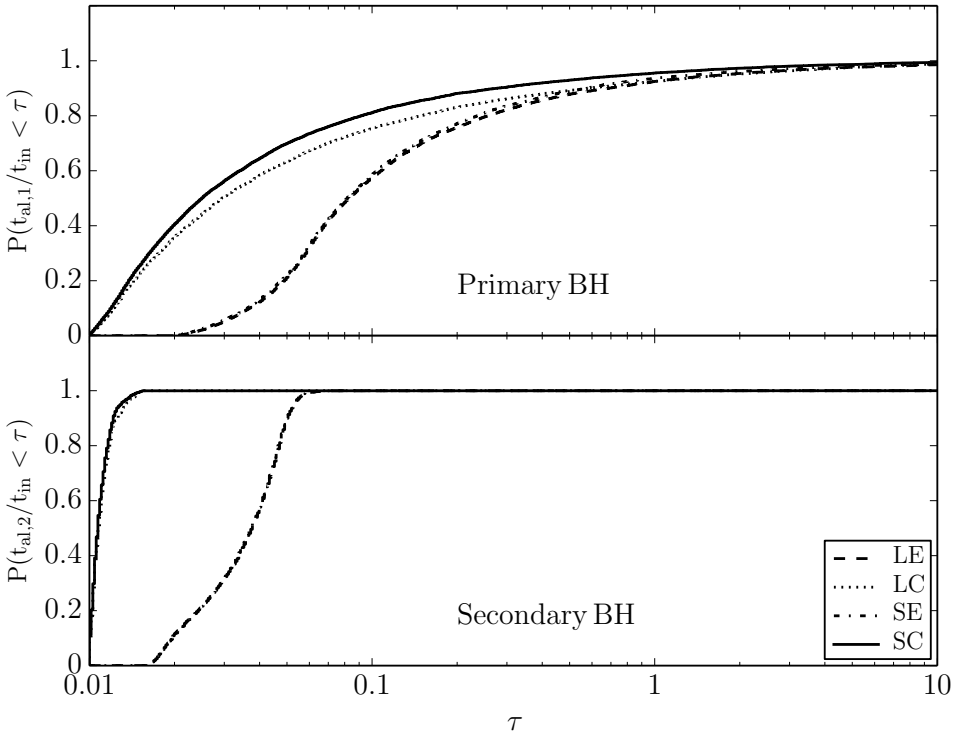

Figure 5.6: Fraction of BH spins in binary systems that align within a factor τ of the inspiral time $t_{\rm in}$, as predicted using the publicly available distributions by [37]. Alignment predictions using the model presented here can be read off at $\tau = 1$: all four distributions show that $\sim 8\%$ of BH primaries may fail to align during the gas-driven inspiral, while strong differential accretion quickly aligns all secondaries. Fractions P at larger and lower values of τ predict the alignment likelihood in case of systematic modelling errors on either the inspiral or the alignment time.

BHs predicted by the E models are ideal targets for strong-gravity precession effects in the late inspiral and merger (Chapters 2 and 3).

Fig. 5.6 also provides intuition on the consequences of systematic errors in our timescale estimates. If the inspiral (alignment) time is larger (smaller) by a factor $\tau = 10$, all binaries in the sample align by the end of the gas-driven inspiral. On the other hand, if the inspiral (alignment) process is 10 times faster (slower), i.e. $\tau = 0.1$, only 60%-80% of the primaries align.

5.3.3 Differential misalignment and kick velocity

The most notable consequence of our findings is a clear prediction for the spin-orientation angles at the onset of the GW-driven inspirals: a non-negligible fraction of SMBH binaries approaches the GW-driven phase with $\theta_1 \neq 0$ and $\theta_2 \simeq 0$.

If the binary lies in the same plane as the circumbinary disc ([255, 367], see Sec. 5.4), the angles θ_i may be taken as estimates of the misalignment between the BH spins and the

binary angular momentum $\mathbf{L}_{\rm bin}$, and used to estimate the properties of the post-merger BH. While final mass [51] and spin [53] do not critically depend on the spin misalignments, these are crucial to predict the final recoil [115, 215] (cf. our previous discussion in Sec. 4.2.1). The largest kick velocities (up to ~ 5000 Km s^{-1}) are attained for maximally spinning, equal-mass BH mergers with moderately large misalignments $\theta_i \sim 50^\circ$ [332, 333].

Here we perform a preliminary study to estimate the impact of our findings on the kick velocity distribution. To maximize the effect, we consider maximally spinning BHs in binaries with mass ratio $q = 0.2$, right at the onset of the misaligned regime highlighted in Sec. 5.3.1 (cf. Fig. 5.4). Numerical-relativity fitting formulae are available to compute kick velocities, but –as explored in details in Chapter 2– precession effects during the GW-driven inspiral must be taken into account, especially for configurations with sensibly different spin tilts $\theta_1 \neq \theta_2$ [463, 270, 271, 269, 76, 204, 206, 205]. GWs start driving the merger at the decoupling radius [35, 213, 371]

$$r_{\rm dec} \simeq 760 \frac{G M_{\rm bin}}{c^2} \left(\frac{\alpha}{0.2}\right)^{-2/5} \left(\frac{H/r}{0.001}\right)^{-4/5} \frac{(7.2\,q)^{2/5}}{(1+q)^{4/5}} \,, \tag{5.24}$$

where the angular momentum losses in GWs dominate over the viscous evolution of the disc. We first transfer the spin orientations from the initial separation $r_{\rm dec} = 760\, G M_{\rm bin}/c^2$ to $r_{\rm fin} = 10\, G M_{\rm bin}/c^2$ using precession-averaged binary transfer as presented in Sec. 2.3.3; and we finally apply the numerical-relativity fitting formula of Eq. (4.11) at $r_{\rm fin}$ [333]. We assume a random initial value of $\Delta\Phi$ at $r_{\rm dec}$ [c.f. Eq. (2.4)]. In order to disentangle the dependence of the kick velocity on the spin orientations, here we maximize over the orbital phase at merger Θ (thus only showing the maximum kick allowed in each configuration). The relevance of Θ on the results presented in this Section can be easily predicted because the kick velocity scales roughly as $v_k \propto \cos\Theta$, c.f. e.g. Eq. (2) in [115]. The kick velocity is independent of $M_{\rm bin}$.

Fig. 5.7 relates the spin orientation at the decoupling radius to the maximum kick velocities allowed in each configuration. Notably, higher kicks are found in the $\theta_1 \neq 0$, $\theta_2 \simeq 0$ region, which we predict to be populated by the Bardeen-Petterson effect ($\sim 8\%$ of the cases from the models used in Sec. 5.3.2). This behavior can be read in light of our innovative multi-timescale approach to BH spin precession (Chapter 2). Kicks are suppressed (enhanced) by spin-precession effects for binaries in the librating about $\Delta\Phi = 0$ ($\Delta\Phi = \pi$) family [271]. Configurations lying in the $\theta_1 \neq 0$, $\theta_2 \simeq 0$ region of the parameter space are likely to be attracted into the $\Delta\Phi = \pi$ family (Sec. 2.4.2): as binaries approach the merger phase, most of their spin-precession cycles are spent with the two spins forming an angle $\sim \pi$ when projected onto the orbital plane. These configurations are qualitatively

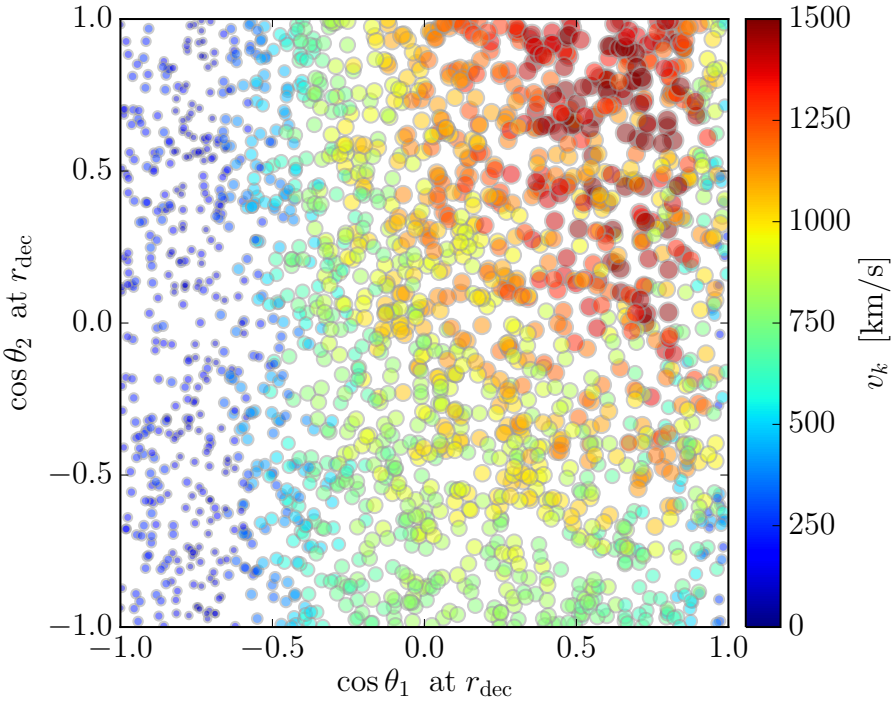

Figure 5.7: Maximum kick velocity $v_{\rm kick}$ (colour scale and marker size) as a function of the misalignment angles $\cos\theta_i = \mathbf{S_i}\cdot\mathbf{L}_{\rm bin}$, measured at the decoupling radius $r_{\rm dec}$ (x and y axes for primary and secondary BHs respectively). We consider maximally spinning BH binaries with $q = 0.2$, predicted to be at the onset of the misaligned regime unveiled by our astrophysical model. Large kicks are foreseen in the $\theta_1 \neq 0$, $\theta_2 \simeq 0$ region, predicted to be astrophysically relevant. Superkicks with $v_k \gtrsim 2000$ km/s are not likely in gas-rich environments because binaries with larger mass ratio are expected to align before mergers.

similar to the standard *superkick* configuration [115, 215] and notably lead to high kick velocities.

Our prediction is that, if merging, rapidly rotating BHs are present in gas-rich environments, kicks as large as $v_k \sim 1500$ km/s can happen. Such kicks can make the BH wander in the galaxy outskirts for times as long as $10 - 100$ Myr with displacements of $\sim 10^3$pc [219, 290, 489, 209], possibly at the level of observational consequences [287]. Larger values of v_k are only possible in merging binaries with mass ratio closer to the equal-mass case [551] (for more quantitative information see e.g. Fig. 3 in [333]). Both BHs in these binaries are predicted to be found aligned at merger $\theta_1 \sim \theta_2 \sim 0$ (Sec. 5.3.1), which limits the kick velocity to ~ 300 km/s. Our analysis shows that *superkicks* with $v_k \gtrsim 2000$ km/s are disfavoured in gas-rich environments where the Bardeen-Petterson effect comes into play.

5.4 Light secondaries prevent primaries from aligning

Alignment of BH spins in merging BH binaries may be differential. Using a semi-analytical model, we find that light secondaries may accrete almost all mass leaking through the binary gap and prevent primary BHs from alignment. In particular, such a differential alignment occurs for binaries with mass ratio $q \lesssim 0.2$. Gaseous interactions have enough time to align both spins in binaries with mass ratio closer to the equal-mass case (Sec. 5.3.1). We implement our analysis in terms of a timescale argument, comparing the time needed to align the BH spins via the Bardeen-Petterson effect $t_{\rm al}$ to the total time available in the gas-driven inspiral phase $t_{\rm in}$. The alignment and the inspiral processes are coupled by the accretion rates: while the binary migration is set by the circumbinary disc mass rate, alignment is powered by the mass accreting onto each BH. Mass from the circumbinary disc is expected to pile up at the outer edge of the cleared cavity, suppressing the alignment process. On top of this, mass leaking through the cavity is found to preferentially accrete onto the secondary BH which orbits closer to the disc edge. This causes the alignment time of the primary BH to be several orders of magnitudes longer than that of the secondary, and possibly even longer than the inspiral time. Differential accretion is a key feature, previously neglected, in tackling the spin-alignment problem: for comparison, Miller and Krolik [367] only quoted a factor of $\sim q^{-1/2}$ between the alignment times of the two BHs. While powerful for its simplicity, our timescale argument fails to capture the dynamics of the alignment process: more elaborate models involving numerical simulations are needed to predict the residual misalignment of primary BHs that cannot be aligned through the Bardeen-Petterson effect, and to estimate how close to complete alignment secondaries can be found in realistic environments.

We present preliminary results to address the relevance of our findings for the SMBH cosmic history. Using publicly available synthetic populations, we find that binaries in differential misalignment are expected in realistic cosmological scenarios (Sec. 5.3.2). A fraction of $\sim$ 8% of the BH primaries are found misaligned at merger even in models predicting large spin magnitudes, which allows for the possibility of large kick velocities. Merging BHs with spin angles $\theta_2 \sim 0$ and $\theta_1 \neq 0$ are subject to the largest kick velocities available for their mass ratio and spin magnitudes. In particular, misaligned primaries in BH binaries with $q \simeq 0.2$ may suffer kicks as large as $\sim$ 1500 km/s, while higher mass ratios are needed to obtain "proper" *superkicks* (Sec. 5.3.3). Binaries approaching the merger phase with differentially misaligned spins will exhibit pronounced precession effects in the later GW-driven inspiral phase [463, 269]. Orbital plane precession modulates the amplitude of the GW cycles, encoding information about the astrophysical environment

in the emitted GW pattern [208, 529, 514]. These features may in principle be used to constrain our models using future space-based GW observations, although more work is needed to quantify these statements.

Several assumptions have been made in developing our models, some of them worthy of future improvements. First and perhaps most importantly, our model estimates whether spin misalignments, *if present*, are carried over towards merger. The same dynamical processes that bring the binary together may play a role in determining the spin directions before Type II migration takes place. While star scattering is unlikely to affect the spin orientations because it does not present any preferred direction, this may not be the case for previous larger-scale gas interactions. DF inside a gaseous environment may be crucial to promote the binary formation: even if short (~ 10 Myr; [178, 162]), this phase presents interesting dynamics involving tidal shocks and nuclear cusp disruption [523] whose possible consequences on the spin directions still need to be explored. Secondly, our model only estimates whether the BH spins align to the angular momentum of the disc, while strong-gravity effects in the late inspiral and merger phase depend on the misalignments between the BH spins and the binary angular momentum. The further assumption of alignment between the binary orbital plane and the circumbinary disc [255] is necessary to estimate the properties of the post-merger BHs, in particular the kick velocity. Thirdly, we have neglected the BH mass growth during the alignment process. Differential accretion brings binaries towards larger mass ratios on timescales $\sim M/\dot{M}$. While this effect can be safely neglected on the timescale of the alignment process $t_{\rm al} \sim 10^{-3} M/\dot{M}$ [cf. Eq. (5.15)], it may not be negligible on the timescale of the inspiral. However, this point may only be important for aligned binaries which do not present large kick velocities anyway. As extensively discussed in Sec. 5.2.4, we also neglect the presence of the companion when estimating the alignment time (cf. [367]). However, Fig. 5.1 shows that this effect (a factor of ~ 2 in $t_{\rm al}$) mostly affects $q \sim 1$ binaries where both BHs aligns anyway. This point is worth further investigation, but sensible modelling efforts are likely to be required because the presence of two external torques (Lense-Thirring precession and the companion) cannot be fully captured within a timescale argument [349]. Finally, we have assumed that all values of q are allowed on cosmological grounds. Assuming the BH mass correlates with the galaxy mass, galaxy pairs with $q \lesssim 0.1$ may fail in forming close binaries because of strong tidal interactions before the galactic merger [500, 111, 523]. Mass stripped away from the secondary galaxy may sensibly increase the delay time between the galaxy and the BH mergers, possibly even preventing the BH binary formation.

We stress that the impact of the disc aspect ratio on the Bardeen-Petterson effect is

still not understood and can potentially be crucial. Both the migration process (Sec. 5.2.1) and gas streaming through the binary cavity (Sec. 5.2.5) have only been simulated with significantly thicker discs (typically $H/r \sim 0.01 - 0.1$) than those predicted for discs surrounding SMBHs ($H/r \sim 0.001$, see Sec. 5.2.2). In particular, a significantly lower amount of gas may be able to leak through the cavity in thinner discs, possibly slowing down the alignment process. Although we are aware of the computational constraints in simulating thin discs, we stress that such simulations are needed to validate the analytical expressions assumed here, and we point towards the importance of pushing these numerical efforts to lower values of the aspect ratio.[8]

Merging SMBH binaries are unique systems where gravity and astrophysics both play together to shape the dynamics. BH spin alignment (or misalignment) is an imprint of angular momentum transfer between the astrophysical and the relativistic side of BH binaries whose potential still needs to be fully uncovered.

[8]Since our findings presented in this Chapter were first presented [211], they had stimulated further studies in this direction: see [551, 435].

Chapter 6

Direct measurements of black-hole kicks

Outlook

Generic BH binaries radiate GWs anisotropically, imparting a recoil, or kick, velocity to the merger remnant. If a component of the kick along the line-of-sight is present, GWs emitted during the final orbits and merger will be gradually Doppler-shifted as the kick builds up. We develop a simple prescription to capture this effect in existing waveform models, showing that future GW experiments will be able to perform direct measurements, not only of the BH kick velocity, but also of its accumulation profile. In particular, the eLISA space mission will measure SMBH kick velocities as low as $\sim 500\ \mathrm{km\,s^{-1}}$, which are expected to be a common outcome of BH binary coalescence following galaxy mergers. BH kicks thus constitute a promising new observable in the growing field of GW astronomy.

Executive summary

This Chapter is organized as follows. In Sec. 6.1 we introduce our innovative approach to perform direct measurements of BH kicks. This is then further explored using back-of-the-envelope arguments (Sec. 6.2) and numerical models (Sec. 6.3). We draw our conclusions in Sec. 6.4.

The material presented in this Chapter is based on [207] and consists in a first analysis of the subject. A detailed follow-up study is currently underway [373].

6.1 Direct vs. indirect observations of recoiling BHs

With the first GW detection [13], merging BH binaries have entered the realm of observational astronomy. GW150914 constitutes not only the first direct detection of GWs, but also the first observation of a stellar-mass BH binary. The identification of SMBH binary candidates has (so far) only been possible through electromagnetic observations [465, 166]. The most promising candidates have been identified as double-core radio galaxies [446] and quasars with periodic behaviors [518, 218]. Upcoming GW observations will revolutionize the field of BH binary astrophysics: stellar-mass BH binaries will be targeted by a world-wide network of ground-based interferometers [23, 41, 430] while in space the recent success of the LISA pathfinder mission [32] has paved the way for eLISA [469] which will observe hundreds (if not thousands) of supermassive BH binaries out to cosmo- logical redshifts and open the era of multi-frequency GW astronomy [473].

In this Chapter, we present a preliminary analysis to show that the enormous potential of future GW observations is further enriched by the direct observability of BH kicks. BH binaries radiate GWs anisotropically which leads to a net emission of linear momentum and, by conservation of momentum, to a recoil of the final remnant. This effect has been studied extensively using PN and numerical techniques; see e.g. [122] and references therein. The key findings of these studies are that the merger of non-spinning BHs can only produce kicks of $\sim 170\,\mathrm{km\,s^{-1}}$ [216], but that recoil velocities as large as $\sim 5000\,\mathrm{km\,s^{-1}}$ are possible if rapidly rotating BHs with suitable spin orientations collide [215, 115, 332]. These exceptionally large recoils are commonly refered to as *superkicks* and their dynamics can be attributed to anti-parallel spin components in the orbital plane [276].

BH kicks have striking astrophysical consequences, especially for SMBHs. Superkicks of $\mathcal{O}(1000)\,\mathrm{km\,s^{-1}}$ easily exceed the escape velocity of even the most massive galaxies [362], and may thus eject BHs from their hosts [437]. Such ejections would affect the fraction of galaxies hosting central BHs (see Chapter 4 for BCGs and Chapter 5 for gas-

rich environments) and, consequently, the expected event rates for eLISA [470]. Even smaller recoil velocities $\lesssim 500\,\mathrm{km\,s^{-1}}$ affect the dynamics of galaxy cores by displacing the post-merger BHs for time scales as large as $\sim 10\,\mathrm{Myr}$ [219, 288]. BH kicks may lead to a variety of electromagnetic signatures [287] and observational strategies [433, 90] have recently been proposed for their detection. Candidates are present but their nature is debated (see [287, 294] and references therein) and, overall, BH kicks remain elusive.

If GW observations of a BH binary provide accurate measurements of the component masses and spins, it is in principle possible to use numerical relativity results (such as those reported in Sec 4.2.1) to infer the kick that the binary should have received around merger (this was not possibile for GW150914 because of the poor determination of the spin paramters [15]). Such an approach, however, would be of *indirect* nature and crucially relies on the validity of the assumptions in the numerical modeling process. For instance, it would *not* provide an additional consistency check of the predictions of GR. As argued here, it is possible instead to *directly* measure BH kicks from the GW signal alone. If the kick is directed towards (away from) the Earth, then the latter part of the waveform will be blue (red) shifted relative to the early part. Roughly speaking, different, Doppler-shifted mass parameters would be inferred from the inspiral and ringdown parts of the signal if analyzed separately. More precisely, by observing the differential Doppler-shift throughout the signal, one can directly measure the change in speed of the system's center of mass as a function of time.

6.2 Doppler mass shift

In the absence of a mass or length scale in vacuum GR, the GW frequency f enters the binary dynamics exclusively in the dimensionless form fM, where M is the total mass of the binary (in this Chapter we use natural units $G = c = 1$). This scale invariance implies a complete degeneracy between a frequency shift and a rescaling of the total mass of the system. For example, the cosmological redshift z of a BH binary merely enters in the predicted GW emission through a rescaling of the total mass by a factor $(1 + z)$ and, hence, GW observation of the binary only measures the combination $M(1 + z)$ [297]. BH kicks produce a similar effect: at linear order, the motion of the center of mass shifts the emitted GW frequency by a factor $1 + \mathbf{v_k} \cdot \hat{\mathbf{n}}$ whilst leaving the amplitude unaffected ($\mathbf{v_k}$ is the kick velocity with magnitude v_k and the unit vector $\hat{\mathbf{n}}$ denotes the direction of the line-of-sight from observer to source). There is, however, one crucial difference: while cosmological redshift homogeneously affects the entire signal, a frequency shift due to BH kicks gradually accumulates during the last orbits and merger. This point is illustrated

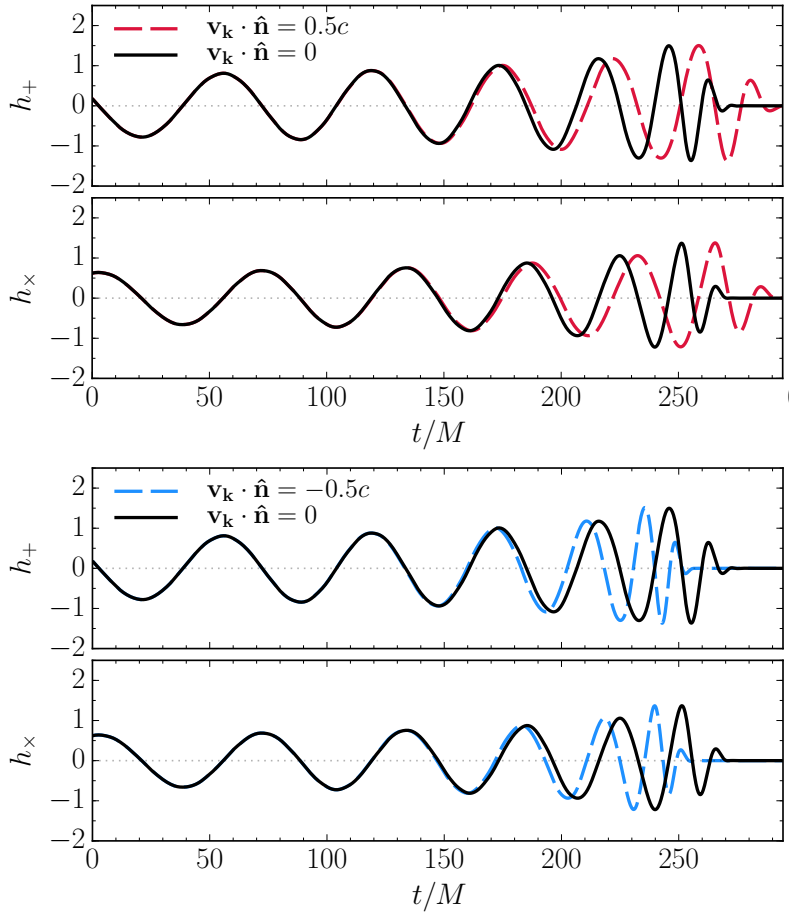

Figure 6.1: GW shift due to BH kicks (artificially exaggerated to demonstrate the key features). As the kick velocity builds up during the last few orbits and merger, the emitted GWs are progressively redshifted (top) or blueshifted (bottom), depending on the sign of the projection of the kick velocity $\mathbf{v_k}$ onto the line-of-sight $\hat{\mathbf{n}}$. This is equivalent to differentially rescaling the binary's total mass in the phase evolution from M to $M(1 + \mathbf{v_k}\cdot\hat{\mathbf{n}})$. These figures have been produced by artificially imparting kicks of $\mathbf{v_k}\cdot\hat{\mathbf{n}} = \pm 0.5c$ to non-spinning equal-mass binaries, assuming a Gaussian kick model with $\sigma = 60\,M$ [see Eqs. (6.5)-(6.6) with $\alpha_n = 0$ for $n \geq 1$].

in Fig. 6.1: as a kick is imparted to the merging BHs, the emitted GWs are progressively blue- or red-shifted. The frequency of the signal changes as if the mass of the system was varied from M in the early inspiral to $M(1 + \mathbf{v_k}\cdot\hat{\mathbf{n}})$ by the end of the ringdown.

The detectability of this effect can be estimated using the following back-of-the-envelope argument. Imagine breaking a BH binary waveform into two parts: inspiral and ringdown, $h(t) = h_i(t) + h_r(t)$. For simplicity, assume that the kick is imparted instantaneously at merger so that only h_r is affected. Let M_i and M_r respectively denote the total binary mass as measured from h_i and h_r alone. Neglecting the energy radiated in GWs[1], the effect of a kick is to Doppler-shift the final mass according to $M_r = M_i(1 + \mathbf{v_k}\cdot\hat{\mathbf{n}})$. The

[1]This effect is not negligible in magnitude, resulting in a reduction of the mass by ~ 5 %, but can be estimated accurately from the waveform and thus be accounted for.

inspiral part h_i of the GW signal generally contains a larger fraction of the Signal-to-Noise Ratio (SNR) than the ringdown part h_r, so the detectability of the kick will be limited by the measurement of M_r: kicks of magnitude v_k can be detected if M_r is measured with a fractional accuracy of $\lesssim v_k/c$ ($\sim 1\%$ for a superkick along the line of sight). The ringdown waveform can be modeled using the least damped quasi-normal mode for a Schwarzschild BH [75]

$$h_r(t) \simeq A \exp\left(-0.089 \frac{t}{M_r}\right) \sin\left(0.37 \frac{t}{M_r}\right) \tag{6.1}$$

which gives a squared SNR

$$\rho_r^2 = \frac{1}{S_n} \int_0^\infty h_r(t)^2 \, \mathrm{d}t \simeq \frac{2.66 M_r A^2}{S_n} \,, \tag{6.2}$$

assuming white noise in a detector with Power Spectral Density (PSD) $S_n(f) = S_n = \text{const}$. The error on the measurement of M_r can be estimated using the linear signal approximation, [187]

$$\left(\frac{1}{\Delta M_r}\right)^2 = \frac{1}{S_n} \int_0^\infty \left(\frac{\partial}{\partial M} h_r(t)\right)^2 \mathrm{d}t \simeq \frac{25.6 A^2}{M_r S_n} \,, \tag{6.3}$$

Therefore, the fractional error on M_r is given by

$$\frac{\Delta M_r}{M_r} \simeq \frac{0.322}{\rho_r} \,. \tag{6.4}$$

This back-of-the-envelope argument suggests that kicks along the line-of-sight with magnitude $v_k \sim 0.003c \simeq 900\,\mathrm{km\,s^{-1}}$ can be measured with GW observations if the SNR in the ringdown is $\rho_r \sim 100$. Direct detection of BH kicks will be very challenging, if not impossible, with current ground-based detectors. For instance, the rather loud event GW150914 has a ringdown SNR $\rho_r \sim 5$ [17], which would only allow us to measure unrealistically large kicks $v_k \sim 0.06c$. On the other hand, BH kicks are very promising observables for space-based detectors, where SNRs in the ringdown can reach $\rho_r \sim 10^3$ [196]. This will allow for measurements of SMBH kicks with magnitude as low as $v_k \sim 100\,\mathrm{km\,s^{-1}}$, which are expected to be ubiquitous [76, 335]. The detectability of the kick is governed by the ringdown part of the SNR ρ_r, which has also been found to be important to detect the GW memory effect (see [184] where kicks are also mentioned) and test the Kerr hypothesis via BH spectroscopy [75].

6.3 Kicked waveforms

In order to investigate the detectability of BH kicks more quantitatively, we need a waveform model that captures the cumulative frequency shift they introduce. Doppler shifts due to BH kicks can be straightforwardly incorporated into any pre-existing waveform model (which does not include the kick) by substituting $M \to M \times [1+v(t)]$ in the phase evolution, where $v(t)$ is the projection of the center-of-mass velocity due to the kick onto the line-of-sight. Here, we only consider the non-relativistic Doppler shift; relativistic corrections enter at the order $\mathcal{O}(v_k^2) \lesssim 10^{-4}$, well below the magnitude relevant for our analysis. The profile $v(t)$ is taken such that $v(t) \to 0$ as $t \to -\infty$ and $v(t) \to \mathbf{v_k} \cdot \hat{\mathbf{n}}$ as $t \to \infty$. A common observation in NR simulations is that the kick is imparted over a time $2\sigma \sim 20M$ centered on the merger, at a rate $\mathrm{d}v/\mathrm{d}t$ which is approximately of Gaussian shape [101, 330], possibly with some deceleration after merger (*antikick*) [291, 442]. In contrast to the kick speed, relatively little is known regarding the kick profile beyond these qualitative observations. We therefore adopt a flexible model for the kick profile. We expand $\mathrm{d}v/\mathrm{d}t$ according to

$$\frac{\mathrm{d}}{\mathrm{d}t}v(t) = \mathbf{v_k} \cdot \mathbf{n} \frac{\sum_n \alpha_n \phi_n(t)}{\int_{-\infty}^{\infty} \sum_n \alpha_n \phi_n(t)\, \mathrm{d}t}\,, \tag{6.5}$$

$$\phi_n(t) = \frac{1}{\sigma\sqrt{2^n n! \sqrt{\pi}}} \exp\left(-\frac{(t-t_c)^2}{2\sigma^2}\right) H_n\left(\frac{t-t_c}{\sigma}\right), \tag{6.6}$$

where H_n are the Hermite polynomials, t_c is the time of coalescence, σ controls the duration over which the kick is accumulated and the α_n weigh the various components. The functions $\phi_n(t)$ constitute a complete basis (they are actually the familiar solutions for the quantum harmonic oscillator) and so they can model all possible kick profiles. This basis is particularly appealing, because the first two terms $n = 0, 1$ model Gaussian acceleration profiles and antikicks, respectively. The case $\sigma = 0$ and $\alpha_n = 0$ for $n \geq 1$ corresponds to a kick instantaneously imparted at t_c, as assumed in the back-of-the-envelope argument presented above. We have tested this prescription against 200 numerical-relativity waveforms from the public SXS (Simulating eXtreme Spacetimes) catalogue [376], finding that the radiated-momentum profiles obtained from integrating the $l \leq 6$ modes of the Newman-Penrose scalar Ψ_4 are well approximated by the first two terms of the expansion of Eqs. (6.5-6.6). For systems with kicks above $500\,\mathrm{km\,s^{-1}}$, residuals in v_k are less than 17% in all cases, and typically less than 4% [373].

For a given waveform approximant, GW detector, and binary parameters, we generate two signals: a standard waveform $h_0(t)$ and a second 'kicked' waveform $h_k(t)$. The two

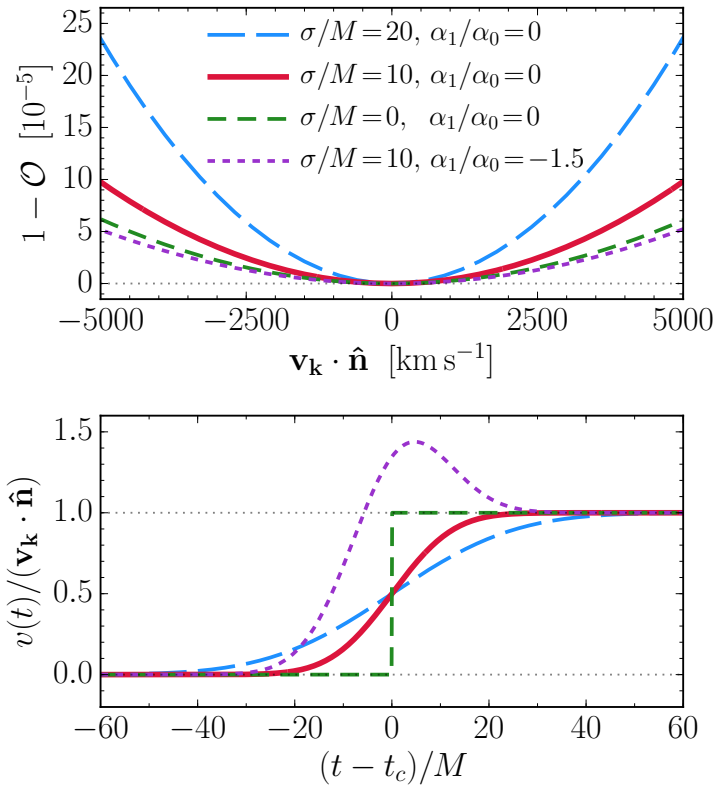

Figure 6.2: Mismatches introduced by BH recoils. The top panel shows the mismatch $1-\mathcal{O}$ between (i) a standard waveform of equal-mass non-spinning BH binaries of total mass M and (ii) a 'kicked' waveform which includes the Doppler-shifting effects of a velocity profile $v(t)$. Each line corresponds to a different kick profile $v(t)$, as shown in the bottom panel. All models shown here assume $\alpha_n = 0$ for $n \geq 2$. The $\sigma = 10M$, $\alpha_1/\alpha_0 = 0$ model (solid line) is used in Fig. 6.3.

waveforms can be compared by calculating their overlap

$$\mathcal{O} = \max_{t_c,\phi_c} \frac{(h_0|h_k)}{\sqrt{(h_0|h_0)(h_k|h_k)}}\,, \tag{6.7}$$

where $(h_0|h_k)$ is the noise-weighted inner product [374] and t_c (ϕ_c) is the time (phase) of coalescence. Approximately, two waveforms are distinguishable (and the kick detectable) if $\mathcal{O} \lesssim 1-\rho^{-2}$ [314], where $\rho = \sqrt{(h_0|h_0)}$ is the SNR (of the full waveform). This assumes the kick is not degenerate with other parameters, which is expected as the kick mostly affects the ringdown and not the entire signal.

This procedure is illustrated in Fig. 6.2 using a simple controlled experiment. We consider 6 inspiral cycles, merger and ringdown of an equal-mass non-spinning BH binary (a similar set-up to that used in Fig. 6.1). For simplicity, and to ensure that the results are not detector specific, the overlaps have been computed using a flat PSD. Artificially imposed recoils of $\sim 1000\ \mathrm{km\,s^{-1}}$ introduce mismatches $(1-\mathcal{O}) \sim 10^{-5}$. Kicks are more likely to be detected if they are imparted over a longer period of time (i.e. larger σ) because dephasing starts to occur earlier in the inspiral (this effect can be seen in Fig. 6.1 where a larger value of $\sigma = 60\,M$ was used). Note that the overlaps are approximately symmetric with respect to the transformation $\mathbf{v_k} \to -\mathbf{v_k}$, i.e. blueshifts and redshifts are equally detectable. This property can be shown to hold exactly at linear order in v_k [373].

We next explore more realistic scenarios by using numerical-relativity fitting formulae to predict the kick velocity. For this purpose, we generate two BH binary populations for the LIGO and eLISA detectors. LIGO (eLISA) sources were selected randomly from the following distributions: uniform total mass $M \in [10M_\odot, 100M_\odot]$ ($[10^5 M_\odot, 10^6 M_\odot]$) and mass ratio $q \in [0.05, 1]$; uniform dimensionless spin magnitudes $\chi_1,\ \chi_2 \in [0, 1]$; isotropic inclination and spin directions at a reference GW frequency $f_{\rm ref} = 20$ Hz (2 mHz); isotropic sky location; sources are distributed homogeneously in comoving volume with comoving distance $D_c \in [0.1\,{\rm Gpc}, 1\,{\rm Gpc}]$ ($[1\,{\rm Gpc}, 10\,{\rm Gpc}]$) assuming the Planck cosmology [24]. We use the LIGO 'Zero-Det-High-P' PSD of [488] with lower cutoffs $f_{\rm low} = 10$ Hz, and the two possible eLISA PSDs 'N2A5L6' and 'N2A1L4' of [282] with $f_{\rm low} = 0.3$ mHz (the former being more optimistic; for simplicity we neglect the spacecraft orbital motion which can be separately accounted for). For each binary, we estimate the kick velocity using the fitting formula summarized in Sec. 4.2.1. In order to return accurate estimates, the kick formula requires as input the BH spin parameters at separations $r \sim 10M$, comparable to the initial separations of the numerical-relativity simulations used in the formula's calibration. Otherwise, resonant effects [463] are not adequately accounted for and lead to erroneous kick magnitudes [271]. We bridge the separation range between $f_{\rm ref}$ and $r = 10\ M$ using orbit-averaged PN evolutions, as described in Chapter 2. The numerical-relativity fitting formula then provides expressions for the kick components parallel and orthogonal to the binary orbital angular momentum $\mathbf{L}$: $v_\parallel$ and $v_\perp$ [c.f. Eqs.(4.12-4.14)]. The projection of the kick velocity along the line-of-sight is given by

$$\mathbf{v_k} \cdot \hat{\mathbf{n}} = v_\parallel \cos\Theta \cos\iota - v_\perp \cos\Theta' \sin\iota\,, \tag{6.8}$$

where $\cos\iota = \hat{\mathbf{L}} \cdot \hat{\mathbf{n}}$ is the cosine of the inclination at $r = 10M$, Θ is related to the direction of the orbital-plane components of the spins at merger [101, 331], and Θ' sets the direction of the orbital-plane component of the kick [373]. In practice, both Θ and Θ' depend on the initial separation of the binary in the numerical-relativity simulations. While the Θ dependence has been studied extensively in the literature [101, 331], the impact of Θ' and its relation with Θ have, to our knowledge, not yet been explored. In the following, both angles are drawn uniformly in $[0, \pi]$. For each system, we generate two waveforms, h_0 and h_k, using the inspiral-merger-ringdown approximant 'IMRPhenomPv2' of [224, 274, 253] which accounts for spin precession. We have verified our results for the overlaps are insensitive to the choice of the waveform approximant, even when non-precessing models are used. In the following, we assume a "Gaussian" kick model, described by $\alpha_n = 0$ for $n \geq 1$ and $\sigma = 10M$ (solid curve in Fig. 6.2); cf. [101].

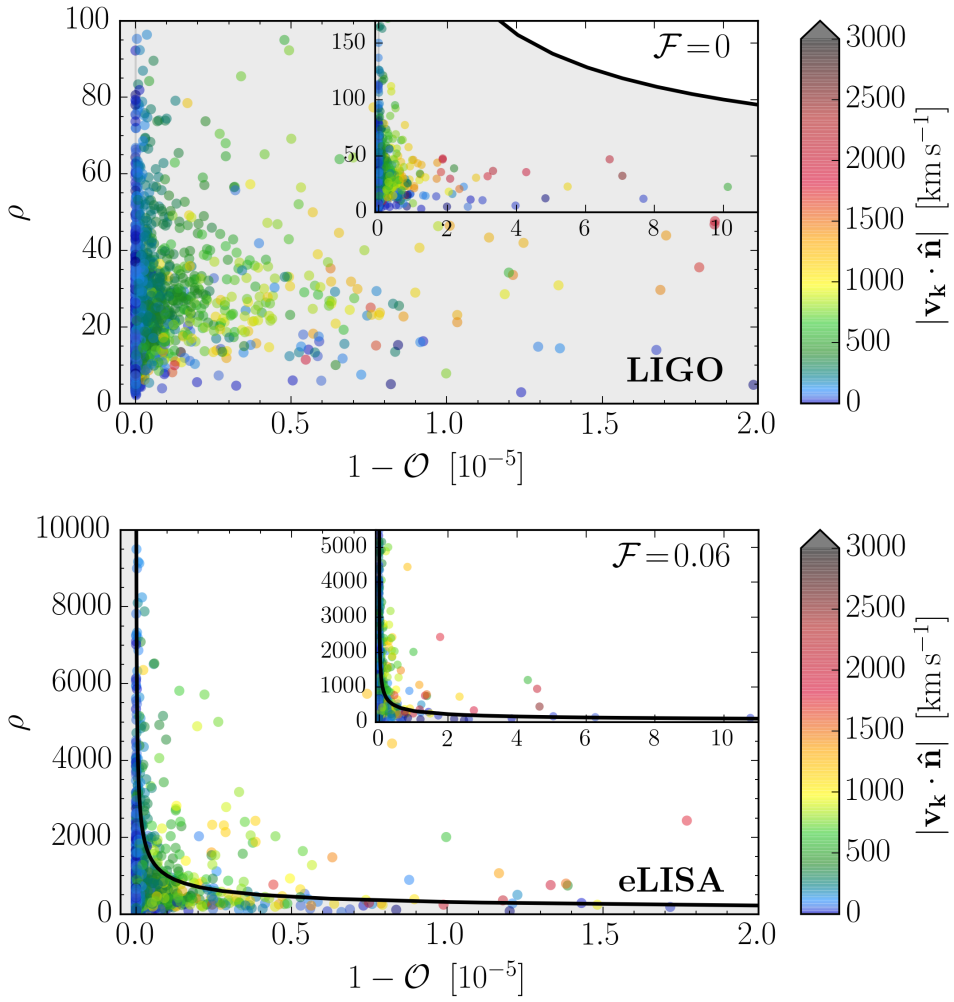

Figure 6.3: Detectability of BH kicks with LIGO (top) and eLISA (bottom). For each simulated source we compute the overlap $\mathcal{O}$ between standard and 'kicked' waveforms, and compare it with the SNR ρ. Kick velocities –here encoded in the color bar– are imparted using numerical-relativity fitting formulae. BH kicks are detectable for the fraction $\mathcal{F}$ of the sources above the black line, $\mathcal{O} < 1-\rho^{-2}$. eLISA results have here been generated with the 'N2A5L6' PSD of [282].

Our results are summarized in Fig. 6.3. As suggested by our previous argument, none of the LIGO sources have mismatches high enough to detect the kick. The eLISA case is different: $\sim 1\%$ to 6% (depending on the PSD) of the simulated sources have $\mathcal{O} < 1-\rho^{-2}$ and therefore present detectable BH kicks. Kicks with a projected magnitude $\mathbf{v_k}\cdot\hat{\mathbf{n}} \gtrsim 500$ km s^{-1} at $\rho \gtrsim 1000$ will be generically observable, but even some of the lower kicks with $\mathbf{v_k}\cdot\hat{\mathbf{n}} \sim 100$ km s^{-1} may be accessible. In the fortunate case of a *superkick* directed along the line-of-sight ($|\mathbf{v_k}\cdot\hat{\mathbf{n}}| \sim 3000$ km s^{-1}), the effect may be so prominent to be distinguishable at SNRs as low as $\rho \sim 50$. As eLISA is expected to measure up to $\mathcal{O}(100)$ BH binaries per year [469, 282], our study suggests that ~ 6 yr^{-1} (~ 30 in total for a 5-yr mission lifetime) sources may present detectable kicks. Although more realistic astrophysical modeling is needed to better quantify this fraction, our simple study shows that direct detection of

BH recoils is well within the reach of eLISA. Third-generation ground-based detectors will also present promising opportunities: repeating the calculations of the LIGO population of binaries but observed with ET (assuming the 'ET-D-sum' PSD of [240], with $f_{\rm low} = 1$ Hz) we find $\sim 5\%$ of binaries possess detectable kicks.

GW observations not only have the potential to measure the magnitude of the BH kick, but also the details of how the velocity accumulates with time. By expanding $v(t)$ according to Eqs. (6.5-6.6), one can take the kick model parameters $\mathbf{v_k}\cdot\hat{\mathbf{n}}$, σ and α_n to be free parameters of the waveform model, and treat them on an equal footing with masses, spins, inclination angles, etc. Consider, for example, a *golden system* at $\rho = 10^4$ with component masses of $1.3\times10^6\,M_\odot$ (chosen to maximize the mismatch caused by the kick), misaligned extremal spins and inclination such that $\mathbf{v_k}\cdot\hat{\mathbf{n}} \sim 5000\,{\rm km\,s^{-1}}$ km. A Fisher matrix calculation of the intrinsic parameters of this binary suggests that eLISA will be capable of measuring the kick velocity with precision $\Delta v_k \sim 200\,{\rm km\,s^{-1}}$, the kick duration with precision $\Delta\sigma \sim 1\,M$ and the presence of an antikick at the level of $\Delta(\alpha_1/\alpha_0) \sim 0.1$ (considering a two-component kick model, i.e. $\alpha_n = 0$ for $n \geq 2$) [373]. This Fisher matrix analysis revealed no strong degeneracies between the kick and other parameters, thus further justifying our previous use of the overlap as a detectability criterion for the kick. Finally, note that *superkicks* have $v_\parallel \gg v_\perp$ so that face-on or face-off binaries $|\hat{\mathbf{L}}\cdot\hat{\mathbf{n}}| \sim 1$ generate the largest velocity components along the line of sight and, hence, are most favorable for a direct kick measurement.

6.4 Evidence for the linear momentum carried by GWs

BH kicks leave a clear imprint on the GW waveform emitted during the late stages of the inspiral, merger and ringdown of BH binaries. eLISA and, likely, third-generation ground-based detectors will be able to *directly* detect the presence of a kick from the distortion of the waveform for a significant fraction of the binaries observed. By comparing the directly measured kicks (both magnitude and profile) to the kick predictions from numerical relativity for a binary with measured masses and spins, it will be possible to verify whether linear momentum is radiated as predicted by GR. Much like the Hulse-Taylor pulsar provided the first evidence that GWs carry away energy in accordance with the expectation of GR [250, 502], and GW150914 provided the first direct evidence of the GWs themselves [13], a direct measurement of a BH kick will provide the first direct evidence for the linear momentum carried by GWs.

Chapter 7

Stellar collapse in scalar-tensor theories of gravity

Outlook

We present numerical-relativity simulations of spherically symmetric core collapse and compact-object formation in ST theories of gravity. The additional scalar degree of freedom introduces a propagating monopole GW mode. Detection of monopole scalar waves with current and future GW experiments may constitute smoking gun evidence for strong-field modifications of GR. We collapse both polytropic and more realistic pre-SN profiles using a high-resolution shock-capturing scheme and an approximate prescription for the nuclear Equation of State (EOS). The most promising sources of scalar radiation are protoneutron stars collapsing to BH. In case of a Galactic core collapse event forming a BH, Advanced LIGO may be able to place independent constraints on the parameters of the theory at a level comparable to current Solar-System and binary-pulsar measurements. In the region of the parameter space admitting spontaneously scalarised stars, transition to configurations with prominent scalar hair before BH formation further enhances the emitted signal. Although a more realistic treatment of the microphysics is necessary to fully investigate the occurrence of spontaneous scalarisation of NS remnants, we speculate that formation of such objects could constrain the parameters of the theory beyond the current bounds obtained with Solar-System and binary-pulsar experiments.

Executive summary

This Chapter is organised as follows. In Sec. 7.1 we introduce our analysis and review previous works on the topic. The action and the evolution equations of the theory are presented in Sec. 7.2. Additional physical ingredients entering our simulations are given in Sec. 7.3. Our numerical procedure is described in Sec. 7.4. We present our results on core collapse dynamics and monopole GW emission in Sec. 7.5. We summarise our findings in Sec. 7.6.

The material presented in this Chapter is based on [210].

7.1 Compact-object formation to test GR

GR is currently assumed to be the standard theory of gravity, and has so far passed all experimental tests with flying colours [71, 17, 544, 428]. Theoretical and observational evidence, however, suggests that some modifications of GR may be inevitable. Cosmological and astrophysical observations require most of the energy content of the Universe to be present in the form of dark energy and dark matter [78, 136, 495]. On theoretical grounds, GR is expected to represent the low-energy limit of a more fundamental (quantum) theory [108]. Presently considered candidates for such theories predict modifications of GR at higher energies which also provide means to circumvent the formation of mathematical singularities inevitable in GR [233].

Attempts to generalise GR in these directions often involve additional fields that mediate the gravitational interaction together with the spacetime metric. The simplest class of such models is that of ST theories, where one scalar field is included in the gravitational sector of the action. Ever since the pioneering work of Jordan, Fierz, Brans, and Dicke [263, 186, 98], ST theories have received a great deal of attention, both from a theoretical and a phenomenological point of view (see e.g. [143, 128, 193, 494, 181] and references therein). This class of theories is *simple enough* to allow for detailed predictions to be worked out, but also *complicated enough* to introduce a richer phenomenology leading to potentially observable deviations from GR. ST theories make predictions in the largely untested strong-field regime, while remaining compatible with the weak-field constraints imposed on GR by Solar System experiments (cf. Sec. 7.3.2 below).

BH spacetimes might at first glance appear to represent an ideal testing ground for strong-field effects. The classical uniqueness theorems, first proven for Brans-Dicke theory [232, 507, 124] and later extended to a wider range of ST theories (see [62, 237] for reviews), however, strongly constrain the potential for deviations of BH spacetimes in ST

theory from their GR counterparts. At leading PN order, for example, the dynamics of a BH binary in Brans-Dicke theory is indistinguishable from the GR case [545]. Indeed, considering the ST field equations given below as Eqs. (7.5)-(7.8), one immediately sees that vacuum solutions of GR are also solutions to the ST equations with a constant scalar field. Non-trivial BH dynamics can still be obtained by relaxing some of the fundamental ingredients of the no-hair theorems as for example a non-vanishing potential term [235] or non-asymptotic flatness [73]. Due to the additional coupling introduced by the energy momentum tensor in the ST equations, however, compact matter sources such as NSs and collapsing protoneutron stars forming BHs appear to be more promising objects for exploring observational signatures of ST theories.

Guided by this expectation, we shall focus on the formation of compact objects through gravitational collapse. Gravitational collapse is the expected evolutionary endpoint of stars of Zero-Age Main Sequence (ZAMS) mass of $10M_\odot \lesssim M \lesssim 130M_\odot$ [391, 133, 498]. After exhausting their available fuel, the star's central core (mostly made of iron group nuclei) collapses under the strength of gravity as it exceeds its effective Chandrasekhar mass [81]. Collapse proceeds until mass densities become comparable to those of nuclear matter. Thereafter, the increasingly repulsive character of the nuclear interactions leads to core bounce, which results in an outgoing hydrodynamic shock. The outgoing shock soon stalls because of dissociation of nuclei and neutrino emission in the post-shock region, and must be revived to successfully drive a SN explosion [81]. The physical mechanism responsible for the shock revival is still a topic of active research (see e.g. [258] and references therein). Multi-dimensional fluid instabilities and neutrino interactions are generally believed to play a crucial role in driving most SN explosions with the possible exception of hyper-energetic ones [110, 516]. One single core-collapse SN provides photon luminosities comparable to those of an entire galaxy and outshines all stars in the Universe in neutrinos. If the explosion is successful, a NS is left behind. If the explosion fails or is very weak, continued accretion will push the central NS over its maximum mass of $2-3\,M_\odot$ and lead to the formation of a BH. The details of BH formation depend on the structure of the progenitor star and on the nuclear EOS [391].

ST theories may play a crucial role in this picture of NS and BH formation. A peculiar non-linear effect called "spontaneous scalarisation" [144, 145] – somewhat similar to spontaneous magnetisation in ferromagnets – represents a particularly strong form of non-trivial scalar-field dynamics leading to additional branches of stationary NS families (see also [52, 404, 486] for dynamical scalarisation in binary NS systems). Moreover, ST theories provide a new channel for emission of GWs in stellar collapse. Whereas in GR

conservation of mass and momentum exclude monopole and dipole radiation, monopole waves are permitted in ST theories in the form of scalar radiation, the so-called *breathing mode*. Detection of this breathing mode generated by a galactic SN would constitute smoking-gun evidence for a deviation from GR in the strong-field regime. Such tests of GR represent a major scientific goal [17] of the new era of GW astronomy initiated with the recent breakthrough detection of GW150914 [13], and thus add to the enormous scientific potential of exploring the physics of stellar collapse with GWs (see Ref. [402] for a comprehensive review on the topic).

The impact of ST theories on the equilibrium structure of NSs has been extensively studied in the literature (see, e.g., [144, 160, 359, 490, 247, 405]). Surprisingly few studies, however, have been devoted to their formation processes. Following pioneering numerical relativity simulations in Brans-Dicke theory [351], early studies have been devoted to dust-fluid collapse [457, 458, 485, 227]. The collapse of NSs into BHs [387] and the transition between different static NS branches [386] was first addressed by Novak using pseudo-spectral methods. To the best of our knowledge, the only published simulations of NS formation in ST theories have been presented by Novak and Ibáñez in [388], who combined pseudo-spectral techniques and high-resolution shock-capturing to study core collapse. The only other study we are aware of is [155], which numerically models the collapse of spherically symmetric fluids with a Γ-law EOS in Brans-Dicke theory and finds the monopole radiation to dominate at frequencies near the GW detectors' maximum sensitivity regime $f \sim 100$ Hz, independently of the Brans-Dicke coupling parameter. The systematic exploration of GW emission from core collapse in ST theories thus represents a largely uncharted area in SN research. The dawning age of observational GW physics makes the filling of this gap a timely task.

For this purpose, we have extended the open-source code GR1D of O'Connor and Ott [390] to ST theory and performed numerical simulations of NS and BH formation following core collapse to address the detectability of the monopole GWs with Advanced LIGO [3, 10] and the proposed ET [429]. We tackle the following questions.

- Are non-trivial scalar-field profiles and correspondingly large amplitudes in the scalar radiation naturally triggered in compact remnants following stellar collapse?

- Can future GW observations of core collapse provide smoking gun evidence for deviations from GR in the framework of ST theories?

Throughout this Chapter, we generally use geometrical units $c = G = 1$, but occasionally restore factors of G for clarity of presentation.

7.2 Evolution equations

In this Section, we first review different ways to formulate ST theories and then arrive at the equations for the metric, scalar field, and matter sector in general covariant form (Sec. 7.2.1). Next, we derive the hydrodynamic equations for the matter sources, the metric and scalar field for the specific case of radial-gauge, polar-slicing coordinates (Sec. 7.2.2).

7.2.1 A tale of two formulations

In ST theories, gravity is mediated by the spacetime metric $g_{\mu\nu}$ and an additional scalar field ϕ. The most general action which (i) involves a single scalar field coupled non-minimally to the metric, (ii) is invariant under space-time diffeomorphisms, (iii) is at most quadratic in derivatives of the field, and (iv) satisfies the weak equivalence principle can be written in the form [143, 71, 451]

$$S = \int dx^4 \sqrt{-g} \left[\frac{F(\phi)}{16\pi G} R - \frac{1}{2} g^{\mu\nu} (\partial_\mu \phi)(\partial_\nu \phi) - V(\phi) \right] + S_m(\psi_m, g_{\mu\nu}) \,. \tag{7.1}$$

Here, d^4x is the standard coordinate volume element, R is the Ricci scalar built from $g_{\mu\nu}$, $g = \det g_{\mu\nu}$ and the symbol ψ_m collectively denotes all non-gravitational fields. The theory has only two free functions of the scalar field: the potential $V = V(\phi)$ and the coupling function $F = F(\phi)$[1]. If the potential V is a slowly varying function of ϕ – as expected on cosmological grounds, see [142] – it causes negligible effects on the propagation of ϕ on stellar scales. For simplicity, we thus set $V = 0$; GR is then recovered for $F = 1$. Details on the choice of the coupling function F are postponed to Sec. 7.3.2.

The weak equivalence principle – which has been verified experimentally to very high precision [544] – is guaranteed to hold as long as the matter part of the action S_m does not couple to the scalar field, and its motion is therefore governed by the geodesics of the metric $g_{\mu\nu}$. In this formulation, the scalar field does not interact with ordinary matter directly, but influences the motion of particles exclusively through its coupling with the spacetime metric.

The theory described by the action (7.1) is said to be formulated in the *Jordan frame* [263]. Probably the most famous case of a ST theory, though by now severely constrained by solar-system tests [79], is Brans-Dicke theory [98]: the specific theory obtained by setting $F(\phi) = 2\pi\phi^2/\omega_{\rm BD}$ where $\omega_{\rm BD}$ is constant [451].

Alternatively to the above Jordan-frame description, ST theories can also be formulated

[1] Another common notation for the coupling function is $A = F^{-1/2}$ (see, e.g., [143, 144, 145]) .

in the so-called *Einstein frame*. Here, one considers the conformal transformation

$$\bar{g}_{\mu\nu} = F g_{\mu\nu}\,, \tag{7.2}$$

and the action of Eq. (7.1) becomes

$$S = \frac{1}{16\pi G}\int dx^4\sqrt{-\bar{g}}\left[\bar{R} - 2\bar{g}^{\mu\nu}(\partial_\mu\varphi)(\partial_\nu\varphi)\right] + S_m[\psi_m, \bar{g}_{\mu\nu}/F]\,. \tag{7.3}$$

The Ricci scalar $\bar{R}$ is now built from the Einstein metric $\bar{g}_{\mu\nu}$ and φ is a redefinition of the scalar field ϕ through [451, 452],

$$\frac{\partial\varphi}{\partial\phi} = \sqrt{\frac{3}{4}\frac{{F_{,\phi}}^2}{F^2} + \frac{4\pi G}{F}}\,. \tag{7.4}$$

The key advantage resulting from this conformal transformation is a minimal coupling between the conformal metric and the scalar field, evident at the level of the action. The fact that such a redefinition of the theory exists has an important consequence for attempts to constrain the theory's parameters through observations of compact objects: BHs are less suitable to obtain such constraints because the action (7.3) in vacuum ($S_m = 0$) reduces to the Einstein-Hilbert action of GR with a minimally coupled scalar field. In the action as well as the field equations given further below, it is evident that matter sources represent an additional and more straightforward channel to couple the metric and scalar sectors.

The equations of motion in the Jordan frame can be obtained by varying the action (7.1) with respect to the spacetime metric $g_{\mu\nu}$ and the scalar field ϕ:

$$G_{\mu\nu} = \frac{8\pi}{F}\left(T^F_{\mu\nu} + T^\phi_{\mu\nu} + T_{\mu\nu}\right)\,, \tag{7.5}$$

$$T^F_{\mu\nu} = \frac{1}{8\pi}(\nabla_\mu\nabla_\nu F - g_{\mu\nu}\nabla^\rho\nabla_\rho F)\,, \tag{7.6}$$

$$T^\phi_{\mu\nu} = \partial_\mu\phi\partial_\nu\phi - \frac{1}{2}g_{\mu\nu}\partial^\nu\phi\partial_\nu\phi\,, \tag{7.7}$$

$$\nabla^\rho\nabla_\rho\phi = -\frac{1}{16\pi}F_{,\phi}R\,. \tag{7.8}$$

Combining the Bianchi identities with the field equations can be shown to imply that the matter part of the energy momentum tensor,

$$T_{\mu\nu} = \frac{2}{\sqrt{-g}}\frac{\delta S_m}{\delta g_{\mu\nu}}\,, \tag{7.9}$$

is conserved on its own, i.e.

$$\nabla_\mu T^{\mu\nu} = 0\,. \tag{7.10}$$

This feature makes the Jordan frame particularly suitable for studying stellar collapse: the matter equations, which are expected to develop shocks, do not need to be modified from their GR counterparts (cf. Sec. 7.2.2.3). The drawback of this choice is that the scalar field is not minimally coupled to the metric, i.e. the Hilbert term in the action (7.1) acquires a ϕ-dependent factor. This factor $F(\phi)$ leads to the term $T^F_{\mu\nu}$ on the right-hand side of Eq. (7.5) additionally to the minimally coupling term $T^\phi_{\mu\nu}$ and the standard matter sources $T_{\mu\nu}$.

7.2.2 Equation of motions

We now restrict the equations of motion to spherical symmetry in radial-gauge, polar-slicing coordinates [449]. The line element in the Jordan frame is

$$ds^2 = g_{\mu\nu}dx^\mu dx^\nu = -\alpha^2 dt^2 + X^2 dr^2 + \frac{r^2}{F}d\Omega^2\,, \tag{7.11}$$

where the metric functions $\alpha = \alpha(t,r)$ and $X = X(t,r)$ can be more conveniently rewritten in terms of the metric potential,

$$\Phi = \ln(\sqrt{F}\alpha)\,, \tag{7.12}$$

and the enclosed mass,

$$m = \frac{r}{2}\left(1 - \frac{1}{FX^2}\right)\,. \tag{7.13}$$

Note that in Eq. (7.11) we multiplied the angular part of the metric $d\Omega^2$ by a factor $1/F$, thus effectively imposing the radial gauge in the Einstein frame. In this formulation, the (Jordan-frame) areal radius is given by $r/\sqrt{F}$. This choice allows for comparisons with [387, 386, 388], where the analysis is entirely carried out in the Einstein frame. Likewise, Φ and m are Einstein-frame variables and their definition in terms of the Jordan metric components in Eqs. (7.12), (7.13) acquires factors of F.

Following [390], we assume ideal hydrodynamics as described by an energy-momentum tensor of the form

$$T_{\alpha\beta} = \rho h u_\alpha u_\beta + P g_{\alpha\beta}\,, \tag{7.14}$$

and the matter current density

$$J^\alpha = \rho u^\alpha \,. \tag{7.15}$$

Here ρ is the baryonic density, P is the fluid pressure, h is the specific enthalpy (which is related to the specific internal energy ϵ and the pressure P by $h = 1 + \epsilon + P/\rho$), and u^μ is the 4-velocity of the fluid. Spherical symmetry implies

$$u^\mu = \frac{1}{\sqrt{1-v^2}} \left[\frac{1}{\alpha},\ \frac{v}{X},\ 0,\ 0 \right], \tag{7.16}$$

where $v = v(t, r)$.

The equations of motion can be reformulated in flux conservative form using *conserved* variables and thus become amenable to a numerical treatment using high-resolution shock-capturing schemes [189, 188]. These conserved variables D, S^r and τ are related to the to the *primitive* variables ρ, ϵ, v and P by

$$D = \frac{\rho X}{F\sqrt{F}\sqrt{1-v^2}} \,, \tag{7.17}$$

$$S^r = \frac{\rho h v}{F^2(1-v^2)} \,, \tag{7.18}$$

$$\tau = \frac{\rho h}{F^2(1-v^2)} - \frac{P}{F^2} - D \,. \tag{7.19}$$

The definitions above generalise Eq. (8) in [390] to ST theory. We take advantage of the Einstein-frame scalar-field redefinition $\phi \to \varphi$ of Eq. (7.4) because it simplifies the wave equation (7.8). Moreover, the space of ST theories and the weak-field experimental constraints are traditionally described in terms of φ (cf. Sec. 7.3.2). Following [387, 386, 388], we introduce auxiliary variables for the derivatives of the scalar field defined by

$$\eta = \frac{\partial_r \varphi}{X} \,, \tag{7.20}$$

$$\psi = \frac{\partial_t \varphi}{\alpha}. \tag{7.21}$$

7.2.2.1 Metric equations.

The evolution equations (7.5–7.7) for the metric potential Φ and the mass function m expressed in terms of the conserved variables read

$$\partial_r \Phi = X^2 F \left[\frac{m}{r^2} + 4\pi r \left(S^r v + \frac{P}{F^2} \right) + \frac{r}{2F} (\eta^2 + \psi^2) \right], \tag{7.22}$$

$$\partial_r m = 4\pi r^2 (\tau + D) + \frac{r^2}{2F} (\eta^2 + \psi^2), \tag{7.23}$$

$$\partial_t m = r^2 \frac{\alpha}{X} \left(\frac{1}{F} \eta\psi - 4\pi S^r \right). \tag{7.24}$$

These equations are not independent; the last equation for $\partial_t m$ directly follows from the other two combined with the conservation of the energy momentum tensor (7.10). For convenience, we follow standard practice and compute the metric functions using the constraints (7.22), (7.23) and discard the time evolution equation for m.

From Eq. (7.22), we further notice that the metric potential Φ is determined only up to an additive constant. In GR, this freedom is commonly used to match the outer edge of the computational domain to an external Schwarzschild metric. This cannot be done in ST theories, as such theories do not obey a direct analogue of the Birkhoff theorem [85, 298]. We therefore specify a boundary condition for Φ using the method put forward by Novak [387]: Φ is constrained on the outer boundary of the computational domain by requiring that

$$K = \frac{e^{\Phi}}{\sqrt{1 - \frac{2m}{r}}} \tag{7.25}$$

is approximately constant in the weak-field regime, far away from the star. K is then evaluated for the initial profile (cf. Sec. 7.2), fixed to be constant during the evolution and determines Φ on the outer edge of the grid $r = R_{\rm out}$ by inverting (7.25)[2]

$$\Phi(R_{\rm out}) = \ln \left(K \sqrt{1 - \frac{2m(R_{\rm out})}{R_{\rm out}}} \right). \tag{7.26}$$

Note that the Birkhoff theorem in GR corresponds to the case $K = 1$. The error incurred from this procedure can be estimated by comparing results obtained for different extents of the computational domain. We obtain variations of order $|\Delta\varphi/\varphi| \sim 10^{-3}$ at the radius of extraction when the grid extent is decreased by a factor 2 (cf. Sec. 7.4.1 for more details on our numerical setup). Similar errors are detected in the collapse of a ST polytrope if K

[2] Assuming the outer region of the numerical domain is in the weak-field regime, this choice is equivalent to $\alpha \to 1$ at $r \to \infty$, c.f. [387] (see also Sec. 7.3.3 below).

is set to 1, rather than evaluated from the initial profile

7.2.2.2 Scalar-field equations.

The wave equation for the scalar field (7.8) can be written as a first-order system using the definitions (7.20-7.21) and the identity $\partial_t\partial_r\eta = \partial_r\partial_t\eta$ to obtain

$$\partial_t\varphi = \alpha\psi \ , \tag{7.27}$$

$$\partial_t\eta = \frac{1}{X}\partial_r\left(\alpha\psi\right) - rX\alpha\eta(\eta\psi - 4\pi F\, S^r) + \frac{F_{,\varphi}}{2F}\alpha\eta\psi \ , \tag{7.28}$$

$$\begin{aligned}\partial_t\psi = {} & \frac{1}{r^2X}\partial_r\left(\alpha r^2\eta\right) + rX\alpha\psi(\eta\psi - 4\pi F\, S^r) \\ & - \frac{F_{,\varphi}}{2F}\alpha\psi^2 + 2\pi\alpha\left(\tau - S^r v + D - 3\frac{P}{F^2}\right)F_{,\varphi} \ .\end{aligned} \tag{7.29}$$

In order to prescribe the behaviour of φ at the outer boundary, we consider the asymptotic behaviour of the scalar field at spatial infinity [143]

$$\varphi(r) = \varphi_0 + \frac{\omega}{r} + \mathcal{O}\left(\frac{1}{r^2}\right) \ , \tag{7.30}$$

where $\varphi_0 = \text{const}$ and and ω denotes the *scalar charge* of the star. Physically, we require that no radiation enters the spacetime from infinity and therefore impose an outgoing boundary condition [492] at spatial infinity

$$\lim_{r\to\infty}\varphi(t,r) = \varphi_0 + \frac{f(t-r)}{r} + \mathcal{O}(r^{-2}) \, , \tag{7.31}$$

where f is a free function of retarded time. This condition can be translated into the following differential expressions for η and ψ,

$$\partial_t\psi + \partial_r\psi + \frac{\psi}{r} = 0 \, , \tag{7.32}$$

$$\partial_t\eta + \partial_r\eta + \frac{\eta}{r} - \frac{\varphi - \varphi_o}{r^2} = 0 \, , \tag{7.33}$$

and the scalar field φ is directly obtained from Eq. (7.27). As shown in more detail below [see Eq. (7.51) and the following discussion], the value of φ_0 is degenerate with one of the parameters used to describe the coupling function and is set to zero in our study without loss of generality.

In practice, our computational domain extends to large but finite radii and we approximate the physical boundary conditions by imposing Eqs. (7.32), (7.33) at the outer

edge rather than at infinity. As already mentioned, we have tested the influence of the outer boundary location on our results and observe only tiny variations of the order of $|\Delta\varphi/\varphi| \sim 10^{-3}$ in the extraction region when comparing with simulations performed with $R_{\rm out}$ twice as large.

7.2.2.3 Matter equations in flux-conservative form.

The evolution equations (7.5–7.8) can be conveniently written in flux-conservative form [307, 188],

$$\partial_t \mathbf{U} + \frac{1}{r^2}\partial_r \left[r^2 \frac{\alpha}{X} \mathbf{f(U)} \right] = \mathbf{s(U)}\,, \tag{7.34}$$

where $\mathbf{U}$ is the vector of the conserved variables $\mathbf{U} = [D, S^r, \tau]$ defined in Eqs. (7.17-7.19). The fluxes $\mathbf{f(U)} = [f_D, f_{S^r}, f_\tau]$ and the source $\mathbf{s(U)} = [s_D, s_{S^r}, s_\tau]$ are given by

$$f_D = Dv\,, \tag{7.35}$$

$$f_{S^r} = S^r v + \frac{P}{F^2}\,, \tag{7.36}$$

$$f_\tau = S^r - Dv\,, \tag{7.37}$$

$$s_D = -D\frac{F_{,\varphi}}{2F}\alpha(\psi + \eta v)\,, \tag{7.38}$$

$$\begin{aligned} s_{S^r} = {} & (S^r v - \tau - D)\alpha X F \left(8\pi r \frac{P}{F^2} + \frac{m}{r^2} - \frac{F_{,\varphi}}{2F^2 X}\eta \right) + \frac{\alpha X}{F} P \frac{m}{r^2} + 2\frac{\alpha P}{r X F^2} \\ & - 2r\alpha X S^r \eta\psi - \frac{3}{2}\alpha \frac{P}{F^2}\frac{F_{,\varphi}}{F}\eta - \frac{r}{2}\alpha X(\eta^2 + \psi^2)\left(\tau + \frac{P}{F^2} + D\right)(1 + v^2)\,, \end{aligned} \tag{7.39}$$

$$\begin{aligned} s_\tau = {} & -\left(\tau + \frac{P}{F^2} + D\right) r\alpha X \left[(1+v^2)\eta\psi + v(\eta^2 + \psi^2)\right] \\ & + \frac{\alpha}{2}\frac{F_{,\varphi}}{F}\left[Dv\eta + \left(S^r v - \tau + 3\frac{P}{F^2} \right)\psi \right]\,. \end{aligned} \tag{7.40}$$

Note that Ref. [388] misses a factor $1/a$ (in their notation) inside the argument of the radial derivative in their Eq. (11). Inclusion of this factor and pulling the term proportional to ηv in Eq. (7.38) out of the radial derivative enables us to cast the evolution equation for D in the same form (7.34) as the other matter equations. For the integration of the evolution equation for D, we therefore do not need the additional considerations described in Sec. 2.1 of [388].

The hyperbolic structure of the system of equations (7.34) is dictated by the Jacobian

matrix of the fluxes [59],

$$\mathbf{J_U} = \frac{\partial \mathbf{f(U)}}{\partial \mathbf{U}} \,. \tag{7.41}$$

The characteristic speeds associated with the propagation of the matter fields are the eigenvalues λ of $\mathbf{J_U}$,

$$\lambda = \left[v, \frac{v + c_s}{1 + v\, c_s}, \frac{v - c_s}{1 - v\, c_s} \right] \,. \tag{7.42}$$

Here $c_s = \sqrt{(dP/d\rho)_S/h}$ (S is the entropy) is the local speed of sound given for our choice of EOS of the form $P = P(\rho, \epsilon)$ by

$$h\, c_s^2 = \frac{\partial P}{\partial \rho} + \frac{P}{\rho^2} \frac{\partial P}{\partial \epsilon} \,. \tag{7.43}$$

The characteristic speeds are therefore exactly the same as in GR, since they do not depend on the conformal factor F. The high-resolution shock-capturing scheme implemented in GR1D for GR [390] can therefore be used in ST theories as well, provided the conserved variables $\mathbf{U}$ and their fluxes $\mathbf{f(U)}$ are generalised using the expressions presented above.

7.3 Physical setup

In this Section, we discuss in more detail the physical ingredients entering our simulations. We discuss the EOS for the fluid used in our work (Sec. 7.3.1), the various choices for the coupling function that relate the physical metric to its conformally rescaled counterpart (Sec. 7.3.2) and the initial stellar profiles used in our study (Sec. 7.3.3). We also provide information on the quantities used to compare GW signals and detector sensitivities in the context of monopole waves (Sec. 7.3.4).

7.3.1 Equation of state

An EOS is required to close the hydrodynamical system of equations. Specifically, it provides a prescription for the pressure P and other thermodynamic quantities as a function of the mass density, internal energy (or temperature), and possibly the chemical composition. Here we study stellar collapse using the so-called *hybrid* EOS. This EOS was introduced in [259] and qualitatively captures in closed analytic form the expected stiffening of the nuclear matter EOS at nuclear density and includes nonisentropic (thermal) effects to model the response of shocked material. The hybrid EOS was widely used in early multi-dimensional core-collapse simulations (e.g. [555, 156]), and the results of simulations using a hybrid EOS have been compared in detail with those obtained with modern finite-temperature

EOSs [157, 158].

The hybrid EOS consists of a *cold* and a *thermal* part:

$$P = P_{\rm c} + P_{\rm th}\,. \tag{7.44}$$

The cold component P_c is modelled in piecewise polytropic form with adiabatic indices Γ_1 and Γ_2,

$$P_{\rm c} = \begin{cases} K_1\rho^{\Gamma_1} & \text{if} \quad \rho \leq \rho_{\rm nuc}\,, \\ K_2\rho^{\Gamma_2} & \text{if} \quad \rho > \rho_{\rm nuc}\,. \end{cases} \tag{7.45}$$

This expression models both the pressure contribution from relativistic electrons, which dominates at $\rho \leq \rho_{\rm nuc}$, and the stiffening at nuclear density due to the repulsive character of the nuclear force. The two components are matched at "nuclear density" which we set to $\rho_{\rm nuc} = 2 \times 10^{14}$ g/cm^3 following [156]. We set $K_1 = 4.9345 \times 10^{14}$ [cgs], as predicted for a relativistic degenerate gas of electrons with electron fraction $Y_e = 0.5$ [479], while $K_2 = K_1\rho_{\rm nuc}^{\Gamma_1-\Gamma_2}$ is then obtained from requiring continuity in P at $\rho = \rho_{\rm nuc}$. The specific internal energy follows from the first law of thermodynamics applied to the case of adiabatic processes

$$\epsilon_{\rm c} = \begin{cases} \frac{K_1}{\Gamma_1-1}\rho^{\Gamma_1-1} & \text{if} \quad \rho \leq \rho_{\rm nuc}\,, \\ \frac{K_2}{\Gamma_2-1}\rho^{\Gamma_2-1} + E_3 & \text{if} \quad \rho > \rho_{\rm nuc}\,, \end{cases} \tag{7.46}$$

where the integration constant E_3 is determined by continuity at $\rho = \rho_{\rm nuc}$. The thermal contribution $P_{\rm th}$ is described by a Γ-law with adiabatic index $\Gamma_{\rm th}$,

$$P_{\rm th} = (\Gamma_{\rm th} - 1)\rho\epsilon_{\rm th}\ , \tag{7.47}$$

where $\epsilon_{\rm th} = \epsilon - \epsilon_{\rm c}$ is the thermal contribution to the internal energy, computed from the primitive variable ϵ. The flow is adiabatic before bounce, implying that $\epsilon \simeq \epsilon_{\rm c}$ and the total pressure is described by considering only its cold contribution. At core bounce, however, the hydrodynamic shock results in nonadiabatic flow and thus triggers the onset of a non-negligible thermal contribution to the EOS.

We consider a hybrid EOS characterised by three parameters: Γ_1, Γ_2 and $\Gamma_{\rm th}$. The physical range of these adiabatic indices has been explicitly studied in [157, 158], where 2+1 GR simulations of core collapse were used to compute the effective adiabatic index of the finite-temperature EOSs of Lattimer and Swesty [304, 305] and Shen et al. [481, 482].

In the collapse phase, electron capture decreases the effective adiabatic index below the value $\Gamma_1 = 4/3$ predicted for a relativistic gas of electrons. More precisely, comparisons with more detailed simulations yields a range from $\Gamma_1 \simeq 1.32$ to $\Gamma_1 \simeq 1.28$ [157, 158, 483]. In particular, lower values of Γ_1 are found when deleptonisation is taken into account because electron capture onto nuclei before neutrino trapping decreases Y_e for given ρ, thus softening the EOS. Collapse is stopped by the stiffening of the EOS at nuclear density which raises the effective adiabatic index Γ_2 above 4/3. Dimmelmeier et al. [158] finds $\Gamma_2 \simeq 3.0$ for the Shen et al. EOS and $\Gamma_2 \simeq 2.5$ for the Lattimer-Swesty EOS. Finally, the thermal adiabatic index Γ_th models a mixture of relativistic and non-relativistic gas, and is therefore physically bounded to $4/3 < \Gamma_\mathrm{th} < 5/3$. We select fiducial values $\Gamma_1 = 1.3$, $\Gamma_2 = 2.5$, $\Gamma_\mathrm{th} = 1.35$ for our code tests presented in Sec. 7.4, and explore a more extended parameter grid around this model in Sec. 7.5.

7.3.2 Coupling function

As introduced in Sec. 7.2.1, ST theories with a single scalar field and vanishing potential are described by a single free function $F(\varphi)$. The phenomenology of ST theories is simplified, however, by the fact that all modifications of gravity at first PN order depend only on two parameters. These are the asymptotic values of the first and second derivatives of $\ln F$ [143, 145, 128][3],

$$\alpha_0 = -\frac{1}{2}\frac{\partial \ln F}{\partial \varphi}\bigg|_{\varphi=\varphi_0}, \qquad \beta_0 = -\frac{1}{2}\frac{\partial^2 \ln F}{\partial \varphi^2}\bigg|_{\varphi=\varphi_0}. \tag{7.48}$$

The effective gravitational constant determining the attraction between two bodies as measured in a Cavendish experiment is

$$\tilde{G} = G(1+\alpha_0^2)\,, \tag{7.49}$$

where G is the bare gravitational constant entering the action. Furthermore, the Eddington Parameterised post-Newtonian parameters [171, 543] can be expressed exclusively in terms of α_0 and β_0 through

$$\beta^\mathrm{PPN} - 1 = \frac{\alpha_0^2\beta_0}{2(1+\alpha_0^2)^2}\,, \qquad \gamma^\mathrm{PPN} - 1 = -2\frac{\alpha_0^2}{1+\alpha_0^2}\,. \tag{7.50}$$

For an interpretation of these equations in terms of fundamental interactions, see [146]. In consequence, weak-field deviations from GR are completely determined by the Taylor

[3] We introduce factors $-1/2$ in Eq. (7.48), and consequently a factor -2 in Eq. (7.51), to be consistent with previous studies, e.g., Refs. [143, 144, 145].

expansion of $\ln F$ to quadratic order about $\lim_{r\to\infty}\varphi = \varphi_0$. For these reasons, most of the literature on ST theories has focused on coupling functions of quadratic form [144, 145] and we follow this approach by employing a coupling function

$$F = \exp\left[-2\alpha_0(\varphi-\varphi_0) - \beta_0(\varphi-\varphi_0)^2\right] . \tag{7.51}$$

The asymptotic value φ_0 does not represent an additional degree of freedom in the theory because it can be reabsorbed by a field redefinition $\varphi \to \varphi + \varphi_0$ [142] and we therefore set $\varphi_0 = 0$ without loss of generality.[4] We can furthermore assume $\alpha_0 \geq 0$ because the sign of α_0 is degenerate with the field redefinition $\varphi \to -\varphi$. Despite its apparent simplicity, this two-parameter family of ST theories is representative of all ST theories with the same phenomenology up to first PN order. Brans-Dicke theory [98] is a special case of Eq. (7.51) with the Brans-Dicke parameter [defined above Eq. (7.2)] given by $\omega_{\rm BD} = (1-6\alpha_0^2)/2\alpha_0^2$ and $\beta_0 = 0$. It is worth mentioning here that theories with the coupling function (7.51) and strictly vanishing potential have been shown to exhibit non-viable cosmological evolutions [149, 148]; however, this can be cured by introducing a suitable (sufficiently flat) potential which leaves the phenomenology on stellar scales unchanged [260, 454].

It is well known that all deviations in the structure of spherically symmetric bodies in ST theory from their general relativistic counterparts are given in terms of a series of PN terms proportional to α_0^2 [143, 179]; cf. also Eq. (7.50) above. Any ST theory with $\alpha_0 = 0$ is therefore perturbatively equivalent to GR and current observations (see below) constrain α_0 to be very small. In 1993, however, Damour and Esposito-Farèse [144, 145] discovered a remarkable non-perturbative effect called *spontaneous scalarisation*, which introduces macroscopic modifications to the structure of NSs even when α_0 is very small or vanishes [248]. For certain values $\beta_0 < 0$, there exists a threshold in the compactness (M/R, where M is the total mass of the object and R is its radius) of stellar structure at which spherically symmetric equilibrium solutions develop significant scalar hair. One can find three distinct solutions in this regime: besides a weakly scalarised solution where the ratio between the scalar charge and the star's mass ω/M is of the order of α_0, two strong-field solutions appear where this ratio is of order unity [386, 226]. If $\alpha_0 = 0$, the weak-field solution is a GR star and the two strong field solutions coincide. Notably, scalarised solutions are present for compactness values of order $M/R \gtrsim 0.2$ [179], as realised in NSs. When present, scalarised neutron stars can be energetically favoured over their weak-field counterparts [144, 145, 225], allowing for the possibility of dynamical transitions between

[4] The class of theories here parameterised by (α_0, β_0) can equivalently be represented using $F = \exp(-2\beta_0\varphi^2)$ but keeping φ_0 as an independent parameter, as done, e.g., by [144].

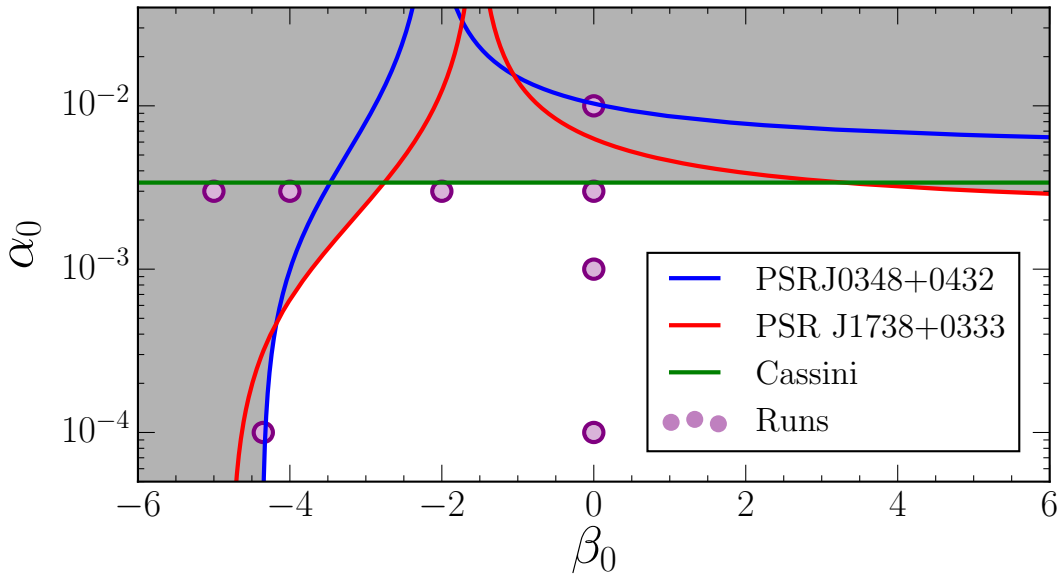

Figure 7.1: Experimental constraints on the ST-theory parameters (α_0, β_0) entering the coupling function F. The shaded area is currently ruled out by observations; GR lies at $\alpha_0 = \beta_0 = 0$. The most stringent constraints on α_0 are provided by the Cassini space mission while the binary-pulsar experiments impose strong bounds on β_0. Circles mark our choices for (α_0, β_0) used in Sec. 7.5. This figure is produced using the data published in Fig. 6.3 of [71].

the two branches of solutions [386]. Spontaneously scalarised stars have been found for $\beta_0 \lesssim -4.35$ [386, 226], but the exact value of this threshold depends on the EOS.

The (α_0, β_0) parameter space of ST theories has been severely constrained by observations. Solar System probes include measurements of Mercury's perihelion shift [478], Lunar Laser Ranging [546], light deflection measured with Very-Long-Baseline Interferometry [480], and the impressive bound $\alpha_0 < 3.4 \times 10^{-3}$ obtained with the Cassini space mission [79]. Timing of binary pulsars currently provides the tightest constraints in the β_0 direction of the parameter space [540]. In particular, observations from pulsars PSR J1738+0333 [192] and PSR J0348+0432 [30] (both orbiting a white dwarf companion) rule out a wide range of theories exhibiting prominent spontaneous scalarisation. Current observational constraints are summarised in Fig. 7.1 where the shaded area is now excluded. Note, however, that the binary-pulsar constraints apply to the case of a single massless scalar field. Scalar-tensor theories with multiple scalar fields [247] or with one massive field [436] may still lead to spontaneously scalarised neutron stars over a wide range of the theories' parameters without coming into conflict with the binary pulsar observations.

7.3.3 Initial profiles

We perform simulations of stellar collapse starting from two types of initial data: (i) polytropic models generated in the static limit of the ST theory equations and (ii) "realistic" SN progenitors obtained from stellar evolutionary computations performed by Woosley & Heger [547].

(i) In the static limit, the evolution equations presented in Sec. 7.2.2.1–7.2.2.3 reduce to (cf. [144, 247])

$$\partial_r \Phi = FX^2 \left(\frac{m}{r^2} + 4\pi r \frac{P}{F^2} + \frac{r}{2F}\eta^2 \right) , \tag{7.52}$$

$$\partial_r m = 4\pi r^2 \frac{\rho h - P}{F^2} + \frac{r^2}{2F}\eta^2 , \tag{7.53}$$

$$\partial_r P = -\rho h F X^2 \left(\frac{m}{r^2} + 4\pi r \frac{P}{F^2} + \frac{r}{2F}\eta^2 \right) + \rho h \frac{F_{,\varphi}}{2F} X\eta , \tag{7.54}$$

$$\partial_r \varphi = X\eta , \tag{7.55}$$

$$\partial_r \eta = -2\frac{\eta}{r} - 2\pi X \frac{\rho h - 4P}{F^2} F_{,\varphi} - \eta F X^2 \left(\frac{m}{r^2} + 4\pi r \frac{P}{F^2} + \frac{r}{2F}\eta^2 \right) + \frac{X}{2}\frac{F_{,\varphi}}{F}\eta^2 , \tag{7.56}$$

which generalise the Tolman–Oppenheimer–Volkoff [510, 396] equations to ST theory. As in GR, the equation for the metric potential Φ decouples from the remainder and we need an EOS $P = P_{\rm EOS}(\rho)$ to close the system.

In practice, we integrate the system (7.52)–(7.56) outwards starting at the origin where boundary and regularity conditions require

$$\Phi(0) = 0 , \quad m(0) = 0 , \quad P(0) = P_{\rm EOS}(\rho_c) , \quad \varphi(0) = \varphi_c , \quad \eta(0) = 0 . \tag{7.57}$$

Here, P_c (or, alternatively, ρ_c) is a free parameter determining the overall mass and size of the star and the central value of the scalar field φ_c is related through the integration to the value of φ at infinity. In our case, the boundary condition for the scalar field is $\varphi(r \to \infty) = \varphi_0 = 0$ and the task is to identify the "correct" central value φ_c that satisfies the outer boundary condition. From a numerical point of view, this task represents a *two point boundary value problem* [422] and we use a *shooting algorithm* to solve it. For this purpose, we note that the integration terminates at the stellar surface r_s defined as the innermost radius where $P = 0$. From this radius r_s, we could in principle continue the integration to infinity by setting the matter

sources to zero and switching to a compactified radial coordinate such as $y \equiv 1/r$. We have found such a scheme to work successfully [247], but here we implement an equivalent, but conceptually simpler algorithm. The numerical solution computed for $r \leq r_s$ can be matched to a vacuum solution at $r > r_s$ to relate the scalar field at the stellar surface φ_s to its asymptotic value φ_0 at $r = \infty$ [144]:

$$\varphi_s = \varphi_0 - \frac{X_s \eta_s}{\sqrt{(\partial_r \Phi_s)^2 + X_s^2 \eta_s^2}} \operatorname{arctanh} \frac{\sqrt{(\partial_r \Phi_s)^2 + X_s^2 \eta_s^2}}{\partial_r \Phi_s + 1/r_s} \,, \tag{7.58}$$

where the subscript s denotes quantities evaluated at r_s. The shooting algorithm starts the integration of Eqs. (7.52–7.56) with some initial guess $\varphi(0)$, obtains the corresponding φ_s and then iteratively improves the choice of $\varphi(0)$ until it leads to a φ_s that satisfies Eq. (7.58) within some numerical tolerance (10^{-10} for the absolute difference in our case).

The central density or pressure can be freely chosen and parameterises the family of static solutions for a given ST theory (α_0, β_0) in the same way as it does in GR. The members of this one-parameter family of solutions are often characterised by their total gravitational mass which is given by [144]

$$m_\infty = r_s^2 \partial_r \Phi_s \sqrt{1 - \frac{2m_s}{r_s}} \exp\left[- \frac{\partial_r \Phi_s}{\sqrt{(\partial_r \Phi_s)^2 + X_s^2 \eta_s^2}} \operatorname{arctanh} \frac{\sqrt{(\partial_r \Phi_s)^2 + X_s^2 \eta_s^2}}{\partial_r \Phi_s + 1/r_s} \right] . \tag{7.59}$$

All polytropic initial profiles used in this work are generated using a polytropic EOS $P = K\rho^\Gamma$ with $K = 4.9345 \times 10^{14}$ [cgs], $\Gamma = 4/3$ and central mass density $\rho_c = 10^{10}\,\mathrm{g\ cm^{-3}}$; these parameters are considered qualitatively reasonable approximations to model iron cores supported by the degeneracy pressure of relativistic electrons [479]. In particular, the choice $\rho_c = 10^{10}\,\mathrm{g\ cm^{-3}}$ results in stars with baryonic mass $\sim 1.44 M_\odot$, slightly below the Chandrasekhar limit [81].

(ii) We also perform core collapse simulations using more realistic pre-SN models. Woosley and Heger (WH) [547] evolved non-rotating single stars up to the point of iron core collapse [536, 548]. Here, we consider two specific models of their catalogue obtained from the evolution of stars with ZAMS mass $M_{\mathrm{ZAMS}} = 12 M_\odot$ and $40 M_\odot$. We refer to these models as WH12 and WH40 respectively. Model WH12 has a steep density gradient outside its iron core, which results in a low accretion rate after bounce. Even if no explosion occurs, the delay to BH formation would be multiple seconds and no BH forms over the time we simulate. Model WH40, on the other hand, has a very shallow density gradient, resulting in a high accretion rate after bounce. This

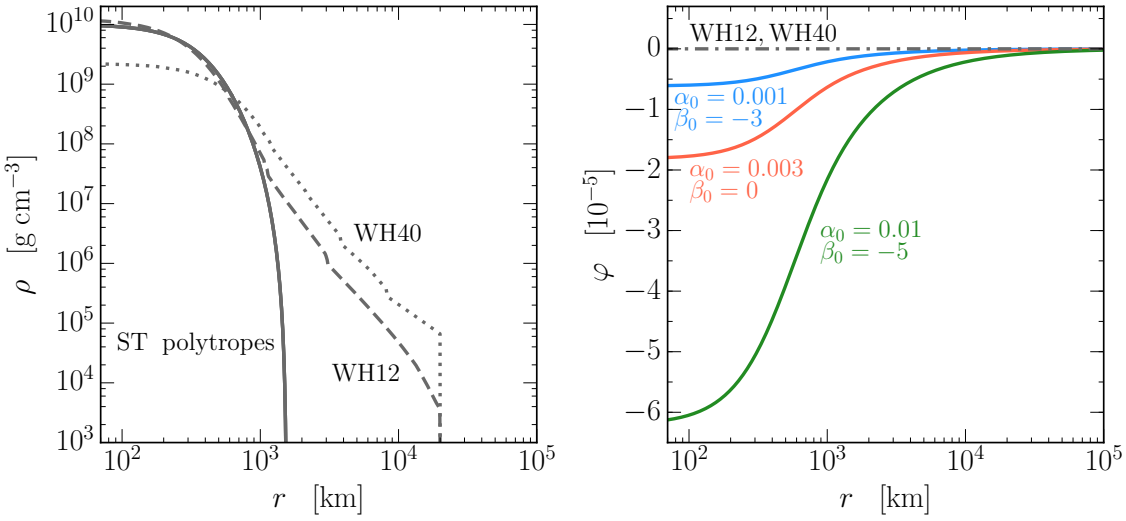

Figure 7.2: Mass-density (left panel) and scalar-field (right panel) profiles for the initial data considered in this study. In particular, dashed and dotted lines show the $M_{\rm ZAMS} = 12M_\odot$ (WH12) and $M_{\rm ZAMS} = 40M_\odot$ (WH40) pre-SN models of Woosley and Heger [547] while the solid lines show three $\Gamma = 4/3$ polytropes generated in ST theories with $(\alpha_0, \beta_0) = (0.001, -3), (0.003, 0), (0.01, -5)$. The mass-density distributions of all three ST polytropes are indistinguishable from their GR counterparts. The more realistic models WH12 and WH40 mostly differ from the polytropic ones through the presence of outer low-density layers. Note that we cut the WH models at $r_{\rm s} = 2 \times 10^4\,{\rm km}$ and pad them with an artificial atmosphere of $\rho_{\rm atm} = 1\,{\rm g\,cm^{-3}}$. The scalar field is more pronounced in models with higher α_0, but the low compactness of these models prevents spontaneous scalarisation. The scalar field is initialised to zero when the WH models are evolved.

pushes the protoneutron star over its maximum mass and leads to BH formation within a few hundred milliseconds of bounce (cf. [391]). Hence, we use model WH12 to explore ST theory for a scenario in which core collapse results in a stable NS and model WH40 for a scenario in which the protoneutron star collapses to a BH.

Since WH12 and WH40 are Newtonian models, we initialise the scalar-field variables φ, ψ and η to 0. An unfortunate consequence of this artificial (but unavoidable) approximation is that no scalar-field dynamics occur at all if $\alpha_0 = 0$: all source terms on the right-hand side of Eqs. (7.27–7.29) vanish at all times, and the evolution proceeds exactly as in GR. We overcome this problem, by using small but non-zero values for α_0, which triggers a brief initial transient in the scalar field that afterwards settles down into a smooth but non-trivial configuration eventually leading to significant scalar field dynamics as the collapse progresses through increasingly compact stages of the core.

For both classes of initial data there remains one degree of freedom that we need to specify: the metric function Φ is determined by Eq. (7.52) only up to an additive constant. While our integration in case (i) starts with $\Phi(0) = 0$, we can trivially shift the profile of $\Phi(r)$ by

a constant (leaving all other variables unchanged) and still have a solution of the system of Eqs. (7.52)-(7.56). We use this freedom to enforce that the physical metric component $g_{tt} = 1$ as $r \to \infty$, so that coordinate time is identical to the proper time measured by an observer at infinity. In practice, this is achieved by using very large grids and fitting $\Phi = \Phi_0 + \Phi_1/r$ on the outer parts. Φ_0 is then the constant we subtract from the entire profile $\Phi(r)$. The realistic initial models of case (ii) above are calculated without a scalar field and in that case our procedure is equivalent to the standard matching in GR based on the Birkhoff theorem.

For illustration, we show in Fig. 7.2 some of the initial profiles used in this study. Because of the low compactness of iron cores, the polytropic profiles for all values of $\alpha_0 \leq 0.01$ present very similar mass-density distributions which also very closely resemble their GR counterpart. The magnitude of the scalar field inside the star increases as larger values are chosen for α_0 (cf. right panel of Fig. 7.2) while outside the star φ rapidly approaches the $1/r$ behaviour of Eq. (7.30). In the left panel of Fig. 7.2, we also see that the realistic pre-SN models WH12 and WH40 are well approximated by a $\Gamma = 4/3$ polytrope in their central regions $r \lesssim 10^3$ km; outer less degenerate layers of lighter elements, however, substantially broaden the mass-density distribution outside the iron core.

In order to overcome instabilities arising in our numerical scheme due to zero densities ρ [390], we add an artificial atmosphere outside the stellar surface r_s. More specifically, we pad the polytropic profiles with a layer of constant mass density $\rho_{\rm atm} = 1$ g cm^{-3}. The WH models are cut at $r_{\rm s} = 2 \times 10^4$ km (cf. Fig. 7.2) and padded with an artificial atmosphere of $\rho_{\rm atm} = 1$ g cm^{-3}. By comparing evolutions using different values for the atmospheric density, we find the atmosphere to be completely irrelevant to the dynamics of the star, but we observe that significantly larger values than $\rho_{\rm atm} = 1$ g cm^{-3} unphysically affect the propagation of the scalar wave signal such that the wave signal does not converge in the limit of large extraction radii. We estimate the resulting error for our choice by comparison with otherwise identical simulations using instead $\rho_{\rm atm} = 10$ g cm^{-3}; the observed differences are $|\Delta h(t)|/h(t) \sim 0.3\%$ in the extracted waveform [cf. Eq. (7.66) below].

7.3.4 GW extraction and detector sensitivity curves

The output of a GW detector $s(t) = n(t) + h(t)$ is the sum of noise $n(t)$ and signal $h(t)$. For quadrupole GWs, as present in GR, $h(t)$ is related to the metric perturbation $h_{+,\times}$ in the transverse traceless gauge through the beam pattern functions $A_{+,\times}$: $h(t) = A_+ h_+(t) + A_\times h_\times(t)$ [372]. Monopole GWs are present in ST theory and are related to the

dynamics of the scalar field φ. In this case, the detector response $h(t) = A_\circ h_\circ(t)$ is given by the metric perturbation $h_\circ(t)$ weighted by the corresponding beam pattern $A_\circ$ [383, 553][5]. If we denote by $\tilde{h}(f)$ and $\tilde{n}(f)$ the Fourier transform of $h(t)$ and $n(t)$, respectively, the (one-sided) noise power spectral density $S_n(f)$ is defined as

$$\langle \tilde{n}(f)\tilde{n}^*(f')\rangle = \frac{1}{2}\delta(f-f')S_n(f)\,, \tag{7.60}$$

where $\langle\cdot\rangle$ denotes a time average for stationary stochastic noise. The signal-to-noise ratio is defined as (see [374] where the numerical factor is derived; see also [456])

$$\rho^2 = \int_0^\infty \frac{4|\tilde{h}(f)|^2}{S_n(f)} df\,. \tag{7.61}$$

The characteristic strains for noise and signal are defined as

$$h_n(f) = \sqrt{f\,S_n(f)}\,, \qquad h_c(f) = 2f|\tilde{h}(f)| \tag{7.62}$$

such that ρ^2 can be written as the squared ratio between signal and noise:

$$\rho^2 = \int_{-\infty}^{+\infty} \left[\frac{h_c(f)}{h_n(f)}\right]^2 d\ln f\,. \tag{7.63}$$

The most common convention used to display detector sensitivity curves involves plotting the square root of the power-spectral density

$$\sqrt{S_n(f)} = \frac{h_n(f)}{\sqrt{f}}\,; \tag{7.64}$$

and the analogous quantity [374]

$$\sqrt{S_h(f)} = \frac{h_c(f)}{\sqrt{f}} = 2\sqrt{f}|\tilde{h}(f)|\,, \tag{7.65}$$

which characterises the GW signal.[6] In the following we will use sensitivity curves $\sqrt{S_n(f)}$ for:

(i) the Advanced LIGO detectors [3, 10] in their zero-detuned high-power configuration, as anticipated in [488];

[5] The most sensitive directions corresponding to A_+, $A_\times$ and $A_\circ$ are all different from each other. If only these three polarisations are present, a network of four detectors can in principle disentangle them and estimate the source direction [485]. Note also that optimally oriented sources correspond to $A_+ = 1$, $A_\times = 1$ but $A_\circ = 1/2$ [383, 553].

[6] The convention for $\sqrt{S_h(f)}$ used in [387] differs by a factor 2 when compared to those of [374] used here.

(ii) the proposed ET [429], using the analytic fit reported in [456].

Scalar waves are also promising sources for future GW experiments targeting the deci-Hertz regime, such as the proposed space mission DECIGO (DECi-hertz Interferometer Gravitational-wave Observatory) [266].

In contrast to GR, ST theories admit gravitational radiation in spherical symmetry, specifically in the form of a radiative monopole of the scalar field or, equivalently, a so-called *breathing mode* when considering the Jordan frame. The metric perturbation of a monopole scalar wave in ST theory is [143]

$$h_{\circ}(t) = \frac{2}{D}\alpha_0 r(\varphi - \varphi_0)\,, \tag{7.66}$$

where D is the distance between the detector and the source and the scalar field φ is evaluated at radius r. The factor α_0 is due to the coupling between the scalar field and the detector and limits the potential of GW observations to constrain ST theories [49]. For simplicity, we only consider optimally oriented sources, such that $h(t) = A_{\circ}h_{\circ}(t) = h_{\circ}(t)/2$ [383, 553].

In analysing our simulations, we proceed as follows. At a given radius $r_{\rm ext}$, we extract $\varphi(t)$ and compute $h(t)$. In order to eliminate the brief unphysical transient (cf. Sec. 7.4.1), we truncate this early part from the time domain waveform $h(t)$. We then obtain $\tilde{h}(f)$ numerically using a Fast Fourier Transform (FFT) algorithm. To reduce spectral leakage, the FFT algorithm is applied to data $h(t)$ mirrored about the latest timestep available and the result $\tilde{h}(f)$ is normalised accordingly [257]. This confines spectral leakage to frequencies $f \gtrsim 200$ Hz (cf. the tails in Figs. 7.7 and 7.8) where the signal is very weak. Finally, we compute $\sqrt{S_h(f)}$ from Eq.(7.65) and compare it with the detectors' sensitivity curves $\sqrt{S_n(f)}$.

7.4 Numerical implementation

In this Section, we provide details of our numerical scheme, stressing the modifications needed in ST theories with respect to the GR version of the code (Sec 7.4.1). We present the convergence properties in Sec. 7.4.2.

7.4.1 Second-order finite differences and high-resolution shock capturing

Our numerical code is built on top of GR1D, an open-source spherically-symmetric FORTRAN 90+ code developed by O'Connor and Ott [390]. GR1D has been applied to a range of problems in stellar collapse and BH formation (e.g., [391, 392]). Its most recent GR version is

available at [401] and includes energy-dependent neutrino radiation transport [389].

As in the GR case, the constraint equations (7.22) and (7.23) for the metric functions Φ and m are integrated using standard second-order quadrature. In the scalar-field equations (7.27–7.29), the source terms are discretised using centred second-order stencils. Due to the potential formation of shocks in the matter variables, their evolution is handled with a high-resolution shock capturing scheme as described in detail in Sec. 2.1 of [390]. For our evolutions in ST theory, we extended the flux and source terms of GR1D in accordance with our Eqs. (7.35)–(7.40). Integration in time of the evolution equations for the matter and scalar fields is performed using the method of lines with a second-order Runge-Kutta algorithm. One significant difference from the GR case arises from the presence of the scalar field as a dynamical degree of freedom with the characteristic speed of light, whereas in spherical symmetry in GR we only have to consider the characteristic speed of sound for the matter degrees of freedom (cf. Sec. 7.2.2.3). In order to satisfy the Courant-Friedrichs-Lewy stability condition we therefore determine the timestep using the speed of light instead of the speed of sound, which results in smaller values for the allowed timestep as compared with the corresponding evolutions in GR.

As discussed in Sec. 7.2.2.3, a key ingredient in the implementation of shock capturing methods is the use of a system of evolution equations in flux conservative form which is available in terms of the conserved variables D, S^r, τ but not in the primitive variables ρ, v and ϵ. The primitive variables appear in the constraint equations for the metric, the flux terms of the shock-capturing scheme, in the EOS, and also form convenient diagnostic output. Conversion between the two sets of variables is thus required at each timestep. This process is straightforward for the direction primitive $\rightarrow$ conserved; cf. Eqs. (7.17–7.19). The reverse transformation, however, is non-trivial because of the presence of the pressure P which is an intrinsic function of ρ and ϵ given by the EOS. This conversion is performed iteratively using a Newton-Raphson algorithm: given an initial guess $\hat{P}$ for the pressure from the previous timestep, we first calculate in this order

$$v = \frac{S^r}{\tau + \hat{P}/F^2 + D}\,, \tag{7.67}$$

$$\rho = \frac{F^{3/2} D}{X}\sqrt{1 - v^2}\,, \tag{7.68}$$

$$\epsilon = h - \frac{\hat{P}}{\rho} - 1 = \frac{F^2(\tau + D)(1 - v^2) - \hat{P}v^2}{\rho} - 1\,. \tag{7.69}$$

Then we compute an updated estimate for the pressure from the EOS $P = P(\rho, \epsilon)$, and iterate this procedure until convergence.

The evolution of the scalar field turns out to be susceptible to numerical noise near the origin $r = 0$, which represents a coordinate singularity. In order to obtain long-term stable evolutions, we add artificial dissipation terms of Berger-Oliger type [222] to the scalar evolution equations. Specifically, we add a dissipation term of the form $\mathcal{D} \times \Delta r^4 \times \partial^4 u / \partial r^4$ to the right-hand-side of Eqs. (7.27)–(7.29), where u stands for either of the scalar-field variables, Δr is the width of the grid cell, and $\mathcal{D}$ is a dissipation coefficient. In practice, we obtain good results using $\mathcal{D} = 2$.

In all our simulations, the grid functions exhibit much stronger spatial variation in the central region of the star than in the wave zone. In order to accommodate these space dependent requirements on the resolution of our computational domain, we use a numerical domain composed of an inner grid with constant and an outer grid with logarithmic spacing. This setup enables us to capture the dynamics of the inner core with high accuracy while maintaining a large grid for GW extraction at tolerable computational cost. Unless specified otherwise, we use the following grid setup. The outer edge of the grid is placed at $R_{\rm out} = 1.8 \times 10^5$ km and the two grid components are matched at $R_{\rm match} = 40$ km. The cell width of the inner grid is $\Delta r = 0.25$ km. The total number of zones is set to $N_{\rm zones} = 5000$, such that 160 (4840) zones are present in the inner (outer) grid. 4 ghost cells are added at both $r = 0$ and $r = R_{\rm out}$ for implementing symmetry and boundary conditions. GW signals are extracted at $r_{\rm ext} = 3 \times 10^4$ km, which is well outside the surface of the star but sufficiently far from the outer edge of the grid $R_{\rm out}$ to avoid contamination from numerical noise from the outer boundary. We simulate the evolution for 0.7 s to allow for the entire GW signal to cross the extraction region.

Radial gauge, polar slicing coordinates are not well adapted to BH spacetimes: as the star approaches BH formation, the lapse function α tends to zero in the inner region [25] and inevitably introduces significant numerical noise. The stellar evolution, however, is effectively frozen as $\alpha \to 0$. Following Novak [387], we handle BH formation by explicitly stopping the evolution of the matter variables while we let the scalar field propagate outwards. In practice, we freeze the matter evolution whenever the central value of α becomes smaller than $\alpha_T = 5 \times 10^{-3}$. By varying the threshold α_T over two orders of magnitude, we verified this procedure introduces a negligible error $|\Delta\varphi|/\varphi \lesssim 1\%$ on the extracted wave signal in case of BH formation.

A final note on the numerical methods concerns the time window used for the wave extraction. As mentioned in Sec. 7.2, our initial data for the realistic progenitor models require us to trigger scalar dynamics by using a small but non-zero value for α_0 that induces a brief transient in the wave signal. This transient is not part of the physical signal we

are interested in and is removed by calculating waveforms in an interval starting not at zero retarded time, but shortly afterwards: we use for this purpose the time window $[t_i, t_f]$ with $t_i = r_{\rm ext}/c + 0.006$ s to $t_f = r_{\rm ext}/c + 0.6$ s from the beginning of the simulation. This provides us with waveforms of total length $\Delta t \sim 0.6$ s corresponding to a lower bound $f \sim 1.7$ Hz in the frequency domain. Note that our waveforms are significantly longer than those obtained in previous studies of collapse in ST theories [388].

7.4.2 Self-convergence test

Here we present the convergence properties of our dynamical code. Given three simulations of increasing resolutions with grid spacings $\Delta r_1 > \Delta r_2 > \Delta r_3$, the self-convergence factor Q of a quantity q is defined by

$$Q = \frac{q_1 - q_2}{q_2 - q_3} = \frac{(\Delta r_1)^n - (\Delta r_2)^n}{(\Delta r_2)^n - (\Delta r_3)^n}\,, \tag{7.70}$$

where q_i indicates the quantity q obtained at resolution Δr_i and n is the convergence order of the implemented numerical scheme.

We collapse a $\Gamma = 4/3$ polytropic core in ST theory with $\alpha_0 = 10^{-4}$ and $\beta_0 = -4.35$ using the hybrid EOS with $\Gamma_1 = 1.3$, $\Gamma_2 = 2.5$ and $\Gamma_{\rm th} = 1.35$. This model is evolved for three uniformly spaced[7] grids of size $R_{\rm out} = 2{\times}10^3$ km with $N = 6000, 12000$ and 24000 grid cells. For these grids, we expect $Q = 2$ ($Q = 4$) for first- (second-) order convergence. The bottom panels of Fig. 7.3 show the convergence properties of the gravitational mass m and the scalar field φ at various timesteps. Solid lines show the difference between the coarse and the medium resolution runs $q_1 - q_2$; dashed (dotted) lines show the difference between the medium and the fine resolution runs $q_2 - q_3$ multiplied by the expected first- (second-) order self-convergence factor $Q = 2$ ($Q = 4$). Second-order convergence is achieved if the solid and dotted lines coincide, while the code is only first-order convergent if the solid and dashed lines coincide. The evolution of ρ and φ is displayed in the top panels for orientation.

The enclosed gravitational mass m shows good second-order convergence properties before bounce $t \lesssim 38$ ms, while convergence deteriorates to first order as the shock propagates outwards at $t \gtrsim 38$ ms. This is a characteristic feature of high-resolution shock-capturing schemes; they are second-order (or higher) schemes for smooth fields, but become first-order accurate in the presence of discontinuities [390]. Note that the behaviour of the total gravitational and baryonic mass is more complex than in the GR limit where both are

[7] For the convergence analysis, we use uniform grids exclusively, i.e. do not switch to a logarithmic spacing in the outer parts. Non-linear grid structure would make a quantitative convergence analysis highly complicated.

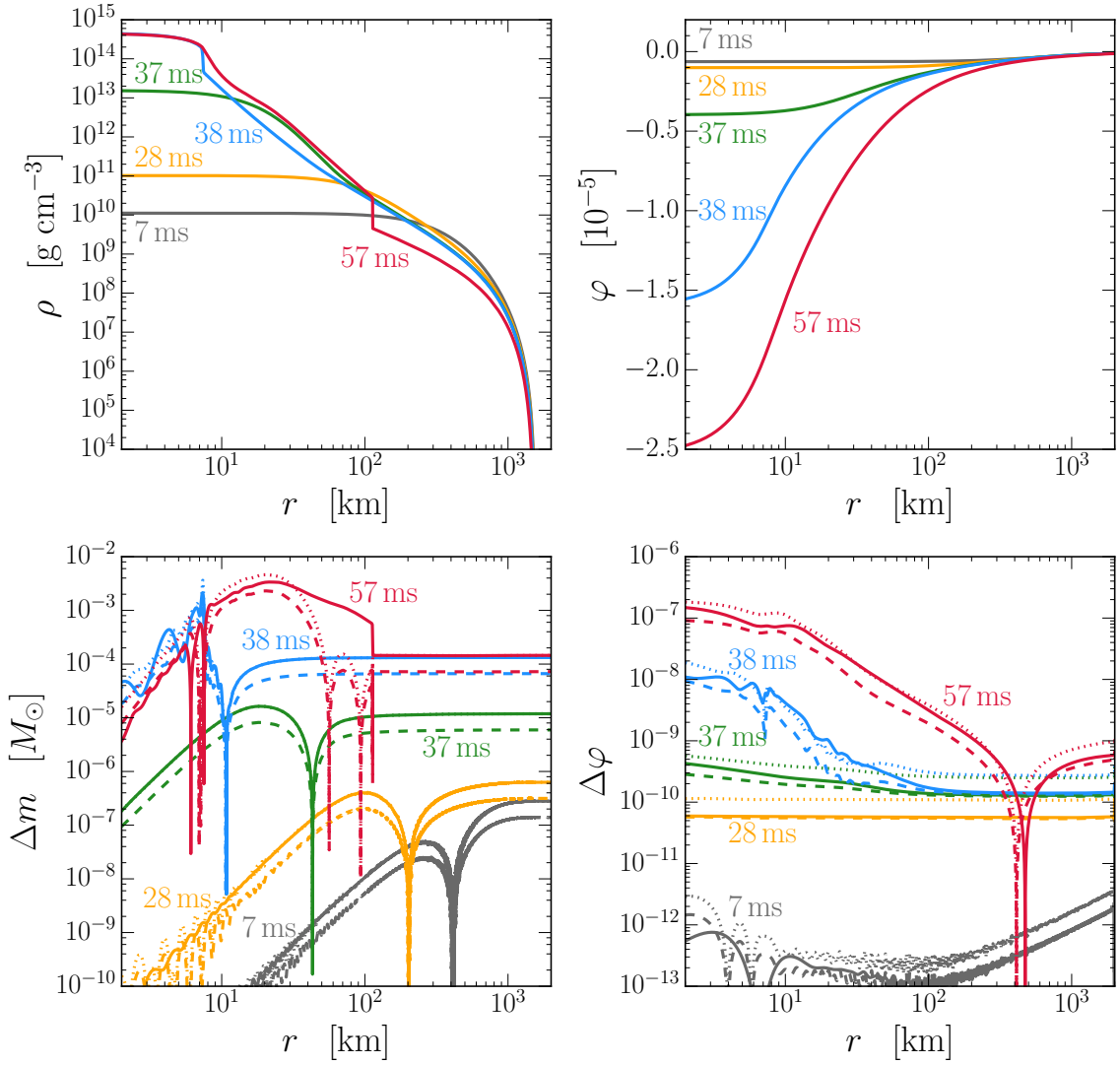

Figure 7.3: Convergence test of stellar collapse in ST theory with $\alpha_0 = 10^{-4}$ and $\beta_0 = -4.35$. A polytropic core is collapsed using the fiducial hybrid EOS for three different resolutions (see text for details). The top panels show the evolution of the mass density ρ (left) and the scalar-field φ (right) for the highest-resolution run at $t = 7$ (grey), 28 (yellow), 37 (green), 38 (blue), 57 (red) ms after starting the simulations. Bounce happens at $t \sim 38$ ms and the shock reaches the surface of the star at $t \sim 131$ ms. The bottom panels show the self-convergence properties of the gravitational mass m (left) and the scalar field φ (right) at the same times. As detailed in the text, solid and dotted (dashed) lines are expected to coincide for second- (first-) order convergence. We initially observe second order convergence which decreases to first order due to (i) the shock capturing scheme when a discontinuity forms at bounce and (ii) numerical noise in the scalar field propagating in from the outer boundary.

conserved because of the absence of gravitational radiation in spherical symmetry and the vanishing of the source term s_D in Eq. (7.38). The convergence properties of the scalar field are more complicated. While evolved with a second-order accurate scheme, we observe that the scalar field's convergence may deteriorate for the following two reasons: (i) the drop to first-order convergence of the matter fields which source the scalar dynamics; (ii) numerical noise generated at the outer boundary, especially during the early transient (note that in this convergence analysis the outer boundary is located much closer to the core than in our production runs because of the limit imposed by a strictly uniform grid). The observed convergence in the scalar field bears out these effects. Initially convergent at second order, we note a drop to roughly first order after one light crossing time $R_{\rm out}/c \sim 7$ ms. As the noise is gradually dissipated away, the convergence increases back towards second order, but drops once more to first order at the time the shock forms in the matter profile around 38 ms.

We also tested the convergence of the scalar waveform $\varphi(t)$ extracted at finite radius in these simulations and observe first-order convergence which we attribute to the relatively small total computational domain such that the outer boundary effects discussed above causally affect the extraction radius early in the simulation. The resulting uncertainty in the waveform is obtained by comparing the finite resolution result with the Richardson extrapolated (see, e.g., [296]) waveform. We find a relative error of 10% which we regard as a conservative estimate since the production runs have much larger computational domains.

7.5 Results and discussion

In this Section, we present the results of our simulations. After illustrating the main features of stellar collapse in ST theories (Sec. 7.5.1), we present our predictions for monopole gravitational radiation (Sec. 7.5.2). All waveforms presented in this Section are publicly available at [202].

7.5.1 Core-collapse dynamics

The main features of the core-collapse dynamics are summarised in Figs. 7.4 and 7.5. We present the collapse of both a polytropic core and two realistic pre-SN models (Sec. 7.3.3) in ST theory with $\alpha_0 = 10^{-4}$ and $\beta_0 = -4.35$. These parameter choices lie on the edge of the parameter space region compatible with binary pulsar experiments (cf. Fig. 7.1) and marginally allow for spontaneous scalarisation [386, 226]. Collapse is performed using the hybrid EOS (Sec. 7.3.1) with fiducial values $\Gamma_1 = 1.3$, $\Gamma_2 = 2.5$ and $\Gamma_{\rm th} = 1.35$.

Since $\Gamma_1 < 4/3$, the initial iron cores are not equilibrium solutions of the evolution

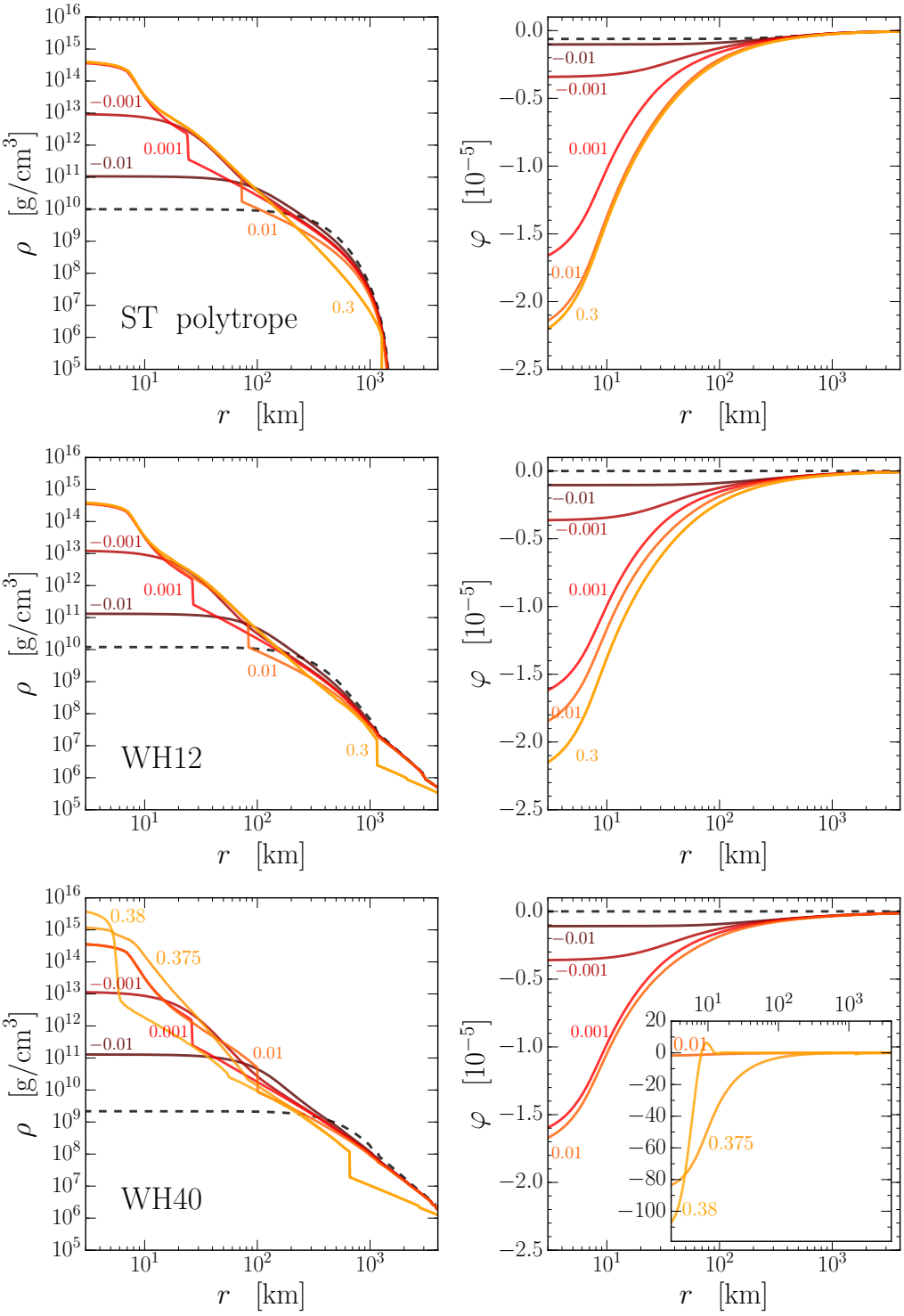

Figure 7.4: Collapse of a $\Gamma = 4/3$ polytrope (top), the $12M_\odot$ (centre) and $40M_\odot$ (bottom) pre-SN profiles of [547] in ST theory with $\alpha_0 = 10^{-4}$ and $\beta_0 = -4.35$, assuming $\Gamma_1 = 1.3$, $\Gamma_2 = 2.5$ and $\Gamma_{\rm th} = 1.35$. The evolution of the mass density ρ (left) and the scalar field φ (right) is shown as a function of the radius r at various timesteps $t - t_B = -0.01, -0.001, 0.001, 0.1, 0.3, 0.375, 0.38$ s, measured from the bounce time t_B. Timesteps are coloured from darker (early times) to lighter (late times) solid lines as labelled; initial profiles are shown with black dashed lines. The inset in the bottom right panel shows the wide variation of the scalar field when a BH is formed. An animated version of this figure is available online at [202].

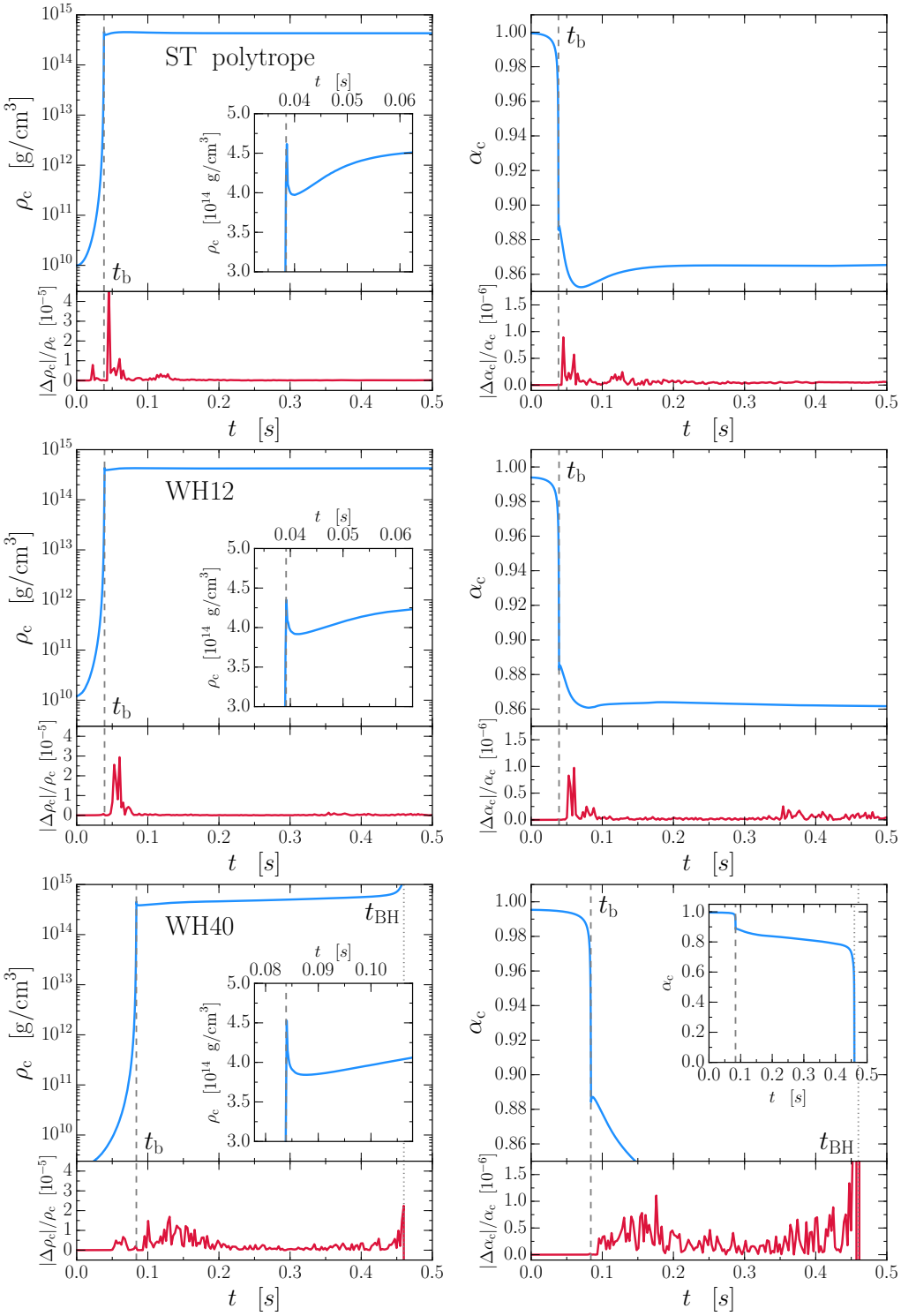

Figure 7.5: Evolution of the central values of the mass density ρ_c (left panels) and lapse function α_c (right panel) through collapse, bounce and late time evolution in ST theory with $\alpha_0 = 10^{-4}$ and $\beta_0 = -4.35$. We use the hybrid EOS with fiducial parameters ($\Gamma_1 = 1.3$, $\Gamma_2 = 2.5$ and $\Gamma_{\rm th} = 1.35$) and three different initial profiles: ST polytrope (top), WH12 (centre) and WH40 (bottom). Gray dashed lines mark the bounce time t_b; the WH40 profile first collapses to a protoneutron star and then to a BH at $t_{\rm BH} \sim 0.46\,$s marked by grey dotted lines. Relative differences with analogous simulations performed in GR are shown in the lower subpanels (red lines). Deviations in the dynamics are very small: of the order of $|\Delta\rho_c|/\rho_c \sim 10^{-5}$ and $|\Delta\alpha_c|/\alpha_c \sim 10^{-6}$.

equations and collapse is triggered dynamically. While the polytropic profile collapses smoothly from the very beginning of the simulation, a brief transient in the scalar-field evolution is present in the early stages of the collapse of both the WH12 and WH40 models. As already mentioned in Sec. 7.3.3, this is due to the fact that these initial models are Newtonian and their initially vanishing scalar profiles are not fully consistent with the ST theory used in the evolution. This transient generates a pulse in the scalar field propagating outwards at the speed of light. The scalar field quickly settles down in the stellar interior while the spurious pulse reaches the outer edge of the grid at $R_{\rm out}/c \sim 0.6$ s where it is absorbed by the outgoing boundary condition.

As the collapse proceeds in either of the three models, the central mass density increases from its initial value up to beyond nuclear densities $\rho_{\rm nuc} \simeq 2 \times 10^{14}$ g cm^{-3}. The EOS suddenly stiffens to an effective adiabatic index $\Gamma_2 \gg 4/3$ and the inner core bounces after $t_b \sim 38$, 39, and 84 ms from the beginning of the simulations, for the ST polytrope, WH12 and WH40 profile, respectively.[8] Core bounce launches a hydrodynamic shock into the outer core. Due to the steep density profile of the polytrope, the shock explodes the polytrope promptly, reaching its surface at ~ 130 ms from the start of the simulation. Since we set $\Gamma_{\rm th} = 1.35$ to qualitatively account for reduced pressure due to nuclear dissociation and neutrino losses, the pressure behind the shock is not sufficient to lead to a prompt explosion of the more realistic WH12 and WH40 progenitors. The shock stalls and only secularly moves to larger radii as the accretion rate decreases. Core bounce is paralleled by a small reversal in the scalar field amplitude. For example, in the collapse of the polytropic model shown in Fig. 7.4, the central value of φ reaches a minimum $\sim -2.6 \times 10^{-5}$ at bounce before settling down to $\sim -2.3 \times 10^{-5}$. A more detailed description of the scalar field dynamics is postponed to Sec. 7.5.2.

The inner regions of the promptly exploding polytropic model settle down to a stable compact remnant with compactness $m/r \sim 0.053$ (measured from the metric potential at $r = 10$ km). While simulations with model WH12 show that the shock stalls and then only slowly shifts to larger radii, the low accretion rate in this model does not increase its compactness above the values that we find for the polytropic model. In both models, the scalar charge ω evolves from $\sim -10^{-4}\ M_\odot$ to $\sim -2 \times 10^{-4}\ M_\odot$ during the entire evolution and thus remains of the order of $\omega/M \sim \alpha_0$, as predicted for weakly scalarised NS solutions (cf. Sec. 7.3.2). In both simulations, the NSs do not evolve to strongly spontaneously scalarised solutions because the compactness of the core remains lower than the threshold at which multiple solutions appear ($m/r \sim 0.2$ [179]).

[8] The WH40 profile takes longer to reach $\rho_{\rm nuc}$ because of its lower initial central density (cf. Fig. 7.2).

On the other hand, the WH40 model forms a protoneutron star that subsequently collapses to a BH within $t_{\rm BH} \sim 0.46\,$s from the beginning of the simulation ($\sim 0.38\,$s from bounce). The high accretion rate in this model quickly increases the central compactness. As BH formation is approached, our gauge choice causes the lapse function α to collapse to zero near the origin (Fig. 7.5) and the dynamics of the inner region effectively freezes. In this regime, spontaneously scalarised NS solutions are not only present but energetically favourable [144, 145, 225]. While collapsing towards a BH, the core first transits through a spontaneously scalarised NS. BH formation generates strong scalar-field excitation, enhanced in this case ($\beta_0 = -4.35$) by spontaneous scalarisation (cf. Sec. 7.5.2.2). The central value φ_c, which through collapse and bounce remains close to values of the order of $\sim -10^{-5}$, increases in magnitude to $\sim -2 \times 10^{-3}$. This signal propagates outwards at the speed of light, rapidly leaves the region of the stalled shock, and reaches the extraction radius after about ~ 0.56 s from the beginning of the simulation.

Our gauge choice does not allow us to follow the evolution of the inner region of the star beyond BH formation. Following [387], we terminate the evolution of the matter variables at the onset of BH formation in order to ensure numerical stability. At this point, the inner core has reached a compactness of ~ 0.466, close to the BH value of 0.5. We are still able to gain insight into the late-time behaviour of the scalar field, however, by solving the wave equation (7.8) on the now frozen background (cf. Fig. 7.4). We observe in these evolutions that, as the NS (now spontaneously scalarised) collapses to a BH, the scalar field slowly relaxes to a flat profile as predicted by the no-hair theorems [232, 507, 124, 62, 130].

Overall, the entire dynamics strongly resembles GR. The scalar field is mostly driven by the matter evolution, which in turn is largely independent of the scalar field propagation. This point is illustrated in Fig. 7.5, where the central values of the mass density ρ_c and lapse function α_c obtained in ST theory and in GR are compared. The relative differences between these two scenarios are about $|\Delta\rho_c|\rho_c \sim 10^{-5}$ and $|\Delta\alpha_c|/\alpha_c \sim 10^{-6}$ throughout collapse, bounce, and (eventually) BH formation.

7.5.2 Monopole GW emission

Unlike GR, ST theories of gravity admit propagating monopole GWs. This breathing mode of the scalar field is potentially detectable with current and future GW interferometers which have therefore the potential of constraining the parameters of the theory. We now analyse the scalar GW signal extracted from our numerical simulations, separately discussing the effects of the EOS and the ST parameters.

7.5.2.1 Effect of the EOS

As detailed in Sec. 7.3.1, the hybrid EOS is a simplified EOS model that qualitatively approximates more sophisticated microphysical EOSs in the core collapse context (e.g., [304]). The hybrid EOS is characterised by three adiabatic indices for the pre-bounce dynamics (Γ_1), the repulsion at nuclear densities (Γ_2), and the response of the shocked material ($\Gamma_{\rm th}$). The effect of the EOS on the emitted GW waveforms is explored in Fig. 7.6, where we show time-domain monopole waveforms $h(t) \propto r\varphi$ [cf. Eq. (7.66) with $\varphi_0 = 0$] for various choices of Γ_1, Γ_2, and $\Gamma_{\rm th}$. All simulations shown in Fig. 7.6 are performed in ST theory with $\alpha_0 = 10^{-4}$ and $\beta_0 = -4.35$, the lower limit of β_0 compatible with present observations, using the WH12 and WH40 initial profiles. We plot the GW signals as a function of the retarded time $t - r/c$, such that the origin corresponds to a single light-crossing time at the extraction radius $r_{\rm ext} = 3 \times 10^4$ km.

The structure of the emitted signals displayed in Fig. 7.6 consists of the following four main stages.

1. The initial pulse of spurious radiation arises from the initialisation of the scalar field, as already pointed out in Secs. 7.3.3 and 7.5.1. This pulse propagates outwards and leaves the extraction region after a retarded time of about 0.006 s.

2. As the core collapses, the scalar field signal significantly grows in amplitude. Although the first ~ 0.02 s of the waveform appear to be rather insensitive to the EOS, the adiabatic indices strongly affect the total amount of time the star spends in the collapse phase before bounce. In the hybrid EOS, this is controlled by Γ_1. Collapse is triggered by $\Gamma_1 \leq 4/3$ and the smaller Γ_1, the more rapid the collapse and the smaller the mass of the inner core that collapses homologously (e.g., [555, 157]). We note that in reality (and in simulations using more realistic microphysics), Γ_1 is not a parameter. Instead, the effective adiabatic index is a complex function of the thermodynamics and electron capture during collapse [157, 158]. Figure 7.6 shows that core bounce occurs in our simulations at retarded time $t - r_{\rm ext}/c \sim 0.03, 0.04, 0.08$ s $(0.06, 0.07, 0.14)$ for model WH12 (WH40) and $\Gamma_1 = 1.28, 1.3, 1.32$ respectively. The bounce itself is a rapid process with a duration of $\Delta t \sim 1 - 2$ ms.

3. After bounce, the scalar field in the inner core settles down to a non-trivial profile, as illustrated in Fig. 7.4. The post-bounce value of φ at $r_{\rm ext}$, hence the value of $h(t)$, encodes information about all three adiabatic indices. In particular, larger values of Γ_1 and smaller values of $\Gamma_{\rm th}$ both produce stronger wave signals $h(t)$, which can be intuitively understood as follows. Larger values of Γ_1 result in a more massive

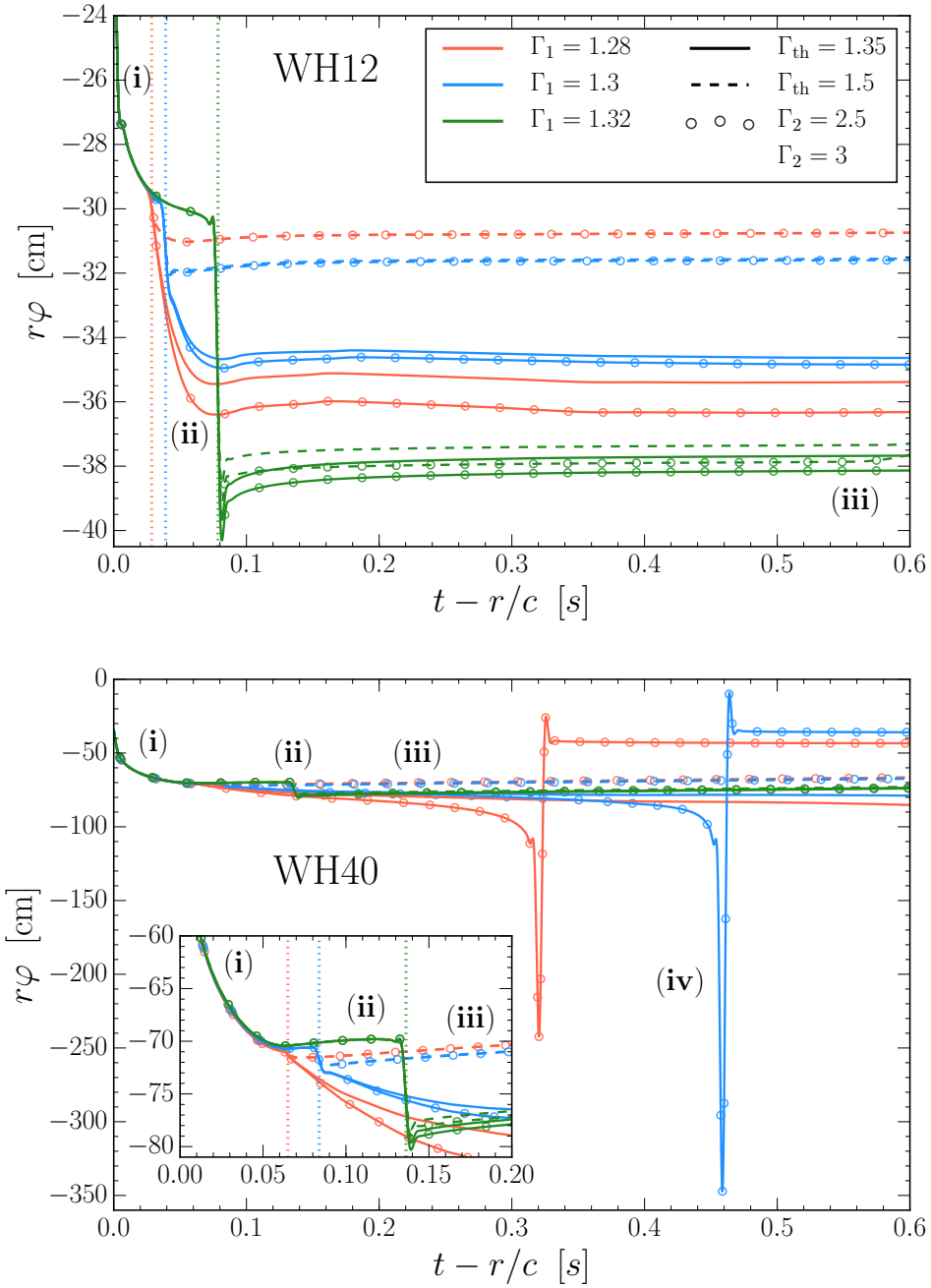

Figure 7.6: Effect of the hybrid EOS adiabatic indices on the emitted monopole gravitational waveform $h(t) \propto r\varphi$ [cf. Eq.(7.66)]. The signal is plotted against the retarded time $t - r/c$ at the extraction radius. Simulations are performed using the preSN initial profiles WH12 (top) and WH40 (bottom) in ST theory with $\alpha_0 = 10^{-4}$ and $\beta_0 = -4.35$. The curves encode the value of Γ_1 in their brightness (colour) and the value of $\Gamma_{\rm th}$ in their line style: $\Gamma_1 = 1.28$ (red), 1.3 (blue), 1.35 (green); $\Gamma_{\rm th} = 1.35$ (solid), 1.5 (dashed). For each of these combinations, two curves are present: circles mark simulations with $\Gamma_2 = 2.5$, while no symbols are shown for $\Gamma_2 = 3$. For some cases, these two curves overlap to such high precision that they become indistinguishable in the plot. The lower-case Roman labels refer to the key phases of the GW signal described in Sec. 7.5.2.1: **(i)** initial pulse of the spurious radiation; **(ii)** collapse and bounce; **(iii)** NS configuration; **(iv)** BH formation. The bounce time is marked with vertical dotted lines following the same colour codes of the other curves. Note that Γ_1 is the only adiabatic index that has an effect on the bounce time. Waveforms presented in this figure are available at [202].

inner core in the pre-bounce stage because the speed of sound is larger and, hence, more matter remains in sonic contact in the central region. At bounce, this implies a more compact core and a correspondingly larger amplitude in the scalar wave. Smaller values of $\Gamma_{\rm th}$ imply lower pressure in the shocked material, and, therefore, material that accretes through the shock settles faster onto the protoneutron star. In terms of microphysical processes, this effect is driven by neutrino cooling [157, 158], which is not included in our simulations. In contrast, we find that Γ_2 has a relatively minor effect on this phase of the wave signal: the scalar field profile is only slightly more pronounced for lower values of Γ_2, which result in a deeper bounce and a more compact postbounce configuration. Note that in the waveforms shown in Fig. 7.6, both $\Gamma_{\rm th}$ and Γ_2 only affect the wave signal at and after bounce. This is expected, since $\Gamma_{\rm th}$ only plays a role in the presence of shocked material and Γ_2 affects only the high density regime of the EOS not encountered in the collapse evolution prior to bounce.

4. Two of the simulations shown in Fig. 7.6 (namely $\Gamma_1 = 1.28, 1.3$; $\Gamma_2 = 2.5$; $\Gamma_{\rm th} = 1.35$) for the WH40 profile collapse to BHs. BH formation is triggered when the protoneutron star exceeds its maximum mass and is therefore facilitated and accelerated by smaller values of the adiabatic indices. BH formation generates a very large pulse in the scalar field which dominates the entire GW signal. Spontaneous scalarisation (marginally allowed for the value $\beta_0 = -4.35$ chosen here) before BH formation further enhances the signal. The amplitude of the scalar field signal from this phase is more than an order of magnitude larger than the bounce signal in the absence of BH formation. We expect BH-forming collapse events to be the most promising source of monopole GWs in the context of ST theory.

7.5.2.2 Effect of the ST parameters.

As introduced in Sec. 7.3.2, PN deviations from GR in ST theories only depend on two parameters, α_0 and β_0. While α_0 mainly controls the perturbative deviation from GR, β_0 is responsible for non-linear effects such as spontaneous scalarisation. Our primary interest in this Section is to explore the effect of these parameters on the detectability of signals with current and future GW detectors and, in particular, comparison with their sensitivity curves.

Figures 7.7 and 7.8 show frequency domain waveforms $\sqrt{S_h(f)}$ compared with the expected (design) sensitivity curves $\sqrt{S_n(f)}$ of Advanced LIGO and ET. We use the WH12 and WH40 initial profiles, together with the hybrid EOS with fiducial values $\Gamma_1 = 1.3$,

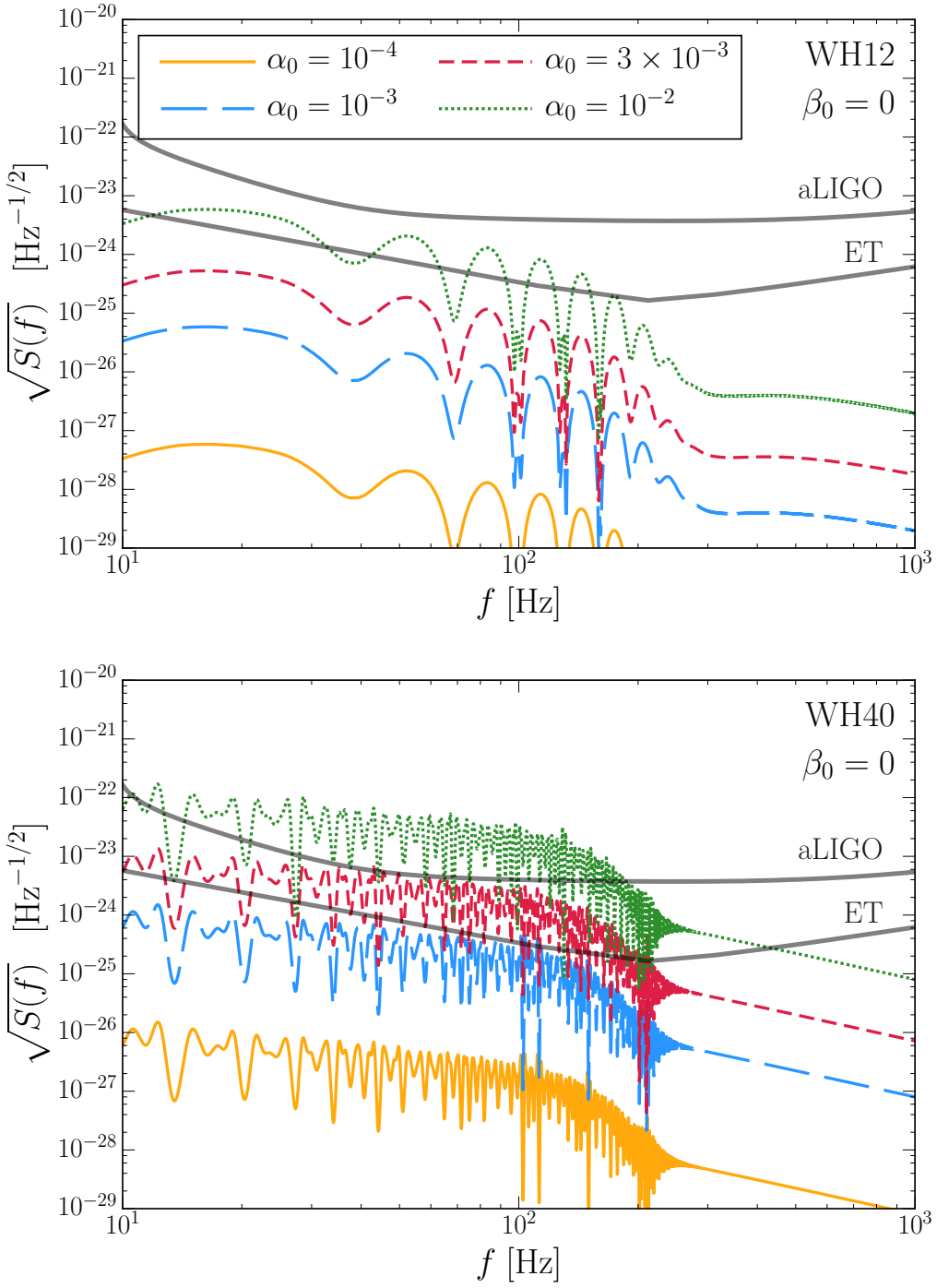

Figure 7.7: Effect of α_0 on frequency domain waveforms for monopole GWs emitted during stellar collapse. The $M_{\rm ZAMS} = 12M_\odot$ (top) and $40M_\odot$ (bottom) pre-SN models of Ref. [547] are evolved using the hybrid EOS with $\Gamma_1 = 1.3$, $\Gamma_2 = 2.5$ and $\Gamma_{\rm th} = 1.35$. Four simulations are presented for fixed $\beta_0 = 0$ (equivalent to Brans-Dicke theory): $\alpha_0 = 10^{-4}$ (orange, solid), 10^{-3} (blue, long-dashed), 3×10^{-3} (red, short-dashed), 10^{-2} (green, dotted). These values are compared with current experimental constraints in Fig. 7.1. We consider optimally oriented sources placed at $D = 10$ kpc and compare them with the expected sensitivity curves of Advanced LIGO and ET. Waveforms presented in this figure are available at [202].

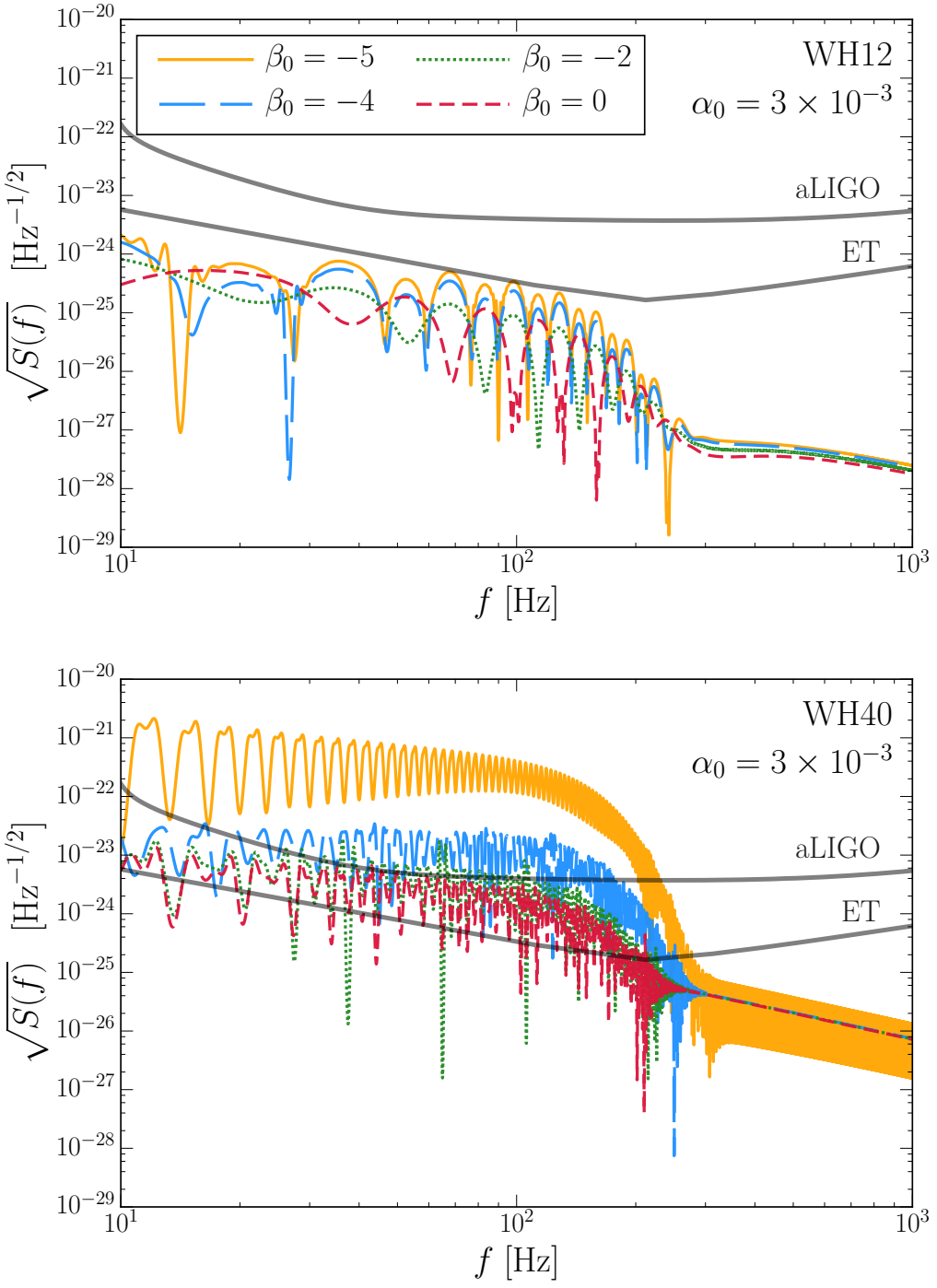

Figure 7.8: Effect of β_0 on frequency domain waveforms for monopole GWs emitted during stellar collapse. The $M_{\rm ZAMS} = 12M_\odot$ (top) and $40M_\odot$ (bottom) pre-SN models of Ref. [547] are evolved using the hybrid EOS with $\Gamma_1 = 1.3$, $\Gamma_2 = 2.5$ and $\Gamma_{\rm th} = 1.35$. Four simulations are presented for fixed $\alpha_0 = 3 \times 10^{-3}$ (marginally allowed by solar-system constraints): $\beta_0 = -5$ (orange, solid), -4 (blue, long-dashed), -2 (green, dotted), 0 (red, short-dashed). These values are compared with current experimental constraints in Fig. 7.1. We consider optimally oriented sources placed at $D = 10$ kpc and compare them with the expected sensitivity curves of Advanced LIGO and ET. Waveforms presented in this figure are available at [202].

$\Gamma_2 = 2.5$, and $\Gamma_{\rm th} = 1.35$ (cf. Sec. 7.3.1). To better disentangle the effect of the two ST parameters, Fig. 7.7 (7.8) presents a series of simulations where only α_0 (β_0) varies while the other parameter is kept fixed at $\beta_0 = 0$ ($\alpha_0 = 3 \times 10^{-3}$). These two parameter sets overlap at $\alpha_0 = 3 \times 10^{-3}$ and $\beta_0 = 0$ and this specific simulation is shown in both figures. The location of our runs in the (α_0, β_0) parameter space is shown in Fig. 7.1. Throughout our analysis, we consider optimally oriented sources placed at a fiducial distance of $D = 10$ kpc, i.e. within the Milky Way.

As mentioned above, the most pronounced feature in the emitted waveform arises from the collapse of the protoneutron star to a BH. As a consequence, the GW strains emitted during collapse of the $M_{\rm ZAMS} = 40 M_\odot$ profile WH40 are over an order of magnitude larger than the corresponding signals obtained from the collapse of the WH12 profile. BH formation (possibly enhanced by spontaneous scalarisation – see below) following the protoneutron star phase is the most promising signature of monopole GWs in the context of ST theory.

Simulations presented in Fig. 7.7 are performed in ST theory with $\beta_0 = 0$ and various values of α_0, equivalent to Brans-Dicke theory with $\omega_{\rm BD} = (1 - 6\alpha_0^2)/2\alpha_0^2$. Since spontaneously scalarised stars are not permitted in this regime, this set of simulations illustrates the effect of perturbative deviations from GR. In ST theory with $\alpha_0 \sim 3 \times 10^{-3}$, just compatible with the Cassini bound, GW signals generated by BH formation in our Galaxy, are marginally detectable by second-generation ground-based detectors and fall well into the sensitivity range of future experiments like ET. Observation of a BH forming core collapse event with Advanced LIGO therefore has the potential of independently constraining ST theory at a level comparable with the most stringent present tests. Future third-generation observatories, on the other hand, will be able to push the constraint to new levels: $\alpha_0 \lesssim \times 10^{-4}$ corresponding to $|\gamma^{\rm PPN} - 1| \lesssim 2 \times 10^{-8}$; cf. Eq. (7.50). On the other hand, our present results suggest that core collapse forming NSs (such as in our WH12 model) will at best allow for an independent confirmation of existing bounds, even when observed with third-generation observatories.

By analysing the curves in Fig. 7.7 quantitatively, we observe that the amplitude of the GW signal scales approximately as α_0^2. One factor of α_0 is evidently due to the local coupling between the scalar field and the detector [see Eq. (7.66)]. In our simulations, however, we find that the amplitude of the emitted scalar field φ also depends (roughly linearly) on α_0. This second factor of α_0 is entirely due to the source dynamics and therefore separate from that arising in the coupling between the wave and the detector at the moment of observation. Even though the dynamics in the matter variables only mildly

deviates from the GR case (cf. Fig. 7.5), such perturbative deviations from GR of the order α_0 can leave a significant imprint on the generation of monopole GWs.

The strongest effect of β_0 on the structure of NSs is that of allowing for spontaneously scalarised stars in the range $\beta_0 \lesssim -4.35$. In fact, it is precisely the strength of this effect that enables binary pulsar observations to severely constrain β_0 as displayed in Fig. 7.1. For our simulations using values of β_0 significantly above the spontaneous scalarisation threshold of about -4.35, we only identify a relatively minor variation of the scalar wave with β_0. This is well illustrated by the curves in Fig. 7.8 corresponding to $\beta_0 = 0$ and -2. Deviations of this kind can become particularly pronounced for $\beta_0 \lesssim -4.35$ *if* the strongly non-linear effects of spontaneous scalarisation are triggered [386, 226, 144, 145]; cf. Fig. 7.8. Whether this effect is triggered in our simulations and, in consequence, the shape and magnitude of the resulting waveform, critically depends on the stellar progenitor.

- If the core collapse leads to a protoneutron star that subsequently collapses to a BH, spontaneous scalarisation can be triggered by the high compactness reached shortly before BH formation, leading to a large enhancement of the GW signal. In the bottom panel of Fig. 7.8, we compare the frequency-domain GW signals for the BH-forming WH40 progenitor. Spontaneous scalarisation occurs in a very strong way for the model with $\beta_0 = -5$ (already ruled out by current constraints) and leads to an enhancement of $\sim$two orders of magnitude in the amplitude compared to models that do not exhibit this strong non-linear behaviour (cases with $\beta_0 = 0$ and $\beta_0 = -2$). The waveform of the model with $\beta = -4$ (still allowed) is also somewhat enhanced by non-linear scalar field dynamics. Given the quantitative differences between these waveforms, present and future detectors have the potential of either observing scalar waves from BH-forming core collapse events or use their absence in the data stream to constrain the parameter β_0 beyond current limits. This will, however, require that other uncertain parameters such as the distance to the source etc. can be determined with high precision.

- None of our simulations of the progenitor model WH12 leads to BH formation in the time simulated. This is so because this moderate-mass progenitor has a steep density gradient outside its core and thus a lower postbounce accretion rate. If no explosion is launched, a BH would still result, though on a timescale of $\mathcal{O}(10)$ s [391]. Furthermore, we do not observe any signature of spontaneous scalarisation in the waveform or in the protoneutron star of the WH12 model, even for the extreme case $\beta_0 = -5$ (cf. Fig. 7.8, top panel). An analogous conclusion holds for collapse of ST polytropes, cf. Sec. 7.3.3. The reason for this absence of spontaneous scalarisation in

these models lies in the insufficient compactness of their protoneutron stars. At the end of our simulations, the protoneutron star in model WH12 has a compactness of $m/r \sim 0.05$ (at $r = 10$ km), significantly lower than the threshold of ~ 0.2 at which multiple families of stationary solutions appear [179].

The final compactness reached by NS remnants is naturally model dependent and the microphysics implemented in our analysis is greatly simplified by the use of the hybrid EOS. The possibility of triggering spontaneous scalarisation in stellar core collapse forming NSs (as opposed to BHs) clearly requires further exploration with more realistic finite-temperature EOS, which is left to future work. Dissociation of accreting heavy nuclei at the shock and neutrino cooling act indeed in the direction of lowering the effective adiabatic index in the postshock region, thus facilitating a more rapid increase in the protoneutron star's mass and compactness [432]. We probe this expectation within our current framework by evolving the WH12 model with an adiabatic index $\Gamma_{\rm th}$ artificially lowered to 1.25. With such a low value of $\Gamma_{\rm th}$, the shock stalls at a small radius and material accreting through the shock quickly settles onto the protoneutron star, driving up its mass and compactness. At the end of our simulation, at 0.7 s, the protoneutron star in this model has reached a compactness of ~ 0.18 and is spontaneously scalarised. Configurations with non-trivial scalar-field profiles are energetically favoured over their weak-field counterparts and the dynamical evolutions naturally settle there. The GW strain $\sqrt{S_h(f)}$ increases by roughly two orders of magnitude when compared to runs performed using the more realistic value $\Gamma_{\rm th} = 1.35$. Galactic signals from spontaneously scalarised NSs, if formed in core collapse, will likely be detectable by Advanced LIGO even beyond the Cassini bound $\alpha_0 = 3 \times 10^{-3}$. Given its observational potential, this topic definitely merits further investigation with more realistic microphysics.

7.6 Future prospects and improvements

Our study presents an extension of the open-source code GR1D [390] to ST theories of gravity. The required additions to GR1D can be summarised as follows:

1. generalisation of the flux and source terms in the high-resolution shock capturing scheme according to (7.35)–(7.40) as well as the constraint equations (7.22), (7.23) for the metric components;

2. implementation of the evolution of the scalar field according to Eqs. (7.27)–(7.29) using standard finite differencing;

3. outgoing radiation boundary condition for the scalar field (7.32), (7.33).

The scalar field furthermore introduces a new radiative degree of freedom propagating at the speed of light, which requires a smaller numerical timestep. All presented time evolutions start from one of two types of initial data, (i) polytropic models obtained by solving the time independent limit of the evolution equations and (ii) more realistic pre-SN models from ZAMS stars of masses 12 and $40M_\odot$ [547].

In this framework, we have simulated a large number of collapse scenarios which are characterised by five parameters: the linear and quadratic coefficients α_0 and β_0 determining the coupling function of the ST theory and the adiabatic indices Γ_1, Γ_2 and $\Gamma_{\rm th}$, characterising the phenomenological hybrid EOS used in the time evolution. We summarise our main observations as follows.

- The most prominent GW signals are detected from the collapse of progenitor stars that form BHs after a protoneutron star phase (such as the $M_{\rm ZAMS} = 40M_\odot$ model of [547]), as opposed to collapse events forming long-term stable NSs. The collapse of protoneutron stars to BHs is the most promising dynamical feature for monopole gravitational radiation in the context of ST theories.

- The dynamical features in the matter fields (density, mass function, pressure) resemble closely those obtained in the general relativistic limit $\alpha_0 = \beta_0 = 0$. In other words, the effect of the scalar field on the matter dynamics is weak.

- The opposite is not true. The scalar radiation or GW *breathing mode* is sensitive to the specifics of the collapse dynamics as well as the choice of ST parameters α_0 and β_0. The observed dependencies are of the kind one would intuitively expect. EOS and progenitors giving rise to more compact post-collapse configurations result in stronger radiation and the amplitude of the scalar wave sensitively increases with α_0 with approximately a quadratic dependence.

- The ST parameter β_0 is known to generate strongly non-linear effects in the scalar field for $\beta_0 \lesssim -4.35$, the so-called *spontaneous scalarisation* [144, 145]. For progenitors collapsing to BHs after a protoneutron star phase, transition of the central core to a spontaneously scalarised configuration before BH formation further enhances the outgoing GW signal. For progenitors forming NSs but not BHs, we do not find spontaneously scalarised configurations for physically plausible values of the adiabatic indices in our hybrid EOS. We attribute this to the stellar compactness achieved in those collapse scenarios being insufficient to trigger spontaneous scalarisation. This

observation may be an artefact of our simplistic treatment of microphysics in our simulations

- We have extracted waveforms from a large set of simulations and compared their amplitude for the case of a fiducial distance $D = 10$ kpc with the sensitivity curves of Advanced LIGO and ET. Given the present constraints from the Cassini probe, $\alpha_0 \lesssim 3 \times 10^{-3}$, scalar radiation may be marginally detectable from galactic sources. This offers the possibility of providing constraints on ST theory with GW observations in case of a favourable event occurring in the Milky Way. Considerable power is emitted at low frequencies $f \lesssim 10$ Hz, thus making core collapse in ST theory ideal sources for future experiments such as DECIGO [266].

The impact of more realistic microphysics, as for example nuclear dissociation at the shock and neutrino cooling, on the compactness of the core and, thus, its degree of scalarisation, represents one key extension left for future work. Our analysis has shown that the massive increase in wave amplitudes due to spontaneous scalarisation and BH formation has the potential to drastically increase the range for detection. The $\mathcal{O}(10^3)$ waveforms generated for this work were completed in less than a week using $\mathcal{O}(10^2)$ CPU cores simultaneously. A moderate increase in the computational resources will make simulations using tabulated finite-temperature EOS feasible. Since the matter fields' dynamics is very similar to the GR case, one may perhaps take advantage of existing GR simulations and simulate the scalar field evolution using such GR results as backgrounds. A further numerical improvement may consist in computing (perhaps iteratively) approximate initial conditions for the scalar field from existing pre-collapse stellar models (such as WH12 and WH40 used in this study), in order to reduce the brief unphysical transient in the GW signal.

Aside from the treatment of the microphysics, our study offers further scope for extension. The effects of multiple scalar fields in ST theories on gravitational collapse remains largely unknown in spite of some early studies [143] (see [247] for an analysis of static NS solutions in this framework), but represents a relatively minor addition to our code. The same holds for ST theories with non-vanishing potential, as for example massive fields [26, 436].

As GW physics and astronomy are ushering in a new era, the community will be offered a wealth of unprecedented opportunities to observationally test generalisations of GR. Stellar collapse clearly offers a vast potential for such fundamental tests.

Bibliography

[1] Aasi J., Abadie J., Abbott B.P., Abbott R., Abbott T., Abernathy M.R., Accadia T., Acernese F., Adams C., Adams T., et al. (2014). "Gravitational Waves from Known Pulsars: Results from the Initial Detector Era". *Astrophysical Journal*, **785**:119. 1309.4027.

[2] Aasi J., Abadie J., Abbott B.P., Abbott R., Abbott T., Abernathy M.R., Accadia T., Acernese F., Adams C., Adams T., et al. (2015). "Characterization of the LIGO detectors during their sixth science run". *Classical and Quantum Gravity*, **32**(11):115012. 1410.7764.

[3] Aasi J., Abbott B.P., Abbott R., Abbott T., Abernathy M.R., Ackley K., Adams C., Adams T., Addesso P., et al. (2015). "Advanced LIGO". *Classical and Quantum Gravity*, **32**(7):074001. 1411.4547.

[4] Abadie J., Abbott B.P., Abbott R., Abbott T.D., Abernathy M., Accadia T., Acernese F., Adams C., Adhikari R., Affeldt C., et al. (2012). "All-sky search for gravitational-wave bursts in the second joint LIGO-Virgo run". *Physical Review D*, **85**(12):122007. 1202.2788.

[5] Abadie J., Abbott B.P., Abbott R., Abernathy M., Adams C., Adhikari R., Ajith P., Allen B., Allen G., Amador Ceron E., et al. (2010). "Calibration of the LIGO gravitational wave detectors in the fifth science run". *Nuclear Instruments and Methods in Physics Research A*, **624**:223–240. 1007.3973.

[6] Abbott B.P., Abbott R., Abbott T.D., Abernathy M.R., Acernese F., Ackley K., Adams C., Adams T., Addesso P., Adhikari R.X., et al. (2016). "Astrophysical Implications of the Binary Black-hole Merger GW150914". *Astrophysical Journal Letters*, **818**:L22. 1602.03846.

[7] Abbott B.P., Abbott R., Abbott T.D., Abernathy M.R., Acernese F., Ackley K., Adams C., Adams T., Addesso P., Adhikari R.X., et al. (2016). "Binary Black Hole Mergers in the first Advanced LIGO Observing Run". *ArXiv e-prints*. 1606.04856.

[8] Abbott B.P., Abbott R., Abbott T.D., Abernathy M.R., Acernese F., Ackley K., Adams C., Adams T., Addesso P., Adhikari R.X., et al. (2016). "GW150914: First results from the search for binary black hole coalescence with Advanced LIGO". *Physical Review D*, **93**(12):122003. 1602.03839.

[9] Abbott B.P., Abbott R., Abbott T.D., Abernathy M.R., Acernese F., Ackley K., Adams C., Adams T., Addesso P., Adhikari R.X., et al. (2016). "GW150914: Implications for the Stochastic Gravitational-Wave Background from Binary Black Holes". *Physical Review Letters*, **116**(13):131102.

[10] Abbott B.P., Abbott R., Abbott T.D., Abernathy M.R., Acernese F., Ackley K., Adams C., Adams T., Addesso P., Adhikari R.X., et al. (2016). "GW150914: The Advanced LIGO Detectors in the Era of First Discoveries". *Physical Review Letters*, **116**(13):131103.

[11] Abbott B.P., Abbott R., Abbott T.D., Abernathy M.R., Acernese F., Ackley K., Adams C., Adams T., Addesso P., Adhikari R.X., et al. (2016). "GW151226: Observation of Gravitational Waves from a 22-Solar-Mass Binary Black Hole Coalescence". *Physical Review Letters*, **116**(24):241103. 1606.04855.

[12] Abbott B.P., Abbott R., Abbott T.D., Abernathy M.R., Acernese F., Ackley K., Adams C., Adams T., Addesso P., Adhikari R.X., et al. (2016). "Localization and Broadband Follow-up of the Gravitational-wave Transient GW150914". *Astrophysical Journal Letters*, **826**:L13. 1602.08492.

[13] Abbott B.P., Abbott R., Abbott T.D., Abernathy M.R., Acernese F., Ackley K., Adams C., Adams T., Addesso P., Adhikari R.X., et al. (2016). "Observation of Gravitational Waves from a Binary Black Hole Merger". *Physical Review Letters*, **116**(6):061102. 1602.03837.

[14] Abbott B.P., Abbott R., Abbott T.D., Abernathy M.R., Acernese F., Ackley K., Adams C., Adams T., Addesso P., Adhikari R.X., et al. (2016). "Observing gravitational-wave transient GW150914 with minimal assumptions". *Physical Review D*, **93**(12):122004. 1602.03843.

[15] Abbott B.P., Abbott R., Abbott T.D., Abernathy M.R., Acernese F., Ackley K., Adams C., Adams T., Addesso P., Adhikari R.X., et al. (2016). "Properties of the Binary Black Hole Merger GW150914". *Physical Review Letters*, **116**(24):241102.

[16] Abbott B.P., Abbott R., Abbott T.D., Abernathy M.R., Acernese F., Ackley K., Adams C., Adams T., Addesso P., Adhikari R.X., et al. (2016). "Prospects for

Observing and Localizing Gravitational-Wave Transients with Advanced LIGO and Advanced Virgo". *Living Reviews in Relativity*, **19**. 1304.0670.

[17] Abbott B.P., Abbott R., Abbott T.D., Abernathy M.R., Acernese F., Ackley K., Adams C., Adams T., Addesso P., Adhikari R.X., et al. (2016). "Tests of General Relativity with GW150914". *Physical Review Letters*, **116**(22):221101. 1602.03841.

[18] Abbott B.P., Abbott R., Abbott T.D., Abernathy M.R., Acernese F., Ackley K., Adams C., Adams T., Addesso P., Adhikari R.X., et al. (2016). "The Rate of Binary Black Hole Mergers Inferred from Advanced LIGO Observations Surrounding GW150914". *ArXiv e-prints*. 1602.03842.

[19] Abbott B.P., Abbott R., Abbott T.D., Abernathy M.R., Acernese F., Ackley K., Adams C., Adams T., et al. (2016). "An improved analysis of GW150914 using a fully spin-precessing waveform model". *ArXiv e-prints*. 1606.01210.

[20] Abbott B.P., Abbott R., Abbott T.D., Abernathy M.R., Acernese F., Ackley K., Adams C., Adams T., et al. (2016). "Directly comparing GW150914 with numerical solutions of Einstein's equations for binary black hole coalescence". *ArXiv e-prints*. 1606.01262.

[21] Abbott B.P., Abbott R., Acernese F., Adhikari R., Ajith P., Allen B., Allen G., Alshourbagy M., Amin R.S., Anderson S.B., et al. (2009). "An upper limit on the stochastic gravitational-wave background of cosmological origin". *Nature*, **460**:990–994. 0910.5772.

[22] Abbott B.P., Abbott R., Adhikari R., Ajith P., Allen B., Allen G., Amin R.S., Anderson S.B., Anderson W.G., Arain M.A., et al. (2009). "LIGO: the Laser Interferometer Gravitational-Wave Observatory". *Reports on Progress in Physics*, **72**(7):076901. 0711.3041.

[23] Acernese F., Agathos M., Agatsuma K., Aisa D., Allemandou N., Allocca A., Amarni J., Astone P., Balestri G., Ballardin G., et al. (2015). "Advanced Virgo: a second-generation interferometric gravitational wave detector". *Classical and Quantum Gravity*, **32**(2):024001. 1408.3978.

[24] Ade P.A.R., Aghanim N., Arnaud M., Ashdown M., Aumont J., Baccigalupi C., Banday A.J., Barreiro R.B., Bartlett J.G., et al. (2015). "Planck 2015 results. XIII. Cosmological parameters". *ArXiv e-prints*. 1502.01589.

[25] Alcubierre M. (2008). *Introduction to 3+1 Numerical Relativity*. Oxford University Press.

[26] Alsing J., Berti E., Will C.M., Zaglauer H. (2012). "Gravitational radiation from compact binary systems in the massive Brans-Dicke theory of gravity". *Physical Review D*, **85**(6):064041. 1112.4903.

[27] Amaro-Seoane P., Aoudia S., Babak S., Binétruy P., Berti E., Bohé A., Caprini C., Colpi M., Cornish N.J., Danzmann K., et al. (2012). "Low-frequency gravitational-wave science with eLISA/NGO". *Classical and Quantum Gravity*, **29**(12):124016. 1202.0839.

[28] Amaro-Seoane P., Aoudia S., Babak S., Binétruy P., Berti E., Bohé A., Caprini C., Colpi M., Cornish N.J., Danzmann K., et al. (2013). "eLISA: Astrophysics and cosmology in the millihertz regime". *GW Notes, Vol. 6, p. 4-110*, **6**:4–110. 1201.3621.

[29] Amaro-Seoane P., Gair J.R., Pound A., Hughes S.A., Sopuerta C.F. (2015). "Research Update on Extreme-Mass-Ratio Inspirals". *Journal of Physics Conference Series*, **610**(1):012002. 1410.0958.

[30] Antoniadis J., Freire P.C.C., Wex N., Tauris T.M., Lynch R.S., van Kerkwijk M.H., Kramer M., Bassa C., Dhillon V.S., Driebe T., et al. (2013). "A Massive Pulsar in a Compact Relativistic Binary". *Science*, **340**:448. 1304.6875.

[31] Apostolatos T.A., Cutler C., Sussman G.J., Thorne K.S. (1994). "Spin-induced orbital precession and its modulation of the gravitational waveforms from merging binaries". *Physical Review D*, **49**:6274–6297.

[32] Armano M., Audley H., Auger G., Baird J.T., Bassan M., Binetruy P., Born M., Bortoluzzi D., Brandt N., Caleno M., et al. (2016). "Sub-Femto-g Free Fall for Space-Based Gravitational Wave Observatories: LISA Pathfinder Results". *Physical Review Letters*, **116**(23):231101.

[33] Armano M., Benedetti M., Bogenstahl J., Bortoluzzi D., Bosetti P., Brandt N., Cavalleri A., Ciani G., Cristofolini I., Cruise A.M., et al. (2009). "LISA Pathfinder: the experiment and the route to LISA". *Classical and Quantum Gravity*, **26**(9):094001.

[34] Armitage P.J. (2010). *Astrophysics of Planet Formation*. Cambridge, UK, Cambridge University Press.

[35] Armitage P.J., Natarajan P. (2002). "Accretion during the Merger of Supermassive Black Holes". *Astrophysical Journal Letters*, **567**:L9–L12. astro-ph/0201318.

[36] Artymowicz P., Lubow S.H. (1994). "Dynamics of binary-disk interaction. 1: Resonances and disk gap sizes". *Astrophysical Journal*, **421**:651–667.

[37] Arun K.G., Babak S., Berti E., Cornish N., Cutler C., Gair J., Hughes S.A., Iyer B.R., Lang R.N., Mandel I., et al. (2009). "Massive black-hole binary inspirals: results

from the LISA parameter estimation taskforce". *Classical and Quantum Gravity*, **26**(9):094027. 0811.1011.

[38] Arun K.G., Buonanno A., Faye G., Ochsner E. (2009). "Higher-order spin effects in the amplitude and phase of gravitational waveforms emitted by inspiraling compact binaries: Ready-to-use gravitational waveforms". *Physical Review D*, **79**(10):104023. 0810.5336.

[39] Arun K.G., Buonanno A., Faye G., Ochsner E. (2011). "Erratum: Higher-order spin effects in the amplitude and phase of gravitational waveforms emitted by inspiraling compact binaries: Ready-to-use gravitational waveforms [Phys. Rev. D 79, 104023 (2009)]". *Physical Review D*, **84**(4):049901.

[40] Ascaso B., Lemaux B.C., Lubin L.M., Gal R.R., Kocevski D.D., Rumbaugh N., Squires G. (2014). "The violent youth of bright and massive cluster galaxies and their maturation over 7 billion years". *Monthly Notices of the Royal Astronomical Society*, **442**:589–615. 1309.6643.

[41] Aso Y., Michimura Y., Somiya K., Ando M., Miyakawa O., Sekiguchi T., Tatsumi D., Yamamoto H. (2013). "Interferometer design of the KAGRA gravitational wave detector". *Physical Review D*, **88**(4):043007. 1306.6747.

[42] Astone P., Baggio L., Bassan M., Bignotto M., Bonaldi M., Bonifazi P., Cavallari G., Cerdonio M., Coccia E., Conti L., et al. (2010). "IGEC2: A 17-month search for gravitational wave bursts in 2005-2007". *Physical Review D*, **82**(2):022003. 1002.3515.

[43] Astone P., Ballantini R., Babusci D., Bassan M., Carelli P., Cavallari G., Cavanna F., Chincarini A., Coccia E., Cosmelli C., et al. (2006). "Status report on the EXPLORER and NAUTILUS detectors and the present science run". *Classical and Quantum Gravity*, **23**:S57–S62.

[44] Babak S., Gair J.R., Petiteau A., Sesana A. (2011). "Fundamental physics and cosmology with LISA". *Classical and Quantum Gravity*, **28**(11):114001. 1011.2062.

[45] Baker J.G., Centrella J., Choi D.I., Koppitz M., van Meter J. (2006). "Gravitational-Wave Extraction from an Inspiraling Configuration of Merging Black Holes". *Physical Review Letters*, **96**(11):111102. gr-qc/0511103.

[46] Balbus S.A. (1991). "On magnetothermal instability in cluster cooling flows". *Astrophysical Journal*, **372**:25–30.

[47] Barausse E. (2012). "The evolution of massive black holes and their spins in their galactic hosts". *Monthly Notices of the Royal Astronomical Society*, **423**:2533–2557. 1201.5888.

[48] Barausse E., Bellovary J., Berti E., Holley-Bockelmann K., Farris B., Sathyaprakash B., Sesana A. (2015). "Massive Black Hole Science with eLISA". *Journal of Physics Conference Series*, **610**(1):012001. 1410.2907.

[49] Barausse E., Cardoso V., Pani P. (2014). "Can environmental effects spoil precision gravitational-wave astrophysics?" *Physical Review D*, **89**(10):104059. 1404.7149.

[50] Barausse E., Cardoso V., Pani P. (2015). "Environmental Effects for Gravitational-wave Astrophysics". *Journal of Physics Conference Series*, **610**(1):012044. 1404.7140.

[51] Barausse E., Morozova V., Rezzolla L. (2012). "On the Mass Radiated by Coalescing Black Hole Binaries". *Astrophysical Journal*, **758**:63. 1206.3803.

[52] Barausse E., Palenzuela C., Ponce M., Lehner L. (2013). "Neutron-star mergers in scalar-tensor theories of gravity". *Physical Review D*, **87**(8):081506. 1212.5053.

[53] Barausse E., Rezzolla L. (2009). "Predicting the Direction of the Final Spin from the Coalescence of Two Black Holes". *Astrophysical Journal Letters*, **704**:L40–L44. 0904.2577.

[54] Bardeen J.M. (1973). "Timelike and null geodesics in the Kerr metric." In *Black Holes (Les Astres Occlus)*, edited by C. Dewitt, B.S. Dewitt, pages 215–239.

[55] Bardeen J.M., Petterson J.A. (1975). "The Lense-Thirring Effect and Accretion Disks around Kerr Black Holes". *Astrophysical Journal Letters*, **195**:L65.

[56] Barker B.M., Oconnell R.F. (1979). "The gravitational interaction: Spin, rotation, and quantum effects - A review". *General Relativity and Gravitation*, **11**:149–175.

[57] Baruteau C., Masset F. (2013). "Recent Developments in Planet Migration Theory". In *Lecture Notes in Physics, Berlin Springer Verlag*, edited by J. Souchay, S. Mathis, T. Tokieda, volume 861, page 201. 1203.3294.

[58] Bate M.R., Lubow S.H., Ogilvie G.I., Miller K.A. (2003). "Three-dimensional calculations of high- and low-mass planets embedded in protoplanetary discs". *Monthly Notices of the Royal Astronomical Society*, **341**:213–229. astro-ph/0301154.

[59] Baumgarte T.W., Shapiro S.L. (2010). *Numerical Relativity: Solving Einstein's Equations on the Computer*. Cambridge, UK, Cambridge University Press.

[60] Begelman M.C., Blandford R.D., Rees M.J. (1980). "Massive black hole binaries in active galactic nuclei". *Nature*, **287**:307–309.

[61] Begelman M.C., Volonteri M., Rees M.J. (2006). "Formation of supermassive black holes by direct collapse in pre-galactic haloes". *Monthly Notices of the Royal Astronomical Society*, **370**:289–298. astro-ph/0602363.

[62] Bekenstein J.D. (1997). "Black Hole Hair: Twenty-Five Years After". In *Second International A.D. Sahkarov Conference on Physics*, edited by A.J. Dremin, A.M. Semikhatov, page 216. gr-qc/9605059.

[63] Belczynski K., Taam R.E., Rantsiou E., van der Sluys M. (2008). "Black Hole Spin Evolution: Implications for Short-Hard Gamma-Ray Bursts and Gravitational Wave Detection". *Astrophysical Journal*, **682**:474-486. astro-ph/0703131.

[64] Bell E.F., McIntosh D.H., Katz N., Weinberg M.D. (2003). "The Optical and Near-Infrared Properties of Galaxies. I. Luminosity and Stellar Mass Functions". *Astrophysical Journal Supplement*, **149**:289–312. astro-ph/0302543.

[65] Bell E.F., Phleps S., Somerville R.S., Wolf C., Borch A., Meisenheimer K. (2006). "The Merger Rate of Massive Galaxies". *Astrophysical Journal*, **652**:270–276. astro-ph/0602038.

[66] Bellovary J., Volonteri M., Governato F., Shen S., Quinn T., Wadsley J. (2011). "The First Massive Black Hole Seeds and Their Hosts". *Astrophysical Journal*, **742**:13. 1104.3858.

[67] Benacquista M.J., Downing J.M.B. (2013). "Relativistic Binaries in Globular Clusters". *Living Reviews in Relativity*, **16**. 1110.4423.

[68] Berczik P., Merritt D., Spurzem R., Bischof H.P. (2006). "Efficient Merger of Binary Supermassive Black Holes in Nonaxisymmetric Galaxies". *Astrophysical Journal Letters*, **642**:L21–L24. astro-ph/0601698.

[69] Bernardi M., Meert A., Sheth R.K., Vikram V., Huertas-Company M., Mei S., Shankar F. (2013). "The massive end of the luminosity and stellar mass functions: dependence on the fit to the light profile". *Monthly Notices of the Royal Astronomical Society*, **436**:697–704. 1304.7778.

[70] Bernardi M., Shankar F., Hyde J.B., Mei S., Marulli F., Sheth R.K. (2010). "Galaxy luminosities, stellar masses, sizes, velocity dispersions as a function of morphological type". *Monthly Notices of the Royal Astronomical Society*, **404**:2087–2122. 0910.1093.

[71] Berti E., Barausse E., Cardoso V., Gualtieri L., Pani P., Sperhake U., Stein L.C., Wex N., Yagi K., Baker T., et al. (2015). "Testing general relativity with present and future astrophysical observations". *Classical and Quantum Gravity*, **32**(24):243001. 1501.07274.

[72] Berti E., Cardoso V., Gonzalez J.A., Sperhake U., Hannam M., Husa S., Brügmann B. (2007). "Inspiral, merger, and ringdown of unequal mass black hole binaries: A multipolar analysis". *Physical Review D*, **76**(6):064034. gr-qc/0703053.

[73] Berti E., Cardoso V., Gualtieri L., Horbatsch M., Sperhake U. (2013). "Numerical simulations of single and binary black holes in scalar-tensor theories: Circumventing the no-hair theorem". *Physical Review D*, **87**(12):124020. 1304.2836.

[74] Berti E., Cardoso V., Starinets A.O. (2009). "Quasinormal modes of black holes and black branes". *Classical and Quantum Gravity*, **26**(16):163001. 0905.2975.

[75] Berti E., Cardoso V., Will C.M. (2006). "Gravitational-wave spectroscopy of massive black holes with the space interferometer LISA". *Physical Review D*, **73**(6):064030. gr-qc/0512160.

[76] Berti E., Kesden M., Sperhake U. (2012). "Effects of post-Newtonian spin alignment on the distribution of black-hole recoils". *Physical Review D*, **85**(12):124049. 1203.2920.

[77] Bertin G. (2000). *Dynamics of Galaxies*. Cambridge, UK, Cambridge University Press.

[78] Bertone G., Hooper D., Silk J. (2005). "Particle dark matter: evidence, candidates and constraints". *Physics Reports*, **405**:279–390. hep-ph/0404175.

[79] Bertotti B., Iess L., Tortora P. (2003). "A test of general relativity using radio links with the Cassini spacecraft". *Nature*, **425**:374–376.

[80] Best P.N., von der Linden A., Kauffmann G., Heckman T.M., Kaiser C.R. (2007). "On the prevalence of radio-loud active galactic nuclei in brightest cluster galaxies: implications for AGN heating of cooling flows". *Monthly Notices of the Royal Astronomical Society*, **379**:894–908. astro-ph/0611197.

[81] Bethe H.A. (1990). "Supernova mechanisms". *Reviews of Modern Physics*, **62**:801–866.

[82] Binétruy P., Bohé A., Caprini C., Dufaux J.F. (2012). "Cosmological backgrounds of gravitational waves and eLISA/NGO: phase transitions, cosmic strings and other sources". *Journal of Cosmology and Astroparticle Physics*, **6**:027. 1201.0983.

[83] Binney J. (1980). "The radius-dependence of velocity dispersion in elliptical galaxies". *Monthly Notices of the Royal Astronomical Society*, **190**:873–880.

[84] Binney J., Tremaine S. (1987). *Galactic dynamics*. Princeton, NJ, Princeton University Press.

[85] Birkhoff G.D., Langer R.E. (1923). *Relativity and modern physics*. Cambridge, MA, Harvard University Press.

[86] Blanchet L. (2014). "Gravitational Radiation from Post-Newtonian Sources and Inspiralling Compact Binaries". *Living Reviews in Relativity*, **17**. 1310.1528.

[87] Blanchet L., Buonanno A., Faye G. (2006). "Higher-order spin effects in the dynamics of compact binaries. II. Radiation field". *Physical Review D*, **74**(10):104034. gr-qc/0605140.

[88] Blecha L., Cox T.J., Loeb A., Hernquist L. (2011). "Recoiling black holes in merging galaxies: relationship to active galactic nucleus lifetimes, starbursts and the M_{BH}-σ_* relation". *Monthly Notices of the Royal Astronomical Society*, **412**:2154–2182. 1009.4940.

[89] Blecha L., Loeb A. (2008). "Effects of gravitational-wave recoil on the dynamics and growth of supermassive black holes". *Monthly Notices of the Royal Astronomical Society*, **390**:1311–1325. 0805.1420.

[90] Blecha L., Sijacki D., Kelley L.Z., Torrey P., Vogelsberger M., Nelson D., Springel V., Snyder G., Hernquist L. (2016). "Recoiling black holes: prospects for detection and implications of spin alignment". *Monthly Notices of the Royal Astronomical Society*, **456**:961–989. 1508.01524.

[91] Bogdanović T. (2015). "Supermassive Black Hole Binaries: The Search Continues". *Astrophysics and Space Science Proceedings*, **40**:103. 1406.5193.

[92] Bogdanović T., Reynolds C.S., Miller M.C. (2007). "Alignment of the Spins of Supermassive Black Holes Prior to Coalescence". *Astrophysical Journal Letters*, **661**:L147–L150. astro-ph/0703054.

[93] Bohé A., Faye G., Marsat S., Porter E.K. (2015). "Quadratic-in-spin effects in the orbital dynamics and gravitational-wave energy flux of compact binaries at the 3PN order". *Classical and Quantum Gravity*, **32**(19):195010. 1501.01529.

[94] Bohé A., Marsat S., Faye G., Blanchet L. (2013). "Next-to-next-to-leading order spin-orbit effects in the near-zone metric and precession equations of compact binaries". *Classical and Quantum Gravity*, **30**(7):075017. 1212.5520.

[95] Bolton C.T. (1972). "Identification of Cygnus X-1 with HDE 226868". *Nature*, **235**:271–273.

[96] Bonetti M., Haardt F., Sesana A., Barausse E. (2016). "Post-Newtonian evolution of massive black hole triplets in galactic nuclei - I. Numerical implementation and tests". *Monthly Notices of the Royal Astronomical Society*, **461**:4419–4434. 1604.08770.

[97] Bowyer S., Byram E.T., Chubb T.A., Friedman H. (1965). "Cosmic X-ray Sources". *Science*, **147**:394–398.

[98] Brans C., Dicke R.H. (1961). "Mach's Principle and a Relativistic Theory of Gravitation". *Physical Review*, **124**:925–935.

[99] Brenneman L. (2013). *Measuring the Angular Momentum of Supermassive Black Holes*. Springer Briefs in Astronomy.

[100] Brown D.A., Lundgren A., O'Shaughnessy R. (2012). "Nonspinning searches for spinning black hole-neutron star binaries in ground-based detector data: Amplitude and mismatch predictions in the constant precession cone approximation". *Physical Review D*, **86**(6):064020. 1203.6060.

[101] Brügmann B., González J.A., Hannam M., Husa S., Sperhake U. (2008). "Exploring black hole superkicks". *Physical Review D*, **77**(12):124047. 0707.0135.

[102] Bryan G.L., Norman M.L. (1998). "Statistical Properties of X-Ray Clusters: Analytic and Numerical Comparisons". *Astrophysical Journal*, **495**:80–99. astro-ph/9710107.

[103] Bundy K., Fukugita M., Ellis R.S., Targett T.A., Belli S., Kodama T. (2009). "The Greater Impact of Mergers on the Growth of Massive Galaxies: Implications for Mass Assembly and Evolution since z sime 1". *Astrophysical Journal*, **697**:1369–1383. 0902.1188.

[104] Buonanno A. (2007). "Gravitational waves". In *Proceedings of Les Houches Summer School, Particle Physics and Cosmology: The Fabric of Spacetime*. 0709.4682.

[105] Buonanno A., Chen Y., Damour T. (2006). "Transition from inspiral to plunge in precessing binaries of spinning black holes". *Physical Review D*, **74**(10):104005. gr-qc/0508067.

[106] Buonanno A., Iyer B.R., Ochsner E., Pan Y., Sathyaprakash B.S. (2009). "Comparison of post-Newtonian templates for compact binary inspiral signals in gravitational-wave detectors". *Physical Review D*, **80**(8):084043. 0907.0700.

[107] Buonanno A., Kidder L.E., Lehner L. (2008). "Estimating the final spin of a binary black hole coalescence". *Physical Review D*, **77**(2):026004. 0709.3839.

[108] Burgess C.P. (2004). "Quantum Gravity in Everyday Life: General Relativity as an Effective Field Theory". *Living Reviews in Relativity*, **7**. gr-qc/0311082.

[109] Burke C., Collins C.A. (2013). "Growth of brightest cluster galaxies via mergers since z=1". *Monthly Notices of the Royal Astronomical Society*, **434**:2856–2865. 1307.1702.

[110] Burrows A., Dessart L., Livne E., Ott C.D., Murphy J. (2007). "Simulations of Magnetically Driven Supernova and Hypernova Explosions in the Context of Rapid Rotation". *Astrophysical Journal*, **664**:416–434. astro-ph/0702539.

[111] Callegari S., Mayer L., Kazantzidis S., Colpi M., Governato F., Quinn T., Wadsley J. (2009). "Pairing of Supermassive Black Holes in Unequal-Mass Galaxy Mergers". *Astrophysical Journal Letters*, **696**:L89–L92. 0811.0615.

[112] Campanelli M., Lousto C., Zlochower Y., Merritt D. (2007). "Large Merger Recoils and Spin Flips from Generic Black Hole Binaries". *Astrophysical Journal Letters*, **659**:L5–L8. gr-qc/0701164.

[113] Campanelli M., Lousto C.O., Marronetti P., Zlochower Y. (2006). "Accurate Evolutions of Orbiting Black-Hole Binaries without Excision". *Physical Review Letters*, **96**(11):111101. gr-qc/0511048.

[114] Campanelli M., Lousto C.O., Nakano H., Zlochower Y. (2009). "Comparison of numerical and post-Newtonian waveforms for generic precessing black-hole binaries". *Physical Review D*, **79**(8):084010. 0808.0713.

[115] Campanelli M., Lousto C.O., Zlochower Y., Merritt D. (2007). "Maximum Gravitational Recoil". *Physical Review Letters*, **98**(23):231102. gr-qc/0702133.

[116] Caprini C., Hindmarsh M., Huber S., Konstandin T., Kozaczuk J., Nardini G., No J.M., Petiteau A., Schwaller P., Servant G., et al. (2016). "Science with the space-based interferometer eLISA. II: gravitational waves from cosmological phase transitions". *Journal of Cosmology and Astroparticle Physics*, **4**:001. 1512.06239.

[117] Cardoso V., Gualtieri L., Herdeiro C.A.R., Sperhake U. (2015). "Exploring New Physics Frontiers Through Numerical Relativity". *Living Reviews in Relativity*, **18**. 1409.0014.

[118] Carollo C.M., Franx M., Illingworth G.D., Forbes D.A. (1997). "Ellipticals with Kinematically Distinct Cores: V - I Color Images with WPFC2". *Astrophysical Journal*, **481**:710–734. astro-ph/9701218.

[119] Carrasco E.R., Gomez P.L., Verdugo T., Lee H., Diaz R., Bergmann M., Turner J.E.H., Miller B.W., West M.J. (2010). "Strong Gravitational Lensing by the Supermassive cD Galaxy in Abell 3827". *Astrophysical Journal Letters*, **715**:L160–L164. 1004.5410.

[120] Casares J., Jonker P.G. (2014). "Mass Measurements of Stellar and Intermediate-Mass Black Holes". *Space Science Reviews*, **183**:223–252. 1311.5118.

[121] Catinella B., Schiminovich D., Kauffmann G., Fabello S., Wang J., Hummels C., Lemonias J., Moran S.M., Wu R., Giovanelli R., et al. (2010). "The GALEX Arecibo SDSS Survey - I. Gas fraction scaling relations of massive galaxies and first data release". *Monthly Notices of the Royal Astronomical Society*, **403**:683–708. 0912.1610.

[122] Centrella J., Baker J.G., Kelly B.J., van Meter J.R. (2010). "Black-hole binaries, gravitational waves, and numerical relativity". *Reviews of Modern Physics*, **82**:3069–3119. 1010.5260.

[123] Chandrasekhar S. (1943). "Dynamical Friction. I. General Considerations: the Coefficient of Dynamical Friction." *Astrophysical Journal*, **97**:255.

[124] Chase J.E. (1970). "Event Horizons in Static Scalar-Vacuum Space-Times". *Communications in Mathematical Physics*, **19**:276–288.

[125] Chatziioannou K., Cornish N., Klein A., Yunes N. (2014). "Detection and parameter estimation of gravitational waves from compact binary inspirals with analytical double-precessing templates". *Physical Review D*, **89**(10):104023. 1404.3180.

[126] Chatziioannou K., Cornish N., Klein A., Yunes N. (2015). "Spin-precession: Breaking the Black Hole-Neutron Star Degeneracy". *Astrophysical Journal Letters*, **798**:L17. 1402.3581.

[127] Chatziioannou K., Klein A., Cornish N., Yunes N. (2016). "Analytic gravitational waveforms for generic precessing compact binaries". *ArXiv e-prints*. 1606.03117.

[128] Chiba T., Harada T., Nakao K. (1997). "Chapter 6. Gravitational Physics in Scalar-Tensor Theories —Tests of Strong Field Gravity—". *Progress of Theoretical Physics Supplement*, **128**:335–372.

[129] Cho H.S., Ochsner E., O'Shaughnessy R., Kim C., Lee C.H. (2013). "Gravitational waves from black hole-neutron star binaries: Effective Fisher matrices and parameter estimation using higher harmonics". *Physical Review D*, **87**(2):024004. 1209.4494.

[130] Chruściel P.T., Costa J.L., Heusler M. (2012). "Stationary Black Holes: Uniqueness and Beyond". *Living Reviews in Relativity*, **15**. 1205.6112.

[131] Civano F., Elvis M., Lanzuisi G., Aldcroft T., Trichas M., Bongiorno A., Brusa M., Blecha L., Comastri A., Loeb A., et al. (2012). "Chandra High-resolution observations of CID-42, a Candidate Recoiling Supermassive Black Hole". *Astrophysical Journal*, **752**:49. 1205.0815.

[132] Civano F., Elvis M., Lanzuisi G., Jahnke K., Zamorani G., Blecha L., Bongiorno A., Brusa M., Comastri A., Hao H., et al. (2010). "A Runaway Black Hole in COSMOS: Gravitational Wave or Slingshot Recoil?" *Astrophysical Journal*, **717**:209–222. 1003.0020.

[133] Clausen D., Piro A.L., Ott C.D. (2015). "The Black Hole Formation Probability". *Astrophysical Journal*, **799**:190. 1406.4869.

[134] Clifton T., Ferreira P.G., Padilla A., Skordis C. (2012). "Modified gravity and cosmology". *Physics Reports*, **513**:1–189. 1106.2476.

[135] Colpi M. (2014). "Massive Binary Black Holes in Galactic Nuclei and Their Path to Coalescence". *Space Science Reviews*, **183**:189–221. 1407.3102.

[136] Copeland E.J., Sami M., Tsujikawa S. (2006). "Dynamics of Dark Energy". *International Journal of Modern Physics D*, **15**:1753–1935. hep-th/0603057.

[137] Cossins P., Lodato G., Clarke C.J. (2009). "Characterizing the gravitational instability in cooling accretion discs". *Monthly Notices of the Royal Astronomical Society*, **393**:1157–1173. 0811.3629.

[138] Cuadra J., Armitage P.J., Alexander R.D., Begelman M.C. (2009). "Massive black hole binary mergers within subparsec scale gas discs". *Monthly Notices of the Royal Astronomical Society*, **393**:1423–1432. 0809.0311.

[139] Cutler C., Flanagan É.E. (1994). "Gravitational waves from merging compact binaries: How accurately can one extract the binary's parameters from the inspiral waveform?" *Physical Review D*, **49**:2658–2697. gr-qc/9402014.

[140] Dal Canton T., Lundgren A.P., Nielsen A.B. (2015). "Impact of precession on aligned-spin searches for neutron-star-black-hole binaries". *Physical Review D*, **91**(6):062010. 1411.6815.

[141] Damour T. (2001). "Coalescence of two spinning black holes: An effective one-body approach". *Physical Review D*, **64**(12):124013. gr-qc/0103018.

[142] Damour T. (2007). "Binary Systems as Test-beds of Gravity Theories". In *6th SIGRAV Graduate School in Contemporary Relativity and Gravitational Physics: A Century from Einstein Relativity: Probing Gravity Theories in Binary Systems*, edited by M. Colpi, et al. 0704.0749.

[143] Damour T., Esposito-Farese G. (1992). "Tensor-multi-scalar theories of gravitation". *Classical and Quantum Gravity*, **9**:2093–2176.

[144] Damour T., Esposito-Farese G. (1993). "Nonperturbative strong-field effects in tensor-scalar theories of gravitation". *Physical Review Letters*, **70**:2220–2223.

[145] Damour T., Esposito-Farèse G. (1996). "Tensor-scalar gravity and binary-pulsar experiments". *Physical Review D*, **54**:1474–1491. gr-qc/9602056.

[146] Damour T., Esposito-Farèse G. (1996). "Testing gravity to second post-Newtonian order: A field-theory approach". *Physical Review D*, **53**:5541–5578. gr-qc/9506063.

[147] Damour T., Gopakumar A., Iyer B.R. (2004). "Phasing of gravitational waves from inspiralling eccentric binaries". *Physical Review D*, **70**(6):064028. gr-qc/0404128.

[148] Damour T., Nordtvedt K. (1993). "General relativity as a cosmological attractor of tensor-scalar theories". *Physical Review Letters*, **70**:2217–2219.

[149] Damour T., Nordtvedt K. (1993). "Tensor-scalar cosmological models and their relaxation toward general relativity". *Physical Review D*, **48**:3436–3450.

[150] Danzmann K., Rüdiger A. (2003). "LISA technology - concept, status, prospects". *Classical and Quantum Gravity*, **20**:S1–S9.

[151] De Lucia G., Blaizot J. (2007). "The hierarchical formation of the brightest cluster galaxies". *Monthly Notices of the Royal Astronomical Society*, **375**:2–14. astro-ph/0606519.

[152] de Ravel L., Le Fèvre O., Tresse L., Bottini D., Garilli B., Le Brun V., Maccagni D., Scaramella R., Scodeggio M., Vettolani G., et al. (2009). "The VIMOS VLT Deep Survey. Evolution of the major merger rate since z ˜1 from spectroscopically confirmed galaxy pairs". *Astronomy and Astrophysics*, **498**:379–397. 0807.2578.

[153] Decarli R., Dotti M., Mazzucchelli C., Montuori C., Volonteri M. (2014). "New insights on the recoiling/binary black hole candidate J0927+2943 via molecular gas observations". *Monthly Notices of the Royal Astronomical Society*, **445**:1558–1566. 1409.1585.

[154] Devecchi B., Rasia E., Dotti M., Volonteri M., Colpi M. (2009). "Imprints of recoiling massive black holes on the hot gas of early-type galaxies". *Monthly Notices of the Royal Astronomical Society*, **394**:633–640. 0805.2609.

[155] Dimmelmeier H. (1998). "Numerical calculations of hydrodynamic gravitational collapse and its observational consequences in scalar-tensor theories of gravity." Thesis. http://hdl.handle.net/11858/00-001M-0000-0013-59C8-2.

[156] Dimmelmeier H., Font J.A., Müller E. (2002). "Relativistic simulations of rotational core collapse II. Collapse dynamics and gravitational radiation". *Astronomy and Astrophysics*, **393**:523–542. astro-ph/0204289.

[157] Dimmelmeier H., Ott C.D., Janka H.T., Marek A., Müller E. (2007). "Generic Gravitational-Wave Signals from the Collapse of Rotating Stellar Cores". *Physical Review Letters*, **98**(25):251101. astro-ph/0702305.

[158] Dimmelmeier H., Ott C.D., Marek A., Janka H.T. (2008). "Gravitational wave burst signal from core collapse of rotating stars". *Physical Review D*, **78**(6):064056. 0806.4953.

[159] Do T., Wright S.A., Barth A.J., Barton E.J., Simard L., Larkin J.E., Moore A.M., Wang L., Ellerbroek B. (2014). "Prospects for Measuring Supermassive Black Hole Masses with Future Extremely Large Telescopes". *Astronomical Journal*, **147**:93. 1401.7988.

[160] Doneva D.D., Yazadjiev S.S., Stergioulas N., Kokkotas K.D. (2013). "Rapidly rotating neutron stars in scalar-tensor theories of gravity". *Physical Review D*, **88**(8):084060. 1309.0605.

[161] D'Orazio D.J., Haiman Z., MacFadyen A. (2013). "Accretion into the central cavity of a circumbinary disc". *Monthly Notices of the Royal Astronomical Society*, **436**:2997–3020. 1210.0536.

[162] Dotti M., Colpi M., Haardt F., Mayer L. (2007). "Supermassive black hole binaries in gaseous and stellar circumnuclear discs: orbital dynamics and gas accretion". *Monthly Notices of the Royal Astronomical Society*, **379**:956–962. astro-ph/0612505.

[163] Dotti M., Colpi M., Pallini S., Perego A., Volonteri M. (2013). "On the Orientation and Magnitude of the Black Hole Spin in Galactic Nuclei". *Astrophysical Journal*, **762**:68. 1211.4871.

[164] Dotti M., Merloni A., Montuori C. (2015). "Linking the fate of massive black hole binaries to the active galactic nuclei luminosity function". *Monthly Notices of the Royal Astronomical Society*, **448**:3603–3607. 1502.03101.

[165] Dotti M., Ruszkowski M., Paredi L., Colpi M., Volonteri M., Haardt F. (2009). "Dual black holes in merger remnants - I. Linking accretion to dynamics". *Monthly Notices of the Royal Astronomical Society*, **396**:1640–1646. 0902.1525.

[166] Dotti M., Sesana A., Decarli R. (2012). "Massive Black Hole Binaries: Dynamical Evolution and Observational Signatures". *Advances in Astronomy*, **2012**:940568. 1111.0664.

[167] Dotti M., Volonteri M., Perego A., Colpi M., Ruszkowski M., Haardt F. (2010). "Dual black holes in merger remnants - II. Spin evolution and gravitational recoil". *Monthly Notices of the Royal Astronomical Society*, **402**:682–690. 0910.5729.

[168] Drever R.W.P. (1983). "Interferometric detectors for gravitational radiation." In *Lecture Notes in Physics, Berlin Springer Verlag*, volume 124, pages 321–338.

[169] Duffell P.C., Haiman Z., MacFadyen A.I., D'Orazio D.J., Farris B.D. (2014). "The Migration of Gap-opening Planets is Not Locked to Viscous Disk Evolution". *Astrophysical Journal Letters*, **792**:L10. 1405.3711.

[170] Dürmann C., Kley W. (2015). "Migration of massive planets in accreting disks". *Astronomy and Astrophysics*, **574**:A52. 1411.3190.

[171] Eddington A.S. (1923). *The mathematical theory of relativity*. Cambridge, UK, Cambridge University Press.

[172] Einstein A. (1916). "Die Grundlage der allgemeinen Relativitätstheorie". *Annalen der Physik*, **354**:769–822.

[173] Einstein A. (1916). "Näherungsweise Integration der Feldgleichungen der Gravitation". *Sitzungsberichte der Königlich Preußischen Akademie der Wissenschaften (Berlin)*, pages 688–696.

[174] Einstein A. (1918). "Über Gravitationswellen". *Sitzungsberichte der Königlich Preußischen Akademie der Wissenschaften (Berlin)*, pages 154–167.

[175] Einstein A., Rosen N. (1937). "On Gravitational Waves". *Journal of The Franklin Institute*, **223**:43–54.

[176] ESA Cosmic Vision Program (2015). sci.esa.int/cosmic-vision.

[177] Escala A., Larson R.B., Coppi P.S., Mardones D. (2004). "The Role of Gas in the Merging of Massive Black Holes in Galactic Nuclei. I. Black Hole Merging in a Spherical Gas Cloud". *Astrophysical Journal*, **607**:765–777. astro-ph/0310851.

[178] Escala A., Larson R.B., Coppi P.S., Mardones D. (2005). "The Role of Gas in the Merging of Massive Black Holes in Galactic Nuclei. II. Black Hole Merging in a Nuclear Gas Disk". *Astrophysical Journal*, **630**:152–166. astro-ph/0406304.

[179] Esposito-Farèse G. (2004). "Tests of Scalar-Tensor Gravity". In *Phi in the Sky: The Quest for Cosmological Scalar Fields*, edited by C.J.A.P. Martins, P.P. Avelino, M.S. Costa, K. Mack, M.F. Mota, M. Parry, volume 736 of *American Institute of Physics Conference Series*, pages 35–52. gr-qc/0409081.

[180] Fanidakis N., Baugh C.M., Benson A.J., Bower R.G., Cole S., Done C., Frenk C.S. (2011). "Grand unification of AGN activity in the ΛCDM cosmology". *Monthly Notices of the Royal Astronomical Society*, **410**:53–74. 0911.1128.

[181] Faraoni V. (2004). *Cosmology in Scalar-Tensor Gravity*. Kluwer Academic Publishers.

[182] Farr B., Ochsner E., Farr W.M., O'Shaughnessy R. (2014). "A more effective coordinate system for parameter estimation of precessing compact binaries from gravitational waves". *Physical Review D*, **90**(2):024018. 1404.7070.

[183] Farris B.D., Duffell P., MacFadyen A.I., Haiman Z. (2014). "Binary Black Hole Accretion from a Circumbinary Disk: Gas Dynamics inside the Central Cavity". *Astrophysical Journal*, **783**:134. 1310.0492.

[184] Favata M. (2009). "Gravitational-wave memory revisited: Memory from the merger and recoil of binary black holes". *Journal of Physics Conference Series*, **154**(1):012043. 0811.3451.

[185] Faye G., Blanchet L., Buonanno A. (2006). "Higher-order spin effects in the dynamics of compact binaries. I. Equations of motion". *Physical Review D*, **74**(10):104033. gr-qc/0605139.

[186] Fierz M. (1956). "On the physical interpretation of P.Jordan's extended theory of gravitation". *Helvetica Physica Acta*, **29**:128–134.

[187] Finn L.S. (1992). "Detection, measurement, and gravitational radiation". *Physical Review D*, **46**:5236–5249. gr-qc/9209010.

[188] Font J.A. (2008). "Numerical Hydrodynamics and Magnetohydrodynamics in General Relativity". *Living Reviews in Relativity*, **11**.

[189] Font J.A., Miller M., Suen W.M., Tobias M. (2000). "Three-dimensional numerical general relativistic hydrodynamics: Formulations, methods, and code tests". *Physical Review D*, **61**(4):044011. gr-qc/9811015.

[190] Fragos T., Tremmel M., Rantsiou E., Belczynski K. (2010). "Black Hole Spin-Orbit Misalignment in Galactic X-ray Binaries". *Astrophysical Journal Letters*, **719**:L79–L83. 1001.1107.

[191] Frank J., Rees M.J. (1976). "Effects of massive central black holes on dense stellar systems". *Monthly Notices of the Royal Astronomical Society*, **176**:633–647.

[192] Freire P.C.C., Wex N., Esposito-Farèse G., Verbiest J.P.W., Bailes M., Jacoby B.A., Kramer M., Stairs I.H., Antoniadis J., Janssen G.H. (2012). "The relativistic pulsar-white dwarf binary PSR J1738+0333 - II. The most stringent test of scalar-tensor

gravity". *Monthly Notices of the Royal Astronomical Society*, **423**:3328–3343. 1205.1450.

[193] Fujii Y., Maeda K.I. (2003). *The Scalar-Tensor Theory of Gravitation*. Cambridge, UK, Cambridge University Press.

[194] Futamase T., Itoh Y. (2007). "The Post-Newtonian Approximation for Relativistic Compact Binaries". *Living Reviews in Relativity*, **10**.

[195] Gair J.R., Porter E.K. (2012). "Observing extreme-mass-ratio inspirals with eLISA/NGO". In *proceedings of 9th LISA Symposium*. 1210.8066.

[196] Gair J.R., Vallisneri M., Larson S.L., Baker J.G. (2013). "Testing General Relativity with Low-Frequency, Space-Based Gravitational-Wave Detectors". *Living Reviews in Relativity*, **16**. 1212.5575.

[197] Gallant A. (2014). "pdoc". pypi.python.org/pypi/pdoc.

[198] Gammie C.F. (2001). "Nonlinear Outcome of Gravitational Instability in Cooling, Gaseous Disks". *Astrophysical Journal*, **553**:174–183. astro-ph/0101501.

[199] Gergely L.Á., Biermann P.L. (2009). "The Spin-Flip Phenomenon in Supermassive Black hole binary mergers". *Astrophysical Journal*, **697**:1621–1633. 0704.1968.

[200] Gerosa D. (2015). www.damtp.cam.ac.uk/user/dg438/spinprecession www.davidegerosa.com/spinprecession.

[201] Gerosa D. (2015). "Rival Families: Waveforms from Resonant Black-Hole Binaries as Probes of Their Astrophysical Formation History". *Astrophysics and Space Science Proceedings*, **40**:137.

[202] Gerosa D. (2016). www.damtp.cam.ac.uk/user/dg438/corecollapse www.davidegerosa.com/spinprecession.

[203] Gerosa D., Kesden M. (2016). "PRECESSION: Dynamics of spinning black-hole binaries with python". *Physical Review D*, **93**(12):124066. 1605.01067.

[204] Gerosa D., Kesden M., Berti E., O'Shaughnessy R., Sperhake U. (2013). "Resonant-plane locking and spin alignment in stellar-mass black-hole binaries: A diagnostic of compact-binary formation". *Physical Review D*, **87**(10):104028. 1302.4442.

[205] Gerosa D., Kesden M., O'Shaughnessy R., Klein A., Berti E., Sperhake U., Trifirò D. (2015). "Precessional Instability in Binary Black Holes with Aligned Spins". *Physical Review Letters*, **115**(14):141102. 1506.09116.

[206] Gerosa D., Kesden M., Sperhake U., Berti E., O'Shaughnessy R. (2015). "Multi-timescale analysis of phase transitions in precessing black-hole binaries". *Physical Review D*, **92**(6):064016. 1506.03492.

[207] Gerosa D., Moore C.J. (2016). "Black Hole Kicks as New Gravitational Wave Observables". *Physical Review Letters*, **117**(1):011101. 1606.04226.

[208] Gerosa D., O'Shaughnessy R., Kesden M., Berti E., Sperhake U. (2014). "Distinguishing black-hole spin-orbit resonances by their gravitational-wave signatures". *Physical Review D*, **89**(12):124025. 1403.7147.

[209] Gerosa D., Sesana A. (2015). "Missing black holes in brightest cluster galaxies as evidence for the occurrence of superkicks in nature". *Monthly Notices of the Royal Astronomical Society*, **446**:38–55. 1405.2072.

[210] Gerosa D., Sperhake U., Ott C.D. (2016). "Numerical simulations of stellar collapse in scalar-tensor theories of gravity". *Classical and Quantum Gravity*, **33**(13):135002. 1602.06952.

[211] Gerosa D., Veronesi B., Lodato G., Rosotti G. (2015). "Spin alignment and differential accretion in merging black hole binaries". *Monthly Notices of the Royal Astronomical Society*, **451**:3941–3954. 1503.06807.

[212] Gertsenshteĭn M.E., Pustovoĭt V.I. (1963). "On the Detection of Low-Frequency Gravitational Waves". *Soviet Journal of Experimental and Theoretical Physics*, **16**:433.

[213] Gold R., Paschalidis V., Etienne Z.B., Shapiro S.L., Pfeiffer H.P. (2014). "Accretion disks around binary black holes of unequal mass: General relativistic magnetohydrodynamic simulations near decoupling". *Physical Review D*, **89**(6):064060. 1312.0600.

[214] González G., Viceré A., Wen L. (2013). "Gravitational wave astronomy". *Frontiers of Physics*, **8**:771–793.

[215] González J.A., Hannam M., Sperhake U., Brügmann B., Husa S. (2007). "Supermassive Recoil Velocities for Binary Black-Hole Mergers with Antialigned Spins". *Physical Review Letters*, **98**(23):231101. gr-qc/0702052.

[216] González J.A., Sperhake U., Brügmann B., Hannam M., Husa S. (2007). "Maximum Kick from Nonspinning Black-Hole Binary Inspiral". *Physical Review Letters*, **98**(9):091101. gr-qc/0610154.

[217] Goodman J. (2003). "Self-gravity and quasi-stellar object discs". *Monthly Notices of the Royal Astronomical Society*, **339**:937–948. astro-ph/0201001.

[218] Graham M.J., Djorgovski S.G., Stern D., Glikman E., Drake A.J., Mahabal A.A., Donalek C., Larson S., Christensen E. (2015). "A possible close supermassive black-hole binary in a quasar with optical periodicity". *Nature*, **518**:74–76. 1501.01375.

[219] Gualandris A., Merritt D. (2008). "Ejection of Supermassive Black Holes from Galaxy Cores". *Astrophysical Journal*, **678**:780-797. 0708.0771.

[220] Guo Q., White S., Boylan-Kolchin M., De Lucia G., Kauffmann G., Lemson G., Li C., Springel V., Weinmann S. (2011). "From dwarf spheroidals to cD galaxies: simulating the galaxy population in a ΛCDM cosmology". *Monthly Notices of the Royal Astronomical Society*, **413**:101–131. 1006.0106.

[221] Gupta A., Gopakumar A. (2014). "Probing evolution of binaries influenced by the spin-orbit resonances". *Classical and Quantum Gravity*, **31**(10):105017. 1312.0217.

[222] Gustafsson B., Kreiss H.O., Oliger J. (1995). *Time-Dependent Problems and Difference Methods*. Wiley, New York, second edition.

[223] Haiman Z., Kocsis B., Menou K. (2009). "The Population of Viscosity- and Gravitational Wave-driven Supermassive Black Hole Binaries Among Luminous Active Galactic Nuclei". *Astrophysical Journal*, **700**:1952–1969. 0904.1383.

[224] Hannam M., Schmidt P., Bohé A., Haegel L., Husa S., Ohme F., Pratten G., Pürrer M. (2014). "Simple Model of Complete Precessing Black-Hole-Binary Gravitational Waveforms". *Physical Review Letters*, **113**(15):151101. 1308.3271.

[225] Harada T. (1997). "Stability Analysis of Spherically Symmetric Star in Scalar-Tensor Theories of Gravity". *Progress of Theoretical Physics*, **98**:359–379. gr-qc/9706014.

[226] Harada T. (1998). "Neutron stars in scalar-tensor theories of gravity and catastrophe theory". *Physical Review D*, **57**:4802–4811. gr-qc/9801049.

[227] Harada T., Chiba T., Nakao K.I., Nakamura T. (1997). "Scalar gravitational wave from Oppenheimer-Snyder collapse in scalar-tensor theories of gravity". *Physical Review D*, **55**:2024–2037. gr-qc/9611031.

[228] Harry G.M. (2010). "Advanced LIGO: the next generation of gravitational wave detectors". *Classical and Quantum Gravity*, **27**(8):084006.

[229] Harry I.W., Nitz A.H., Brown D.A., Lundgren A.P., Ochsner E., Keppel D. (2014). "Investigating the effect of precession on searches for neutron-star-black-hole binaries with Advanced LIGO". *Physical Review D*, **89**(2):024010. 1307.3562.

[230] Hartle J.B. (2003). *Gravity : an introduction to Einstein's general relativity*. San Francisco, CA, Addison Wesley.

[231] Hatcher A. (2002). *Algebraic Topology*. Cambridge, UK, Cambridge University Press.

[232] Hawking S.W. (1972). "Black holes in the Brans-Dicke: Theory of gravitation". *Communications in Mathematical Physics*, **25**:167–171.

[233] Hawking S.W., Penrose R. (1970). "The Singularities of Gravitational Collapse and Cosmology". *Proceedings of the Royal Society of London Series A*, **314**:529–548.

[234] Hayasaki K., Mineshige S., Sudou H. (2007). "Binary Black Hole Accretion Flows in Merged Galactic Nuclei". *Publications of the Astronomical Society of Japan*, **59**:427–441. astro-ph/0609144.

[235] Healy J., Bode T., Haas R., Pazos E., Laguna P., Shoemaker D.M., Yunes N. (2012). "Late inspiral and merger of binary black holes in scalar-tensor theories of gravity". *Classical and Quantum Gravity*, **29**(23):232002. 1112.3928.

[236] Heckman T.M., Kauffmann G., Brinchmann J., Charlot S., Tremonti C., White S.D.M. (2004). "Present-Day Growth of Black Holes and Bulges: The Sloan Digital Sky Survey Perspective". *Astrophysical Journal*, **613**:109–118. astro-ph/0406218.

[237] Herdeiro C.A.R., Radu E. (2015). "Asymptotically flat black holes with scalar hair: A review". *International Journal of Modern Physics D*, **24**:1542014-219. 1504.08209.

[238] Hernquist L. (1990). "An analytical model for spherical galaxies and bulges". *Astrophysical Journal*, **356**:359–364.

[239] Hewish A., Bell S.J., Pilkington J.D.H., Scott P.F., Collins R.A. (1968). "Observation of a Rapidly Pulsating Radio Source". *Nature*, **217**:709–713.

[240] Hild S., Freise A. (2015). www.et-gw.eu/etsensitivities.

[241] Hindmarsh A. (1982). *ODEPACK, a systematized collection of ODE solvers*. Lawrence Livermore National Laboratory.

[242] Hinshaw G., Larson D., Komatsu E., Spergel D.N., Bennett C.L., Dunkley J., Nolta M.R., Halpern M., Hill R.S., Odegard N., et al. (2013). "Nine-year Wilkinson Microwave Anisotropy Probe (WMAP) Observations: Cosmological Parameter Results". *Astrophysical Journal Supplement*, **208**:19. 1212.5226.

[243] Hlavacek-Larrondo J., Fabian A.C., Edge A.C., Ebeling H., Allen S.W., Sanders J.S., Taylor G.B. (2013). "The rapid evolution of AGN feedback in brightest cluster galaxies: switching from quasar-mode to radio-mode feedback". *Monthly Notices of the Royal Astronomical Society*, **431**:1638–1658. 1211.5606.

[244] Hoffman L., Loeb A. (2007). "Dynamics of triple black hole systems in hierarchically merging massive galaxies". *Monthly Notices of the Royal Astronomical Society*, **377**:957–976. astro-ph/0612517.

[245] Hopkins P.F., Croton D., Bundy K., Khochfar S., van den Bosch F., Somerville R.S., Wetzel A., Keres D., Hernquist L., Stewart K., et al. (2010). "Mergers in ΛCDM: Uncertainties in Theoretical Predictions and Interpretations of the Merger Rate". *Astrophysical Journal*, **724**:915–945. 1004.2708.

[246] Hopkins P.F., Richards G.T., Hernquist L. (2007). "An Observational Determination of the Bolometric Quasar Luminosity Function". *Astrophysical Journal*, **654**:731–753. astro-ph/0605678.

[247] Horbatsch M., Silva H.O., Gerosa D., Pani P., Berti E., Gualtieri L., Sperhake U. (2015). "Tensor-multi-scalar theories: relativistic stars and 3 + 1 decomposition". *Classical and Quantum Gravity*, **32**(20):204001. 1505.07462.

[248] Horbatsch M.W., Burgess C.P. (2011). "Semi-analytic stellar structure in scalar-tensor gravity". *Journal of Cosmology and Astroparticle Physics*, **8**:027. 1006.4411.

[249] Hoyle F., Fowler W.A. (1963). "On the nature of strong radio sources". *Monthly Notices of the Royal Astronomical Society*, **125**:169.

[250] Hulse R.A., Taylor J.H. (1975). "Discovery of a pulsar in a binary system". *Astrophysical Journal Letters*, **195**:L51–L53.

[251] Hunter J.D. (2007). "Matplotlib: A 2D Graphics Environment". *Computing in Science and Engineering*, **9**:90–95.

[252] Hurley J.R., Tout C.A., Pols O.R. (2002). "Evolution of binary stars and the effect of tides on binary populations". *Monthly Notices of the Royal Astronomical Society*, **329**:897–928. astro-ph/0201220.

[253] Husa S., Khan S., Hannam M., Pürrer M., Ohme F., Forteza X.J., Bohé A. (2016). "Frequency-domain gravitational waves from nonprecessing black-hole binaries. I. New numerical waveforms and anatomy of the signal". *Physical Review D*, **93**(4):044006. 1508.07250.

[254] Israel W. (1987). "Dark stars: the evolution of an idea." In *Three Hundred Years of Gravitation*, edited by S.W. Hawking, W. Israel, pages 199–276.

[255] Ivanov P.B., Papaloizou J.C.B., Polnarev A.G. (1999). "The evolution of a supermassive binary caused by an accretion disc". *Monthly Notices of the Royal Astronomical Society*, **307**:79–90. astro-ph/9812198.

[256] Ivanova N., Justham S., Chen X., De Marco O., Fryer C.L., Gaburov E., Ge H., Glebbeek E., Han Z., Li X.D., et al. (2013). "Common envelope evolution: where we stand and how we can move forward". *Astronomy and Astrophysics Reviews*, **21**:59. 1209.4302.

[257] Ivezić Ż., Connolly A., VanderPlas J., Gray A. (2013). *Statistics, Data Mining, and Machine Learning in Astronomy*. Princeton, NJ, Princeton University Press.

[258] Janka H.T., Langanke K., Marek A., Martínez-Pinedo G., Müller B. (2007). "Theory of core-collapse supernovae". *Physics Reports*, **442**:38–74. astro-ph/0612072.

[259] Janka H.T., Zwerger T., Moenchmeyer R. (1993). "Does artificial viscosity destroy prompt type-II supernova explosions?" *Astronomy and Astrophysics*, **268**:360–368.

[260] Järv L., Kuusk P., Saal M. (2008). "Scalar-tensor cosmologies: Fixed points of the Jordan frame scalar field". *Physical Review D*, **78**(8):083530. 0807.2159.

[261] Jenet F., Finn L.S., Lazio J., Lommen A., McLaughlin M., Stairs I., Stinebring D., Verbiest J., Archibald A., Arzoumanian Z., et al. (2009). "The North American Nanohertz Observatory for Gravitational Waves". *ArXiv e-prints*. 0909.1058.

[262] Jones E., Oliphant T., Peterson P., et al. (2001). "SciPy: Open source scientific tools for Python". www.scipy.org.

[263] Jordan P. (1959). "Zum gegenwärtigen Stand der Diracschen kosmologischen Hypothesen". *Zeitschrift fur Physik*, **157**:112–121.

[264] Kalogera V. (2000). "Spin-Orbit Misalignment in Close Binaries with Two Compact Objects". *Astrophysical Journal*, **541**:319–328. astro-ph/9911417.

[265] Katz J.I., Anderson S.F., Grandi S.A., Margon B. (1982). "Nodding motions of accretion rings and disks - A short-term period in SS 433". *Astrophysical Journal*, **260**:780–793.

[266] Kawamura S., Ando M., Seto N., Sato S., Nakamura T., Tsubono K., Kanda N., Tanaka T., Yokoyama J., Funaki I., et al. (2011). "The Japanese space gravitational wave antenna: DECIGO". *Classical and Quantum Gravity*, **28**(9):094011.

[267] Kerr R.P. (1963). "Gravitational Field of a Spinning Mass as an Example of Algebraically Special Metrics". *Physical Review Letters*, **11**:237–238.

[268] Kesden M. (2008). "Can binary mergers produce maximally spinning black holes?" *Physical Review D*, **78**(8):084030. 0807.3043.

[269] Kesden M., Gerosa D., O'Shaughnessy R., Berti E., Sperhake U. (2015). "Effective Potentials and Morphological Transitions for Binary Black Hole Spin Precession". *Physical Review Letters*, **114**(8):081103. 1411.0674.

[270] Kesden M., Sperhake U., Berti E. (2010). "Final spins from the merger of precessing binary black holes". *Physical Review D*, **81**(8):084054. 1002.2643.

[271] Kesden M., Sperhake U., Berti E. (2010). "Relativistic Suppression of Black Hole Recoils". *Astrophysical Journal*, **715**:1006–1011. 1003.4993.

[272] Khan F.M., Just A., Merritt D. (2011). "Efficient Merger of Binary Supermassive Black Holes in Merging Galaxies". *Astrophysical Journal*, **732**:89. 1103.0272.

[273] Khan F.M., Preto M., Berczik P., Berentzen I., Just A., Spurzem R. (2012). "Mergers of Unequal-mass Galaxies: Supermassive Black Hole Binary Evolution and Structure of Merger Remnants". *Astrophysical Journal*, **749**:147. 1202.2124.

[274] Khan S., Husa S., Hannam M., Ohme F., Pürrer M., Forteza X.J., Bohé A. (2016). "Frequency-domain gravitational waves from nonprecessing black-hole binaries. II. A phenomenological model for the advanced detector era". *Physical Review D*, **93**(4):044007. 1508.07253.

[275] Khandai N., Di Matteo T., Croft R., Wilkins S., Feng Y., Tucker E., DeGraf C., Liu M.S. (2015). "The MassiveBlack-II simulation: the evolution of haloes and galaxies to z ~ 0". *Monthly Notices of the Royal Astronomical Society*, **450**:1349–1374. 1402.0888.

[276] Kidder L.E. (1995). "Coalescing binary systems of compact objects to (post)$^{5/2}$-Newtonian order. V. Spin effects". *Physical Review D*, **52**:821–847. gr-qc/9506022.

[277] King A.R., Kolb U. (1999). "The evolution of black hole mass and angular momentum". *Monthly Notices of the Royal Astronomical Society*, **305**:654–660. astro-ph/9901296.

[278] King A.R., Lubow S.H., Ogilvie G.I., Pringle J.E. (2005). "Aligning spinning black holes and accretion discs". *Monthly Notices of the Royal Astronomical Society*, **363**:49–56. astro-ph/0507098.

[279] King A.R., Pringle J.E. (2006). "Growing supermassive black holes by chaotic accretion". *Monthly Notices of the Royal Astronomical Society*, **373**:L90–L92. astro-ph/0609598.

[280] Kitzbichler M.G., White S.D.M. (2008). "A calibration of the relation between the abundance of close galaxy pairs and the rate of galaxy mergers". *Monthly Notices of the Royal Astronomical Society*, **391**:1489–1498. 0804.1965.

[281] Klebesadel R.W., Strong I.B., Olson R.A. (1973). "Observations of Gamma-Ray Bursts of Cosmic Origin". *Astrophysical Journal Letters*, **182**:L85.

[282] Klein A., Barausse E., Sesana A., Petiteau A., Berti E., Babak S., Gair J., Aoudia S., Hinder I., Ohme F., et al. (2016). "Science with the space-based interferometer eLISA: Supermassive black hole binaries". *Physical Review D*, **93**(2):024003. 1511.05581.

[283] Klein A., Cornish N., Yunes N. (2013). "Gravitational waveforms for precessing, quasicircular binaries via multiple scale analysis and uniform asymptotics: The near spin alignment case". *Physical Review D*, **88**(12):124015. 1305.1932.

[284] Klein A., Cornish N., Yunes N. (2014). "Fast frequency-domain waveforms for spin-precessing binary inspirals". *Physical Review D*, **90**(12):124029. 1408.5158.

[285] Klein A., Jetzer P., Sereno M. (2009). "Parameter estimation for coalescing massive binary black holes with LISA using the full 2-post-Newtonian gravitational waveform and spin-orbit precession". *Physical Review D*, **80**(6):064027. 0907.3318.

[286] Klypin A.A., Trujillo-Gomez S., Primack J. (2011). "Dark Matter Halos in the Standard Cosmological Model: Results from the Bolshoi Simulation". *Astrophysical Journal*, **740**:102. 1002.3660.

[287] Komossa S. (2012). "Recoiling Black Holes: Electromagnetic Signatures, Candidates, and Astrophysical Implications". *Advances in Astronomy*, **2012**:364973. 1202.1977.

[288] Komossa S., Merritt D. (2008). "Gravitational Wave Recoil Oscillations of Black Holes: Implications for Unified Models of Active Galactic Nuclei". *Astrophysical Journal Letters*, **689**:L89. 0811.1037.

[289] Komossa S., Merritt D. (2008). "Tidal Disruption Flares from Recoiling Supermassive Black Holes". *Astrophysical Journal Letters*, **683**:L21. 0807.0223.

[290] Komossa S., Zhou H., Lu H. (2008). "A Recoiling Supermassive Black Hole in the Quasar SDSS J092712.65+294344.0?" *Astrophysical Journal Letters*, **678**:L81. 0804.4585.

[291] Koppitz M., Pollney D., Reisswig C., Rezzolla L., Thornburg J., Diener P., Schnetter E. (2007). "Recoil Velocities from Equal-Mass Binary-Black-Hole Mergers". *Physical Review Letters*, **99**(4):041102. gr-qc/0701163.

[292] Kormendy J., Ho L.C. (2013). "Coevolution (Or Not) of Supermassive Black Holes and Host Galaxies". *Annual Review of Astronomy and Astrophysics*, **51**:511–653. 1304.7762.

[293] Kormendy J., Richstone D. (1995). "Inward Bound—The Search For Supermassive Black Holes In Galactic Nuclei". *Annual Review of Astronomy and Astrophysics*, **33**:581.

[294] Koss M., Blecha L., Mushotzky R., Hung C.L., Veilleux S., Trakhtenbrot B., Schawinski K., Stern D., Smith N., Li Y., et al. (2014). "SDSS1133: an unusually persistent transient in a nearby dwarf galaxy". *Monthly Notices of the Royal Astronomical Society*, **445**:515–527. 1401.6798.

[295] Kramer M., Champion D.J. (2013). "The European Pulsar Timing Array and the Large European Array for Pulsars". *Classical and Quantum Gravity*, **30**(22):224009.

[296] Kreiss H.O., Oliger J. (1973). *Methods for the approximate solution of time dependent problems*. World Meteorological Organization, International Council of Scientific Unions.

[297] Krolak A., Schutz B.F. (1987). "Coalescing binaries—Probe of the universe". *General Relativity and Gravitation*, **19**:1163–1171.

[298] Krori K.D., Nandy D. (1977). "Birkhoff's theorem and scalar-tensor theories of gravitation". *Journal of Physics A Mathematical General*, **10**:993–996.

[299] Lacey C., Cole S. (1993). "Merger rates in hierarchical models of galaxy formation". *Monthly Notices of the Royal Astronomical Society*, **262**:627–649.

[300] Lackner C.N., Cen R., Ostriker J.P., Joung M.R. (2012). "Building galaxies by accretion and in situ star formation". *Monthly Notices of the Royal Astronomical Society*, **425**:641–656. 1206.0295.

[301] Lang R.N., Hughes S.A. (2006). "Measuring coalescing massive binary black holes with gravitational waves: The impact of spin-induced precession". *Physical Review D*, **74**(12):122001. gr-qc/0608062.

[302] Lang R.N., Hughes S.A., Cornish N.J. (2011). "Measuring parameters of massive black hole binaries with partially aligned spins". *Physical Review D*, **84**(2):022002. 1101.3591.

[303] Laporte C.F.P., White S.D.M., Naab T., Gao L. (2013). "The growth in size and mass of cluster galaxies since z = 2". *Monthly Notices of the Royal Astronomical Society*, **435**:901–909. 1301.5319.

[304] Lattimer J.M., Douglas Swesty F. (1991). "A generalized equation of state for hot, dense matter". *Nuclear Physics A*, **535**:331–376.

[305] Lattimer J.M., Pethick C.J., Ravenhall D.G., Lamb D.Q. (1985). "Physical properties of hot, dense matter: The general case". *Nuclear Physics A*, **432**:646–742.

[306] Lauer T.R., Faber S.M., Richstone D., Gebhardt K., Tremaine S., Postman M., Dressler A., Aller M.C., Filippenko A.V., Green R., et al. (2007). "The Masses of Nuclear Black Holes in Luminous Elliptical Galaxies and Implications for the Space Density of the Most Massive Black Holes". *Astrophysical Journal*, **662**:808–834. astro-ph/0606739.

[307] Le Veque R.J. (1992). *Numerical Methods for Conservation Laws*. Basel, Switzerland, Birkhäuser Verlag, second edition.

[308] Li S., Liu F.K., Berczik P., Chen X., Spurzem R. (2012). "Interaction of Recoiling Supermassive Black Holes with Stars in Galactic Nuclei". *Astrophysical Journal*, **748**:65. 1201.3407.

[309] Lidman C., Iacobuta G., Bauer A.E., Barrientos L.F., Cerulo P., Couch W.J., Delaye L., Demarco R., Ellingson E., Faloon A.J., et al. (2013). "The importance of major mergers in the build up of stellar mass in brightest cluster galaxies at z = 1". *Monthly Notices of the Royal Astronomical Society*, **433**:825–837. 1305.0882.

[310] Lidman C., Suherli J., Muzzin A., Wilson G., Demarco R., Brough S., Rettura A., Cox J., DeGroot A., Yee H.K.C., et al. (2012). "Evidence for significant growth in the stellar mass of brightest cluster galaxies over the past 10 billion years". *Monthly Notices of the Royal Astronomical Society*, **427**:550–568. 1208.5143.

[311] Lin D.N.C., Papaloizou J. (1979). "Tidal torques on accretion discs in binary systems with extreme mass ratios". *Monthly Notices of the Royal Astronomical Society*, **186**:799–812.

[312] Lin D.N.C., Papaloizou J. (1986). "On the tidal interaction between protoplanets and the protoplanetary disk. III - Orbital migration of protoplanets". *Astrophysical Journal*, **309**:846–857.

[313] Lincoln C.W., Will C.M. (1990). "Coalescing binary systems of compact objects to (post)$^{5/2}$-Newtonian order: Late-time evolution and gravitational-radiation emission". *Physical Review D*, **42**:1123–1143.

[314] Lindblom L., Owen B.J., Brown D.A. (2008). "Model waveform accuracy standards for gravitational wave data analysis". *Physical Review D*, **78**(12):124020. 0809.3844.

[315] Liu F.S., Mao S., Deng Z.G., Xia X.Y., Wen Z.L. (2009). "Major dry mergers in early-type brightest cluster galaxies". *Monthly Notices of the Royal Astronomical Society*, **396**:2003–2010. 0904.2379.

[316] Lodato G. (2007). "Self-gravitating accretion discs". *Nuovo Cimento Rivista Serie*, **30**. 0801.3848.

[317] Lodato G., Gerosa D. (2013). "Black hole mergers: do gas discs lead to spin alignment?" *Monthly Notices of the Royal Astronomical Society*, **429**:L30–L34. 1211.0284.

[318] Lodato G., Natarajan P. (2006). "Supermassive black hole formation during the assembly of pre-galactic discs". *Monthly Notices of the Royal Astronomical Society*, **371**:1813–1823. astro-ph/0606159.

[319] Lodato G., Nayakshin S., King A.R., Pringle J.E. (2009). "Black hole mergers: can gas discs solve the 'final parsec' problem?" *Monthly Notices of the Royal Astronomical Society*, **398**:1392–1402. 0906.0737.

[320] Lodato G., Price D.J. (2010). "On the diffusive propagation of warps in thin accretion discs". *Monthly Notices of the Royal Astronomical Society*, **405**:1212–1226. 1002.2973.

[321] Lodato G., Pringle J.E. (2006). "The evolution of misaligned accretion discs and spinning black holes". *Monthly Notices of the Royal Astronomical Society*, **368**:1196–1208. astro-ph/0602306.

[322] Lodato G., Rice W.K.M. (2004). "Testing the locality of transport in self-gravitating accretion discs". *Monthly Notices of the Royal Astronomical Society*, **351**:630–642. astro-ph/0403185.

[323] Loeb A. (2007). "Observable Signatures of a Black Hole Ejected by Gravitational-Radiation Recoil in a Galaxy Merger". *Physical Review Letters*, **99**(4):041103. astro-ph/0703722.

[324] López-Sanjuan C., Le Fèvre O., de Ravel L., Cucciati O., Ilbert O., Tresse L., Bardelli S., Bolzonella M., Contini T., Garilli B., et al. (2011). "The VIMOS VLT Deep Survey. The contribution of minor mergers to the growth of $L_B \gtrsim L_B^*$ galaxies since z ~1 from spectroscopically identified pairs". *Astronomy and Astrophysics*, **530**:A20. 1009.5921.

[325] López-Sanjuan C., Le Fèvre O., Ilbert O., Tasca L.A.M., Bridge C., Cucciati O., Kampczyk P., Pozzetti L., Xu C.K., Carollo C.M., et al. (2012). "The dominant role of mergers in the size evolution of massive early-type galaxies since z ~ 1". *Astronomy and Astrophysics*, **548**:A7. 1202.4674.

[326] Lorimer D.R., Bailes M., McLaughlin M.A., Narkevic D.J., Crawford F. (2007). "A Bright Millisecond Radio Burst of Extragalactic Origin". *Science*, **318**:777. 0709.4301.

[327] Lotz J.M., Jonsson P., Cox T.J., Croton D., Primack J.R., Somerville R.S., Stewart K. (2011). "The Major and Minor Galaxy Merger Rates at z $<$ 1.5". *Astrophysical Journal*, **742**:103. 1108.2508.

[328] Lousto C.O., Campanelli M., Zlochower Y., Nakano H. (2010). "Remnant masses, spins and recoils from the merger of generic black hole binaries". *Classical and Quantum Gravity*, **27**(11):114006. 0904.3541.

[329] Lousto C.O., Healy J. (2015). "Flip-Flopping Binary Black Holes". *Physical Review Letters*, **114**(14):141101. 1410.3830.

[330] Lousto C.O., Zlochower Y. (2008). "Further insight into gravitational recoil". *Physical Review D*, **77**(4):044028. 0708.4048.

[331] Lousto C.O., Zlochower Y. (2009). "Modeling gravitational recoil from precessing highly spinning unequal-mass black-hole binaries". *Physical Review D*, **79**(6):064018. 0805.0159.

[332] Lousto C.O., Zlochower Y. (2011). "Hangup Kicks: Still Larger Recoils by Partial Spin-Orbit Alignment of Black-Hole Binaries". *Physical Review Letters*, **107**(23):231102. 1108.2009.

[333] Lousto C.O., Zlochower Y. (2013). "Nonlinear gravitational recoil from the mergers of precessing black-hole binaries". *Physical Review D*, **87**(8):084027. 1211.7099.

[334] Lousto C.O., Zlochower Y. (2014). "Black hole binary remnant mass and spin: A new phenomenological formula". *Physical Review D*, **89**(10):104052. 1312.5775.

[335] Lousto C.O., Zlochower Y., Dotti M., Volonteri M. (2012). "Gravitational recoil from accretion-aligned black-hole binaries". *Physical Review D*, **85**(8):084015. 1201.1923.

[336] Lubow S.H., Ogilvie G.I. (2000). "On the Tilting of Protostellar Disks by Resonant Tidal Effects". *Astrophysical Journal*, **538**:326–340. astro-ph/0003028.

[337] Ludlow A.D., Navarro J.F., Angulo R.E., Boylan-Kolchin M., Springel V., Frenk C., White S.D.M. (2014). "The mass-concentration-redshift relation of cold dark matter haloes". *Monthly Notices of the Royal Astronomical Society*, **441**:378–388. 1312.0945.

[338] Lundgren A., O'Shaughnessy R. (2014). "Single-spin precessing gravitational waveform in closed form". *Physical Review D*, **89**(4):044021. 1304.3332.

[339] Lynden-Bell D. (1967). "Statistical mechanics of violent relaxation in stellar systems". *Monthly Notices of the Royal Astronomical Society*, **136**:101.

[340] Lynden-Bell D. (1969). "Galactic Nuclei as Collapsed Old Quasars". *Nature*, **223**:690–694.

[341] Macciò A.V., Dutton A.A., van den Bosch F.C. (2008). "Concentration, spin and shape of dark matter haloes as a function of the cosmological model: WMAP1, WMAP3 and WMAP5 results". *Monthly Notices of the Royal Astronomical Society*, **391**:1940–1954. 0805.1926.

[342] MacFadyen A.I., Milosavljević M. (2008). "An Eccentric Circumbinary Accretion Disk and the Detection of Binary Massive Black Holes". *Astrophysical Journal*, **672**:83-93. astro-ph/0607467.

[343] Maggiore M. (2007). *Gravitational Waves. Vol. 1: Theory and Experiments*. Oxford, UK, Oxford University Press.

[344] Malbon R.K., Baugh C.M., Frenk C.S., Lacey C.G. (2007). "Black hole growth in hierarchical galaxy formation". *Monthly Notices of the Royal Astronomical Society*, **382**:1394–1414. astro-ph/0607424.

[345] Manchester R.N. (2013). "The International Pulsar Timing Array". *Classical and Quantum Gravity*, **30**(22):224010. 1309.7392.

[346] Manchester R.N., Hobbs G., Bailes M., Coles W.A., van Straten W., Keith M.J., Shannon R.M., Bhat N.D.R., Brown A., Burke-Spolaor S.G., et al. (2013). "The Parkes Pulsar Timing Array Project". *Publications of the Astronomical Society of Australia*, **30**:e017. 1210.6130.

[347] Marsat S., Bohé A., Faye G., Blanchet L. (2013). "Next-to-next-to-leading order spin-orbit effects in the equations of motion of compact binary systems". *Classical and Quantum Gravity*, **30**(5):055007. 1210.4143.

[348] Martin R.G., Pringle J.E., Tout C.A. (2007). "Alignment and precession of a black hole with a warped accretion disc". *Monthly Notices of the Royal Astronomical Society*, **381**:1617–1624. 0708.2034.

[349] Martin R.G., Pringle J.E., Tout C.A. (2009). "The shape of an accretion disc in a misaligned black hole binary". *Monthly Notices of the Royal Astronomical Society*, **400**:383–391. 0907.5142.

[350] Martynov D.V., Hall E.D., Abbott B.P., Abbott R., Abbott T.D., Abernathy M.R., Ackley K., Adams C., Addesso P., et al. (2016). "The Sensitivity of the Advanced LIGO Detectors at the Beginning of Gravitational Wave Astronomy". *Physical Review D*, **93**:112004. 1604.00439.

[351] Matsuda T., Nariai H. (1973). "Hydrodynamic Calculations of Spherical Gravitational Collapse in the Scalar-Tensor Theory of Gravity". *Progress of Theoretical Physics*, **49**:1195–1204.

[352] Mayer L. (2013). "Massive black hole binaries in gas-rich galaxy mergers; multiple regimes of orbital decay and interplay with gas inflows". *Classical and Quantum Gravity*, **30**(24):244008. 1308.0431.

[353] Mayer L., Kazantzidis S., Madau P., Colpi M., Quinn T., Wadsley J. (2007). "Rapid Formation of Supermassive Black Hole Binaries in Galaxy Mergers with Gas". *Science*, **316**:1874. 0706.1562.

[354] McClintock J.E., Narayan R., Davis S.W., Gou L., Kulkarni A., Orosz J.A., Penna R.F., Remillard R.A., Steiner J.F. (2011). "Measuring the spins of accreting black holes". *Classical and Quantum Gravity*, **28**(11):114009. 1101.0811.

[355] McConnell N.J., Ma C.P. (2013). "Revisiting the Scaling Relations of Black Hole Masses and Host Galaxy Properties". *Astrophysical Journal*, **764**:184. 1211.2816.

[356] McConnell N.J., Ma C.P., Murphy J.D., Gebhardt K., Lauer T.R., Graham J.R., Wright S.A., Richstone D.O. (2012). "Dynamical Measurements of Black Hole Masses in Four Brightest Cluster Galaxies at 100 Mpc". *Astrophysical Journal*, **756**:179. 1203.1620.

[357] McHugh M.P., Johnson W.W., Hamilton W.O., Hanson J., Heng I.S., McNeese D., Miller P., Nettles D., Weaver J., Zhang P. (2005). "Calibration of the ALLEGRO resonant detector". *Classical and Quantum Gravity*, **22**:S965–S973.

[358] McNamara P., Vitale S., Danzmann K., LISA Pathfinder Science Working Team (2008). "LISA Pathfinder". *Classical and Quantum Gravity*, **25**(11):114034.

[359] Mendes R.F.P. (2015). "Possibility of setting a new constraint to scalar-tensor theories". *Physical Review D*, **91**(6):064024. 1412.6789.

[360] Merritt D. (2006). "Mass Deficits, Stalling Radii, and the Merger Histories of Elliptical Galaxies". *Astrophysical Journal*, **648**:976–986. astro-ph/0603439.

[361] Merritt D., Ekers R.D. (2002). "Tracing Black Hole Mergers Through Radio Lobe Morphology". *Science*, **297**:1310–1313. astro-ph/0208001.

[362] Merritt D., Milosavljević M., Favata M., Hughes S.A., Holz D.E. (2004). "Consequences of Gravitational Radiation Recoil". *Astrophysical Journal Letters*, **607**:L9–L12. astro-ph/0402057.

[363] Merritt D., Poon M.Y. (2004). "Chaotic Loss Cones and Black Hole Fueling". *Astrophysical Journal*, **606**:788–798. astro-ph/0302296.

[364] Merritt D., Schnittman J.D., Komossa S. (2009). "Hypercompact Stellar Systems Around Recoiling Supermassive Black Holes". *Astrophysical Journal*, **699**:1690–1710. 0809.5046.

[365] Meru F., Bate M.R. (2012). "On the convergence of the critical cooling time-scale for the fragmentation of self-gravitating discs". *Monthly Notices of the Royal Astronomical Society*, **427**:2022–2046. 1209.1107.

[366] Miller B., Gallo E., Treu T., Woo J.H. (2012). "AMUSE-Field I: Nuclear X-Ray Properties of Local Field and Group Spheroids across the Stellar Mass Scale". *Astrophysical Journal*, **747**:57. 1112.3985.

[367] Miller M.C., Krolik J.H. (2013). "Alignment of Supermassive Black Hole Binary Orbits and Spins". *Astrophysical Journal*, **774**:43. 1307.6569.

[368] Miller M.C., Miller J.M. (2015). "The masses and spins of neutron stars and stellar-mass black holes". *Physics Reports*, **548**:1–34. 1408.4145.

[369] Milosavljević M., Merritt D. (2001). "Formation of Galactic Nuclei". *Astrophysical Journal*, **563**:34–62. astro-ph/0103350.

[370] Milosavljević M., Merritt D. (2003). "The Final Parsec Problem". In *The Astrophysics of Gravitational Wave Sources*, edited by J.M. Centrella, volume 686 of *American Institute of Physics Conference Series*, pages 201–210. astro-ph/0212270.

[371] Milosavljević M., Phinney E.S. (2005). "The Afterglow of Massive Black Hole Coalescence". *Astrophysical Journal Letters*, **622**:L93–L96. astro-ph/0410343.

[372] Misner C.W., Thorne K.S., Wheeler J.A. (1973). *Gravitation*. San Francisco, CA, W.H. Freeman and Co.

[373] Moore C., Gerosa D. (2016). In preparation.

[374] Moore C.J., Cole R.H., Berry C.P.L. (2015). "Gravitational-wave sensitivity curves". *Classical and Quantum Gravity*, **32**(1):015014. 1408.0740.

[375] Moss G.E., Miller L.R., Forward R.L. (1971). "Photon-noise-limited laser transducer for gravitational antenna." *Applied Optics*, **10**:2495–2498.

[376] Mroué A.H., Scheel M.A., Szilágyi B., Pfeiffer H.P., Boyle M., Hemberger D.A., Kidder L.E., Lovelace G., Ossokine S., Taylor N.W., et al. (2013). "Catalog of 174 Binary Black Hole Simulations for Gravitational Wave Astronomy". *Physical Review Letters*, **111**(24):241104. 1304.6077.

[377] Natarajan P., Pringle J.E. (1998). "The Alignment of Disk and Black Hole Spins in Active Galactic Nuclei". *Astrophysical Journal Letters*, **506**:L97–L100. astro-ph/9808187.

[378] Navarro J.F., Frenk C.S., White S.D.M. (1996). "The Structure of Cold Dark Matter Halos". *Astrophysical Journal*, **462**:563. astro-ph/9508025.

[379] Navarro J.F., Frenk C.S., White S.D.M. (1997). "A Universal Density Profile from Hierarchical Clustering". *Astrophysical Journal*, **490**:493–508. astro-ph/9611107.

[380] Nelson R.P., Papaloizou J.C.B., Masset F., Kley W. (2000). "The migration and growth of protoplanets in protostellar discs". *Monthly Notices of the Royal Astronomical Society*, **318**:18–36. astro-ph/9909486.

[381] Neto A.F., Gao L., Bett P., Cole S., Navarro J.F., Frenk C.S., White S.D.M., Springel V., Jenkins A. (2007). "The statistics of Λ CDM halo concentrations". *Monthly Notices of the Royal Astronomical Society*, **381**:1450–1462. 0706.2919.

[382] Netzer H., Trakhtenbrot B. (2014). "Bolometric luminosity black hole growth time and slim accretion discs in active galactic nuclei". *Monthly Notices of the Royal Astronomical Society*, **438**:672–679. 1311.4215.

[383] Nishizawa A., Taruya A., Hayama K., Kawamura S., Sakagami M.A. (2009). "Probing nontensorial polarizations of stochastic gravitational-wave backgrounds with ground-based laser interferometers". *Physical Review D*, **79**(8):082002. 0903.0528.

[384] Nixon C., King A., Price D. (2013). "Tearing up the disc: misaligned accretion on to a binary". *Monthly Notices of the Royal Astronomical Society*, **434**:1946–1954. 1307.0010.

[385] Nixon C.J., King A.R. (2012). "Broken discs: warp propagation in accretion discs". *Monthly Notices of the Royal Astronomical Society*, **421**:1201–1208. 1201.1297.

[386] Novak J. (1998). "Neutron star transition to a strong-scalar-field state in tensor-scalar gravity". *Physical Review D*, **58**(6):064019. gr-qc/9806022.

[387] Novak J. (1998). "Spherical neutron star collapse toward a black hole in a tensor-scalar theory of gravity". *Physical Review D*, **57**:4789–4801. gr-qc/9707041.

[388] Novak J., Ibáñez J.M. (2000). "Gravitational Waves from the Collapse and Bounce of a Stellar Core in Tensor-Scalar Gravity". *Astrophysical Journal*, **533**:392–405. astro-ph/9911298.

[389] O'Connor E. (2015). "An Open-source Neutrino Radiation Hydrodynamics Code for Core-collapse Supernovae". *Astrophysical Journal Supplement*, **219**:24. 1411.7058.

[390] O'Connor E., Ott C.D. (2010). "A new open-source code for spherically symmetric stellar collapse to neutron stars and black holes". *Classical and Quantum Gravity*, **27**(11):114103. 0912.2393.

[391] O'Connor E., Ott C.D. (2011). "Black Hole Formation in Failing Core-Collapse Supernovae". *Astrophysical Journal*, **730**:70. 1010.5550.

[392] O'Connor E., Ott C.D. (2013). "The Progenitor Dependence of the Pre-explosion Neutrino Emission in Core-collapse Supernovae". *Astrophysical Journal*, **762**:126. 1207.1100.

[393] Ogilvie G.I. (1999). "The non-linear fluid dynamics of a warped accretion disc". *Monthly Notices of the Royal Astronomical Society*, **304**:557–578. astro-ph/9812073.

[394] Ogilvie G.I., Dubus G. (2001). "Precessing warped accretion discs in X-ray binaries". *Monthly Notices of the Royal Astronomical Society*, **320**:485–503. astro-ph/0009264.

[395] Oller-Moreno S. (2015). "parmap: Easy parallelization in Python". pypi.python.org/pypi/parmap.

[396] Oppenheimer J.R., Volkoff G.M. (1939). "On Massive Neutron Cores". *Physical Review*, **55**:374–381.

[397] Oser L., Ostriker J.P., Naab T., Johansson P.H., Burkert A. (2010). "The Two Phases of Galaxy Formation". *Astrophysical Journal*, **725**:2312–2323. 1010.1381.

[398] O'Shaughnessy R., Farr B., Ochsner E., Cho H.S., Kim C., Lee C.H. (2014). "Parameter estimation of gravitational waves from nonprecessing black hole-neutron star inspirals with higher harmonics: Comparing Markov-chain Monte Carlo posteriors to an effective Fisher matrix". *Physical Review D*, **89**(6):064048. 1308.4704.

[399] O'Shaughnessy R., Farr B., Ochsner E., Cho H.S., Raymond V., Kim C., Lee C.H. (2014). "Parameter estimation of gravitational waves from precessing black hole-neutron star inspirals with higher harmonics". *Physical Review D*, **89**(10):102005. 1403.0544.

[400] O'Shaughnessy R., London L., Healy J., Shoemaker D. (2013). "Precession during merger: Strong polarization changes are observationally accessible features of strong-field gravity during binary black hole merger". *Physical Review D*, **87**(4):044038. 1209.3712.

[401] Ott C. (2016). www.stellarcollapse.org/GR1Dv2.

[402] Ott C.D. (2009). "TOPICAL REVIEW: The gravitational-wave signature of core-collapse supernovae". *Classical and Quantum Gravity*, **26**(6):063001. 0809.0695.

[403] Paczynski B. (1976). "Common Envelope Binaries". In *Structure and Evolution of Close Binary Systems*, edited by P. Eggleton, S. Mitton, J. Whelan, volume 73 of *IAU Symposium*, page 75.

[404] Palenzuela C., Barausse E., Ponce M., Lehner L. (2014). "Dynamical scalarization of neutron stars in scalar-tensor gravity theories". *Physical Review D*, **89**(4):044024. 1310.4481.

[405] Palenzuela C., Liebling S.L. (2016). "Constraining scalar-tensor theories of gravity from the most massive neutron stars". *Physical Review D*, **93**(4):044009. 1510.03471.

[406] Pan Y., Buonanno A., Taracchini A., Kidder L.E., Mroué A.H., Pfeiffer H.P., Scheel M.A., Szilágyi B. (2014). "Inspiral-merger-ringdown waveforms of spinning, precessing black-hole binaries in the effective-one-body formalism". *Physical Review D*, **89**(8):084006. 1307.6232.

[407] Papaloizou J.C.B., Pringle J.E. (1983). "The time-dependence of non-planar accretion discs". *Monthly Notices of the Royal Astronomical Society*, **202**:1181–1194.

[408] Peacock J.A. (2003). "Large-scale surveys and cosmic structure". *ArXiv e-prints*. astro-ph/0309240.

[409] Peebles P.J.E. (1980). *The large-scale structure of the universe*. Princeton, NJ, Princeton University Press.

[410] Peebles P.J.E. (1993). *Principles of Physical Cosmology*. Princeton, NJ, Princeton University Press.

[411] Pekowsky L., O'Shaughnessy R., Healy J., Shoemaker D. (2013). "Comparing gravitational waves from nonprecessing and precessing black hole binaries in the corotating frame". *Physical Review D*, **88**(2):024040. 1304.3176.

[412] Penzias A.A., Wilson R.W. (1965). "A Measurement of Excess Antenna Temperature at 4080 Mc/s." *Astrophysical Journal*, **142**:419–421.

[413] Perego A., Dotti M., Colpi M., Volonteri M. (2009). "Mass and spin co-evolution during the alignment of a black hole in a warped accretion disc". *Monthly Notices of the Royal Astronomical Society*, **399**:2249–2263. 0907.3742.

[414] Peters P.C. (1964). "Gravitational Radiation and the Motion of Two Point Masses". *Physical Review*, **136**:1224–1232.

[415] Peters P.C., Mathews J. (1963). "Gravitational Radiation from Point Masses in a Keplerian Orbit". *Physical Review*, **131**:435–440.

[416] Petterson J.A. (1977). "Twisted accretion disks. I - Derivation of the basic equations". *Astrophysical Journal*, **214**:550–559.

[417] Pitkin M., Reid S., Rowan S., Hough J. (2011). "Gravitational Wave Detection by Interferometry (Ground and Space)". *Living Reviews in Relativity*, **14**. 1102.3355.

[418] Poisson E., Will C.M. (2014). *Gravity*. Cambridge, UK, Cambridge University Press.

[419] Posti L., Nipoti C., Stiavelli M., Ciotti L. (2014). "The imprint of dark matter haloes on the size and velocity dispersion evolution of early-type galaxies". *Monthly Notices of the Royal Astronomical Society*, **440**:610–623. 1310.2255.

[420] Postman M., Lauer T.R., Donahue M., Graves G., Coe D., Moustakas J., Koekemoer A., Bradley L., Ford H.C., Grillo C., et al. (2012). "A Brightest Cluster Galaxy with an Extremely Large Flat Core". *Astrophysical Journal*, **756**:159. 1205.3839.

[421] Postnov K.A., Yungelson L.R. (2014). "The Evolution of Compact Binary Star Systems". *Living Reviews in Relativity*, **17**. 1403.4754.

[422] Press W.H., Flannery B.P., Teukolsky S.A., Vetterling W.T. (1989). *Numerical recipes in C. The art of scientific computing*. Cambridge, UK, Cambridge University Press.

[423] Press release (2015). www.cam.ac.uk/research/news/new-insights-found-in-black-hole-collisions.

[424] Press release (2016). www.cam.ac.uk/research/news/using-gravitational-waves-to-catch-runaway-black-holes.

[425] Preto M., Berentzen I., Berczik P., Spurzem R. (2011). "Fast Coalescence of Massive Black Hole Binaries from Mergers of Galactic Nuclei: Implications for Low-frequency Gravitational-wave Astrophysics". *Astrophysical Journal Letters*, **732**:L26. 1102.4855.

[426] Pretorius F. (2005). "Evolution of Binary Black-Hole Spacetimes". *Physical Review Letters*, **95**(12):121101. gr-qc/0507014.

[427] Pringle J.E. (1992). "A simple approach to the evolution of twisted accretion discs". *Monthly Notices of the Royal Astronomical Society*, **258**:811–818.

[428] Psaltis D. (2008). "Probes and Tests of Strong-Field Gravity with Observations in the Electromagnetic Spectrum". *Living Reviews in Relativity*, **11**. 0806.1531.

[429] Punturo M., Abernathy M., Acernese F., Allen B., Andersson N., Arun K., Barone F., Barr B., Barsuglia M., Beker M., et al. (2010). "The Einstein Telescope: a third-generation gravitational wave observatory". *Classical and Quantum Gravity*, **27**(19):194002.

[430] Punturo M., Abernathy M., Acernese F., Allen B., Andersson N., Arun K., Barone F., Barr B., Barsuglia M., Beker M., et al. (2010). "The third generation of gravitational wave observatories and their science reach". *Classical and Quantum Gravity*, **27**(8):084007.

[431] Racine É. (2008). "Analysis of spin precession in binary black hole systems including quadrupole-monopole interaction". *Physical Review D*, **78**(4):044021. 0803.1820.

[432] Radice D., Ott C.D., Abdikamalov E., Couch S.M., Haas R., Schnetter E. (2016). "Neutrino-driven Convection in Core-collapse Supernovae: High-resolution Simulations". *Astrophysical Journal*, **820**:76. 1510.05022.

[433] Raffai P., Haiman Z., Frei Z. (2016). "A statistical method to search for recoiling supermassive black holes in active galactic nuclei". *Monthly Notices of the Royal Astronomical Society*, **455**:484–492. 1509.02075.

[434] Rafikov R.R. (2013). "Structure and Evolution of Circumbinary Disks around Supermassive Black Hole Binaries". *Astrophysical Journal*, **774**:144. 1205.5017.

[435] Ragusa E., Lodato G., Price D.J. (2016). "Suppression of the accretion rate in thin discs around binary black holes". *Monthly Notices of the Royal Astronomical Society*, **460**:1243–1253. 1605.01730.

[436] Ramazanoğlu F.M., Pretorius F. (2016). "Spontaneous scalarization with massive fields". *Physical Review D*, **93**(6):064005. 1601.07475.

[437] Redmount I.H., Rees M.J. (1989). "Gravitational-radiation rocket effects and galactic structure." *Comments on Astrophysics*, **14**:165–175.

[438] Rees M.J. (1978). "Relativistic jets and beams in radio galaxies". *Nature*, **275**:516.

[439] Reynolds C.S. (2013). "The spin of supermassive black holes". *Classical and Quantum Gravity*, **30**(24):244004. 1307.3246.

[440] Reynolds C.S. (2014). "Measuring Black Hole Spin Using X-Ray Reflection Spectroscopy". *Space Science Reviews*, **183**:277–294. 1302.3260.

[441] Rezzolla L., Barausse E., Dorband E.N., Pollney D., Reisswig C., Seiler J., Husa S. (2008). "Final spin from the coalescence of two black holes". *Physical Review D*, **78**(4):044002. 0712.3541.

[442] Rezzolla L., Macedo R.P., Jaramillo J.L. (2010). "Understanding the "Antikick" in the Merger of Binary Black Holes". *Physical Review Letters*, **104**(22):221101. 1003.0873.

[443] Rice W.K.M., Lodato G., Armitage P.J. (2005). "Investigating fragmentation conditions in self-gravitating accretion discs". *Monthly Notices of the Royal Astronomical Society*, **364**:L56–L60. astro-ph/0509413.

[444] Riles K. (2013). "Gravitational waves: Sources, detectors and searches". *Progress in Particle and Nuclear Physics*, **68**:1–54. 1209.0667.

[445] Robaina A.R., Bell E.F., van der Wel A., Somerville R.S., Skelton R.E., McIntosh D.H., Meisenheimer K., Wolf C. (2010). "The Merger-driven Evolution of Massive Galaxies". *Astrophysical Journal*, **719**:844–850. 1002.4193.

[446] Rodriguez C., Taylor G.B., Zavala R.T., Peck A.B., Pollack L.K., Romani R.W. (2006). "A Compact Supermassive Binary Black Hole System". *Astrophysical Journal*, **646**:49–60. astro-ph/0604042.

[447] Roedig C., Dotti M., Sesana A., Cuadra J., Colpi M. (2011). "Limiting eccentricity of subparsec massive black hole binaries surrounded by self-gravitating gas discs". *Monthly Notices of the Royal Astronomical Society*, **415**:3033–3041. 1104.3868.

[448] Roedig C., Sesana A., Dotti M., Cuadra J., Amaro-Seoane P., Haardt F. (2012). "Evolution of binary black holes in self gravitating discs. Dissecting the torques". *Astronomy and Astrophysics*, **545**:A127. 1202.6063.

[449] Romero J.V., Miralles J.M., Ibáñez J.A., Pons J.A. (1997). "General Relativistic Collapse of Hot Stellar Cores". In *Some Topics on General Relativity and Gravitational Radiation*, edited by J.A. Miralles, J.A. Morales, D. Saez, page 289.

[450] Russell H.R., McNamara B.R., Edge A.C., Hogan M.T., Main R.A., Vantyghem A.N. (2013). "Radiative efficiency, variability and Bondi accretion on to massive black holes: the transition from radio AGN to quasars in brightest cluster galaxies". *Monthly Notices of the Royal Astronomical Society*, **432**:530–553. 1211.5604.

[451] Salgado M. (2006). "The Cauchy problem of scalar tensor theories of gravity". *Classical and Quantum Gravity*, **23**:4719–4741. gr-qc/0509001.

[452] Salgado M., Martínez del Río D., Alcubierre M., Núñez D. (2008). "Hyperbolicity of scalar-tensor theories of gravity". *Physical Review D*, **77**(10):104010. 0801.2372.

[453] Salpeter E.E. (1964). "Accretion of Interstellar Matter by Massive Objects." *Astrophysical Journal*, **140**:796–800.

[454] Sampson L., Yunes N., Cornish N., Ponce M., Barausse E., Klein A., Palenzuela C., Lehner L. (2014). "Projected constraints on scalarization with gravitational waves from neutron star binaries". *Physical Review D*, **90**(12):124091. 1407.7038.

[455] Sasaki M., Tagoshi H. (2003). "Analytic Black Hole Perturbation Approach to Gravitational Radiation". *Living Reviews in Relativity*, **6**. gr-qc/0306120.

[456] Sathyaprakash B.S., Schutz B.F. (2009). "Physics, Astrophysics and Cosmology with Gravitational Waves". *Living Reviews in Relativity*, **12**. 0903.0338.

[457] Scheel M.A., Shapiro S.L., Teukolsky S.A. (1995). "Collapse to black holes in Brans-Dicke theory. I. Horizon boundary conditions for dynamical spacetimes". *Physical Review D*, **51**:4208–4235. gr-qc/9411025.

[458] Scheel M.A., Shapiro S.L., Teukolsky S.A. (1995). "Collapse to black holes in Brans-Dicke theory. II. Comparison with general relativity". *Physical Review D*, **51**:4236–4249. gr-qc/9411026.

[459] Scheuer P.A.G., Feiler R. (1996). "The realignment of a black hole misaligned with its accretion disc". *Monthly Notices of the Royal Astronomical Society*, **282**:291.

[460] Schmidt M. (1962). "Spectrum of a Stellar Object Identified with the Radio Source 3c 286." *Astrophysical Journal*, **136**:684.

[461] Schmidt P., Hannam M., Husa S. (2012). "Towards models of gravitational waveforms from generic binaries: A simple approximate mapping between precessing and nonprecessing inspiral signals". *Physical Review D*, **86**(10):104063. 1207.3088.

[462] Schmidt P., Ohme F., Hannam M. (2015). "Towards models of gravitational waveforms from generic binaries: II. Modelling precession effects with a single effective precession parameter". *Physical Review D*, **91**(2):024043. 1408.1810.

[463] Schnittman J.D. (2004). "Spin-orbit resonance and the evolution of compact binary systems". *Physical Review D*, **70**(12):124020. astro-ph/0409174.

[464] Schnittman J.D. (2007). "Retaining Black Holes with Very Large Recoil Velocities". *Astrophysical Journal Letters*, **667**:L133–L136. 0706.1548.

[465] Schnittman J.D. (2011). "Electromagnetic counterparts to black hole mergers". *Classical and Quantum Gravity*, **28**(9):094021. 1010.3250.

[466] Schnittman J.D. (2013). "Astrophysics of super-massive black hole mergers". *Classical and Quantum Gravity*, **30**(24):244007. 1307.3542.

[467] Schnittman J.D., Buonanno A. (2007). "The Distribution of Recoil Velocities from Merging Black Holes". *Astrophysical Journal Letters*, **662**:L63–L66. astro-ph/0702641.

[468] Schucking E. (1989). "The first texas symposium on relativistic astrophysiscs". *Physics Today*, page 49.

[469] Seoane P.A., Aoudia S., Audley H., Auger G., Babak S., Baker J., Barausse E., Barke S., Bassan M., Beckmann V., et al. (2013). "The Gravitational Universe". *ArXiv e-prints*. 1305.5720.

[470] Sesana A. (2007). "Extreme recoils: impact on the detection of gravitational waves from massive black hole binaries". *Monthly Notices of the Royal Astronomical Society*, **382**:L6–L10. 0707.4677.

[471] Sesana A. (2010). "Self Consistent Model for the Evolution of Eccentric Massive Black Hole Binaries in Stellar Environments: Implications for Gravitational Wave Observations". *Astrophysical Journal*, **719**:851–864. 1006.0730.

[472] Sesana A. (2013). "Systematic investigation of the expected gravitational wave signal from supermassive black hole binaries in the pulsar timing band". *Monthly Notices of the Royal Astronomical Society*, **433**:L1–L5. 1211.5375.

[473] Sesana A. (2016). "Prospects for Multiband Gravitational-Wave Astronomy after GW150914". *Physical Review Letters*, **116**(23):231102. 1602.06951.

[474] Sesana A., Barausse E., Dotti M., Rossi E.M. (2014). "Linking the Spin Evolution of Massive Black Holes to Galaxy Kinematics". *Astrophysical Journal*, **794**:104. 1402.7088.

[475] Sesana A., Gair J., Berti E., Volonteri M. (2011). "Reconstructing the massive black hole cosmic history through gravitational waves". *Physical Review D*, **83**(4):044036. 1011.5893.

[476] Shakura N.I., Sunyaev R.A. (1973). "Black holes in binary systems. Observational appearance." *Astronomy and Astrophysics*, **24**:337–355.

[477] Shankar F., Crocce M., Miralda-Escudé J., Fosalba P., Weinberg D.H. (2010). "On the Radiative Efficiencies, Eddington Ratios, and Duty Cycles of Luminous High-redshift Quasars". *Astrophysical Journal*, **718**:231–250. 0810.4919.

[478] Shapiro I.I. (1990). "Solar system tests of general relativity: recent results and present plans". In *General Relativity and Gravitation, 1989*, edited by N. Ashby, D.F. Bartlett, W. Wyss, page 313.

[479] Shapiro S.L., Teukolsky S.A. (1983). *Black Holes, White Dwarfs and Neutron Stars: The Physics of Compact Objects*. Wiley, New York.

[480] Shapiro S.S., Davis J.L., Lebach D.E., Gregory J.S. (2004). "Measurement of the Solar Gravitational Deflection of Radio Waves using Geodetic Very-Long-Baseline Interferometry Data, 1979 1999". *Physical Review Letters*, **92**(12):121101.

[481] Shen H., Toki H., Oyamatsu K., Sumiyoshi K. (1998). "Relativistic equation of state of nuclear matter for supernova and neutron star". *Nuclear Physics A*, **637**:435–450. nucl-th/9805035.

[482] Shen H., Toki H., Oyamatsu K., Sumiyoshi K. (1998). "Relativistic Equation of State of Nuclear Matter for Supernova Explosion". *Progress of Theoretical Physics*, **100**:1013–1031. nucl-th/9806095.

[483] Shen H., Toki H., Oyamatsu K., Sumiyoshi K. (2011). "Relativistic Equation of State for Core-collapse Supernova Simulations". *Astrophysical Journal Supplement*, **197**:20. 1105.1666.

[484] Shi J.M., Krolik J.H., Lubow S.H., Hawley J.F. (2012). "Three-dimensional Magnetohydrodynamic Simulations of Circumbinary Accretion Disks: Disk Structures and Angular Momentum Transport". *Astrophysical Journal*, **749**:118. 1110.4866.

[485] Shibata M., Nakao K., Nakamura T. (1994). "Scalar-type gravitational wave emission from gravitational collapse in Brans-Dicke theory: Detectability by a laser interferometer". *Physical Review D*, **50**:7304–7317.

[486] Shibata M., Taniguchi K., Okawa H., Buonanno A. (2014). "Coalescence of binary neutron stars in a scalar-tensor theory of gravity". *Physical Review D*, **89**(8):084005. 1310.0627.

[487] Shields G.A., Bonning E.W. (2013). "A Captured Runaway Black Hole in NGC 1277?" *Astrophysical Journal Letters*, **772**:L5. 1302.4458.

[488] Shoemaker D. (2009). "Advanced LIGO anticipated sensitivity curves". dcc.ligo.org/cgi-bin/DocDB/ShowDocument?docid=m060056.

[489] Sijacki D., Springel V., Haehnelt M.G. (2011). "Gravitational recoils of supermassive black holes in hydrodynamical simulations of gas-rich galaxies". *Monthly Notices of the Royal Astronomical Society*, **414**:3656–3670. 1008.3313.

[490] Silva H.O., Macedo C.F.B., Berti E., Crispino L.C.B. (2015). "Slowly rotating anisotropic neutron stars in general relativity and scalar-tensor theory". *Classical and Quantum Gravity*, **32**(14):145008. 1411.6286.

[491] Somiya K. (2012). "Detector configuration of KAGRA-the Japanese cryogenic gravitational-wave detector". *Classical and Quantum Gravity*, **29**(12):124007. 1111.7185.

[492] Sommerfeld A. (1949). *Partial differential equation in physics*. New York NY, Academic Press.

[493] Sonnenfeld A., Nipoti C., Treu T. (2014). "Purely Dry Mergers do not Explain the Observed Evolution of Massive Early-type Galaxies since z ˜ 1". *Astrophysical Journal*, **786**:89. 1310.3280.

[494] Sotiriou T.P. (2014). "Gravity and Scalar Fields". In *Lecture Notes in Physics, Berlin Springer Verlag*, edited by E. Papantonopoulos, volume 892, pages 3–24. 1404.2955.

[495] Spergel D.N. (2015). "The dark side of cosmology: Dark matter and dark energy". *Science*, **347**:1100–1102.

[496] Sperhake U. (2015). "The numerical relativity breakthrough for binary black holes". *Classical and Quantum Gravity*, **32**(12):124011. 1411.3997.

[497] Stott J.P., Hickox R.C., Edge A.C., Collins C.A., Hilton M., Harrison C.D., Romer A.K., Rooney P.J., Kay S.T., Miller C.J., et al. (2012). "The XMM Cluster Survey: the interplay between the brightest cluster galaxy and the intracluster medium via AGN feedback". *Monthly Notices of the Royal Astronomical Society*, **422**:2213–2229. 1202.3787.

[498] Sukhbold T., Ertl T., Woosley S.E., Brown J.M., Janka H.T. (2016). "Core-collapse Supernovae from 9 to 120 Solar Masses Based on Neutrino-powered Explosions". *Astrophysical Journal*, **821**:38. 1510.04643.

[499] Syer D., Clarke C.J. (1995). "Satellites in discs: regulating the accretion luminosity". *Monthly Notices of the Royal Astronomical Society*, **277**:758–766. astro-ph/9505021.

[500] Taffoni G., Mayer L., Colpi M., Governato F. (2003). "On the life and death of satellite haloes". *Monthly Notices of the Royal Astronomical Society*, **341**:434–448. astro-ph/0301271.

[501] Tamanini N., Caprini C., Barausse E., Sesana A., Klein A., Petiteau A. (2016). "Science with the space-based interferometer eLISA. III: probing the expansion of the universe using gravitational wave standard sirens". *Journal of Cosmology and Astroparticle Physics*, **4**:002. 1601.07112.

[502] Taylor J.H., Weisberg J.M. (1982). "A new test of general relativity - Gravitational radiation and the binary pulsar PSR 1913+16". *Astrophysical Journal*, **253**:908–920.

[503] Terzić B., Graham A.W. (2005). "Density-potential pairs for spherical stellar systems with Sérsic light profiles and (optional) power-law cores". *Monthly Notices of the Royal Astronomical Society*, **362**:197–212. astro-ph/0506192.

[504] Thorne K.S. (1974). "Disk-Accretion onto a Black Hole. II. Evolution of the Hole". *Astrophysical Journal*, **191**:507–520.

[505] Thorne K.S. (1987). "Gravitational radiation." In *Three Hundred Years of Gravitation*, edited by S.W. Hawking, W. Israel, pages 330–458.

[506] Thorne K.S. (1998). "Probing Black Holes and Relativistic Stars with Gravitational Waves". In *Black Holes and Relativistic Stars*, edited by R.M. Wald, page 41. gr-qc/9706079.

[507] Thorne K.S., Dykla J.J. (1971). "Black Holes in the Dicke-Brans Theory of Gravity". *Astrophysical Journal Letters*, **166**:L35.

[508] Thorne K.S., Hartle J.B. (1985). "Laws of motion and precession for black holes and other bodies". *Physical Review D*, **31**:1815–1837.

[509] Tichy W., Marronetti P. (2008). "Final mass and spin of black-hole mergers". *Physical Review D*, **78**(8):081501. 0807.2985.

[510] Tolman R.C. (1939). "Static Solutions of Einstein's Field Equations for Spheres of Fluid". *Physical Review*, **55**:364–373.

[511] Toomre A. (1964). "On the gravitational stability of a disk of stars". *Astrophysical Journal*, **139**:1217–1238.

[512] Tremaine S., Davis S.W. (2014). "Dynamics of warped accretion discs". *Monthly Notices of the Royal Astronomical Society*, **441**:1408–1434. 1308.1964.

[513] Tremaine S., Richstone D.O., Byun Y.I., Dressler A., Faber S.M., Grillmair C., Kormendy J., Lauer T.R. (1994). "A family of models for spherical stellar systems". *Astronomical Journal*, **107**:634–644. astro-ph/9309044.

[514] Trifirò D., O'Shaughnessy R., Gerosa D., Berti E., Kesden M., Littenberg T., Sperhake U. (2016). "Distinguishing black-hole spin-orbit resonances by their gravitational wave signatures. II. Full parameter estimation". *Physical Review D*, **93**(4):044071. 1507.05587.

[515] Trujillo I., Ferreras I., de La Rosa I.G. (2011). "Dissecting the size evolution of elliptical galaxies since z~ 1: puffing-up versus minor-merging scenarios". *Monthly Notices of the Royal Astronomical Society*, **415**:3903–3913. 1102.3398.

[516] Ugliano M., Janka H.T., Marek A., Arcones A. (2012). "Progenitor-explosion Connection and Remnant Birth Masses for Neutrino-driven Supernovae of Iron-core Progenitors". *Astrophysical Journal*, **757**:69. 1205.3657.

[517] Unnikrishnan C.S. (2013). "IndIGO and LIGO-India Scope and Plans for Gravitational Wave Research and Precision Metrology in India". *International Journal of Modern Physics D*, **22**:1341010. 1510.06059.

[518] Valtonen M.J., Lehto H.J., Nilsson K., Heidt J., Takalo L.O., Sillanpää A., Villforth C., Kidger M., Poyner G., Pursimo T., et al. (2008). "A massive binary black-hole system in OJ287 and a test of general relativity". *Nature*, **452**:851–853. 0809.1280.

[519] van den Bosch R.C.E., Gebhardt K., Gültekin K., van de Ven G., van der Wel A., Walsh J.L. (2012). "An over-massive black hole in the compact lenticular galaxy NGC 1277". *Nature*, **491**:729–731. 1211.6429.

[520] van der Marel R.P., Magorrian J., Carlberg R.G., Yee H.K.C., Ellingson E. (2000). "The Velocity and Mass Distribution of Clusters of Galaxies from the CNOC1 Cluster Redshift Survey". *Astronomical Journal*, **119**:2038–2052. astro-ph/9910494.

[521] van der Walt S., Colbert S., Varoquaux G. (2011). "The numpy array: A structure for efficient numerical computation". *Computing in Science Engineering*, **13**(2):22–30.

[522] van Rossum G., de Boer J. (1991). "Interactively testing remote servers using the python programming language". *CWI Quarterly*, **4**(4):283–303.

[523] Van Wassenhove S., Capelo P.R., Volonteri M., Dotti M., Bellovary J.M., Mayer L., Governato F. (2014). "Nuclear coups: dynamics of black holes in galaxy mergers". *Monthly Notices of the Royal Astronomical Society*, **439**:474–487. 1310.7581.

[524] Vasiliev E., Antonini F., Merritt D. (2014). "The Final-parsec Problem in Nonspherical Galaxies Revisited". *Astrophysical Journal*, **785**:163. 1311.1167.

[525] Vecchio A. (2004). "LISA observations of rapidly spinning massive black hole binary systems". *Physical Review D*, **70**(4):042001. astro-ph/0304051.

[526] Veitch J., Raymond V., Farr B., Farr W., Graff P., Vitale S., Aylott B., Blackburn K., Christensen N., Coughlin M., et al. (2015). "Parameter estimation for compact binaries with ground-based gravitational-wave observations using the LALInference software library". *Physical Review D*, **91**(4):042003. 1409.7215.

[527] Vicari A., Capuzzo-Dolcetta R., Merritt D. (2007). "Consequences of Triaxiality for Gravitational Wave Recoil of Black Holes". *Astrophysical Journal*, **662**:797–807. astro-ph/0612073.

[528] Vinante A. (2006). "Present performance and future upgrades of the AURIGA capacitive readout". *Classical and Quantum Gravity*, **23**:S103–S110.

[529] Vitale S., Lynch R., Veitch J., Raymond V., Sturani R. (2014). "Measuring the Spin of Black Holes in Binary Systems Using Gravitational Waves". *Physical Review Letters*, **112**(25):251101. 1403.0129.

[530] Volonteri M. (2015). www2.iap.fr/users/volonter/LISA_catalogs.html.

[531] Volonteri M., Gültekin K., Dotti M. (2010). "Gravitational recoil: effects on massive black hole occupation fraction over cosmic time". *Monthly Notices of the Royal Astronomical Society*, **404**:2143–2150. 1001.1743.

[532] Volonteri M., Haardt F., Gültekin K. (2008). "Compact massive objects in Virgo galaxies: the black hole population". *Monthly Notices of the Royal Astronomical Society*, **384**:1387–1392. 0710.5770.

[533] Volonteri M., Haardt F., Madau P. (2003). "The Assembly and Merging History of Supermassive Black Holes in Hierarchical Models of Galaxy Formation". *Astrophysical Journal*, **582**:559–573. astro-ph/0207276.

[534] Vosmera J., Gerosa D. (2016). In preparation.

[535] Wang J.M., Hu C., Li Y.R., Chen Y.M., King A.R., Marconi A., Ho L.C., Yan C.S., Staubert R., Zhang S. (2009). "Episodic Random Accretion and the Cosmological Evolution of Supermassive Black Hole Spins". *Astrophysical Journal Letters*, **697**:L141–L144. 0904.1896.

[536] Weaver T.A., Zimmerman G.B., Woosley S.E. (1978). "Presupernova evolution of massive stars". *Astrophysical Journal*, **225**:1021–1029.

[537] Weber J. (1960). "Detection and Generation of Gravitational Waves". *Physical Review*, **117**:306–313.

[538] Webster B.L., Murdin P. (1972). "Cygnus X-1-a Spectroscopic Binary with a Heavy Companion ?" *Nature*, **235**:37–38.

[539] Weinzirl T., Jogee S., Neistein E., Khochfar S., Kormendy J., Marinova I., Hoyos C., Balcells M., den Brok M., Hammer D., et al. (2014). "The HST/ACS Coma Cluster Survey - VII. Structure and assembly of massive galaxies in the centre of the Coma cluster". *Monthly Notices of the Royal Astronomical Society*, **441**:3083–3121. 1310.3755.

[540] Wex N. (2014). "Testing Relativistic Gravity with Radio Pulsars". In *Brumberg Festschrift, edited by S. M. Kopeikein*. 1402.5594.

[541] White S.D.M., Rees M.J. (1978). "Core condensation in heavy halos - A two-stage theory for galaxy formation and clustering". *Monthly Notices of the Royal Astronomical Society*, **183**:341–358.

[542] Wilkins D.C. (1972). "Bound Geodesics in the Kerr Metric". *Physical Review D*, **5**:814–822.

[543] Will C.M. (1993). *Theory and Experiment in Gravitational Physics*. Cambridge, UK, Cambridge University Press.

[544] Will C.M. (2014). "The Confrontation between General Relativity and Experiment". *Living Reviews in Relativity*, **17**. 1403.7377.

[545] Will C.M., Zaglauer H.W. (1989). "Gravitational radiation, close binary systems, and the Brans-Dicke theory of gravity". *Astrophysical Journal*, **346**:366–377.

[546] Williams J.G., Turyshev S.G., Boggs D.H. (2009). "Lunar Laser Ranging Tests of the Equivalence Principle with the Earth and Moon". *International Journal of Modern Physics D*, **18**:1129–1175. gr-qc/0507083.

[547] Woosley S.E., Heger A. (2007). "Nucleosynthesis and remnants in massive stars of solar metallicity". *Physics Reports*, **442**:269–283. astro-ph/0702176.

[548] Woosley S.E., Heger A., Weaver T.A. (2002). "The evolution and explosion of massive stars". *Reviews of Modern Physics*, **74**:1015–1071.

[549] Xu C.K., Zhao Y., Scoville N., Capak P., Drory N., Gao Y. (2012). "Major-merger Galaxy Pairs in the COSMOS Field—Mass-dependent Merger Rate Evolution since z = 1". *Astrophysical Journal*, **747**:85. 1109.3693.

[550] Young M.D., Baird J.T., Clarke C.J. (2015). "The evolution of the mass ratio of accreting binaries: the role of gas temperature". *Monthly Notices of the Royal Astronomical Society*, **447**:2907–2914. 1412.3963.

[551] Young M.D., Clarke C.J. (2015). "Binary accretion rates: dependence on temperature and mass ratio". *Monthly Notices of the Royal Astronomical Society*, **452**:3085–3091. 1507.01850.

[552] Yu Q. (2002). "Evolution of massive binary black holes". *Monthly Notices of the Royal Astronomical Society*, **331**:935–958. astro-ph/0109530.

[553] Yunes N., Siemens X. (2013). "Gravitational-Wave Tests of General Relativity with Ground-Based Detectors and Pulsar-Timing Arrays". *Living Reviews in Relativity*, **16**(9). 1304.3473.

[554] Zhao X., Kesden M., Gerosa D. (2016). In preparation.

[555] Zwerger T., Mueller E. (1997). "Dynamics and gravitational wave signature of axisymmetric rotational core collapse." *Astronomy and Astrophysics*, **320**:209–227.

Acknowledgments

Support

My Ph.D degree was supported by Science and Technology Facilities Council award No. 1344276 and the Isaac Newton Studentship of the University of Cambridge. Travel support is acknowledged from the Department of Applied Mathematics and Theoretical Physics; Ulrich Sperhake's FP7-PEOPLE-2011-CIG Grant No. 293412; and personal grants received from the Darwin College Travel Fund, the Cambridge Philosophical Society, the Rouse Ball Travelling Studentship in Mathematics of Trinity College and the Royal Astronomical Society.

Thanks

First, I thank my Ph.D supervisor Ulrich Sperhake for his guidance in these years, which went well beyond completing this work. I am grateful to your endless interest and curiosity, from numerics to football. I am really honored to be Uli's first student.

I thank my scientific collaborators Emanuele Berti, Michael Kesden, Antoine Klein, Giuseppe Lodato, Christopher Moore, Richard O'Shaughnessy, Christian Ott, Giovanni Rosotti, Alberto Sesana, Daniele Trifiró and Benedetta Veronesi who contributed to the work presented here. I further thank Enrico Barausse, Christopher Berry, Alessandra Buonanno, Priscilla Canizares, Vitor Cardoso, Cathie Clarke, William Cook, Guillame Faye, William Farr, Brian Farris, Pau Figueras, Paulo Freire, Jonathan Gair, Leonardo Gualtieri, Michael Horbatsch, Nathan Johnson-McDaniel, Markus Kunesch, Tod Lauer, Tyson Littenberg, Coleman Miller, Jerome Novak, Evan O'Connor, Gordon Ogilvie, Paolo Pani, Marc Postman, Fethi Ramazanoglu, Christopher Reynolds, Hector O. da Silva, Thomas Sotiriou, Nicola Tamanini, Saran Tunyasuvunakool, Alberto Vecchio, Jakub Vosmera, Norbert Wex, Helvi Witek and Xinyu Zhao, for a variety of discussions, suggestions and technical help received to complete this work. I thank my Ph.D examiners Harvey Reall and Carlos Sopuerta.

I thank the DAMTP HEP-GR group and the IoA GW group for countless stimulating

discussions. I am particularly grateful to my officemates who tolerated my loud voice during phone calls and my Italian curses when my code kept on crashing. I thank British rainy days which, somehow, made me stay in my office working. I thank the Trinity Hall MCR football team for all those games together. I thank all my new Cambridge friends and all people who came across our Cambridge CL community in the past few years: you really made my time here full of wonder. I thank my friends who are away (particularly those who came visiting me in Cambridge) because you showed me friendship is for real. I thank my parents, my brother and my sister, who always supported me with undeserved passion. I thank my grandparents, who are so proud of me; and my in-laws who took me on board.

Above all, I thank my wife Sofia who constantly makes me discover who I am. Thanks for making beautiful things more beautiful.